Multiscale Simulation and Assessment of the Seismic Resilience of Communities

by

Omar A. Sediek

A dissertation submitted in partial fulfillment
of the requirements for the degree of
Doctor of Philosophy
(Civil Engineering and Scientific Computing)
in the University of Michigan
2021

Doctoral Committee:

Professor Sherif El-Tawil, Co-Chair
Associate Professor Jason P. McCormick, Co-Chair
Professor Atul Prakash
Associate Professor Seymour M.J. Spence

Omar A. Sediek

osediek@umich.edu

ORCID iD: 0000-0002-3369-2598

DEDICATION

To my beloved family and friends

ACKNOWLEDGEMENTS

During my Ph.D. journey, I have received a great deal of support and assistance. First, I would like to express my sincere gratitude to my advisors; Professor Sherif El-Tawil and Professor Jason McCormick; who offered me the honor to be one of their students. I learned a lot from them on the personal and academic sides. Their doors were always open to me anytime I needed help. Over the past four years, we have had regular constructive weekly meetings that allowed me to exchange ideas with them and figure out solutions for the tough problems I faced in my research. On the personal side, they appreciated the situation that I am an international student away from my family and friends. Both invited me and other students to their houses, which helped me a lot to overcome the homesickness I felt during these days.

I would also like to thank, Professor Prakash and Professor Spence for agreeing to serve on my dissertation committee. I am truly grateful for the support that they have offered, whether in the form of research advice, a letter of recommendation, serving as an employment reference, or just simple conversations in passing. I have had the privilege of taking the class that Professor Spence has taught, and it strengthened a great deal of admiration and respect that I already had for him.

My sincere thanks also go to the members of Prof. El-Tawil's research group (Andrew, Saqif, Szu-Yun, Tung-Yu, and Yunsu) and friends I have made in CEE (Christian and Malcolm) for sharing their knowledge and life experiences. I would also like to thank Omar Abdelatty,

TABLE OF CONTENTS

LIST OF TABLES

LIST OF FIGURES

LIST OF APPENDICES

ABSTRACT

Quantifying the seismic resilience of communities requires rigorous modeling of their behavior at disparate temporal (earthquakes – seconds vs. recovery – months) and spatial (component - meters vs. system - kilometers) scales. Hence, this dissertation has two main goals. The first one is to investigate the seismic behavior of components with heterogeneous scales in the community (i.e., member, building and community level studies) and further explore the effect of their behavior on the seismic resilience of communities over the relevant time scales. The second goal is to investigate the mutual interdependencies between the different systems of the community (i.e., engineering, social, etc.) during the disaster and the post-disaster recovery stages.

On the member level, measurements obtained from a 3D noncontact laser scanning technique are used to quantify the initial geometric imperfections of steel W-shape members. Based on the measured imperfections, a spectral approach that models the imperfections in each plate of the W-shape member as a 2D field of random vibrations is proposed. It is shown that although geometric imperfections can, in certain situations, influence column buckling behavior, their effect on nonlinear cyclic behavior is generally small and inconsistent. The capabilities of different machine learning classification and regression methods in predicting the seismic collapse behavior of deep steel W-shape columns in SMFs are explored. A dataset of more than nine hundred experimental and numerical results of deep steel W-shape columns with different attributes is assembled. The results suggest that machine learning algorithms that are continually updated with new experimental and computational data could inform future generations of design

specifications. The seismic collapse behavior of SMF hollow structural steel (HSS) columns under combined axial and drift loading is computationally studied through a validated finite element model. The simulation results are used to propose slenderness limits and design guidelines that incorporate key variables identified in the research to permit HSS columns to achieve highly ductile behavior.

On the building level, the extent of debris generation around collapsed reinforced concrete moment frame (RCMRF) buildings is characterized using a validated computational approach. A set of RC moment resisting frame structures with different heights is modeled under different ground motion records scaled up until they induce collapse of the building to assess the seismic debris field under different ground motion histories and building heights. The effect of building code requirements on debris field extent is also investigated.

On the community level, a scalable model that employs a simulation-based dynamic analysis, which models the behavior of the community at each time step as the seismic event occurs (time step in seconds) and as the community recovers after the event (time step in days) is developed. The developed model is employed to simulate the mutual interdependencies between the building portfolio, transportation network, and healthcare system in the community as well as to integrate post-earthquake household decision making when quantifying the seismic resilience of communities subjected to earthquake sequences. Incremental dynamic analysis (IDA) is used to develop fragility curves for mainshock-damaged structures, which are distinguished from the conventional fragility curves of intact structures. The capabilities of the developed models to support hazard mitigation planning are demonstrated through various case studies that highlight the effects of interdependencies between the different systems under consideration. Mitigation

strategies to improve seismic resilience of the prototype communities are also proposed and assessed.

CHAPTER 1

Introduction

1.1   General

The number of recorded natural disasters has increased dramatically over the last 50 years as shown in Figure 1-1. Severe earthquakes are one of the myriad types of disastrous events that communities can face and have catastrophic social and economic impact. It can take years for communities to recover (i.e., return back to their pre-earthquake state) from such events, if ever. Therefore, communities need to be prepared for such events to avoid or mitigate their severe consequences. The 2010 Haiti earthquake is a prominent example of this need. It was one of the most recent destructive earthquakes causing more than 316,000 deaths, around 300,000 injuries, and left around 1.3 million people homeless (DesRoches et al. 2011). The poor pre-earthquake socioeconomic conditions of Haiti severely affected its recovery capability. Due to lack of resources and preparedness for such an event, more than one million victims were left homeless for around 10 months (DesRoches et al. 2011). The overall economic losses associated with this event totaled between $7 and $14 billion (US) representing approximately 100% to 200% of Haiti's gross annual income (DesRoches et al. 2011).

The concept of community resilience has emerged from this need. Community resilience is defined as the ability of the physical infrastructure (e.g., buildings, lifelines, etc.) and socio-economic systems (e.g., organizations, facilities, etc.) to respond effectively and rebound quickly after natural events (e.g., earthquakes, hurricanes, etc.) or manmade disasters (e.g., terroristic

attacks, revolutions, etc.) in such a way so as to minimize social and economic disturbances to communities (Bruneau and Reinhorn 2007). The first step to enhance the seismic resilience of communities is to quantify it so as to be able to measure the effect of different mitigation strategies on the performance of the community.
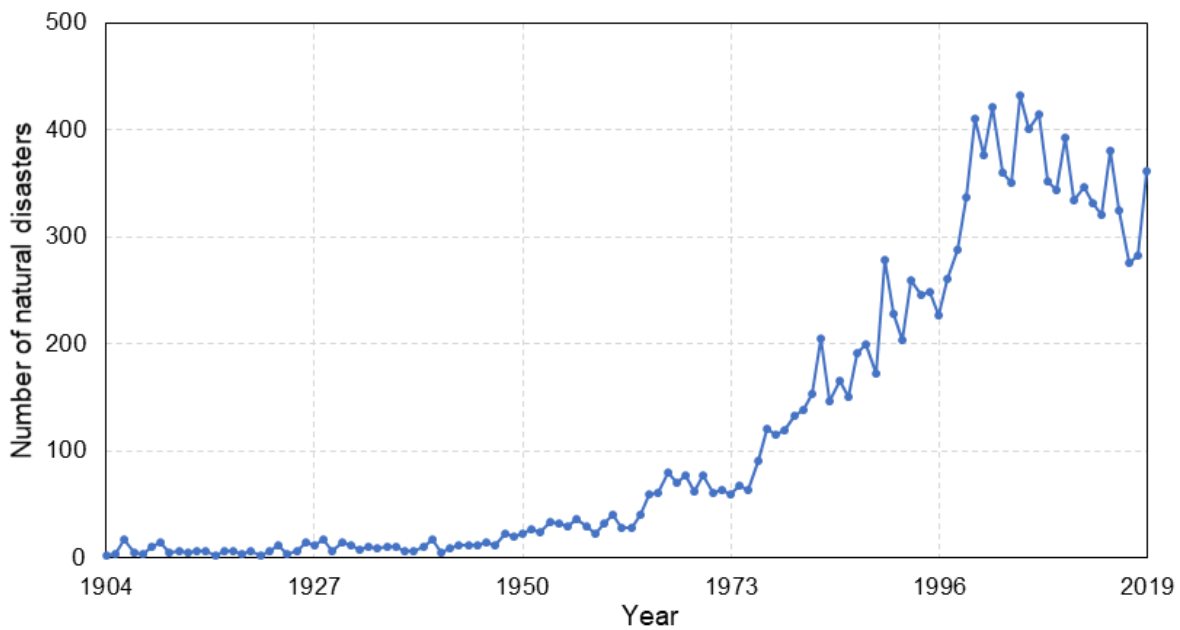
Figure 1-1. Number of recorded natural disaster events, All natural disasters (data from EMDAT 2020)

Quantifying the seismic resilience of communities requires rigorous modeling of their behavior at disparate temporal and spatial scales, e.g., component (meters) versus system level (kilometers), or during the seismic event (seconds) versus during recovery (months). Typical communities consist of different social, engineering, and economic systems of different scales. Detailed simulation models are commonly available to simulate the behavior of a single spatial or temporal level of a community, for example a single phase of a disaster or a specific component in the community. However, the interdependency between the different systems of society is

2

difficult to model and therefore frequently ignored. Interdependencies in modern communities are a double-edged sword. They are necessary to ensure high performance of the interconnected systems, but that interconnection itself also increases the vulnerability of these systems because cascading failures can occur. This effect is not well understood in the literature.

Motivated by these needs, this dissertation has two main goals. The first one is to investigate the seismic behavior of components with heterogeneous scales in the community (i.e., member, building, and community level studies as shown in Figure 1-2), and further explore the effect of their behavior on the seismic resilience of communities. Another key goal of this research is to investigate the mutual interdependencies between different systems of the community during the disaster (i.e., the seismic event) and the post-disaster recovery stages. This approach allows for further quantification of the effect of these interdependencies on community resilience, not only from a civil engineering perspective, but also from the perspective of other fields (e.g., social science).

1.2 Objectives

Along with the primary goals described above, specific objectives of this dissertation are summarized in Figure 1-2 and described as follows:

(1) Use high fidelity computational models to study the seismic inelastic response of different types of steel columns in special moment frames (SMFs). This objective can be divided into the following sub-objectives:

a. Characterize the initial geometric imperfections (IGIs) in steel wide flange (W-shape) members based on measured data from actual members. Synthesize the information to propose modeling recommendations for

3

incorporating IGIs in numerical simulations of steel W-shape members. Study the effect of incorporating IGIs in numerical models of deep steel W-shape columns as part of SMFs using the proposed modeling approach.

b. Explore different classification and regression machine learning methods to rapidly predict the seismic collapse behavior of deep steel W-shape columns subjected to combined axial and lateral loads as part of SMFs in terms of their failure mode and rotational capacity.

c. Develop and validate high fidelity computational models to assess the effect of key variables on the collapse behavior of hollow structural steel (HSS) columns subject to seismic demands in SMFs. Use the insight gained to propose new design guidelines for HSS columns in SMFs if the current AISC limits are not adequate.

(2) Develop and validate high fidelity computational models to assess the seismic collapse behavior of prototype reinforced concrete moment resisting frame (RCMRF) buildings with different heights. Explore the use of machine learning techniques to rapidly classify the collapse mode of RCMRF buildings. Characterize the seismic debris field generated from the collapse of RCMRF buildings using probabilistic methods.

(3) Develop a scalable model that employs a simulation-based dynamic analysis, which models the behavior of the community at each time step as the seismic event occurs (time step in seconds) and as the community recovers after the event (time step in days) to explicitly consider in-event interdependencies that can arise between the different systems making up the community.

(4)   Model the mutual interdependencies between the building portfolios, transportation networks, and healthcare systems in the community by considering the influence of bridge damage and debris from the collapse of buildings on the transportation network and the effect of post-earthquake behavior of the transportation network on mobilization of injuries to hospitals.

(5)   Address broader socio-technical considerations in resilience research by integrating the effect of household decisions in quantifying the seismic resilience of communities subjected to earthquake sequences (i.e., a series of seismic events and their aftershocks).
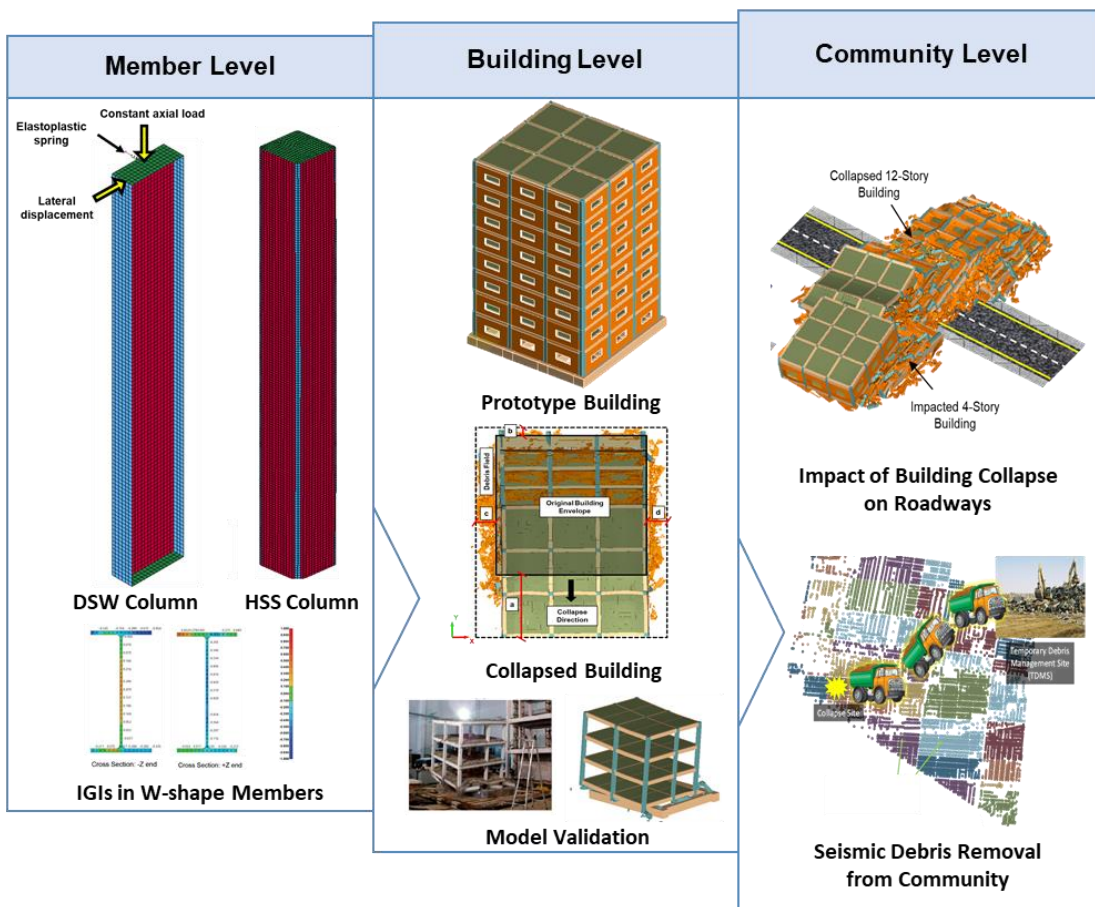
Figure 1-2. Summary of research objectives and scope of the dissertation

1.3   Organization of the Dissertation

A brief description of the seven chapters comprising this dissertation is provided below.

Chapter 1: Introduction. General information underlying the motivation and goals of this research is presented. The key research problems being addressed are outlined. The objectives and organization of this dissertation are also highlighted.

Chapter 2: Seismic Collapse Behavior of Special Moment Frame Steel Columns. This chapter presents three studies focused on the seismic collapse behavior of deep steel W-shape and HSS columns in special moment frames (SMFs).

The first study uses the measurements obtained from a 3D noncontact laser scanning technique to quantify the initial geometric imperfections of steel W-shape members to propose a spectral approach that models the imperfections in each plate of the W-shape member as a 2D field of random vibrations. The proposed modeling approach along with the traditional modal approach are used to study the sensitivity of numerical models to the choice of initial geometric imperfections. The studies are conducted at the member level using a set of deep steel W-shape SMF columns under combined axial and lateral cyclic loading.

The second study explores the capabilities of different machine learning classification and regression methods in predicting the seismic collapse behavior of deep steel W-shape columns in SMFs. The predictions identify the expected failure mode and rotational capacity. A dataset of more than nine hundred experimental and numerical results of deep steel W-shape columns with different attributes is assembled and compiled. The performance of the explored machine learning methods is compared with available methods in the literature and current specifications to predict the seismic collapse behavior of steel deep W-shape columns in SMFs.

The third study describes a computational effort for the seismic collapse behavior of SMF hollow structural steel (HSS) columns under combined axial and drift loading. A set of different HSS profiles are selected to cover a wide range of local and global slenderness ratios. Detailed finite element models of the HSS columns are created and validated against available experimental results. The simulation results are used to propose slenderness limits and design guidelines that incorporate key variables identified in the research to permit HSS columns to achieve highly ductile behavior.

Chapter 3: Seismic Debris Field for Collapsed RC Moment Resisting Frame Buildings. This chapter focuses on estimating the extent of debris generation around collapsed reinforced concrete moment frame (RCMRF) buildings using a validated computational approach that explicitly models the building collapse process and subsequent formation of the debris field. A set of RC moment resisting frame structures with different heights is modeled under different ground motion records scaled up until they induce collapse of the building to assess the seismic debris field under different ground motion histories and building heights. The collapse modes are classified using a deep neural network (DNN) based on ground motion parameters and building height. The extent of debris around the collapsed buildings is modeled in a probabilistic manner and then characterized using linear regression analysis. The effect of building code requirements on debris field extent is also investigated.

Chapter 4: A Scalable Model for In-Event Interdependencies in Community Resilience. This chapter describes a scalable model that employs a simulation-based dynamic analysis, which models the behavior of the community at each time step as the seismic event occurs (time step in seconds) and as the community recovers after the event (time step in days). As such, it permits explicit consideration of in-event interdependencies (i.e., during the hazard and the recovery stage) that can arise between the physical (i.e., buildings-related) and social (i.e., injured people-related)

systems of the community and provides detailed information about the temporal and spatial distribution of injuries/fatalities during the seismic hazard. The capability of the proposed model to support hazard mitigation planning is demonstrated through a case study that highlights the tradeoff between the physical and social costs of different mitigation strategies.

Chapter 5: Modeling Interdependencies Between the Building Portfolio, Transportation Network, and Healthcare System in Community Resilience. This chapter employs the scalable simulation model described in Chapter 4 to model the mutual interdependencies between building portfolios, transportation networks, and healthcare systems in a community. Bridge damage is combined with the accumulation of debris resulting from the collapse of buildings (characterized in Chapter 3) to determine their influence on the transportation network after an earthquake. The post-disaster origin-destination (O-D) patterns of households along with functionality of the road network in the community are used in a traffic analysis to update the traffic flow and time through the links of the transportation network. The updated traffic flow and time are used in a discrete event simulation (DES) environment to simulate the behavior of the healthcare system as well as the debris removal process in the aftermath of seismic events. The capability of the developed model to support hazard mitigation planning is demonstrated through a case study that highlights the mutual interdependencies between the three studied systems.

Chapter 6: Integrating Household Decisions in Quantifying the Seismic Resilience of Communities Subjected to Earthquake Sequences. This chapter employs the scalable simulation model described in Chapter 4 to integrate post-earthquake household decision making when quantifying the seismic resilience of communities subjected to earthquake sequences. A Simple Multi-Attribute Rating Technique (SMART) is used to model post-earthquake household decision making at the building level while earthquake sequences (i.e., aftershocks) are modeled using time-dependent analysis during recovery from the mainshock. Incremental dynamic analysis (IDA) is

used to develop fragility curves for mainshock-damaged structures which are distinguished from the conventional fragility curves of intact structures. The developed simulation model is demonstrated through a case study focused on modeling the seismic resilience of a community that comprises households with different socio-economic characteristics typical of a small U.S. community.

Chapter 7: Summary, Conclusions, and Future Research. This chapter summarizes the key contributions and findings that can be drawn from this research. Recommendations for future research in the area of multiscale simulation of seismic resilience of communities are presented.

1.4 Journal Publications from the Dissertation

The third study in Chapter 2 and the studies in Chapter 3 and Chapter 4 have been published as journal papers in American Society of Civil Engineers (ASCE) journals. The first study in Chapter 2 has been submitted to an ASCE journal and is under review. The second study in Chapter 2 has been submitted to the Engineering Structures journal and is under review. Papers from Chapter 5 and Chapter 6 are in preparation and will soon be submitted for publication. Details are listed below:

Sediek, O.A., Wu, T-Y, Chang, T-H, El-Tawil, S., and McCormick, J., "Measurement, Characterization and Modeling of Initial Geometric Imperfections in Wide-Flange Steel Members Subjected to Combined Axial and Cyclic Lateral Loading," Submitted for Publication in *Journal of Structural Engineering*, ASCE., Under Review. **(Chapter 2, first part)**

Sediek, O.A., Wu, T-Y, McCormick, J., and El-Tawil, S. "Prediction of Seismic Collapse Behavior of Deep Steel Wide-Flange Columns Using Machine Learning Methods and Steel

9

Column Net (SCNet)" Submitted for Publication in *Engineering Structures*, Under Review. **(Chapter 2, second part)**

Sediek, O.A., Wu, T-Y, McCormick, J. and El-Tawil, S. (2020), "Collapse Behavior of Hollow Structural Section Columns Under Combined Axial and Lateral Loading," *Journal of Structural Engineering,* 146 (6), 04020094, DOI: 10.1061/(ASCE)ST.1943-541X.0002637. **(Chapter 2, third part)**

Sediek, O.A., El-Tawil, S. and McCormick, J. (2021), "Seismic Debris Field for Collapsed RC Moment Resisting Frame Buildings," *Journal of Structural Engineering*, 147 (5), DOI: 10.1061/ (ASCE) ST. 1943-541X.0002985. **(Chapter 3)**

Sediek, O.A., El-Tawil, S. and McCormick, J. (2020), "Dynamic Modeling of In-Event Interdependencies in Community Resilience," *Natural Hazards Review*, 21 (4), 04020041, DOI: 10.1061/(ASCE)NH.1527-6996.000041. **(Chapter 4)**

Sediek, O.A., El-Tawil, S. and McCormick, J., "Modeling Interdependencies Between Building Portfolios, Transportation Networks, and Healthcare Systems in Community Resilience" Submitted for Publication in *Natural Hazards Review*, ASCE., Under Review. **(Chapter 5)**

Sediek, O.A., El-Tawil, S. and McCormick, J., "Integrating Household Decisions in Quantifying the Seismic Resilience of Communities Subjected to Earthquake Sequences" In preparation. **(Chapter 6)**

CHAPTER 2

Seismic Collapse Behavior of Special Moment Frame Steel Columns

2.1 General

This chapter presents three studies focused on the seismic collapse behavior of deep W-shape (DSW) and hollow structural steel (HSS) columns as part of special moment frames (SMFs).

The first study uses the measurements obtained from a 3D noncontact laser scanning technique for initial geometric imperfections in steel W-shape members to propose a spectral approach that models the imperfections in each plate of the W-shape member as a 2D field of random vibrations. The proposed modeling approach along with the traditional modal approach are used to study the sensitivity of numerical models to initial geometric imperfections. The studies are conducted at the member level using a set of DSW columns under combined axial and lateral cyclic loading as part of SMFs.

The second study explores the capabilities of different machine learning classification and regression methods in predicting the seismic collapse behavior of DSW columns as part of SMFs identified by their failure mode and rotation capacity. A dataset of more than nine hundred experimental and numerical results of DSW columns with different attributes is assembled and compiled. The performance of the explored machine learning methods is compared with available methods in the literature and current specifications to predict the seismic collapse behavior of steel DSW columns as part of SMFs.

11

The third study describes a computational effort to study the seismic collapse behavior of HSS columns under combined axial and drift loading as part of SMFs. A set of different HSS profiles are selected to cover a wide range of local and global slenderness ratios. Detailed finite element models of the HSS columns are created and validated against available experimental results. The simulation results are used to propose slenderness limits and design guidelines that incorporate key variables identified in the research to permit HSS columns to achieve highly ductile behavior.

2.2 Characterization and Modeling of Initial Geometric Imperfections in Wide-Flange Steel Members

2.2.1 Background

Initial geometric imperfections (IGIs) are introduced into wide-flange steel structural members during manufacturing, shipping and construction. It is common practice in finite element modeling to account for IGIs by superimposing a pre-assumed displacement field onto the mesh geometry (e.g., Elkady and Lignos 2015, 2018, and Cravero et al. 2020). The amplitude of the superimposed field, which is the maximum deviation of the real member from the nominal (i.e., perfect) shape of the member, is commonly selected based on manufacturing tolerances, e.g., in AISC 303 (2016) and ASTM A6 (2019).

Initial geometric imperfections in W-shape members can be categorized into global and local imperfections. Current finite element modeling practice typically accounts for both categories with the belief that this will yield more physically meaningful simulation results or that neglecting initial geometric imperfections will lead to missing a limit state. Global IGIs are generally assumed to be sinusoidal with a maximum amplitude that ranges from $L/1500$ to $L/500$ at member mid-height, where L is the length of the member (e.g., Elkady and Lignos 2015, 2018,

and Cravero et al. 2020). These numbers bracket the allowable limit of L/960 for hot rolled steel columns as specified in ASTM A6 (2019). The distribution of local IGIs is commonly assumed to be a combination of the first local buckling modes with an amplitude of b_f/250 or h/250, where b_f and h are the flange width and web depth of the member, respectively (e.g., Elkady and Lignos 2015,2018). As with global IGIs, these numbers originate from manufacturing tolerances in current specifications, e.g., in AISC 303 (2016).

Characterization of actual global and local IGIs is challenging due to their random nature. Schafer and Pekoz (1998) used a direct current differential transformer (DCDT) to measure both the global and local imperfections along the length of eleven identical cold formed C-sections. The Fourier transform of the measured imperfection profiles showed the existence of periodicity in the distribution of imperfections in the measured specimens. This insight was used to propose an imperfection spectrum that was then used to model artificial imperfection distributions having the same periodicity as the measured ones. Other similar studies can be found in Zhao et al. (2015) and Selvaraj and Madhavan (2018).

Cruise and Gardner (2006) used a series of overlapping measures from spring-loaded linear voltage transducers to measure the global and local imperfections along structural members. The imperfection profiles were characterized using two techniques: a classic Fourier transform and sum of half of sines. Later, Padilla-llano et al. (2014) used three different methods to measure the global and local imperfection distributions in cold-formed steel lipped C-sections: photogrammetry, laser scanning, and dial gauges. The first two methods are noncontact measurement methods that showed many advantages over manual (i.e., contact) methods, such as providing more detailed information about the imperfection distributions (e.g., 3-D point cloud). The measured imperfection profiles were represented using a series of sine terms.

2.2.2 Motivation and Objectives

The theoretical basis for current IGI modeling practice in earthquake engineering is weak. It stems from the thought that perfect members can suffer a bifurcation-type response when loaded, therefore the introduction of IGIs is necessary to direct the member to the 'correct' path. Four problems arise from this idea. First, the 'correct' path is being artificially imposed by selection of a specific IGI. Second, bifurcation behavior will not occur in a meaningful numerical model because the model itself will generate its own IGIs when loaded. The term 'meaningful' here implies a model that adequately considers both geometric and material nonlinearities and is solved on a platform with sufficient numerical precision to handle the small deformations, i.e., 'imperfections', that stem from the interaction of the member with its boundary conditions during the early steps of the analysis (Sediek et al. 2020a). Third, incorporating arbitrary global and local IGIs can introduce unknown interactions between global and local failure modes. Finally, and perhaps most importantly, this approach models a random effect using a deterministic method. Modelers frequently use the amplitude of both types of IGIs as calibration parameters to better match computational results to experimental data. Such calibration lumps the effects of initial stresses and strains in the member as well as boundary constraints under the general IGI guise. Examples of differing practices for modeling IGIs can be found in Fogarty and El-Tawil (2015), Elkady and Lignos (2015), Fogarty et al. (2017), Elkady and Lignos (2018), Wu et al. (2018a), Sediek et al. (2020b) and Cravero et al. (2020).

To the author's knowledge, there are no IGI studies for W-shape steel members. To address this research gap, a 3D noncontact laser scanning technique is employed to measure the initial global and local geometric imperfections in fourteen Taiwanese hot rolled H-section steel members that have similar cross-sectional properties to deep W-shape members used in the U.S. The measured imperfections are then used to characterize initial IGIs in W-shape steel members

using a spectral approach that characterizes IGIs as a random field superimposed on the ideal geometry of the specimen. Modeling recommendations for incorporating IGIs in numerical simulations are proposed then used to integrate IGIs into member level numerical models. The computational results are used to study the effect of incorporating IGIs in simulation models using the traditional modal approach from the literature and the proposed modeling approach, which is based on measured data.

2.2.3 Imperfection Measurement

Specimens Selection[1]

Deep steel W-shape (DSW) columns (W24 or deeper) are widely used in special moment frames (SMFs) in the U.S. to provide highly ductile behavior, as specified in the ASIC Seismic Provisions (2016a), during an earthquake. Seven Taiwanese hot rolled H-sections with dimensions similar to DSW sections often used as columns in the U.S. are considered in duplicate for a total of fourteen members. The sections are selected to cover a wide range of parameters, including local and global slenderness ratios. The chosen sections are shown in Figure 1-1 (circled green squares) along with comparable DSW sections used in the U.S. (black diamonds). The measured specimens are made of SN490B steel (F_y = 325 MPa) and have a length of 1800 mm with cross-sectional properties listed in Table 2-1. The specimens are designated as $d \times b_f$ - 'duplicate number'. For example, Specimen 150×75-1 is the first duplicate of the 150×75×5×7 section (d = 150 mm, b_f = 75mm, t_w = 5mm, and t_f = 7 mm).

---

[1] Dr. Tung-Yu Wu and Mr. Ting-Hao Chang performed the measurements and data processing of the imperfections at the National Taiwan University.

The measured specimens can be classified into three types based on their local slenderness ratios, $b_f/2t_f$ and h/t_w (b_f and t_f are the flange width and thickness, respectively, and h and t_w are the web depth and thickness, respectively), and the AISC high ductility limits (HDLs) for W-shape columns (AISC 2016a) as shown in Figure 1-1. Type I specimens satisfy the highly ductile limits (HDLs) for both $b_f/2t_f$ and h/t_w and can exhibit highly ductile behavior for any axial load level up to 0.9 P_y, where P_y is the axial yield capacity. Type II specimens are highly ductile only for specific axial load ratios based on h/t_w. Type III specimens are not highly ductile based on their $b_f/2t_f$ ratios. For more information about the characteristics of the different types of W-shape sections, the reader is referred to Fogarty and El-Tawil (2015). The global slenderness ratio around the weak axis of the measured specimens (L/r_y) ranges from 55 to 108.
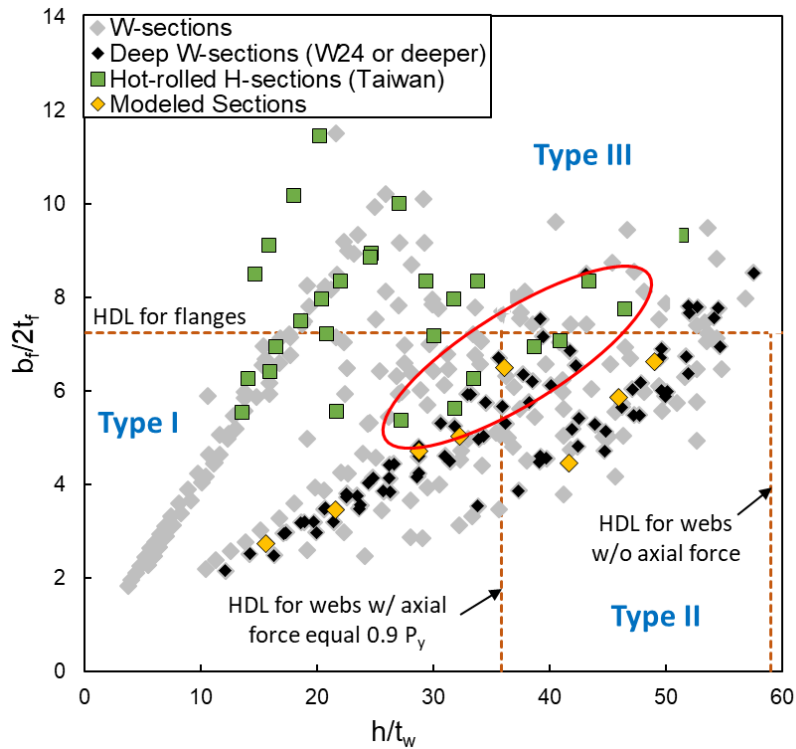
Figure 2-1. Local slenderness ratios of sections used in the measurements (circled green squares)

16

Table 2-1 Properties of measured hot rolled H-sections (all dimensions in mm)

Hot Rolled H-Section	d	b_f	t_w	t_f	r_y	$b_f/2t_f$	h/t_w	L/r_y
$150 \times 75 \times 5 \times 7$	150	75	5.0	7.0	1.66	5.4	27	108
$175 \times 90 \times 5 \times 8$	175	90	5.0	8.0	2.06	5.6	32	87
$198 \times 99 \times 5 \times 8$	198	99	5.0	8.0	2.24	6.2	36	80
$200 \times 100 \times 5.5 \times 8$	200	100	5.5	8.0	2.24	6.3	33	80
$248 \times 124 \times 5 \times 8$	248	124	5.0	8.0	282	7.8	46	64
$250 \times 125 \times 6 \times 9$	250	125	6.0	9.0	2.82	6.9	39	64
$300 \times 150 \times 6.5 \times 9$	300	150	6.5	9.0	3.29	8.3	43	55

Measurement Technique[1]

The specimens are first carefully cleaned of dirt and rust and then painted. A 3D noncontact laser-scanning technique, which has been widely used in different fields (Almutairi et al. 2018; Lee et al. 2020), is used to capture the IGIs. This technique is able to capture the complete geometric profile of the measured specimen with an accuracy of 0.048 mm. Each specimen is placed horizontally on a concrete block as shown in Figure 2-2(a). The 3D laser-scanner (Faro Quantum S Arm) is used to scan each specimen, providing a 3D point cloud for it. The scanning arm has two folds, as shown in Figure 2-2(a). This configuration allows for scanning of specimens with lengths up to 2.5 m by placing the scanning arm on a tripod at the midspan of the specimen. The arm can then be moved on either side of the measured specimen. The articulated scanning arm is a 7-axis arm (three joint translations combined with four joint rotations (360°)) with a spherical working volume to allow full three-dimensional movement of the attached scanning probe at the end of the arm. It has rotary optical encoders on each of its joints. The point cloud is sent to the host computer by processing the signals from these encoders using an error coding and temperature compensation technology (FARO 2016). The measurements were processed at a scan rate of 600,000 points/sec and took an hour for each specimen on average.

The scanning work is performed manually by guiding the scanning arm along the length of the measured specimen. Only the outer surface of the specimens is measured, which is sufficient

17

for the purposes of this study. Figure 2-2(b) and (c) show 3D and cross-sectional measurements for Specimen 248×124-1, respectively. The employed measurement technique provides detailed information about the complete geometric profile of the measured specimens that is then used to characterize the IGIs.

(a)

(b)

(c)
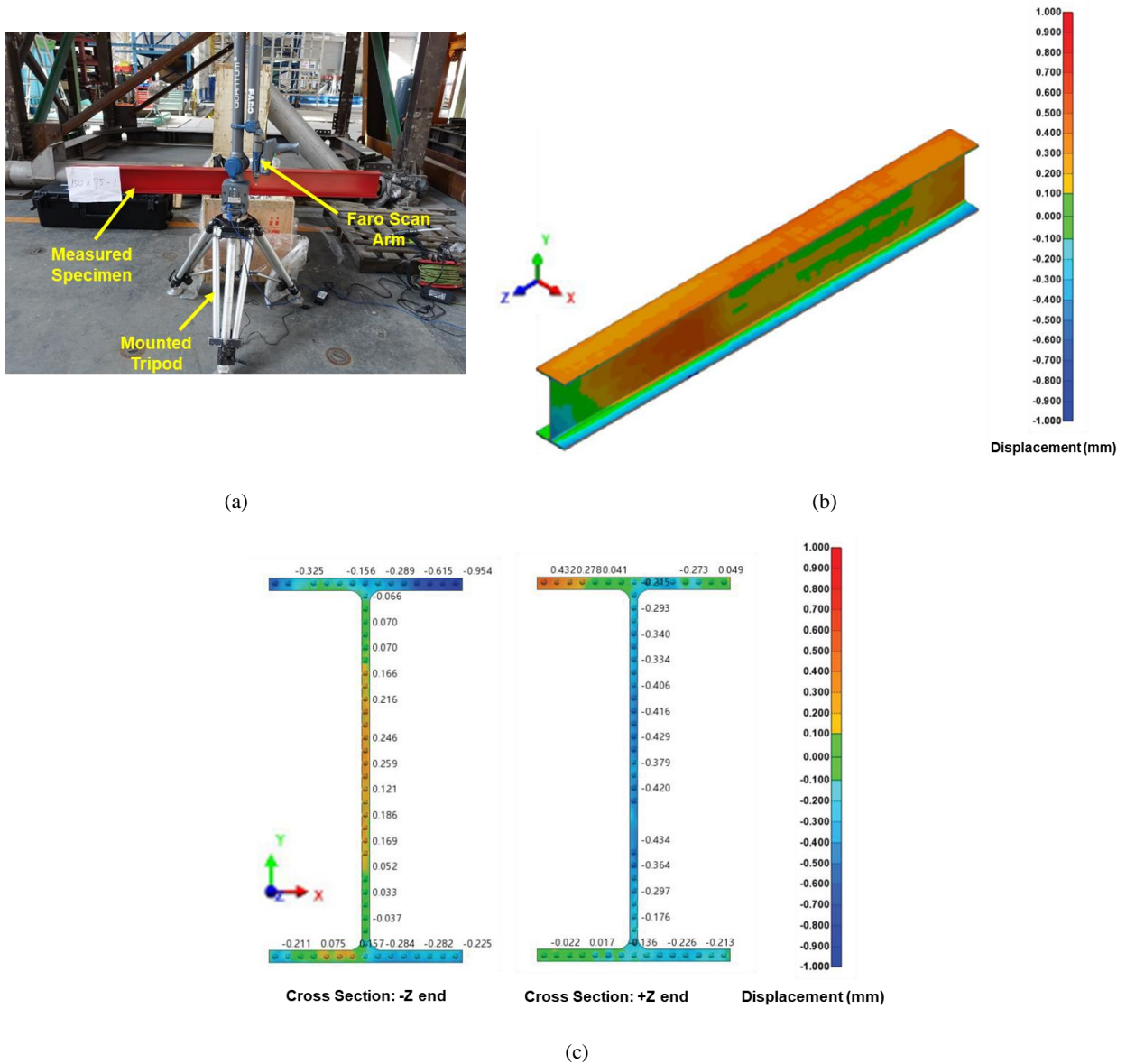
Figure 2-2 Illustration of: (a) Measurement setup; (b) 3D measurements of Specimen 248×124-1; and (c) cross-sectional measurements of Specimen 248×124 -1 (all units are mm)

18

Data Processing[1]

The process of extracting the IGI profiles from the specimen measurements starts with creating 3D models of the "ideal" specimens using the computer-aided drawing (CAD) software, AutoCAD (AutoDesk 2018). The measured data, which are uniformly distributed by specifying a minimum distance between points, is superimposed on the ideal 3D models of the specimens using the iterative least-square method (best-fit alignment) integrated in PolyWorks software. The deviation of measured data from the ideal model, i.e., the IGI profile, is extracted with respect to a designated coordinate system, as seen in Figure 2-2(b) and (c). The coordinates of the measured cross-sectional points on the specimens are extracted every 10 mm through the length of the specimens, resulting in 179 cross-sections for each specimen. Figure 2-3(a) shows the point cloud of an arbitrary cross section of Specimen 175×90-1. It should be noted that there are few cross sections that have only few or even no points at one corner of one of the flanges. To avoid this issue, these problematic cross sections are detected and replaced using shape-preserving piecewise cubic spline interpolation through the length of the specimen.

The mid-line of each cross section is obtained as shown in Figure 2-3(a) in order to assess the amount of imperfection along the length of the members (to exclude the effect of thickness variation) and create finite element models using shell elements. The mid-line of each cross section contains a total of 21 points distributed as 7 points in each of the two flanges and 7 points in the web with two additional common points between the web and the flanges (point 4 and 11 in Figure 2-3(b)). The 2D coordinates of the 21 points on the mid-line of each cross section extracted from measured data are compared to the ones extracted from the 3D ideal models as shown in Figure 2-3(b). The IGI is defined as the difference (in x and y directions) between the coordinates of the measured and ideal points.
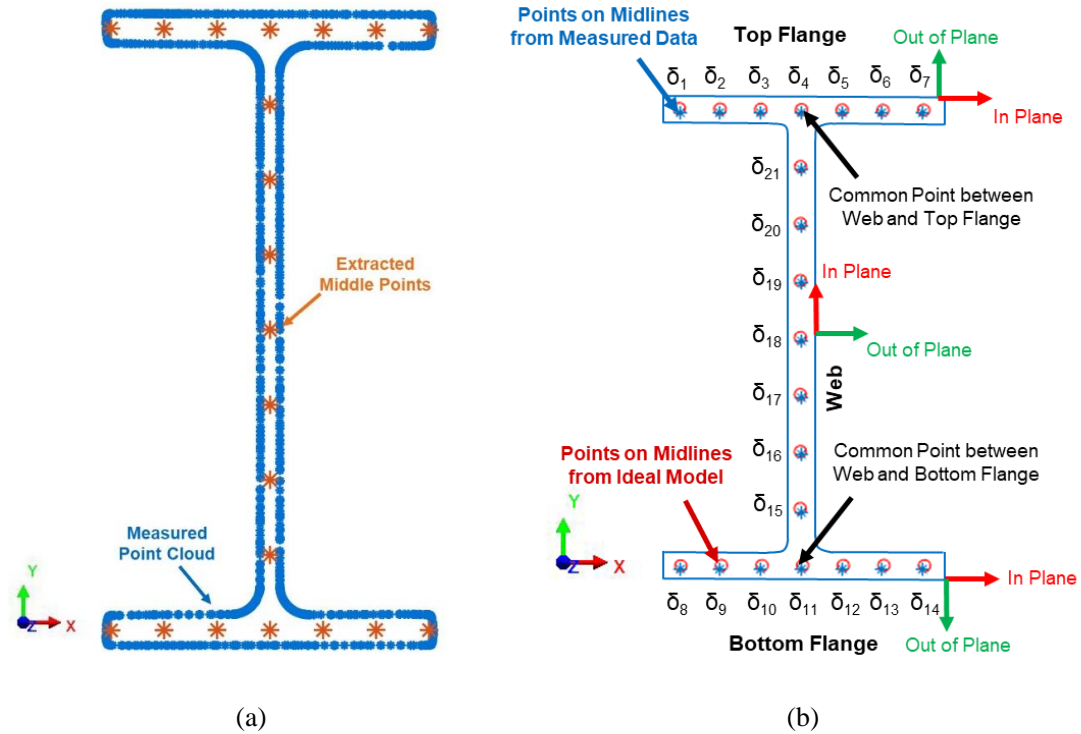
Figure 2-3 Illustration of: (a) measured point cloud for an arbitrary cross section of Specimen 175×90-1; (b) initial imperfection measurement for an arbitrary cross section of Specimen 150×75-1

The measured geometric imperfections (termed δ_1 through δ_{21}) are separated into three groups depending on the member element: top flange ($\delta_1 - \delta_7$), bottom flange ($\delta_8 - \delta_{14}$), and web ($\delta_{15} - \delta_{21}$), with δ_4 and δ_{11} as the two common points between the web and flanges as shown in Figure 2-3(b). Each imperfection group is separated into two categories: in-plane and out-of-plane. For the flanges, the differences between the coordinates of the measured and ideal points in the x and y direction, e.g., δ_{7x} and δ_{7y} at δ_7, are defined as the in-plane and out-of-plane imperfection, respectively (see Figure 2-3(b)). For the web, the directions of the in-plane and out-of-plane imperfections are opposite to those described for the flanges as shown in Figure 2-3(b). The above-described procedures are repeated for each cross section through the length of the measured specimens as shown in Figure 2-4, resulting in an "imperfection profile", which is a deviation plot for each point over the length of the member. In total, there are 21×2 imperfection profiles for

20

each specimen (including both in-plane and out-of-plane profiles). It should be noted that the deflection resulting from the member's self-weight is subtracted from the profiles although it was extremely small compared with the measured imperfections (i.e., with maximum of 0.0022 mm). The specimens are assumed to be cantilevered from both sides of the concrete block when evaluating the deflection resulting from the member's self-weight. Figure 2-5 shows the out-of-plane imperfection profiles for the top flange of Specimen 150×75-1. As shown, few high frequency noise signals exist in the measurements. However, these high frequency noise signals are not the dominant frequencies in the measured imperfection signals as will be discussed later.
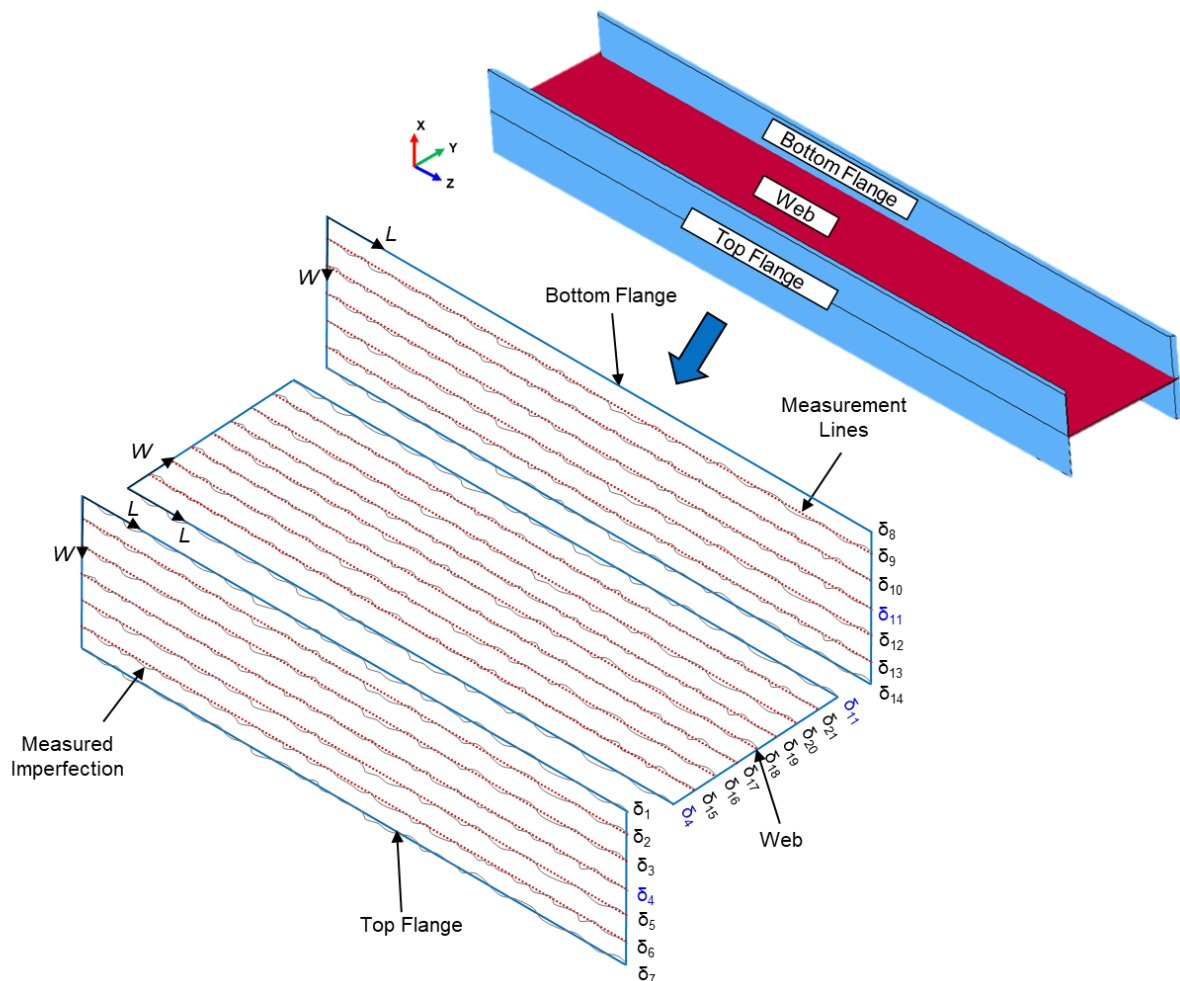
Figure 2-4 Imperfection measurements locations along top flange, bottom flange, and web plates

21
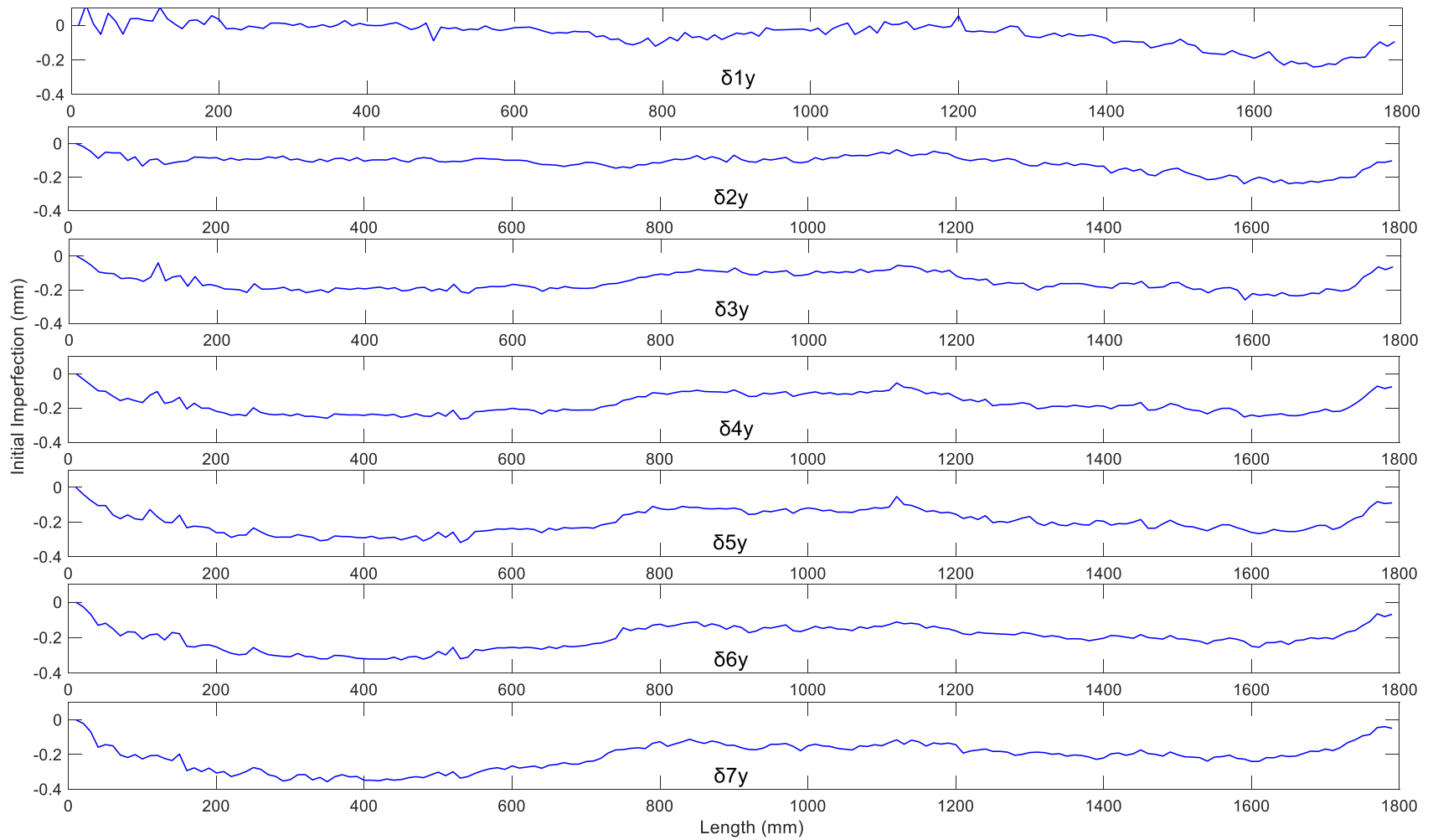
Figure 2-5 Measured out-of-plane imperfection profile for top flange (δ_{1y}- δ_{7y}) in the Specimen 150×75-1

Comparison with Specification Limits

The maximum measured imperfections are compared to the permitted variations in W-shape members indicated in the Standard Specification for General Requirements for Rolled Structural Steel Bars, Plates, Shapes, and Sheet Piling (ASTM A6 2019) as well as the Dimensions, Mass and Permissible Variations of Hot Rolled Steel Sections in Taiwan (CNS 2012). The permitted geometric variations for W-shape members (i.e., IGIs) are classified into local cross-sectional and global variations. The local cross-sectional variations are defined through the variation in section depth (Δd), variation in flange width (Δb_f), flange out-of-square ($T+T'$), web out-of-center (E), and maximum depth at any cross section over theoretical depth (c). The definition of each variation is illustrated graphically in Figure 2-6(a). The global variations are defined through either the maximum global variation around the strong axis (i.e., camber) or around the weak axis (i.e., sweep) as shown in Figure 2-6(b) and (c), respectively.

| (a) | (b) | (c) |
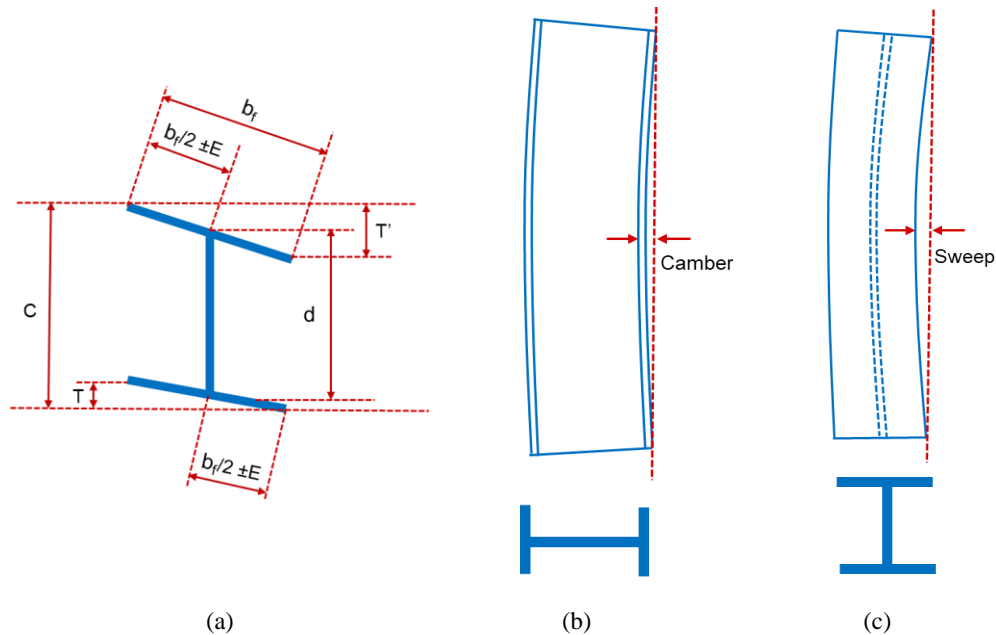
Figure 2-6 Illustration of allowable: (a) local cross-sectional; (b) in-plane global; and (c) out-of-plane global variations in W-shape members specified by ASTM (2019)

The mean, maximum, and standard deviation of the measured Δd, Δbf, $T+T'$, E, c, sweep and camber are evaluated among the fourteen specimens using Equations (2-1) through (2-7) and listed in Table 2-2 with the corresponding allowable values as specified in both ASTM (2019) and CNS (2012). As shown, all of the measured imperfections fall within the allowable specified limits. In fact, the mean measured imperfections are far from the allowable limits in ASTM (2019) and CNS (2012) which implies that using the allowable tolerances as maximum amplitude for initial geometric imperfections in numerical models of W-shape members is not always realistic.

$$\Delta d = \delta_{4y} - \delta_{11y} \tag{2-1}$$

$$\Delta b_f = \begin{cases} \sqrt{\left(b_f + \delta_{7x} - \delta_{1x}\right)^2 + \left(\delta_{7y} - \delta_{1y}\right)^2} - b_f, & \text{top flange} \\ \sqrt{\left(b_f + \delta_{14x} - \delta_{8x}\right)^2 + \left(\delta_{14y} - \delta_{8y}\right)^2} - b_f, & \text{bottom flange} \end{cases} \tag{2-2}$$

$$T + T' = \left|\delta_{7y} - \delta_{1y}\right| + \left|\delta_{14y} - \delta_{8y}\right| \tag{2-3}$$

$$E = \begin{cases} max \left\{ \dfrac{\sqrt{\left(\dfrac{b_f}{2} + \delta_{7x} - \delta_{4x}\right)^2 + \left(\delta_{7y} - \delta_{4y}\right)^2} - \dfrac{b_f}{2}}{\sqrt{\left(\dfrac{b_f}{2} + \delta_{4x} - \delta_{1x}\right)^2 + \left(\delta_{4y} - \delta_{1y}\right)^2} - \dfrac{b_f}{2}} \right. , & \text{top flange} \\[40pt] max \left\{ \dfrac{\sqrt{\left(\dfrac{b_f}{2} + \delta_{14x} - \delta_{11x}\right)^2 + \left(\delta_{14y} - \delta_{11y}\right)^2} - \dfrac{b_f}{2}}{\sqrt{\left(\dfrac{b_f}{2} + \delta_{11x} - \delta_{8x}\right)^2 + \left(\delta_{11y} - \delta_{8y}\right)^2} - \dfrac{b_f}{2}} \right. , & \text{bottom flange} \end{cases} \tag{2-4}$$

$$C = max \begin{Bmatrix} \delta_{1y} \\ \delta_{7y} \end{Bmatrix} - min \begin{Bmatrix} \delta_{8y} \\ \delta_{14y} \end{Bmatrix} \tag{2-5}$$

$$Camber = \frac{\delta_{1y} + \delta_{2y} + \delta_{3y} + \delta_{4y} + \delta_{5y} + \delta_{6y} + \delta_{7y}}{7} \tag{2-6}$$

$$Sweep = \frac{\delta_{2x} + \delta_{6x} + \delta_{9x} + \delta_{13x}}{4} \tag{2-7}$$

24

Table 2-2 Comparison of measured imperfections with permitted variations in W-shape members indicated in ASTM (2019) and CNS (2012)

Parameter	Mean (mm)	Maximum (mm)	Standard of deviation (mm)	Permitted (mm) (ASTM 2019)	Permitted (mm) (CNS 2012)
Δd	0.6	1.8	0.50	4.0	2.0
Δb_f	0.7	1.4	0.40	6.0	2.0
$T+T'$	1.1	2.5	0.70	6.0	Min. of 0.02 b_f and 3.0
E	0.3	0.7	0.10	5.0	2.0
c	0.5	1.6	0.40	6.0	Max. of 0.02 b_f and 3.0
Camber	0.2	0.4	0.07	1.8	1.8
Sweep	0.5	1.6	0.30	1.8	1.8

2.2.4 IGI Modeling

The traditional modal approach (used in the literature) for modeling IGIs in W-shape members is a one-dimensional (1D) modal approach that employs a location-independent superposition of a set of global and local buckling modes into an imperfection field. The mode shapes are obtained from an elastic eigenvalue analysis and scaled such that the maximum deflection is equal to one. The weight of each mode is chosen based on the maximum manufacturing tolerances as discussed earlier. As noted earlier, although the traditional modal approach is quite convenient to implement, there is no evidence from actual measurements of IGIs in W-shape members to assume that they are constrained to follow specific buckling mode shapes.

A two-dimensional (2D) random field spectral method, which considers the web and flange plates to be a random 2D field, is used for characterizing the measured IGIs. This method is more rational than the modal approach because it can explicitly account for the random nature of IGIs

(Zeinoddini and Schafer 2012). Three separate elements of the W-shape cross-section are considered: top flange, bottom flange, and web. The plates are assumed connected together at specific locations as shown in Figure 2-4. The discrete 2D Fourier transform (Bendat and Piersol 1971) is used to investigate periodicity in the measured imperfections using the following equation:

$$S_f(f_l, f_w) = DFT\left(f_0(\hat{l}, \hat{w})\right) = \frac{1}{N_1 N_2} \sum_{n_1=0}^{N_1-1} \left(e^{-2\pi i k_1 (n_1/N_1)} \sum_{n_2=0}^{N_2-1} e^{-2\pi i k_2 (n_2/N_2)} f_0(\hat{l}, \hat{w}) \right) \qquad (2\text{-}8)$$

where f_0 is the measured imperfection field, $\hat{l}$ and $\hat{w}$ is the normalized location (with respect to the plate dimensions) on the 2D plates based on the axes shown in Figure 2-4 (i.e., L and W), N_1 and N_2 are the number of points (discretization) in each direction, f_l and f_w are the imperfection frequencies in L and W directions, respectively, and k_1 and k_2 are the wave numbers in each direction. It should be noted that f_l and f_w are dimensionless based on the fact that the transforms are evaluated using the normalized location (i.e., $\hat{l}$ and $\hat{w}$) instead of the actual location (i.e., l and w). This is attributed to the fact that the measured specimens do not possess the same flange width.

The 2D transform provides information about the amplitude and frequency of the measured imperfection field. The dominant sine waves in the imperfection field are represented by the peaks in the transform. Despite the differences in the measured imperfection fields for the considered specimens, the 2D transforms have relatively similar shapes with one or two peaks at low frequencies in both directions followed by low to no content in higher frequencies. The consistent location of peaks in the 2D transforms reveal the existence of periodicity in the measured imperfection fields, which was also seen by Schafer and Pekoz (1998) in the 1D Fourier transform of the measured imperfection profiles in cold-formed members. Therefore, an average transform

can be used to characterize the IGIs in W-shape members. The average transform for each imperfection profile (i.e., in-plane and out-of-plane) in each plate is obtained from the fourteen measured specimens as shown in Figure 2-7.

The obtained 2D average transforms are termed "imperfection spectrums" following Schafer and Pekoz (1998), although they used the term in a 1D sense instead of the 2D application employed here. The imperfection spectrums can be used to generate new artificial imperfection distributions in the same way an earthquake response spectrum is used to synthesize artificial earthquake signals. More discussion about this type of generation can be found in the literature on random vibrations (Soong and Grigoriu 1993, and Lin 1996) and specific discussions on this particular application (IGIs) can be found in Schafer and Pekoz (1998).

By modifying the 1D approach in Schafer and Pekoz (1998) to 2D, the imperfection signal can be expressed as:

$$
\begin{aligned}
\hat{f}(\hat{l}, \hat{w}) = \sum_{n_1=0}^{N_1-1} \sum_{n_2=0}^{N_2-1} \sigma_{n_1 n_2} \big(& A_{n_1 n_2} \cos(\omega_{n_1} \hat{l}) \cos(\omega_{n_2} \hat{w}) \\
& + B_{n_1 n_2} \sin(\omega_{n_1} \hat{l}) \cos(\omega_{n_2} \hat{w}) \\
& + C_{n_1 n_2} \cos(\omega_{n_1} \hat{l}) \sin(\omega_{n_2} \hat{w}) + D_{n_1 n_2} \sin(\omega_{n_1} \hat{l}) \sin(\omega_{n_2} \hat{w}) \big)
\end{aligned}
\tag{2-9}
$$

where $\hat{f}$ is the generated imperfection signal; $\sigma_{n_1 n_2}$ is the square root of the volume under the n_1, n_2 discretization of the imperfection spectrum; ω_{n_1} and ω_{n_2} are the circular frequencies at the n_1, n_2 discretization of the imperfection spectrum; and $A_{n_1 n_2}$, $B_{n_1 n_2}$, $C_{n_1 n_2}$, and $D_{n_1 n_2}$ are independent gaussian random variables with zero mean and unit variance. The generated imperfection signal, which is sensitive to the number of discretizations (N_1 and N_2) and cut off frequency in each direction (ω_{N_1} and ω_{N_2}), is normalized to have a unit maximum amplitude. N_1, N_2, ω_{N_1} and ω_{N_2} are determined by the modeler. However, the quality of the generated signal with respect to the measured signals can be investigated by performing a 2D Fourier transform of the

generated signals and comparing it to the imperfection spectrums shown in Figure 2-7. It should be also noted that the proposed regeneration approach cuts the high frequency noise imposed during the measurements as was shown in the measured profile in Figure 2-5.
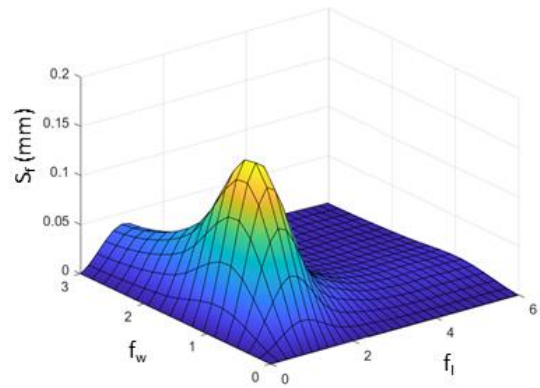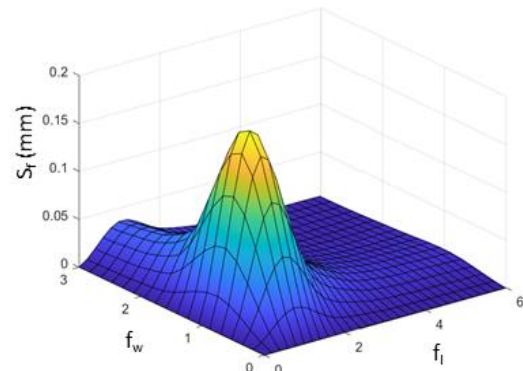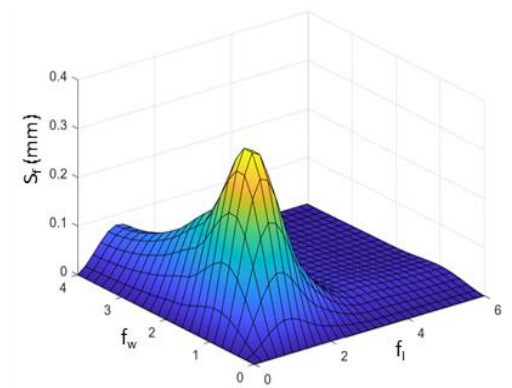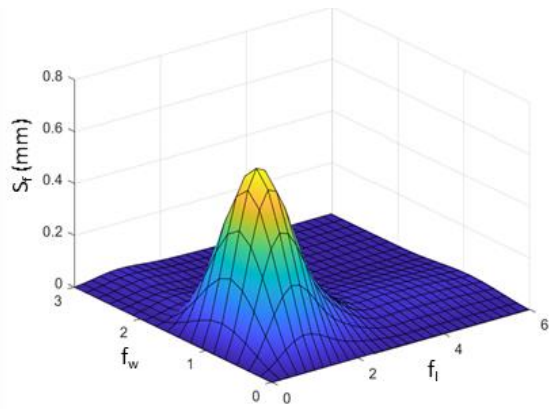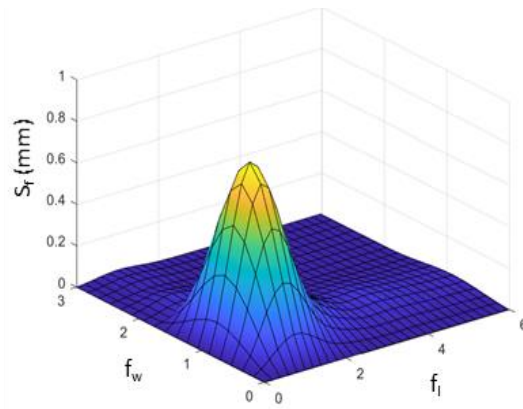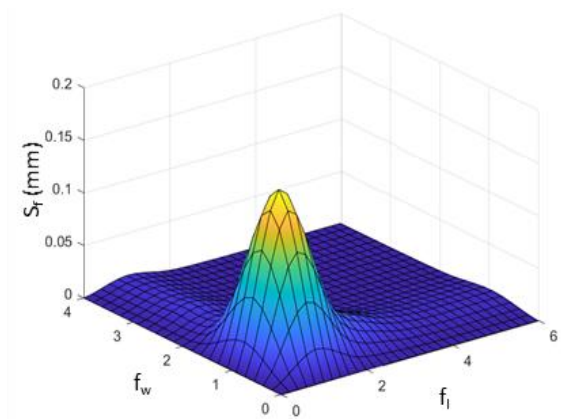
Figure 2-7 Measured average 2D imperfection spectra of: (a) out-of-plane profile of top flange; (b) out-of-plane profile of bottom flange; (c) out-of-plane profile of web; (d) in-plane profile of top flange (e) in-plane profile of bottom flange; and (f) in-plane profile of web

Idealized IGI Spectra

The average 2D imperfection spectrums shown in Figure 2-7 are idealized based on the model defined by Equations 2-10 through 2-12, which are similar to those used for earthquake response spectrum analysis:

$$S_f(f_l, f_w) = min \begin{cases} S_{fl}(f_l) \\ S_{fw}(f_w) \end{cases} \tag{2-10}$$

$$S_{fl}(f_l) = \begin{cases} a_1 f_l, & f_l < f_{la} \\ a_1 f_{la}, & f_{la} \le f_l \le f_{lb} \\ a_2 f_l^{-a_3}, & f_l > f_{lb} \end{cases} \tag{2-11}$$

$$S_{fw}(f_w) = \begin{cases} a_4 f_w, & f_w < f_{wa} \\ a_4 f_{wa}, & f_{wa} \le f_w \le f_{wb} \\ a_5 f_w^{-a_6}, & f_w > f_{wb} \end{cases} \tag{2-12}$$

The average imperfection spectrums are divided into three parts in the two primary directions, *L* and *W* shown in Figure 2-4: linear, constant, and descending power curves. The imperfection frequencies separating those parts are defined as f_{la}, f_{lb}, f_{wa}, and f_{wb}. S_f is the amplitude of the idealized 2D imperfection spectrum. S_{fl} and S_{fw} are the amplitudes of the idealized imperfection spectrums in the *L* and *W* directions, respectively. The parameters $a_1 - a_6$ are obtained using curve fitting for each part in each direction separately (Table 2-3). The resulting idealized imperfection spectrums are plotted in Figure 2-8 with the coefficient of determination R^2 for the total curve shown on each plot. The average R^2 for the idealized curves is 0.855 which is deemed acceptable for such a complex idealization. The idealized imperfection spectrums can then be used to generate new normalized imperfection profiles for different W-shape members using Equation (2-9).

Table 2-3 Parameters of the proposed idealized 2D imperfection spectra

Imperfection Profile	Coefficient									
	f_{la}	f_{lb}	f_{wa}	f_{wb}	a_1 (mm)	a_2 (mm)	a_3	a_4 (mm)	a_5 (mm)	a_6
out-of-plane, top flange	0.80	1.29	0.80	1.15	0.20	0.30	2.37	0.20	0.21	1.61
out-of-plane, bottom flange	0.90	1.29	0.80	1.06	0.21	0.35	2.31	0.24	0.22	1.83
out-of-plane, web	0.95	1.21	0.90	1.15	0.39	0.60	2.13	0.41	0.46	1.29
in-plane, top flange	0.95	1.19	0.80	1.00	0.69	1.06	2.16	0.81	0.72	3.14
in-plane, bottom flange	0.95	1.19	0.75	1.02	0.89	1.38	2.34	1.13	0.97	3.28
in-plane, web	0.95	1.15	0.80	1.02	0.17	0.23	2.11	0.20	0.18	2.57
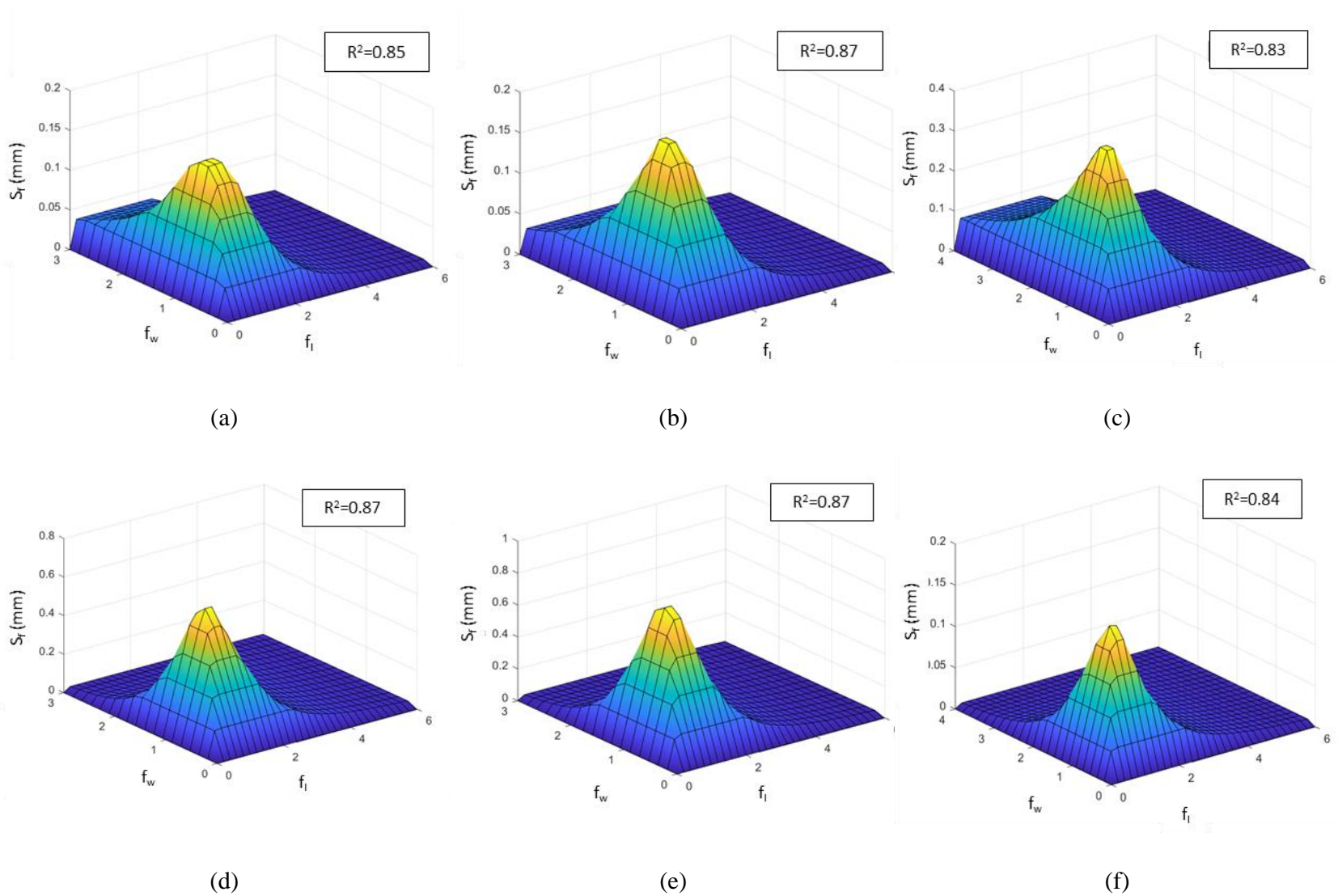
Figure 2-8 Idealized 2D imperfection spectra for: (a) out-of-plane profile of top flange; (b) out-of-plane profile of bottom flange; (c) out-of-plane profile of web; (d) in-plane profile of top flange; (e) in-plane profile of bottom flange; and (f) in-plane profile of web

The maximum amplitudes obtained from the measured results are first normalized to the thickness of each element (i.e., flange and web), which can be treated as a plate. This normalization is attributed to the difference between the web and flange thicknesses of the measured specimens. Then, the normalized values are used in a linear regression analysis to provide mathematical expressions to calculate the maximum amplitude in each direction for each of the three section elements. The imperfection profiles are scaled to the maximum amplitude in each direction. The flanges are assumed to have the same imperfection amplitude, but different profiles (i.e., different spectrums with the same amplitude expression). The maximum amplitudes are expressed as follows:

$$\frac{\delta_{max,out_f}}{t_f} = 0.00017\frac{L}{r_{yf}} - 0.0093\frac{b_f}{2t_f} \tag{2-13}$$

$$\frac{\delta_{max,in_f}}{t_f} = 0.00021\frac{L}{r_{xf}} + 0.019\frac{b_f}{2t_f} \tag{2-14}$$

$$\frac{\delta_{max,out_w}}{t_w} = 0.0017\frac{h}{t_w} + 5.51 * 10^{-5}\frac{L}{r_{yw}} \tag{2-15}$$

$$\frac{\delta_{max,in_w}}{t_w} = 0.00044\frac{h}{t_w} + 0.00097\frac{L}{r_{xw}} \tag{2-16}$$

where δ_{max,out_f} and δ_{max,in_f} are the maximum out-of-plane and in-plane imperfection amplitudes of the flange, respectively; δ_{max,out_w} and δ_{max,in_w} are the maximum out-of-plane and in-plane imperfection amplitudes of the web, respectively; r_{yf} and r_{xf} are the radius of gyration about the weak and strong axes of the flange plate, respectively; and, r_{yw} and r_{xw} are the radius of gyration about the weak and strong axes of the web plate, respectively. The coefficients of determination (R^2) of the proposed expressions are 0.80, 0.85, 0.93, and 0.85 for Equations (2-13) to (2-16), respectively.

2.2.5 Member-Level Computational Model Sensitivity to IGIs

Finite Element Modeling

The effect of incorporating initial geometric imperfections in numerical models of individual column members subjected to combined axial and lateral loads is investigated. A total of sixteen columns with eight different DSW sections (A992 steel) are selected to cover a wide range of local and global slenderness ratios (i.e., h/t_w, $b_f/2t_f$, and L/r_y) as can be seen in Figure 1-1 and Table 2-4. The loading protocol consists a force-controlled constant axial compressive load and a displacement-controlled lateral load applied at the top of the column. Three levels of constant axial compressive loads are investigated: $0.2P_y$, $0.3P_y$, and $0.4P_y$, where P_y is the axial yield capacity. The lateral load regime employs the cyclic ratcheting protocol designated CR2 in Wu et al. (2018a). The protocol was developed to represent the drift history at the top of first-story columns in a special moment resisting frame (SMF) during vertical progressive collapse due to an earthquake.

Table 2-4 Properties of the studied DSW columns

Section (in.×lb/ft)	h/t_w	$b_f/2t_f$	L/r_y
W24×76	49.0	6.6	81.3
W24×76	49.0	6.6	115.6
W24×84	45.9	5.9	80.0
W24×84	45.9	5.9	101.5
W24×335	15.6	2.7	48.3
W24×335	15.6	2.7	79.9
W27×161	36.1	6.5	52.0
W27×161	36.1	6.5	70.6
W27×217	28.7	4.7	50.6
W27×217	28.7	4.7	70.5
W30×148	41.6	4.4	78.9
W30×148	41.6	4.4	100.0
W30×235	32.2	5.0	51.3
W30×235	32.2	5.0	80.3
W30×357	21.6	3.5	49.5
W30×357	21.6	3.5	69.2

Detailed finite element models of the DSW columns are created using the commercial software Hypermesh and analyzed using the explicit solver of the general-purpose finite element software LS-DYNA as shown in Figure 2-9. The columns are discretized using fully integrated shell elements (ELFORM 16) based upon Mindlin–Reissner plate theory and formulated by Engelmann et al. (1989). The mesh size is the same as that used in Wu et al. (2018a), who conducted a mesh sensitivity study. A combined isotropic/kinematic hardening material model (MAT_153) developed by Huang and Mahin (2010) is assigned to the shell elements to capture the cyclic behavior of the studied column. The hardening parameters are calibrated to the true stress-true strain model by Arasaratnam et al. (2011) as done in Wu et al. (2018a). For all column models, the bottom end is assumed to be fully fixed, while in-plane rotation of the top end is restrained by an elastoplastic spring with properties determined by a subassembly analysis as shown in Figure 2-9 (Wu et al. 2018a). The validation of above modeling techniques can be seen in Fogarty el al. (2017), Wu et al. (2019), and Sediek et al. (2020b).

Simulations are conducted three times for each of the studied columns. The first simulation does not contain IGIs. The second employs IGIs as modeled by the "traditional" modal approach where the global imperfection is assumed to be a sinusoidal shape with maximum amplitude similar to Elkady and Lignos (2018), i.e., L/1500 at the mid-height, while the local imperfections are based on the buckling modes specified by Elkady and Lignos (2018) from conventional buckling analysis with amplitudes of b_f/250 and h/250 for the flanges and web, respectively. The third has IGIs computed using the proposed random field spectral approach described earlier. The imperfection profile is generated randomly using Equation (2-9) based on the average 2D imperfection spectrums shown in Figure 2-7 and the maximum amplitude is evaluated using Equations (2-13) through (2-16). It should be noted that the generated imperfection field, being

35

random, is based on one realization. Constructing new imperfection fields will lead to different profiles and thus different simulation results.
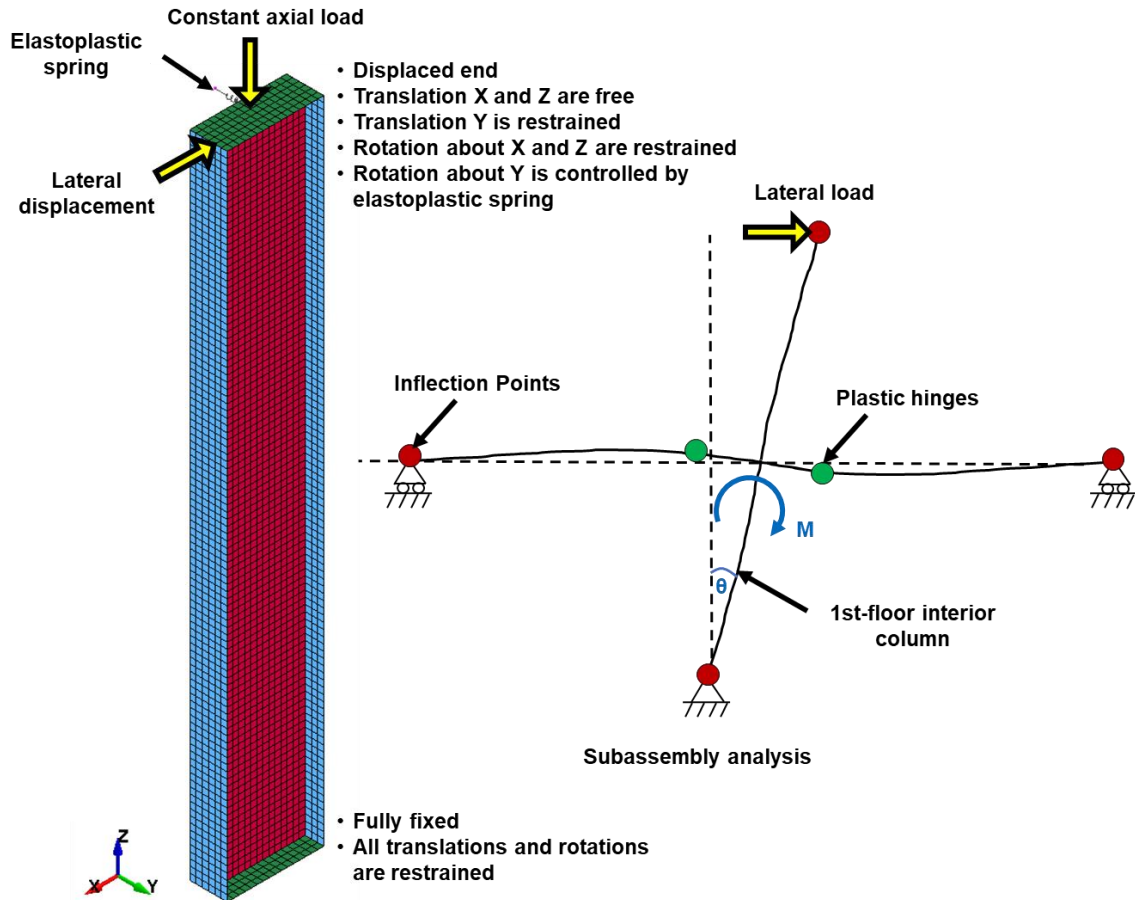
Figure 2-9 Mesh and boundary conditions used in finite element models of studied columns

Performance Parameters

Two performance parameters are used to quantitatively assess the effect of integrating IGIs using both approaches: ratio of maximum moment (RMM) and ratio of dissipated energy (RDE). RMM and RDE are defined as the ratios of the maximum end moment and dissipated energy of the imperfect column (i.e., traditional modal or proposed spectral) to that of the perfect column

(i.e., no imperfection), respectively. Ratios less than unity imply a negative effect of IGIs on the behavior, i.e., IGIs degrade performance as is commonly assumed, and vice versa.

Results and Discussion

The results with respect to the considered performance parameters, RMM and RDE, under different levels of initial axial load are listed in Table 2-5. The columns are designated as W-X-Y, where "W" is the W-shape profile, "X" is the global slenderness ratio (L/r_y), "Y" is the initial axial load ratio. For example, W24×84×80-20 is the W24×80 column with a global slenderness ratio of 80 subjected to an initial axial load of $0.2P_y$.

Effect of Local Slenderness Ratios

Figure 2-10 and Figure 2-11 plot the relationship between the slenderness ratios and performance parameters. Contrary to common assumption, it is evident that incorporating IGIs can sometimes lead to a positive effect on the performance of DSW columns with respect to the perfect case (i.e. without incorporating IGIs) as by shown by the points above the unity lines in Figure 2-10 and Figure 2-11. It is also clear that there is no general positive or negative trend with respect to the slenderness ratios. This lack of consistency can be seen in the different directions of the trend lines of the plots. For example, compare W24×84-80-30 ($h/t_w = 45.9$, $b_f/2t_f = 5.9$) and W24×76-115-30 ($h/t_w = 49$, $b_f/2t_f = 6.6$), which have similar local slenderness ratios (circled in Figure 2-10 and Figure 2-11). The traditional modal approach has a negative effect on both the maximum moment and dissipated energy of W24×84-80-30 (RMM = 0.88, RDE = 0.95), while the effect is positive for W24×76-115-30 (RMM = 1.06, RDE = 1.27). On the other hand, although the proposed spectral imperfection has a negative effect on the maximum moment for both columns (RMM = 0.99 for both columns), it has an inconsistent effect on the dissipated energy (RDE = 0.84 and 1.16 for W24×84-80-30 and W24×76-115-30, respectively). In general, the

37

overall correlation between both approaches is weak. The average correlation coefficient between the results of both approaches is 0.54 and 0.56 for RMM and RDE, respectively.

Effect of IGI Randomness

Two representative columns are used to study the effect of randomness in the imperfection field: W30×357-50-30 (h/t_w = 21.6, $b_f/2t_f$ = 3.5, a stocky Type I column as shown in Figure 1-1) and W24×76-115-30 (h/t_w = 49, $b_f/2t_f$ = 6.6, a slender Type II column as shown in Figure 1-1). Thirty-two different imperfection profiles are randomly generated for each column model using the spectral approach. In addition, the effect of the sign of the global and local imperfections (i.e., positive or negative) in the traditional modal approach is considered through two additional models. Figure 2-12 shows the computed moment-rotation behavior for the 32 spectral realizations, two modal cases and the perfect column. Also shown in Figure 2-12 are the deformed shapes (in the inserts) just before failure of the two columns. For the spectral case, the deformed shapes are for the two realizations with the largest and smallest peak moments.

Comparing Figure 2-12(a) and Figure 2-12(b) shows that in the latter load cycles, the more slender Type II column responses are more sensitive to the spectral imperfection profile than the stockier Type I column. The same sensitivity can also be seen in the modal approach. As shown in Figure 2-12(a), the sign (positive or negative) of the predefined mode shape plays an important role in the effect of IGIs on the behavior of the Type II column. Assuming the imperfection in the positive out-of-plane direction (modal +ve) has a positive effect on the behavior of the Type II column (RMM = 1.06, RDE = 1.27). Assuming it in the negative out-of-plane direction (modal - ve) causes an opposite effect (RMM = 0.96, RDE = 0.85), significantly changing the performance parameters. In spite of these differences, the deformed shapes in the inserts in Figure 2-12(a) and Figure 2-12(b) indicate that the final failure mode is not affected by the randomness in the IGI approach or profile used. An important conclusion from Figure 2-12 is that the perfect column's

38

response lies within the band of results for columns with various types of imperfections supporting the notion that using a perfect column for simulation is a reasonable alternative to incorporating IGIs in this specific problem (i.e., DSW columns subjected to combined axial and lateral loads).

Effect of Axial Load

For both imperfection approaches, the influence of IGIs on the behavior of the studied columns increases with higher axial loads. For example, on average between the two approaches, incorporating IGIs decreases the peak moment of W30×148-100 (h/t_w = 36.1, $b_f/2t_f$ = 6.5) by 5%, 5%, and 12% when the initial axial load is $0.2P_y$, $0.3P_y$, and $0.4P_y$, respectively. It is evident that for a small axial load ratio of $0.2P_y$, the effect of including IGIs is small (-3% and -1.5% on average for RMM and RDE, respectively).

For all axial load ratios, the effect of including IGIs on RMM is relatively small ranging from -14% to +6% with an average of -5% as shown in Table 2-5. However, the effect of including IGIs is more significant on RDE (ranging from -18% to +27%), especially for slender columns (i.e., type II columns in Figure 1). This difference is primarily attributed to the sensitivity of the last (failure) cycle to the assumed imperfection, as is clear in Figure 2-12(a). However, the average effect is still small (-2%).

Table 2-5 Summary of performance parameters

Section (in.×lb/ft)	L/r_y	$P/P_y = 0.2$ Traditional modal		$P/P_y = 0.2$ Proposed Spectral		$P/P_y = 0.3$ Traditional modal		$P/P_y = 0.3$ Proposed Spectral		$P/P_y = 0.4$ Traditional modal		$P/P_y = 0.4$ Proposed Spectral	
		RMM	RDE	RMM	RDE	RMM	RDE	RMM	RDE	RMM	RDE	RMM	RDE
W24×76	81.3	0.95	0.97	1.05	1.00	0.95	1.04	1.02	1.00	0.89	0.96	1.00	1.02
W24×76	115.6	1.03	0.96	1.05	0.93	1.06	1.27	0.99	1.16	1.05	1.04	1.02	1.10
W24×84	80.0	0.91	1.05	0.95	1.01	0.88	0.95	0.99	0.84	0.93	1.11	0.93	0.93
W24×84	101.5	0.98	0.95	1.01	0.93	0.96	0.99	0.98	0.96	0.92	1.15	0.90	1.00
W24×335	48.3	1.00	0.97	1.00	1.01	0.97	0.97	0.98	0.97	0.95	1.01	0.95	1.03
W24×335	79.9	0.99	0.90	1.02	0.93	1.02	0.96	0.98	0.93	0.98	1.00	1.00	0.98
W27×161	52.0	0.92	0.90	0.95	0.93	0.92	0.89	0.98	0.92	0.92	0.90	0.98	0.93
W27×161	70.6	0.91	1.01	1.00	1.02	0.90	0.97	1.00	1.01	0.91	0.90	0.97	0.96
W27×217	50.6	0.93	0.99	0.98	0.95	0.89	0.98	0.97	1.00	0.92	0.93	0.96	1.02
W27×217	70.5	0.97	1.00	0.96	0.98	0.94	1.00	0.98	0.98	0.90	1.02	0.92	1.01
W30×148	78.9	0.93	1.00	0.93	1.03	0.92	0.91	0.92	0.88	0.89	0.95	0.90	0.93
W30×148	100.0	0.93	0.97	0.97	1.04	0.93	0.83	0.97	1.00	0.86	0.82	0.90	0.89
W30×235	51.3	0.91	0.99	0.95	1.01	0.91	0.93	0.93	0.98	0.90	0.91	0.99	0.99
W30×235	80.3	0.93	1.01	0.96	1.00	0.90	1.03	0.93	0.98	0.89	1.01	0.90	0.97
W30×357	49.5	0.99	1.05	1.01	0.99	0.96	1.02	0.97	0.95	0.93	1.00	0.93	0.97
W30×357	69.2	0.98	1.00	1.01	1.05	0.97	1.01	1.02	1.03	0.94	0.98	0.94	0.98
Minimum		0.91	0.90	0.93	0.93	0.88	0.83	0.92	0.84	0.86	0.82	0.90	0.89
Maximum		1.03	1.05	1.05	1.05	1.06	1.27	1.02	1.16	1.05	1.15	1.02	1.10
Average		0.95	0.98	0.99	0.99	0.94	0.98	0.98	0.97	0.92	0.98	0.95	0.98
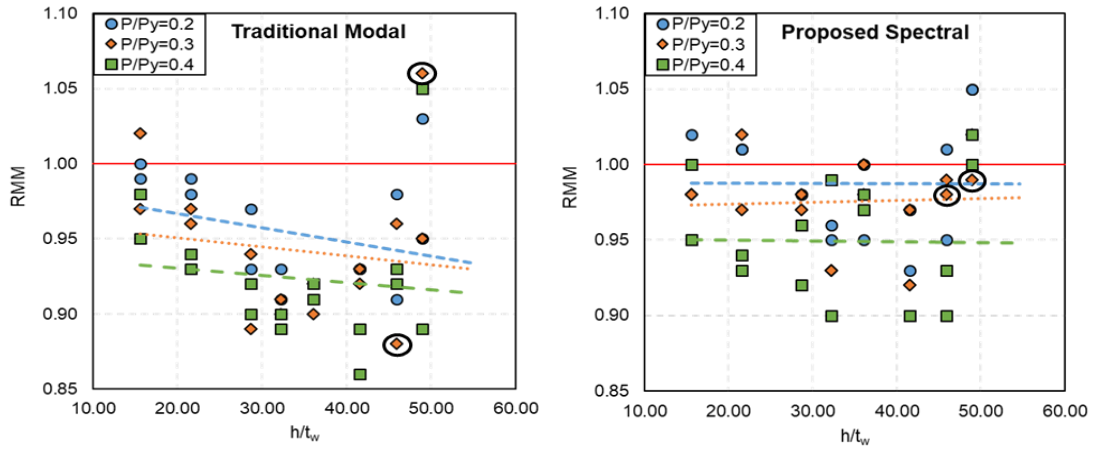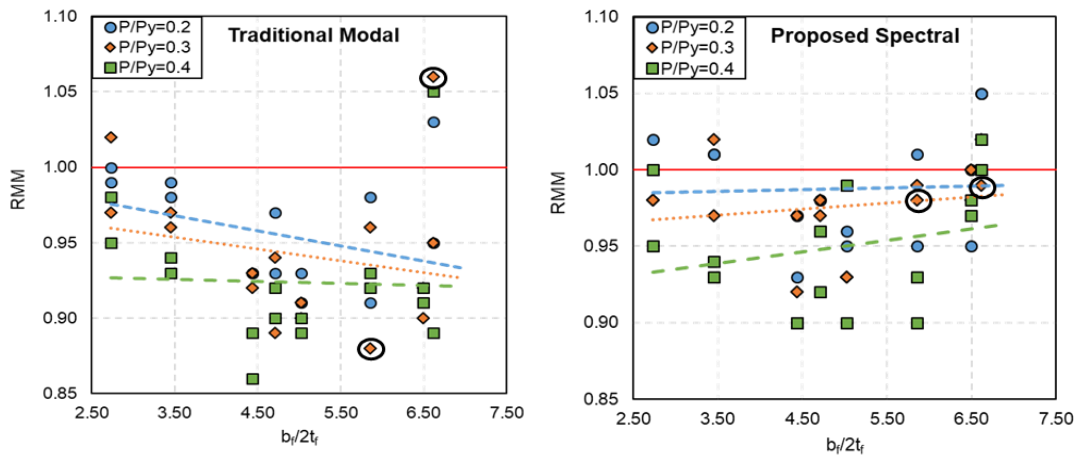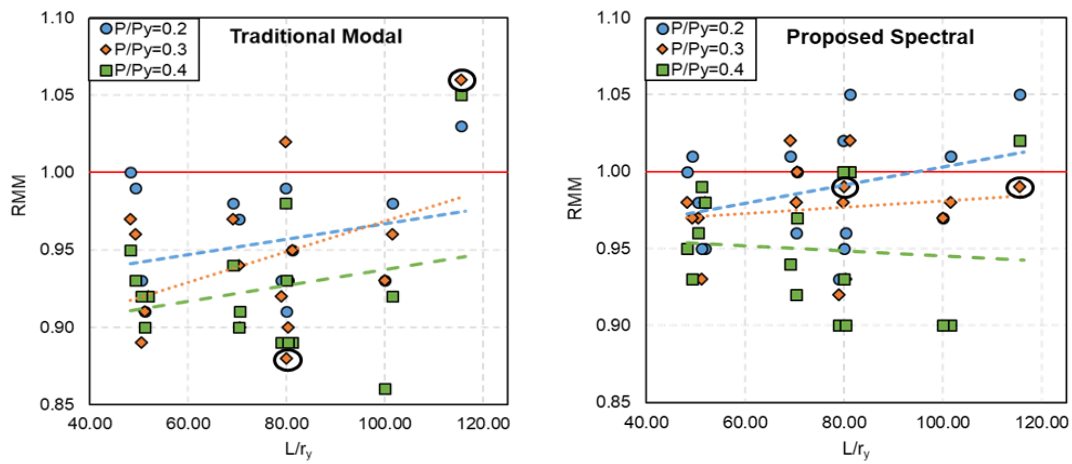
Figure 2-10 Relationship between the effect of IGIs on RMM and: (a) web slenderness ratio (h/t_w); (b) flange slenderness ratio ($b/2t_f$); and (c) column global slenderness ratio (L/r_y)

41
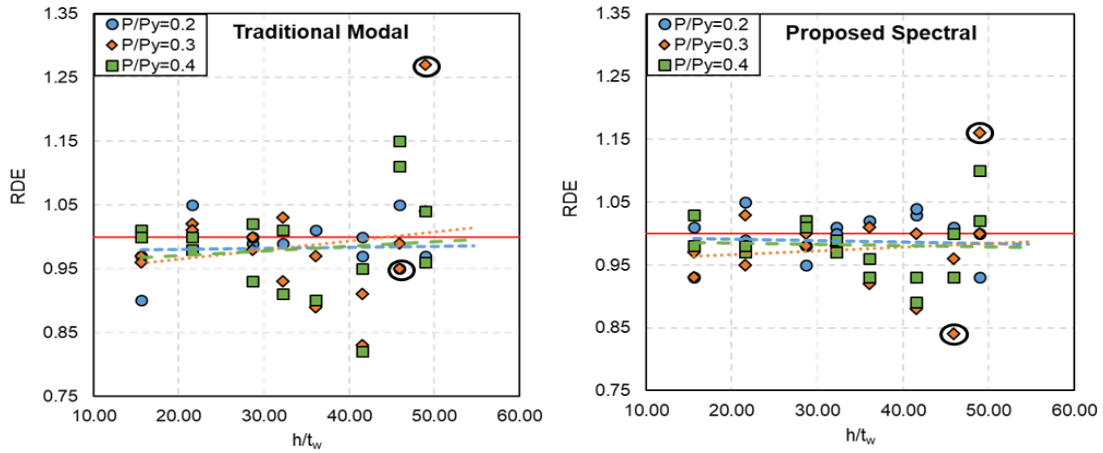
(a)
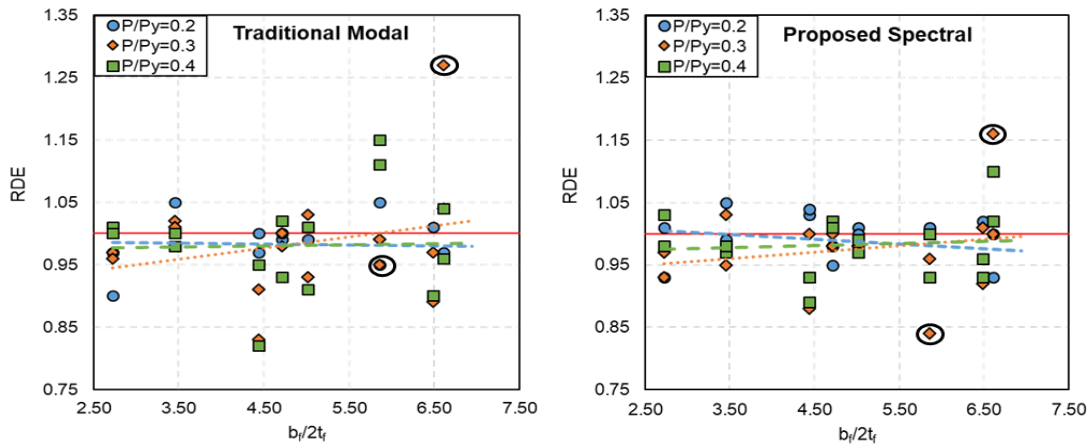
(b)
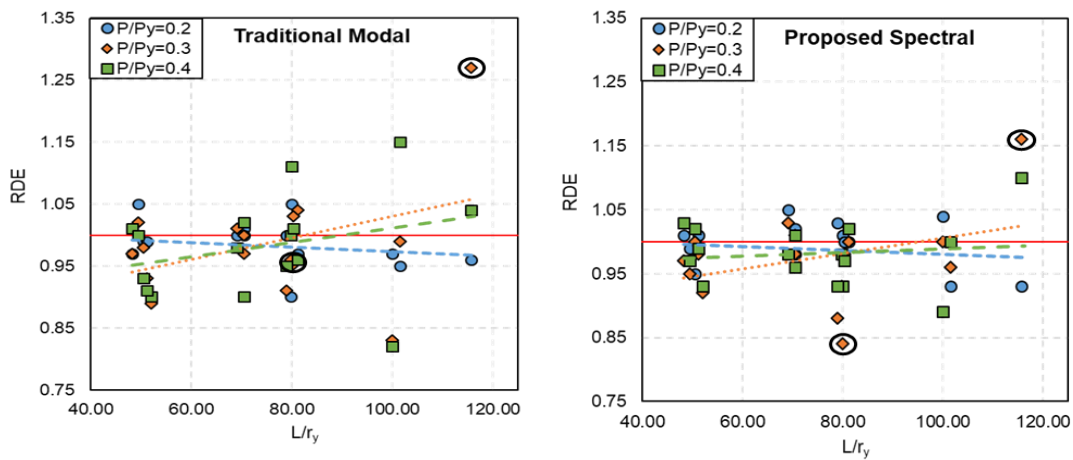
(c)

**Figure 2-11 Relationship between the effect of IGIs on RDE and: (a) web slenderness ratio
(h/t_w); (b) flange slenderness ratio ($b/2t_f$); and (c) column global slenderness ratio (L/r_y)**

42
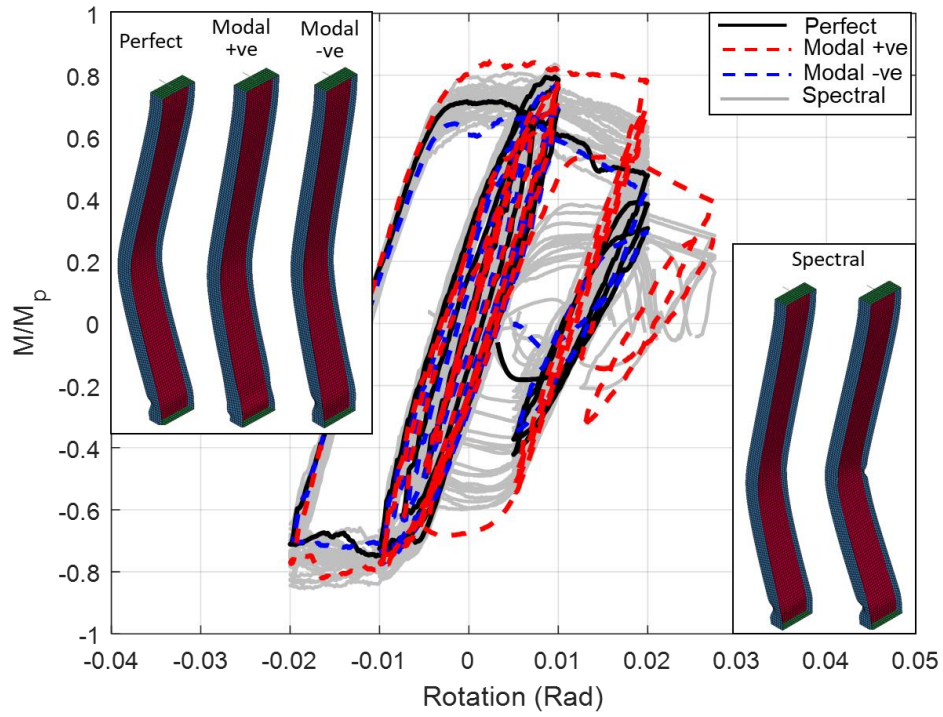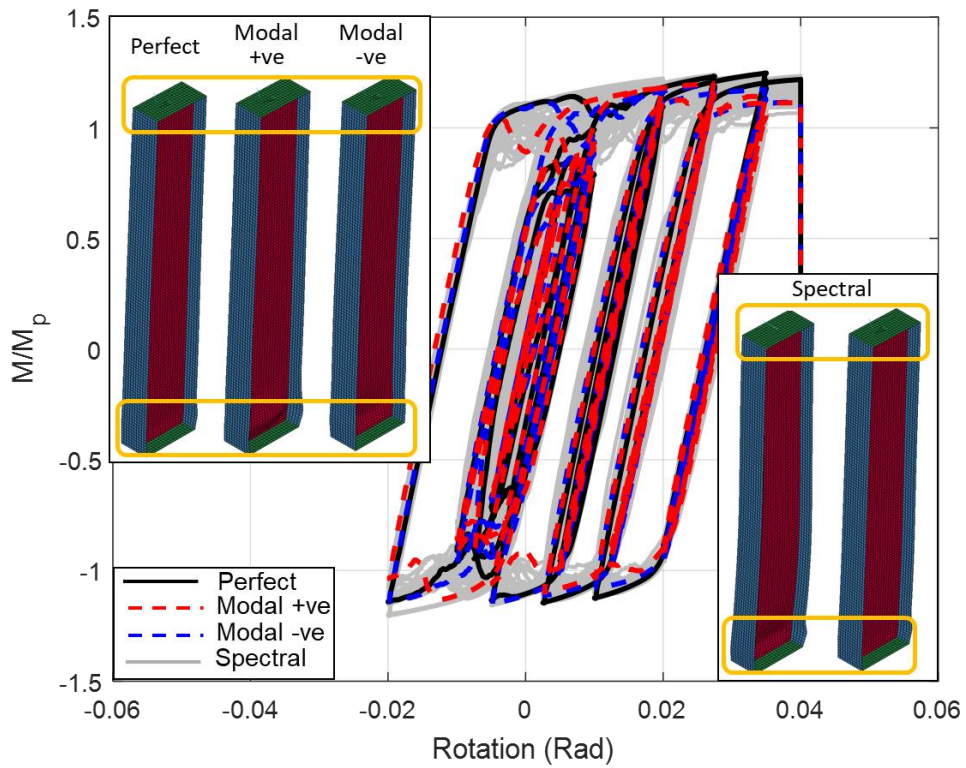
Figure 2-12 Moment-rotation behavior and deformed shape at failure for: (a) W24×76×115-30; and (b) W30×357×50-30 with different IGIs

2.2.6 Practical Implications and Limitations of This Study

This study addresses the specific case of DSW columns subject to combined axial and lateral loading through member level studies. The simulation results show that the effect of incorporating IGIs is small (on average, -4.5% and -2% for RMM and RDE, respectively) when the axial load level is limited to $0.4P_y$, which is rarely exceeded in earthquake engineering practice. Given the limited effect of IGIs in these situations and, more fundamentally, the random nature of IGIs and their inconsistent effect, analysts need not incorporate IGIs into their models. However, the analysis platform must have sufficient numerical precision to capture the small deformations that occur in the early steps of the analysis, which act as self-induced 'imperfections' that promote geometric nonlinearity in the response (Sediek et al. 2020a).

If IGIs must be included in an analysis, for example due to unavailability of a simulation platform with adequate numerical precision, actual measured values should be used, or a realistic method employed for specifying the IGIs. The spectral approach proposed in this study, which is based on measurements from real W-shape members, is an appropriate option. When used in a validation study in which the actual IGIs are not known, the probabilistic nature of the method makes it possible to simulate a range of responses to bracket the likely behavior of a steel member as shown in Figure 2-12. Given that the overall effect of IGIs is small, the traditional modal approach may also be used but with the understanding that: 1) it is not necessarily a conservative approach, and 2) that arbitrary selection of its parameters (IGI amplitudes, number of mode shapes used and their direction) to fit test results may inadvertently mask the effects of initial stresses or boundary constraints, providing false confidence during validation studies.

A limitation of this work is that the measurements were done on stand-alone members and on only fourteen specimens. Additional research is needed to measure IGIs in more single columns

and columns that are part of fabricated subassemblages, where the fabrication process may introduce additional IGIs.

2.3 Prediction of Seismic Collapse Behavior of Deep Steel Wide-Flange Columns Using Machine Learning Methods

2.3.1 Background

The seismic behavior of DSW columns has been studied both experimentally and computationally by multiple researchers including Chi and Uang (2002), Newell and Uang (2006), Elkady and Lignos (2015), Fogarty and El-Tawil (2015), and Cravero et al. (2020). Depending on their geometric properties, boundary conditions and loading, DSW columns can fail in local, global, or coupled local-global modes. Identifying the failure mode is necessary for designing new DSW columns or deciding on viable retrofit and rehabilitation strategies for existing DSW columns. Fogarty et al. (2017) classified the failure mode of DSW columns subjected to combined monotonic lateral load and constant compressive axial load into four categories: global, local, local–global, and local–transition modes. Ozkula et al. (2017a) classified the failure mode of DSW columns with fixed-fixed boundary conditions subjected to combined cyclic lateral load and constant compressive axial load into three categories: symmetric flange, anti-symmetric local, and coupled modes. Ozkula et al. (2017a) also proposed criteria for identifying the failure mode of DSW columns based on their geometric properties (i.e., web and flange dimensions). However, the proposed criteria did not take into account other important attributes such as the boundary conditions and loading protocols.

DSW columns in SMFs must be capable of providing highly ductile behavior. According to AISC Seismic Provisions (AISC 2016a), a highly ductile column, which is classified based on its web and flange slenderness ratios, must "withstand significant plastic rotation of 0.04 rad or

more during the design earthquake". Wu et al. (2018a) observed that current highly ductile limits specified in the AISC Seismic Provisions (AISC 2016a) are unconservative for DSW columns and proposed new limits. Ozkula (2017) proposed new slenderness limits to reduce the axial shortening that was observed in some cyclically tested highly ductile DSW columns.

2.3.2 Motivation and Objectives

Current techniques for classifying the failure mode and determining the rotation capacity of DSW columns have two key limitations. The first is that calibration data sets are based on specific conditions and therefore difficult to generalize beyond those conditions. For example, a data set from a particular study may have axial load levels, lateral loading protocols, and boundary conditions that are different from those in a data set generated by other researchers. The second limitation is that the prediction model established using the non-generalizable database is frequently not validated or tested against test sets with different conditions (e.g., Ozkula et al. 2017a). This approach results in an overfit of the prediction model as noted by many researchers (e.g., Friedman et al. 2001, James et al. 2013, and Mangalathu et al. 2018). To resolve these limitations, this study explores the use of artificial intelligence (AI) to predict the seismic collapse behavior of DSW columns using both training and test data sets.

Artificial intelligence (AI) is defined as utilizing the capabilities of machines to perform jobs that typically require human intelligence. Machine Learning (ML) is a subset of AI that builds mathematical models from sample datasets (i.e., training data) to be able to predict and make decisions for new ones without being explicitly programmed to do so. ML has been widely used in different fields of science, engineering, and finance. ML techniques can be classified into supervised and unsupervised learning. As the name implies, supervised learning is based on prior knowledge of the labeled dataset that enables the ML model to make predictions for new data.

Unsupervised learning is based on inferring the structure of the dataset that is not labeled. ML algorithms can be classified into classification and regression algorithms according to the output parameter. Classification algorithms are used when the output parameter is a discrete category or class, whereas regression algorithms are used when the output parameter is a continuous variable.

Generally, ML algorithms provide advantages over traditional methods in handling complex problems, providing computational efficiency and enabling rapid decision making. ML was introduced to the civil engineering and more specifically earthquake engineering field over the past decade (Xie et al. 2020). Mangalathu and Jeon (2019) compared the performance of different ML techniques in identifying the seismic failure mode of circular reinforced concrete bridge columns. They concluded that artificial neural networks (ANN) provide superior performance amongst all the implemented ML methods as well as available traditional methods. Sediek et al. (2021a) used a deep neural network (DNN) to classify the seismic failure mode of reinforced concrete moment frame buildings. Other notable studies on the use of ML in earthquake engineering can be found in Zhang et al. (2018), Siam et al. (2019), Huang and Burton (2019), Naderpour and Mirrashid (2019), and Mangalathu et al. (2020). To date, there have been no studies aimed at exploring the use of ML for predicting the seismic collapse behavior of DSW columns or any other category of steel columns.

Given the aforementioned advantages of ML techniques, limitations of available methods to predict the seismic collapse behavior of DSW columns, and dearth of research results on the use of ML in this specific area, this study considers different classification and regression ML methods to identify the failure mode and rotation capacity (i.e., cumulative inelastic rotation to failure) of DSW columns subjected to combined axial and lateral loads. The present study assembles an extensive database named Steel Column Net (SCNet) consisting of more than nine hundred experimental and numerical results of DSW columns with different sections, boundary conditions

and axial and lateral loading protocols. The performance of different machine learning classification and regression methods is compared with available methods in the literature and current specifications to predict the seismic collapse behavior of DSW columns.

2.3.3 SCNet Database

Description of SCNet

An entry in the Steel Column Net (SCNet) database is a column with specific attributes (e.g., cross-section characteristics, boundary conditions, axial load etc.). SCNet consists of 599 entries collected from seven available studies in the literature (Fogarty and El-Tawil 2015, Elkady and Lignos 2017a, Fogarty et al. 2017, Ozkula 2017, Ozkula et al. 2017b, Wu et al. 2018a, and Cravero et al. 2020) and 340 entries that are newly simulated for the purpose of the current study[2]. SCNet is documented in Appendix A and summarized in Table 2-6. The thoroughly validated finite element modeling approach developed by Wu et al. (2018a) is used to model the new entries. As mentioned earlier, the model is created using the commercial software Hypermesh and analyzed using the general-purpose finite element software LS-DYNA.

When dealing with ML, there are two types of attributes: continuous and categorical. Continuous attributes can take on any value within a specific range, while categorical attributes can only take on a finite number of values that represent various categories. In this work, eight attributes are used to characterize the entries in SCNet of which five are continuous and 3 are categorical.

---

[2] Dr. Tung-Yu Wu created the numerical models and performed the finite element simulations for the mentioned 340 entries.

For the former, the first two are the local slenderness ratios (h/t_w and $b_f/2t_f$) of the W-shape section. The third attribute is the global slenderness ratio (L/r_y) of the entry. The fourth is the torsional slenderness ($J/S_x h_o$) of the entry, where J is the torsional constant, S_x is the elastic section modulus about x-axis, and h_o is the distance between the flange centroids. The fifth is the initial axial load ratio (P/P_y). The categorical attributes are the boundary conditions, axial loading protocol and lateral loading protocol. The bottom of the column is assumed to be fully fixed for all entries. Four boundary conditions are considered for the top as shown in Table 2-7: (1) fully fixed in all planes [Fixed-Fixed (FF)]; (2) fixed in-plane rotation with free out-of-plane rotation [Fixed – Pinned (FP)]; (3) free in-plane rotation with fixed out-of-plane rotation [Pined – Fixed (PF)]; (4) in-plane rotation is restrained by a rotational spring or flexible beam element with fixed out-of-plane rotation [Spring – Fixed (SF)]. As shown in Figure 2-13, five types of lateral loading protocols are considered: (1) symmetric cyclic (SC); (2) monotonic (M); (3) cyclic – monotonic (CM); (4) cyclic ratcheting (CR); and (5) asymmetric cyclic (AC). Three types of axial loading protocols are considered: (1) constant (C); (2) symmetric cyclic (SC); and (3) monotonic (M).

Table 2-7 lists the range of the continuous attributes and the values that the categorical attributes can take. Figure 2-14 shows the distribution of the attributes and failure modes of the entries in SCNet. Further information about the characteristics of the attributes selected in this work can be found in the studies from which the entries were obtained (see Table 2-6).

Table 2-6 Summary of data entries in SCNet

Study	Type	# Entries	Boundary Conditions	Axial Protocol	Lateral Protocol	Failure Modes	Mapped Modes
Fogarty and El-Tawil (2015)	Numerical	17	FP	SC	SC	Flexural/Torsional	GF
						Local	LF
						Flexural - Local	GLF
Elkady and Lignos (2017a)	Experimental	7	FF, SF	C	SC, CR	Local	LF
Fogarty et al. (2017)	Numerical	37	FP	M	M	Global	GF
						Local	LF
						Local-Global	GLF
						Local-Transition	
Ozkula (2017)	Numerical	240	FF	C	SC	Symmetric Flange	LF
						Asymmetric Local	
						Coupled	GLF
Ozkula et al. (2017b)	Experimental	28	FF, SF	C, SC	M, SC	Symmetric Flange	LF
						Asymmetric Local	
						Coupled	GLF
Wu et al. (2018a)	Numerical	267	SF	C, M	CR	Global	GF
						Local	LF
						Global - Local	GLF
Cravero et al. (2020)	Experimental	3	PF	SC, C	SC	Local	LF
This Study	Numerical	340	All	C	All	Global	GF
						Local	LF
						Global - Local	GLF

FF: Fixed – Fixed (fully fixed in all planes)
PF: Pined – Fixed (fixed in-plane rotation with free out-of-plane rotation)
SF: Spring – Fixed (free in-plane rotation with fixed out-of-plane rotation)
SC: Symmetric Cyclic
M: Monotonic
CR: Cyclic Ratcheting
C: Constant

Table 2-7 Summary of range of attributes in SCNet

Attribute	Minimum			Maximum	
	Continuous Parameters				
Web slenderness ratio (h/t_w)	5.21			57.5	
Flange slenderness ratio ($b_f/2t_f$)	2.34			9.92	
Global Slenderness ratio (L/r_y)	28.9			161.9	
Torsional slenderness ratio (J/S_xh_o)	0.0004			0.038	
Initial axial load ratio (P/P_y)	0			0.75	
	Categorical Parameters				
Axial loading protocol	C		SC		M
Boundary conditions	FF	FP		PF	SF
Lateral loading protocol	SC	M	CM	CR	AC
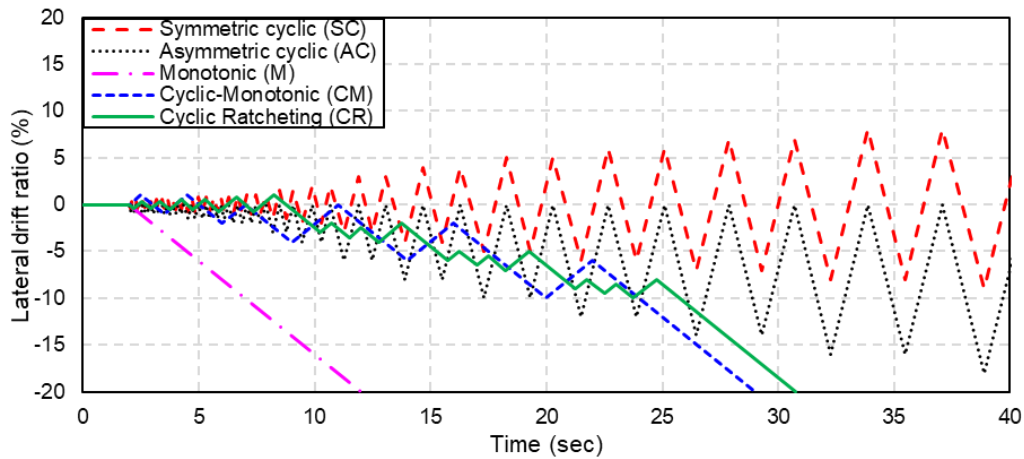
Figure 2-13 Employed lateral drift loading protocols
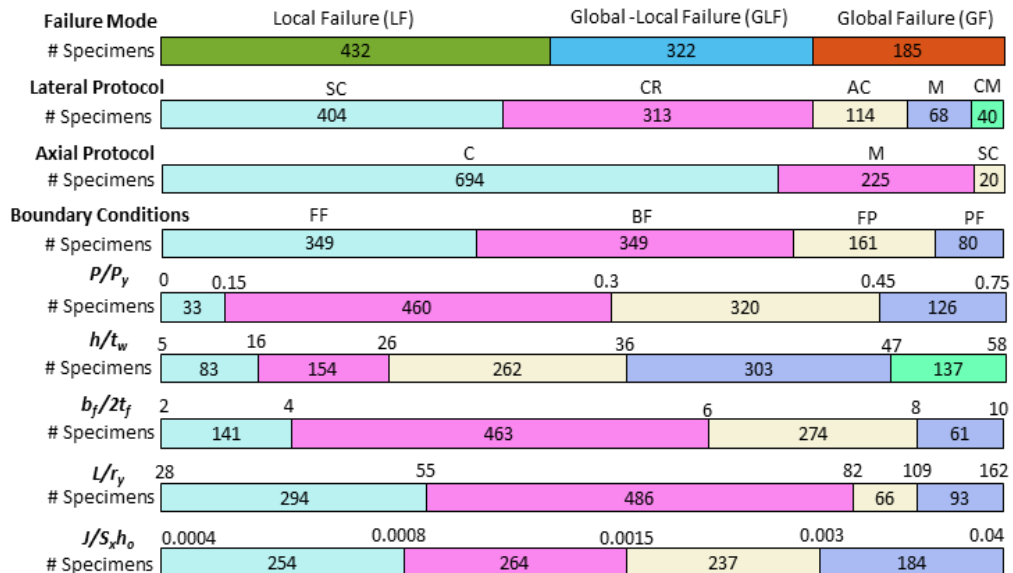
Figure 2-14 Distribution of attributes and failure mode of the DSW entries in SCNet

51

The present study predicts the seismic collapse behavior of DSW columns in terms of their failure mode and rotation. Three failure modes are distinguished (Figure 2-15). Local failure (LF) implies that the column experiences severe local buckling near its ends prior to failure. Global failure (GF) implies that the column fails in a global flexural or lateral torsional mode without experiencing severe local buckling at its ends. Global–local failure (GLF) implies that the column experiences both severe local buckling near is ends and a global flexural or lateral torsional failure, regardless of which occurs first. Although the available categorization of the column failure mode in previous studies is not the same, the failure modes collected from previous studies are mapped to these three categories based on the available description in each study (Table 2-6).

Local Failure (LF)   Global – Local Failure (GLF)   Global Failure (GF)
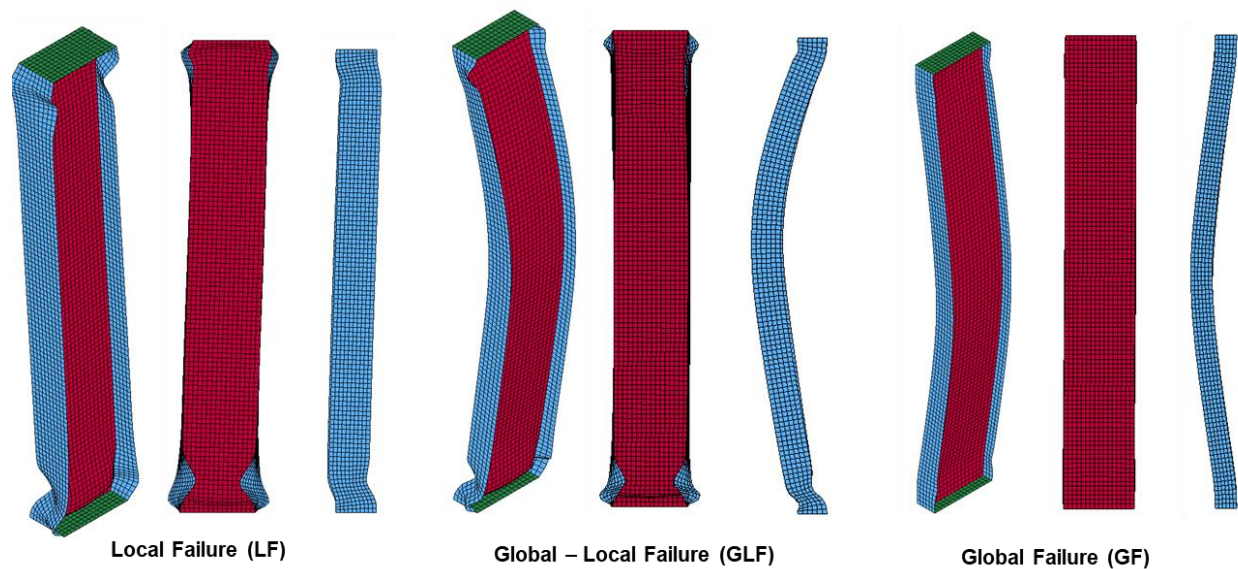
Figure 2-15 Illustration of Failure modes of DSW columns

The rotation capacity of the DSW columns is measured using their cumulative inelastic rotation to failure (CIR), which has been previously used to characterize the ductility of W-shape columns (Elkady and Lignos 2017b). CIR is evaluated as the sum of absolute inelastic drift excursions until failure following the yield drift rotation of the column as shown in Figure 2-16.
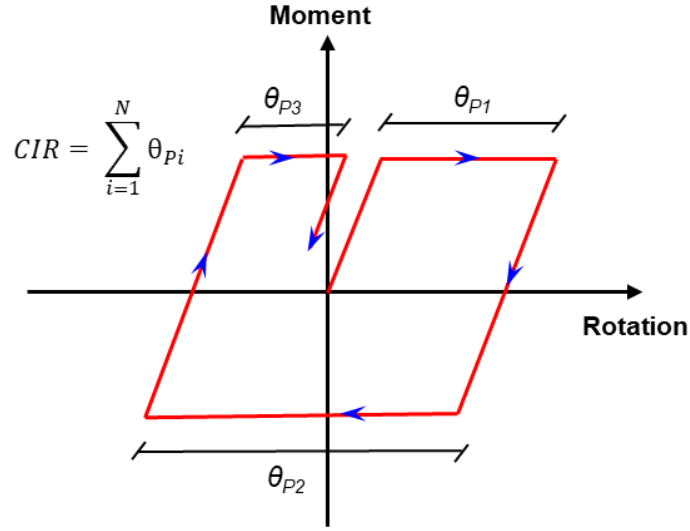
Figure 2-16 Definition of Cumulative Inelastic Rotation (CIR)

The yield drift rotation is evaluated based on Ozkula (2017). The yield rotation (θ_y) is computed as follows:

$$\theta_y = M_y/K_e \qquad (2\text{-}17)$$

where M_y is the yield moment evaluated using the P-M interaction equation in AISC Specification for Structural Steel Buildings (AISC 2016b) and K_e is the rotational stiffness specified by ASCE 41 (ASCE 2006) which is based on the Euler-Bernoulli beam theory for double-curvature bending. M_y is computed as follows:

$$M_y = \begin{cases} \dfrac{9}{8} M_p \left(1 - \dfrac{P}{P_y}\right), & \dfrac{P}{P_y} \geq 0.2 \\[3mm] M_p \left(1 - \dfrac{P}{2P_y}\right), & \dfrac{P}{P_y} < 0.2 \end{cases} \qquad (2\text{-}18)$$

where M_p is the plastic moment of the W-shape section. K_e is computed as follows:

53

$$K_e = \frac{6EI_x}{L}\left(1 - \frac{P}{P_e}\right) \qquad\qquad (2\text{-}19)$$

where E is the modulus of elasticity, I_x is the W-shape section moment of inertia about major axis, and P_e is Euler's critical load of the W-shape column. It should be noted that the columns with CIR values available in SCNet are only 719 of the 939 entries because CIR was not evaluated for all of the columns associated with the study by Ozkula (2017).

Exploratory Data Analysis

Exploratory data analysis (EDA) is the process of evaluating the relationships between the different attributes and output parameters or categories. It is also used to detect outlier data points that are distant from most of the database. EDA is performed on SCNet. For classification of column failure mode, Figure 2-17 plots the relationship between each two continuous attributes and the column failure mode. From Figure 2-17, the following observations can be made:

- As shown in Figure 2-17 (a, c), there is a general trend that columns with larger $b_f/2t_f$ or J/S_xh_o are more susceptible to local failure mode (LF), whereas columns with low $b_f/2t_f$ or J/S_xh_o are dominated by global (GF) and global-local (GLF) modes. However, columns with smaller $b_f/2t_f$ or J/S_xh_o can fail in the LF mode also, which implies that predicting the column failure mode based on the column dimensions alone is not sufficient.

- As shown in Figure 2-17 (a, e), there is a general trend that columns with larger L/r_y are more susceptible to global (GF) and global-local (GLF) modes. Columns with smaller L/r_y can fail in any of the three modes implying that column failure mode is not solely determined by L/r_y.

- Considering all of the plots, the decision surfaces or boundaries between the failure modes are clearly complex and nonlinear.

- As shown in Figure 2-17 (a-j), there is weak correlation between the continuous attributes and column failure mode suggesting that consideration of the other categorical parameters is important for identifying the column failure mode.

Figure 2-18 plots the relationship between each of the continuous attributes and CIR. Also plotted on the figure are trend lines that suggest there is a general negative correlation between h/t_w, $b_f/2t_f$, L/r_y, and P/P_y versus CIR and positive correlation between $J/S_x h_o$ versus CIR. The large scatter of the data points implies the importance of the other categorical parameters in predicting CIR. Therefore, classifying the columns to be highly ductile based on column dimensions (i.e., h/t_w and $b_f/2t_f$) and applied axial load ratio P/P_y only, as specified in the current AISC Seismic Provisions (AISC 2016a), may not be sufficient.
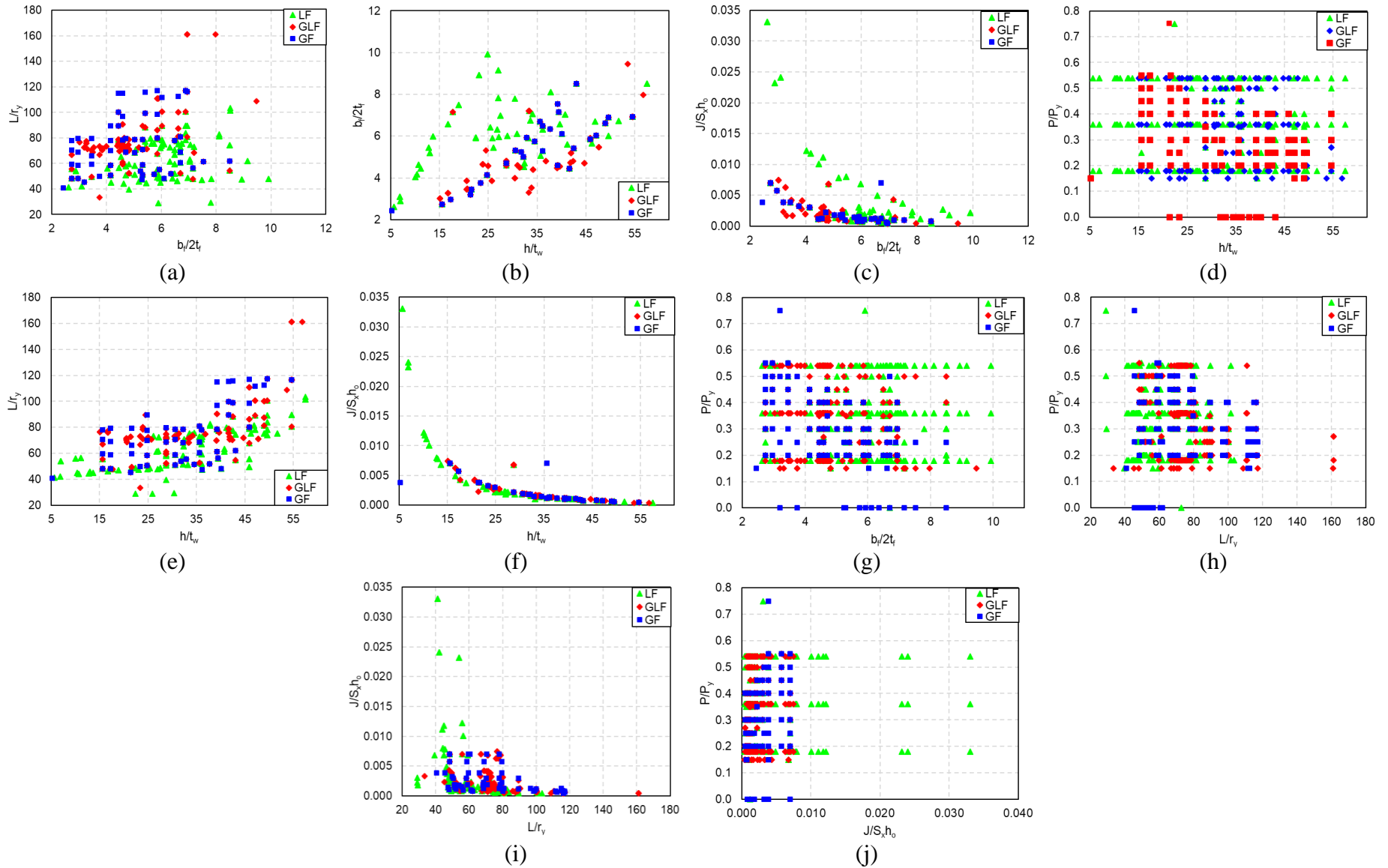
Figure 2-17 Scatter plot of continuous attributes of SCNet with respect to failure mode: (a) L/r_y versus $b_f/2t_f$; (b) $b_f/2t_f$ versus h/t_w; (c) $J/S_x h_o$ versus $b_f/2t_f$; (d) P/P_y versus h/t_w; (e) L/r_y versus h/t_w; (f) $J/S_x h_o$ versus h/t_w; (g) P/P_y versus $b_f/2t_f$; (h) P/P_y versus L/r_y ; (i) $J/S_x h_o$ versus L/r_y ; and (j) P/P_y versus J/S_x

56
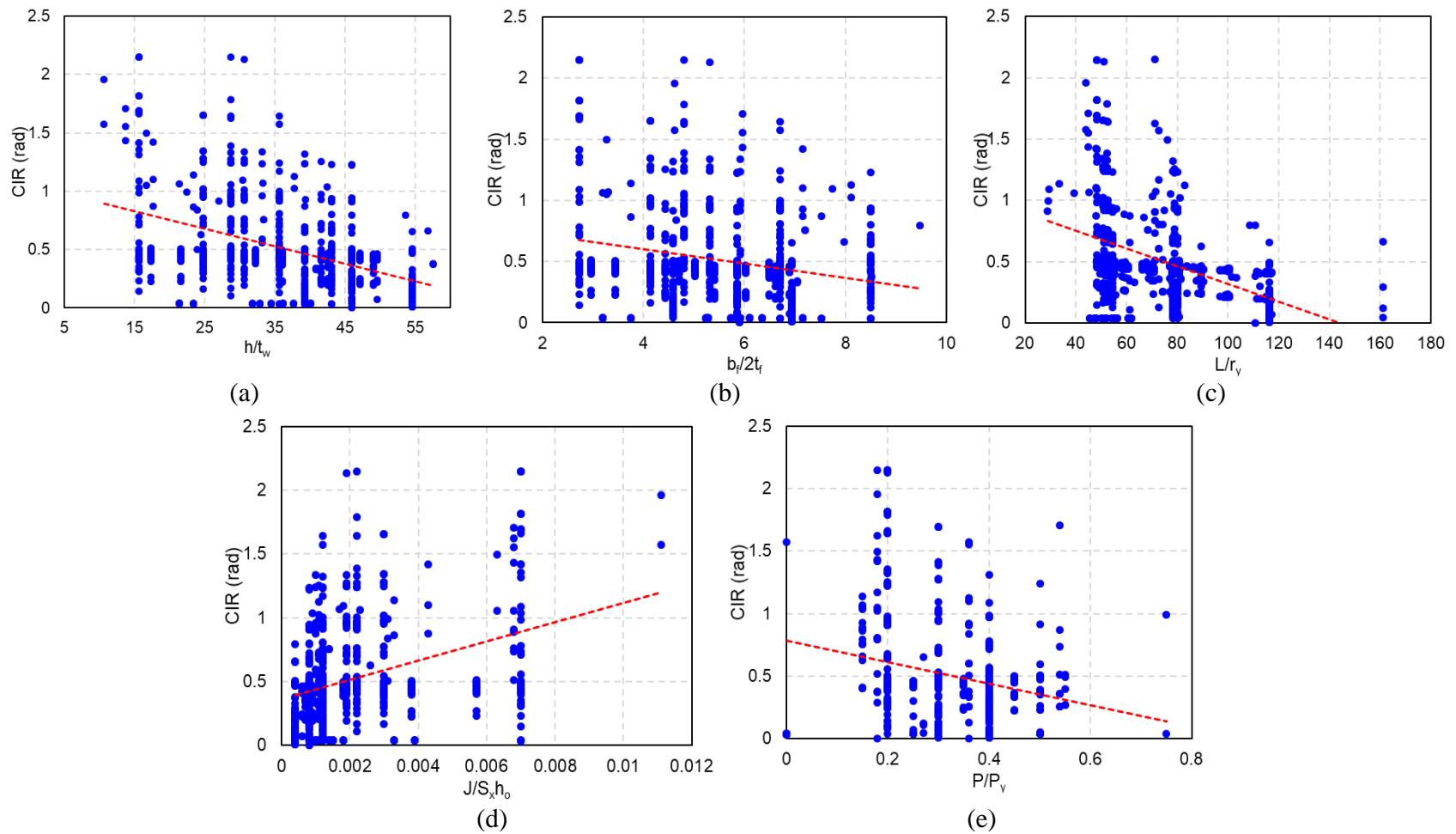
Figure 2-18 Scatter plot of continuous attributes of SCNet with respect to CIR: (a) CIR versus h/t_w (b) CIR versus $b_f/2t_f$; (c) CIR versus L/r_y ; (d) CIR versus $J/S_x h_o$; and (e) CIR versus P/P_y

2.3.4 Classification of Failure Mode

The categorical attributes are converted to dummy continuous variables to facilitate application of the ML algorithms. Each attribute is converted into an $m \times n$ dummy matrix where m is the size of the database (i.e., 939) and n is the number of categories the parameter can take. The dummy variable is a sparse matrix with ones at the location of the category of each observation. For example, there are three categories for the axial loading protocol as shown in Table 2-7 {C, SC, M}. Therefore, the axial loading protocol is converted into a 939×3 dummy variable. For an entry i in SCNet with an SC axial loading protocol, the ith row in the dummy variable will be {0, 1, 0}.

The continuous attributes and dummy variables corresponding to the categorical parameters are used to build an attribute matrix of 939 observations (rows) and 17 features (columns). The attributes matrix is represented as $X = \{X_1, X_2, \ldots, X_{17}\}$, where X_j is an $m \times 1$ vector that denotes attribute j. The definition of X_j's is shown in Table 2-8. It should be noted that $x = \{x_1, x_2, \ldots, x_{17}\}$ denotes the attribute vector of a specific observation in the dataset. The failure mode of the entries is denoted as Y, and l denotes the possible modes ($l = 1$ for GF, $l = 2$ for GLF, and $l = 3$ for LF). SCNet is divided randomly into two subsets: training and test. In the present study, 70% (657 entries) of SCNet is used as a training set to develop the prediction models, whereas the other 30% (282 entries) are kept separate to be used as a test set to evaluate the performance of the trained models as recommended by Friedman et al. (2001). Also, 20% (131 entries) of the training set is used as a validation set to optimize the hyperparameters of the ML algorithms.

Five ML classification methods are explored to predict the failure mode of DSW columns: linear discriminant analysis (LDA), K-nearest neighbor (KNN), support vector machine (SVM),

naïve Bayes (NB), and classification decision trees (CDT). An overview of each method is presented in the following subsection.

Table 2-8 Parameters of the attributes for the machine learning algorithms

Variable	Attribute
X_1	Web slenderness ratio (h/t_w)
X_2	Flange slenderness ratio ($b_f/2t_f$)
X_3	Global slenderness ratio (L/r_y)
X_4	Torsional slenderness (J/S_xh_o)
X_5	Initial axial load ratio (P/P_y)
X_6	FF boundary condition
X_7	FP boundary condition
X_8	PF boundary condition
X_9	SF boundary condition
X_{10}	C axial loading protocol
X_{11}	SC axial loading protocol
X_{12}	M axial loading protocol
X_{13}	SC lateral loading protocol
X_{14}	M lateral loading protocol
X_{15}	CM lateral loading protocol
X_{16}	CR lateral loading protocol
X_{17}	AC lateral loading protocol

Overview of Machine Learning Methods

Linear Discriminant Analysis

Linear discriminant analysis (LDA) uses the attributes of the training dataset to determine the location of a linear decision boundary between the response classes (i.e., column failure modes) by treating the attributes of each class as samples from a multivariate normal distribution. First, the mean vector (μ_l with size 1×17) is calculated for the attributes of the training observations belonging to each class l. The covariance matrix (Σ with size 17×17) is calculated for the observations in the entire training set. Then, the probability density function (PDF) of the multivariate normal distribution is used to fit the observations in the training set belonging to each class l. The edge between the classes is defined by determining the set of points with equal

probabilities. To calculate the probability that class l entails an observation x (i.e., P (Y = l | X = x)), Bayes theorem is used as follows:

$$P(Y = l|X = x) = \frac{P(X = x|Y = l)P(Y = l)}{P(X = x)}$$

(2-20)

For more details about the formulation of LDA, the reader is referred to Fisher (1936).

Support Vector Machine

Support vector machine (SVM) is a widely used machine learning method that categorizes the training dataset by finding a hyperplane (i.e., decision boundary) in an N-dimensional space, where N is the number of features (i.e., 17 in the current study), that separates the data points into different classes while maximizing the distance (i.e., boundary) between the defined hyperplane and data points. Originally, SVM was developed as a binary classification method (i.e., only two classes can be classified) by transforming the attributes into a higher dimension space to determine a linear decision boundary between the classes. Projecting the linear decision boundary from the higher dimension space to the original space produces a non-linear decision boundary in the original space which is the case in most real-life problems and in the present study, as shown from the EDA performed earlier in Figure 2-17.

A kernel function is used to combine the inner product of the attribute vectors with their nonlinear transformations so that the transformations are not evaluated, which is computationally expensive. There are many available kernel functions in the literature (e.g., Polynomial, Gaussian, Gaussian radial basis, Hyperbolic tangent, etc.). Based on a sensitivity study, the quadratic polynomial kernel function is used in the current study. There are many approaches available in the literature to extend SVM to multi-class classification problems (i.e., with three or more

classes). The "one-against-one" approach (Knerr et al. 1990) is used in the current study based on its superior performance in similar SVM multiclass classification problems (Hsu and Lin 2002).

Naïve Bayes

The attribute data is classified in the naïve Bayes (NB) method based on Bayes theorem described by Equation (2-20) (Patil and Sherekar 2013). Similar to LDA, NB assigns an observation x to the class l with the highest conditional probability. The main difference between NB and LDA is that NB assumes a multivariate multinomial distribution for X and that the attributes are statistically independent which can be inferred from the large scatter shown in Figure 2-17.

Classification Decision Trees

Classification decision tree (CDT) is a nonparametric machine learning method that continuously splits the training dataset based on certain decision criteria to partition the data into separate and non-overlapping segments (Breiman et al. 1984). It consists of a set of nodes and branches as shown in Figure 2-19. In Figure 2-19, a CDT representation of the highly ductile limits of W-shape columns in the AISC Seismic Provisions (AISC 2016a) is illustrated as an example. The root node represents the whole training dataset before any splitting. At each decision node, the data is split into two subsets based on the decision criteria defined in the node. Finally, the observation x is assigned to class l at the terminal node (i.e., leaf) based on the attributes of x. There are numerous possible CDTs that can be used to partition the dataset based on the attributes. However, the accuracy of some trees is much better than the others. It is computationally infeasible to try all the possible CDT's and choose the optimal one. Thus, several algorithms are available to find the optimal decision tree with the best accuracy. In the present study, the CART (Breiman et al. 1984) algorithm is used to find the optimal classification decision tree. More information about building and assessing decision trees can be found in Breiman et al. (1984).
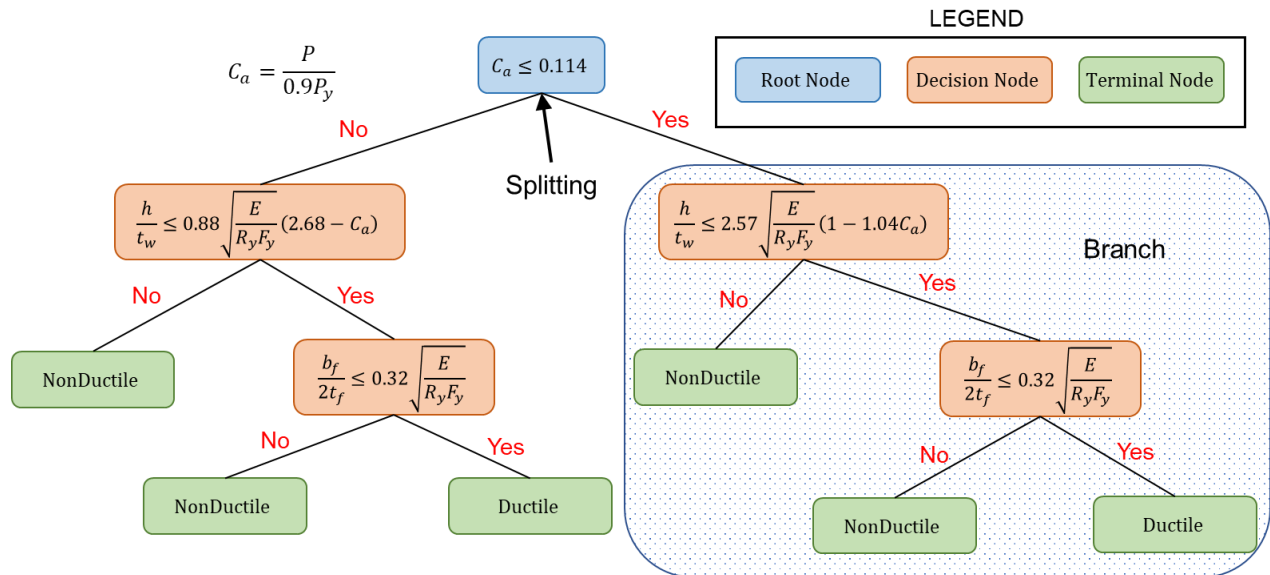
Figure 2-19 Illustration of CDT representation of highly ductile limits in the AISC Seismic Provisions (AISC 2016a)

Performance of Machine Learning Algorithms and Existing Methods in Identifying Column Failure Mode

The performance of the five trained ML classification models described in the previous section is assessed using confusion matrices as shown in Figure 2-20(a-e). A confusion matrix is an $r \times r$ matrix where r is the number of classes in the classification problem. The rows and columns of the confusion matrix represent the true and predicted classes, respectively. The diagonal elements represent the correct classifications meaning the predicted classes match the true ones. For a good ML classification model, confusion matrices should be diagonally dominant with large values on the diagonals (correct classifications) and small values on the off diagonals (misclassifications). For example, Figure 2-20(a) shows the confusion matrix of LDA for the test set. As shown, the matrix is 3×3 corresponding to the three identified failure modes (i.e., GF,

GLF, LF). It is also shown that the trained LDA model is able to correctly predict 47, 75, and 114 global, global-local, and local failure modes, respectively.

Two parameters are used to quantify the results of the confusion matrices: precision and recall. Precision and recall are defined as the percentage of correct predictions for each failure mode with respect to the predicted and true modes, respectively, and are shown on the bottom and right of the confusion matrices, respectively. For example, in Figure 2-20(a), 47 out of 58 entries with GF mode are correctly classified (81% precision for GF mode as shown in the fourth row of the first column in Figure 2-20(a)). Similarly, the precisions of GLF and LF modes are 77.3% and 89.8%, respectively. The recall of GF, GLF, and LF modes using LDA are 85.5%, 77.3%, and 87.7%, respectively.

The accuracy of the trained ML models is defined as the percentage of correctly predicted classes with respect to the database size. Three accuracies are evaluated for each model based on the dataset (i.e., test, training and total). The accuracies of the five trained models are summarized in Table 2-9. From Figure 2-20(a-e) and Table 2-9, the following can be inferred:

- Four of the five ML methods (i.e., LDA, KNN, SVM, and CDT) have good accuracy (i.e., more than 80%) for the test set which provides an unbiased evaluation for the trained models. SVM and CDT have the best performance (test accuracy of 89%).

- The methods that have inherent nonlinear decision boundaries (i.e., KNN, SVM, and CDT) have higher accuracies than those with linear decision boundaries (i.e., LDA and NB). This is attributed to the highly nonlinear nature of the actual decision boundaries between the different classes in SCNet as shown in Figure 2-17.

- All explored ML methods have good performance in identifying the LF mode as shown from the high recall values in Figure 2-20 (i.e., more than 80%). LDA, KNN,

SVM, and CDT have the best performance in identifying the GF mode. Only SVM and CDT have good performance in identifying the GLF mode. This is attributed to the coupled nature of GLF which is not a purely global or local mode. The interaction between global and local buckling in DSW columns subjected to combined axial and lateral demands does not depend only on the geometric parameters of the W-shape section (i.e., continuous attributes) but also on the boundary conditions and loading protocols. This can be clearly shown from the EDA performed in Figure 2-17.

Based on the above discussion, SVM and CDT are adopted as the best ML methods in classifying the failure mode of DSW columns subjected to combined axial and lateral loading. All five trained models can be accessed in MATLAB (i.e., mat) format at Sediek et al. (2020c).

Table 2-9 Accuracy of explored ML and existing methods in identifying column failure mode

ML method	% Test accuracy	% Train accuracy	% Total accuracy
LDA	83.7	75.2	77.7
KNN	85.1	80.9	82.2
SVM	89.0	91.0	90.4
NB	75.5	69.3	71.1
CDT	89.0	90.4	90.0
Ozkula et al. (2017a)	71.3	63.9	66.1

Figure 2-20 Comparison of confusing matrix using ML and existing methods for the test set to classify the column failure mode: (a) LDA; (b) KNN; (c) SVM; (d) NB; (e) CDT; and (f) Ozkula et al. (2017a)

The performance of the trained ML models is compared to the performance of the classification criteria proposed by Ozkula et al. (2017a). The latter differentiates between three column failure modes, as discussed earlier: symmetric flange, anti-symmetric local, and coupled failure modes. The symmetric flange and anti-symmetric local modes are classified as LF based on the definitions presented earlier, whereas the coupled failure mode is mapped as GLF. In the confusion matrix, GF and GLF modes are combined in one class to be consistent with the criteria proposed by Ozkula et al. (2017a). The confusion matrix and accuracy of the proposed criteria are shown in Figure 2-20(f) and Table 2-9, respectively. Ozkula et al. (2017a) classifies the failure mode of the DSW column based on the relative flexural stiffness ratio between the flange and the web which is calculated as follows:

$$\zeta = \left(\frac{4}{C_s}\frac{ht_f}{b_f t_w}\right)\left(\frac{t_f}{t_w}\right)^2 \tag{2-21}$$

where C_s is a non-dimensional web stiffness factor calculated as follows:

$$C_s = \frac{2\pi c \sinh^2 \pi c}{(\sinh \pi c \cosh \pi c - \pi c)} \tag{2-22}$$

where c is the aspect ratio of the web calculated as follows:

$$c = \frac{2\,{}^h/_{b_f}}{3.93t\left(\frac{t_w}{t_f}\right) + 3.54} \tag{2-23}$$

The boundary values of ζ for the three failure modes are 4.25 (from symmetric flange to anti-symmetric local) and 8 (from anti-symmetric local to coupled). The chosen values are based on the results from the experimental and numerical parametric studies they conducted. As shown

66

in Figure 2-20(f) and Table 2-9, the criteria proposed by Ozkula et al. (2017a) do not perform as well as the ML methods for attributes outside the range of their study. The test accuracy of their proposed criteria (i.e., applied on the test set) is 71.3% which is lower than the lowest ML method (i.e., NB with test accuracy of 75.5%). The presented results highlight the advantages provided by the trained ML models over traditional classification methods. The trained SVM and CDT models can be used to "rapidly" and "accurately" identify the seismic failure mode of DSW columns as part of SMFs subjected to different lateral and axial demands.

2.3.5 Prediction of Column Rotation Capacity

The rotation capacity of DSW columns expressed in terms of their CIR is predicted using a subset of SCNet (719 instead of 939 entries, as explained earlier). SCNet is divided into training, validation, and test sets with the same ratios listed earlier resulting in 504, 101, and 215 training, validation, and test entries, respectively. Four machine learning regression methods are explored to predict the CIR of DSW columns from the attributes discussed earlier: stepwise linear regression (SLR), regression decision trees (RDT), support vector regression (SVR), and gaussian process regression (GPR). An overview of each method is presented in the following subsection.

Overview of Machine Learning Methods

Stepwise Linear Regression

Linear regression (LR) is a machine learning model that assumes linear relationship between the predicted variable (i.e., Y) and the attributes (i.e., X). Multiple linear regression (MLR) is a special case of LR with more than one attribute. MLR for the training set can be expressed mathematically as follows:

$$Y = \beta_0 + \beta_1 X_1 + \beta_2 X_2 + \cdots + \beta_{17} X_{17} + \tau \tag{2-24}$$

or in matrix notation as:

$$Y = X'\beta + \tau \tag{2-25}$$

where Y is the output vector, β is the parameter vector, X is the attribute matrix for the training set described earlier with an extra column of ones on the left to account for the intercept (i.e., β_0), and τ is a vector of the error terms between the predicted and actual values. MLR models are fitted by finding the optimal parameter vector $\hat{\beta}$ through minimizing the error vector τ. Many methods are available for fitting MLR models including the ordinary least squares, L^2-norm penalty, and lasso (L^1-norm penalty). Ordinary least square (OLS) is used in the current study, which was found to provide acceptable performance in fitting the data in SCNet, to find $\hat{\beta}$ that minimizes τ which can be expressed as follows:

$$\hat{\beta} = (X^T X)^{-1} X^T Y \tag{2-26}$$

Stepwise linear regression (SLR) is a special case of MLR where the attributes are added to or removed from the fitted model based on their statistical significance. The fitting of the SLR model is performed on multiple successive steps where the model is modified in each step by removing the attributes with low statistical significance and adding other new parameters with high significance. A maximum of 1000 steps is chosen in the current study based on a performed sensitivity study. More details about the fitting process of SLR can be found in Norman and Smith (1998).

Regression Decision Trees

Regression decision tree (RDT) is a special type of decision tree. The main difference between RDT and CDT (described earlier) is that the terminal nodes in Figure 2-19 (i.e., leaves) in RDT have numeric values (i.e., continuous) instead of discrete categories (or classes) as in CDT.

68

The numeric values in the terminal nodes are evaluated based on the average of the observations from the training set in the range of the terminal nodes. The CART (Breiman et al. 1984) algorithm, which has been used earlier in CDT, is also used to find the optimal RDT.

Support Vector Regression

Support vector regression (SVR) is a special type of SVM. Similar to SVM, each input observation x in the training set is first mapped to an N-dimensional space, where N is the number of features (i.e., 17 in the current study). Then, a linear model is constructed in the higher dimensional space. The constructed linear model can be expressed mathematically as:

$$f(x) = \propto^T \Phi(x) + \alpha_o \tag{2-27}$$

where α and α_o are the coefficient and bias vectors, respectively, and $\Phi(x)$ is the nonlinear transformation that maps x to the higher dimension space. The constructed linear model is fitted by finding the optimal parameters α that minimizes the cost function which measures the error between the predicted and actual CIR of the entries in the training set (similar to LR described earlier). For SVR, the ε-intensive loss function proposed by Vapnik (1995) is used. The cost function ensures that all the predicted CIR of the entries in the training set are within ε boundary from the actual ones. In the present study, ε is chosen to be 0.02 based on a performed sensitivity study on the tradeoff between accuracy and overfitting of the model. SVR also ensures the flatness of the fitted linear model by finding $f(x)$ with the minimal norm of the coefficient vector (i.e., $\| \propto$

$\|^2$). More details about the formulation of SVR can be found in Drucker et al. (1997).

Gaussian Process Regression

Gaussian process regression (GPR) is a nonparametric kernel-based probabilistic machine learning method. The same linear regression form expressed by Equation (2-24) is used to fit the

training set. In GPR, the error (or noise) vector τ is assumed to be a vector of independent, identically distributed Gaussian random variables with zero mean and variance σ^2 (i.e. $\tau \sim N(0, \sigma^2)$). The observations in the training set are used to evaluate the variance σ^2 and coefficient vector β through a Gaussian process (GP). GP is a stochastic process that assumes a multivariate Gaussian distribution for any finite collection of random variables. GP is defined by a mean function and a covariance (kernel) function. The mean function is assumed to be constant in the present study, whereas the squared exponential (SE) kernel is used as the covariance function. More details about the GPR method can be found in Rasmussen and William (2006).

Performance of Machine Learning Methods in predicting CIR

The performance of the fitted ML regression models is assessed using the error between the predicted and actual CIR of the entries in the test, training, and total sets. The coefficient of determination (R^2) is used to measure the goodness-of-fit of the regression models. The values of R^2 for the ML regression methods for the test, training, and total sets are summarized in Table 2-10. Figure 2-21 plots the predicted versus actual values of CIR for the entries in the test set for the selected ML regression methods. Points on the diagonal imply perfect match between the predicted and actual values.

As shown from Figure 2-21 and Table 2-10, three of the four ML methods (i.e., SLR, SVR, and GPR) provide acceptable performance (with R^2 greater than 0.80) in predicting CIR of the test set. RDT has good performance in predicting CIR for the training set (R^2=0.90). However, it has poor performance in predicting CIR for the entries in the test set as shown by the large scatter of data around the diagonal line in Figure 2-21(b). This poor performance for the test set is attributed to the inherent discrete process in decision trees when predicting the continuous response variable (i.e., CIR) as discussed earlier. GPR has the best performance amongst all the explored

70

methods with R^2=0.88. Therefore, it is adopted as the best ML regression method in predicting the rotation capacity (expressed in terms of CIR) of DSW columns subjected to combined axial and lateral loading protocols. All four trained models can be accessed in MATLAB (i.e., mat) format at Sediek et al. (2020c).
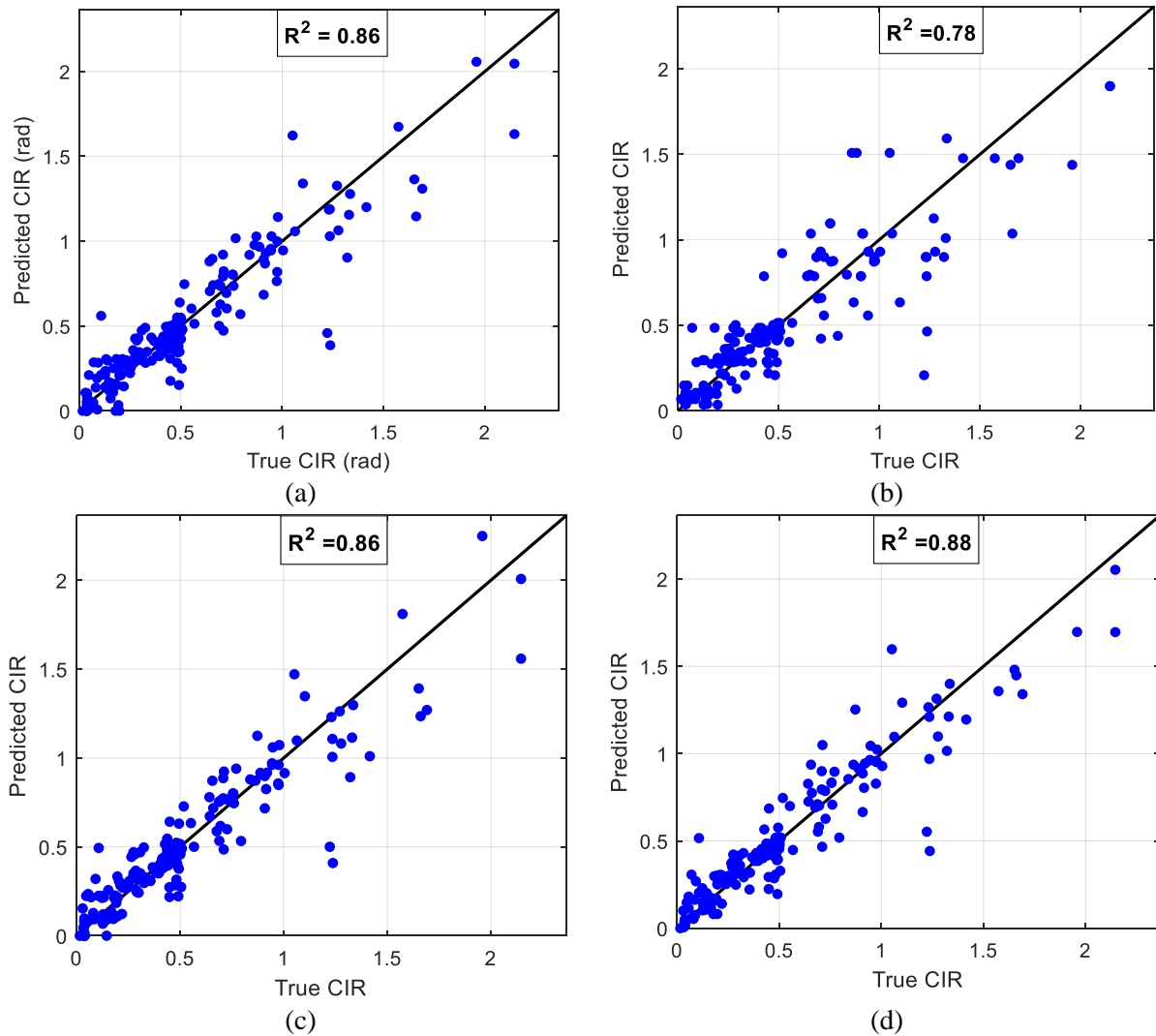
Figure 2-21 Comparison of performance of fitted ML regression models on the test set to predict CIR: (a) SLR; (b) RDT; (c) SVR; and (e) GPR

Table 2-10 Coefficient of determination (R^2) of explored ML regression methods

ML method	Test	Train	Total
SLR	0.86	0.88	0.88
RDT	0.78	0.90	0.86
SVM	0.86	0.90	0.89
GPR	0.88	0.93	0.92

Comparison of Machine Learning Methods with AISC Specifications

The predicted CIR's of the training, test, and total sets are used to identify the highly ductile behavior of DSW columns. The maximum plastic rotation experienced by the column can be evaluated using the CIR of the column and the applied lateral loading protocol by inverting the process shown in Figure 2-16. If the maximum plastic rotation exceeds 0.04 rad, the column is classified as "Ductile". Otherwise, the column is classified as "Non-Ductile". The highly ductile limits for both h/t_w and $b_f/2t_f$ in current AISC Seismic Provisions (AISC 2016a) are summarized in Figure 2-19.

To show the difference between the findings in this study and the current AISC Seismic Provisions (AISC 2016a), the performance of the fitted ML regression models as well as AISC Seismic Provisions (AISC 2016a) in identifying the highly ductile behavior of DSW columns is assessed using the confusion matrices in Figure 2-22. Also, the accuracy of both approaches is summarized in Table 2-11. All of the ML regression methods provide better performance in identifying highly ductile behavior of DWS columns than the AISC Seismic Provisions (AISC 2016a). The adopted GPR model has an accuracy of 87.4% for the test set compared to an accuracy of 66.5% by the AISC Seismic Provisions (AISC 2016a), providing an improvement of around 30% in the accuracy.

72

The misclassified entries can be divided into conservative and unconservative entries. The conservative entries are the entries with true ductile and predicted non-ductile behavior (right upper quadrant of the confusion matrix), whereas the unconservative entries are the opposite (i.e., true non-ductile and predicted ductile, left lower quadrant of the confusion matrix). As shown in Figure 2-22, AISC Seismic Provisions (AISC 2016a) has almost triple the unconservative classifications (46 entries) than the adopted GPR model (17 entries) suggesting superior performance of the fitted ML regression model. Clearly, the ML approach has the potential to accurately predict the seismic collapse behavior of DSW columns with better accuracy than traditional approaches.

Table 2-11 Accuracy of the selected ML regression methods and AISC Seismic Provisions (AISC 2016a) in identifying highly ductile behavior of columns

ML method	% Test accuracy	% Train accuracy	% Total accuracy
SLR	84.2	82.9	83.3
RDT	85.6	89.9	88.6
SVM	82.8	86.5	85.4
GPR	87.4	88.5	88.6
AISC (2016)	66.5	69.8	68.9
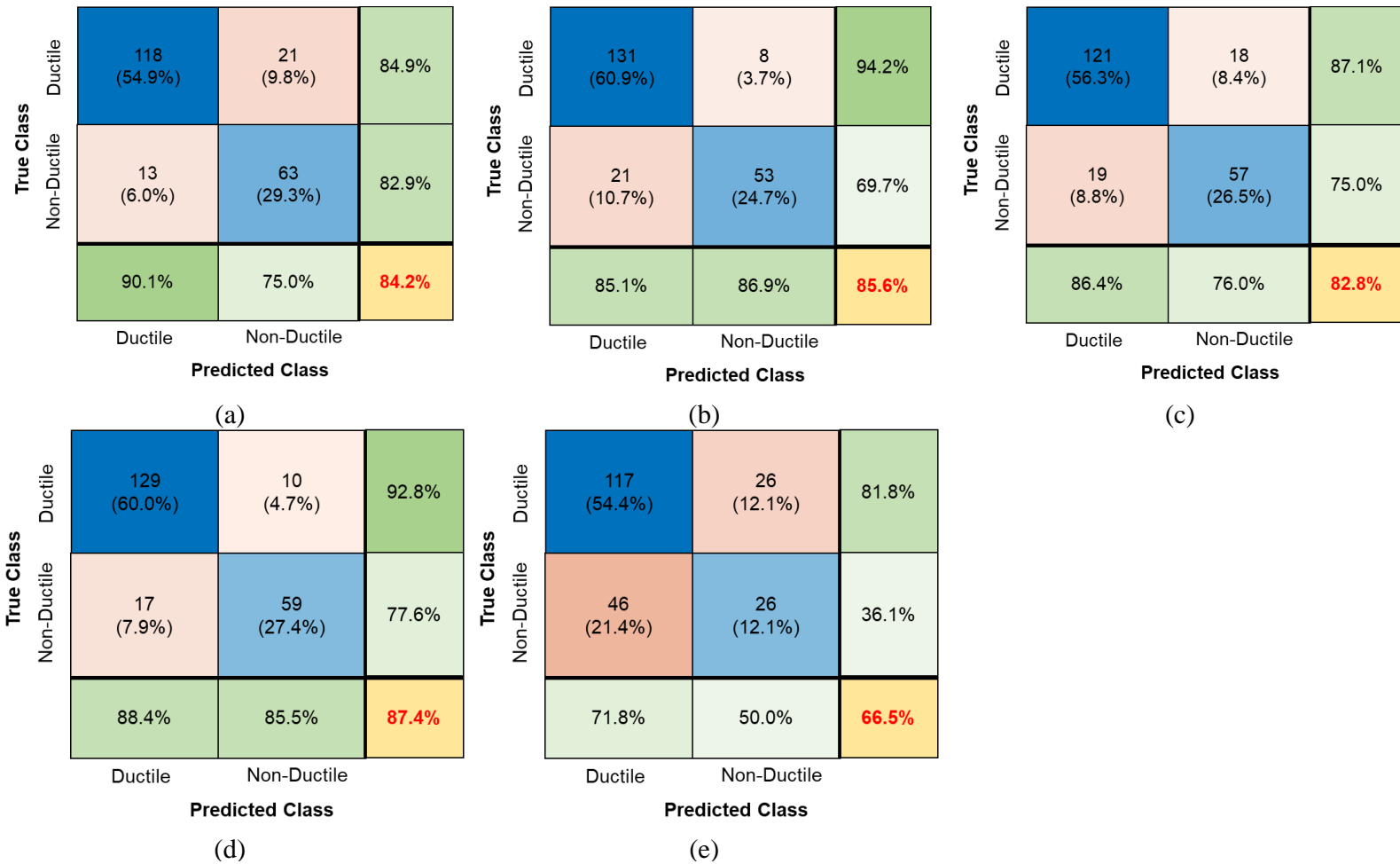
Figure 2-22 Comparison of confusing matrix using ML regression methods and AISC 2016 specifications for the test set to classify the column ductile behavior: (a) SLR; (b) RDT; (c) SVM; (d) GPR; and (e) AISC (2016a)

74

2.3.6 The Promise of Machine Learning for Future Specifications

This study suggests that machine learning could play a role in future generations of design specifications. Since their inception, specifications have sought to develop rules for design that capture the essence of structural response in an accurate and safe manner. The need to simplify the rules so that they can be conveniently incorporated into design documents places inherent constraints on their accuracy. For example, as shown in this work, the current AISC Seismic Provisions (AISC 2016a) specify highly ductile DSW steel column response based on a limited set of parameters. Attempts to improve the seismic provisions as suggested by Wu et al. (2018a) or Ozkula et al. (2017b) are still constrained by the need to propose simplified rules and, as such, the improvements are usually limited and heavily influenced by the parameters of each study. ML algorithms have the ability to transcend these limitations and, in an automated manner: 1) handle the complex relationships between all of the parameters of a particular study, 2) aggregate the results of multiple studies to produce trained algorithms that benefit from all of the studies, and 3) become more accurate as future studies provide new data. These advantages cannot be matched by traditional approaches and as such, it is predicted that ML can play a role in future design specifications as hinted to by the results of this study.

2.4 Collapse Behavior of HSS Columns Under Combined Axial and Lateral Loading

2.4.1 Background

Despite the improvements in the performance of seismically designed moment frames over the past decade, the focus was largely on systems with wide-flange columns. Further improvements may be achieved by considering sections with other beneficial properties such as square, rectangular and circular hollow structural sections (HSS). HSS members, particularly

square and rectangular sections, are often used in steel truss and frame systems based on their high strength-to-weight ratio and large torsional stiffness. Moreover, the distribution of steel at the perimeter of an HSS member provides a higher radius of gyration about its weak axis (r_y) than wide flange columns with similar weight. Therefore, HSS achieve a lower global slenderness ratio about their weak axis (L/r_y), which has been shown as an important parameter affecting the collapse behavior of wide flange columns (Fogarty and El-Tawil 2015, Fogarty et al. 2017and Wu et al. 2018a). These properties of HSS members along with their efficiency under multi-axial loading make them a good choice for columns, beams and bracing members (Packer et al., 2010).

Many numerical and experimental studies have been conducted to evaluate the behavior of HSS members under different loading conditions (Han et al. 2007, Fadden and McCormick 2012 and Lignos et al. 2013). However, most of these studies focused on the application of HSS as braces, which have been widely studied and used in braced frames since the 1970s because of their effectiveness in resisting both tension and compression loads (Tremblay 2002). Early experimental work on the development of HSS as bracing members under cyclic loading was performed at the University of Michigan (Lee and Goel 1987) as well as elsewhere (Foutch et al. 1987, Bertero et al. 1989 and Fukuta et al. 1989). Fell et al. (2006) performed large scale tests on nineteen square HSS, circular HSS and W-shape bracing elements. They reported that width-to-thickness ratio (b/t) is the most important parameter affecting the behavior of braces and that existing seismic design provision limits on b/t (AISC 2005) may not provide sufficient ductility for seismic design.

Fewer studies have focused on HSS columns. Dywer and Galambos (1965) studied the behavior of HSS beam-columns under a constant axial load ratio with increasing bending moments. Cyclic tests have been performed in Japan to experimentally study the seismic performance of HSS columns (Kurata et al. 2005, Nakashima and Liu 2005 and Wang et al.2008). Wang et al. (2008) studied the collapse of a four-story steel moment frame with HSS columns

using online hybrid simulation. It was observed that the varying axial force affects the behavior of the HSS column bases significantly. Suzuki and Lignos (2017) experimentally studied the collapse behavior of full-scale steel HSS and W-shape columns under different loading protocols. A symmetric lateral displacement loading protocol along with a near-collapse lateral displacement protocol, which represents the ratcheting behavior of steel columns in an SMF prior to collapse (Suzuki and Lignos 2014), was used to study the behavior of these beam-columns. They noted that the symmetric loading protocol does not realistically simulate the hysteretic behavior of steel columns at large deformations associated with structural collapse. They also showed that near-collapse protocols reliably represent the cyclic deterioration of the strength of HSS columns. However, only a few HSS sections were considered, and parameters influencing the capacity of HSS columns were not thoroughly quantified.

2.4.2 Motivation and Objectives

The use of HSS columns has the potential to provide enhanced performance for SMFs subject to seismic loads because of their larger radius of gyration about the weak axis (r_y), high strength-to-weight ratio and potential for reduced lateral bracing requirements. The paucity of information about HSS behavior under combined large axial loads and bending moments, as noted in the survey performed earlier, limits this potential. As such, this study seeks to develop a deeper understanding of the collapse behavior of HSS columns. A set of HSS columns that cover a wide range of local and global slenderness ratios is used to computationally study the effect of key parameters on the response of HSS columns. The computational results are used to evaluate the current AISC design guidelines (AISC 2016a) and propose improved provisions suitable for adoption into the current seismic provisions.

2.4.3 Parametric Study of HSS Columns

Prototype Column Selection

It is important for columns in special moment frames (SMFs) to provide highly ductile behavior under earthquake excitations in order to achieve the required seismic drift demands and allow for large energy dissipation capacity. While the high ductility limit for the width-to-thickness ratio (b/t) of HSS members subject to uniform compression is stated explicitly in Chapter D of the seismic provisions (AISC 2016a), there is no explicit high ductility limit for the depth-to-thickness ratio (h/t) of HSS members subject to combined flexure and compression. However, the high ductility limit for webs of built-up box sections can be used for comparison. Table 2-12 summarizes the highly ductile limits. Unlike the high ductility limit for b/t that is a function of only material properties E and F_y, the high ductility limit for the depth-to-thickness ratio (h/t) of a box column also depends on the axial load level, $C_a = P_u/\phi_c P_y$, which is the ratio of the required strength, P_u, to yield strength, $P_y = F_y A_g$, multiplied by the strength reduction factor for compression, $\phi_c = 0.90$. There also is no highly ductile limit for the global slenderness ratio of columns (L/r_y) in the current seismic provisions (AISC 2016a). Thus, the limit for a column with an unbraced beam-to-column connection specified in chapter E of the current seismic provisions (AISC 2016a), which is 60, is used for comparison.

The studied HSS columns are selected to cover a wide range of parameters including local and global slenderness ratios. The distribution of these columns is shown in Figure 2-23 with the high ductility limits of b/t, h/t and L/r_y for ASTM A500 grade B steel indicated. Although the standard grade for square and rectangular HSS sections specified in the current AISC Manual of Steel Construction (2017) is grade C steel, the results of this study are applicable to grade C also because all of the calculations are based on the expected yield strength ($R_y F_y$), which is similar for both grades. The studied columns are classified into three types with respect to current AISC high

ductility limits as discussed earlier for DSW columns. Furthermore, the global slenderness ratio around weak axis (L/r_y) ranges from 31 to 100. This distribution of b/t, h/t and L/r_y ratios allows for a full evaluation of current design assumptions regarding HSS beam-columns leading to potential suggestions for changes to the current seismic design provisions.

Table 2-12 Current AISC 2016 high ductility limits for HSS Columns

Description of Element	Width-to-thickness ratio	Limiting width-to-thickness ratio for high ductile members λ_{hd}
Walls of rectangular HSS used as flanges of beams or columns subjected to uniform compression due to axial, flexure or combined axial and flexure	b/t	$0.65\sqrt{E/R_y F_y}$
Webs of built-up Box sections in flexure or subjected to combined axial and flexure	h/t	*For $C_a \leq 0.114$* $2.57\sqrt{E/R_y F_y}\,(1 - 1.04 C_a)$ *For $C_a > 0.114$* $0.88\sqrt{E/R_y F_y}\,(2.68 - C_a)$ $\geq 1.57\sqrt{E/R_y F_y}$ *Where* $C_a = \dfrac{P_u}{\Phi_c P_y}$
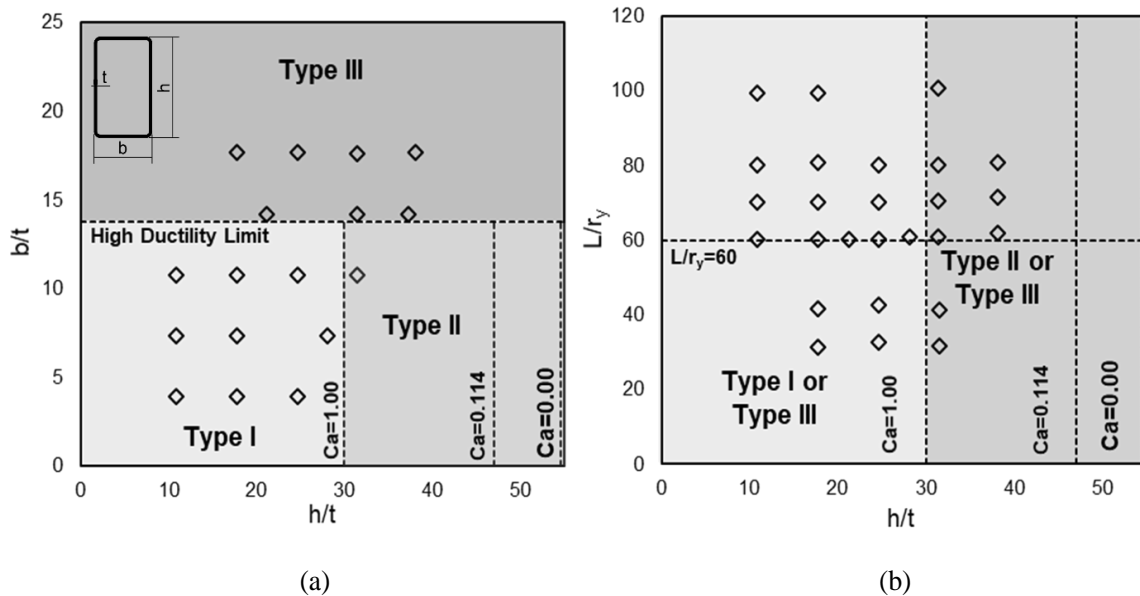
Figure 2-23 Slenderness ratios of studied columns with respect to seismic design provisions (AISC 2016a): (a) local slenderness ratios and (b) global slenderness ratios

Loading Protocols

To study the behavior of HSS beam-columns up to collapse levels, the implemented loading protocols apply a force-controlled constant axial compressive load in addition to a displacement-controlled lateral load. The first protocol is the symmetric cyclic loading protocol (SC) shown in Figure 2-13 and specified in chapter K of the AISC Seismic Provisions (2016a) up to a story drift of 6% to simulate a far-field type earthquake and provide a means of evaluating the moment-rotation behavior of HSS columns under large cyclic deformations. The SC loading protocol has been widely used in studying the seismic behavior of steel columns (Fogarty and El-Tawil 2015), beams (Fadden and McCormick 2012), and braces (Fell et al. 2006).

The second loading protocol is the CR2 protocol, which represents a more realistic drift history of first-story columns as part of SMFs during vertical progressive collapse under earthquakes (Wu et al. 2018a). As discussed earlier, Wu et al. (2018a) developed two loading protocols namely, CR and CR2 by applying and scaling up eleven ground motions from the far-

field record set in FEMA 695 (FEMA 2009) to the three-bay steel SMF of the four-story building outlined in NIST (2010) until collapse. They used the drift history of the first-story columns to develop a representative protocol for collapse of SMFs, which include an initial cyclic behavior followed by ratcheting. The main difference between the CR and CR2 loading protocols is that the dominant failure mode is side-sway and progressive collapse, respectively. Wu et al. (2018a) compared results obtained from the frame level analysis to column level analysis and concluded that the CR2 protocol represents more realistic behavior of first-story columns in a frame system subjected to a ground motion. Consequently, only the CR2 loading protocol is considered in this study.

Performance Parameters

Two performance parameters are considered to evaluate the collapse capacity of HSS columns under the studied loading protocols. The first one is the critical constant axial load ratio (CCALR), which is defined as the maximum axial load ratio that the column can sustain and reach 4% drift under both loading protocols without axial failure (Wu et al. 2018a). The axial failure of the column is defined by the point at which the column is unable to withstand the applied axial load and the axial force in it drops suddenly (Fogarty and El-Tawil 2015), as shown in Figure 2-24(a). CCALR can be used as an indicator of the axial capacity of interior columns in SMFs as they do not experience large variability in their axial load demands during an earthquake (Wu et al. 2018a).

The second performance parameter is the post drift axial strength ratio (PDSR), which is defined as the final squash load a column can reach after reaching 4% lateral drift under both loading protocols as shown in Figure 2-24(b). This parameter can be used as an indicator of the axial capacity of exterior columns in SMFs because they experience variability in their axial load

demands during an earthquake due to overturning moments (Wu et al. 2018a). Exterior columns are assumed to be subjected to increasing axial load at the peak drift to reflect the increase in axial load due to overturning moments.

Both CCALR and PDSR are normalized by the axial yield strength of the section, P_y, based on an expected yield stress of ASTM A500 grade B steel of 444 MPa. For the SC loading protocol, the performance parameter considered to represent the behavior of the studied columns is only CCALR. PDSR is not used as a performance parameter because most of the HSS columns cannot reach 4% drift, at which PDSR is computed, under $P/P_y = 0.30$ or more under the SC protocol.
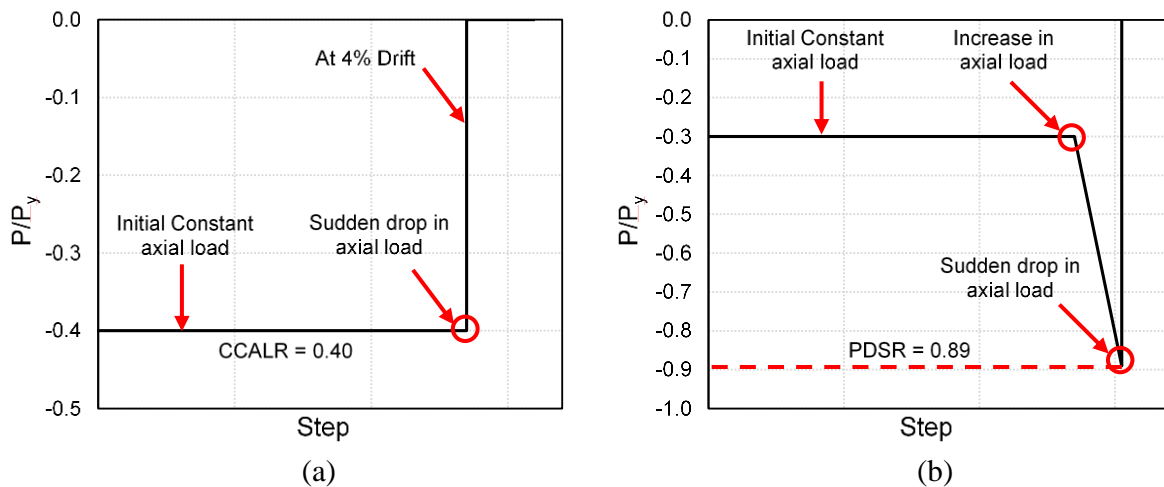
Figure 2-24 Definition of performance parameters: (a) CCALR and (b) PDSR

2.4.4 Finite Element Modeling

Modeling Approach

Similar to the modeling approach for DSW columns described earlier, detailed finite element models of the HSS columns are created using the commercial software Hypermesh and analyzed using the general-purpose finite element software LS-DYNA. The cross-section dimensions are taken as those designated in the AISC Manual of Steel Construction (2017). The

82

thickness of the flat and corner portions of the cross-section are assumed to be the same while the radius of the corner portion is taken as twice the thickness of the section. Again, the fully integrated shell element (ELFORM 16) is used to discretize both the flat and corner portions of the HSS columns.

The strain rate-independent, nonlinear, kinematic hardening material model, MAT_153, (Huang and Mahin 2010) is assigned to the shell elements to capture the cyclic behavior of the HSS columns. The hardening and damage parameters are separately defined for the flat and corner portions of the cross-section to consider the variability of the material properties within the cross section of HSS due to the cold forming process. The parameters are calibrated to available tensile test data of ASTM A500 grade B steel from Fadden and McCormick (2012) using the true stress–true strain model proposed by Arasaratnam et al. (2011), where the results are shown in Figure 2-25.
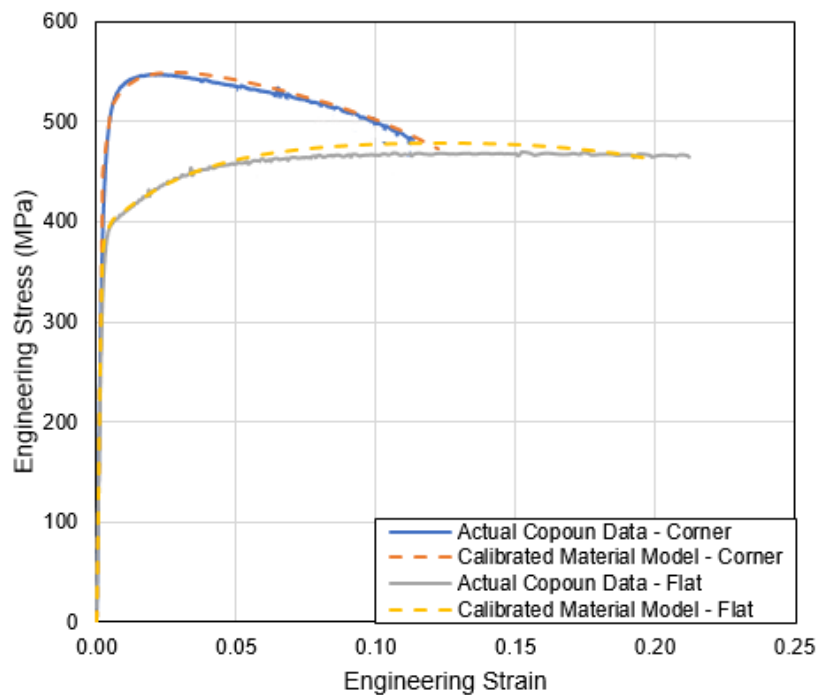
Figure 2-25 Material model calibration with results of actual coupon test data for flat and corner parts of HSS (data from Fadden and McCormick 2012)

The geometry of the columns is modified to include an initial global geometric imperfection assuming a sinusoidal shape with maximum amplitude of L/1000 at the mid-height. The addition of local imperfections was deemed not necessary based on the good results achieved in the validation studies. The element size is selected based on a mesh sensitivity study to reduce numerical error where the mesh size is progressively halved until convergence. For all of the models, the mesh size is chosen so that the corner potion of the cross-section is divided into at least two elements per row. Both ends of the columns are fixed except for x- and z-direction translation, which are free at the top end of the column. The column ends are attached to rigid plates to distribute the axial load over the cross section without causing excessive local deformations. Figure 2-26(a) shows the finite element model mesh and boundary conditions.

Validation

Due to lack of available experimental data for HSS columns under combined axial force and cyclic lateral loading, the finite element modeling approach is validated against cyclic bending tests of HSS beams conducted by Fadden and McCormick (2012) as well as experimental data of W-shape column specimens subjected to combined axial force and cyclic lateral loading in Uang et al. (2015). Details about the validation of the W-shape columns can be found in Fogarty and El-Tawil (2015) and Fogarty et al. (2017). The HSS beams were cantilevered with cyclic displacement applied to the free end. The lateral load is applied using displacement-control up to a rotation of 8% to simulate a far-field type earthquake. Detailed finite element models of these beams are created using the modeling techniques presented in the previous section except that two calibrated vertical springs with stiffness 2100 kN/mm are attached to the beam bottom end. The springs are used to control the in-plane rotation to account for the flexibility at the fixed end during testing. For the parametric study, these springs are not used as full fixity is assumed at the column

base. In addition, the material properties obtained from the coupon tests in Fadden and McCormick (2012) are used to calibrate the material models. Figure 2-26(b) shows the boundary conditions used in the validation finite element model.

Because small rigid body rotations of the HSS beams were observed during testing as described in Fadden and McCormick (2012), the actual rotation applied to the validation models is obtained by subtracting rigid body rotations from the overall measured rotation based on the free end displacement. The comparison between experimental and computational responses of three specimens are shown in Figure 2-27. The models consist of HSS $254 \times 203 \times 6.4$, HSS $254 \times 102 \times 6.4$ and HSS $203 \times 102 \times 9.5$ beams with length of 1537 mm. The hysteric behavior of the HSS beams obtained from the finite element models are in good agreement with the experimental results. In addition to local instabilities, the finite element models capture fracture that initiated in the corners of the HSS and propagated along the walls, as shown in Figure 2-27(b). The difference in the direction of buckling in the sidewall in Figure 2-27(b) is attributed to the specific initial imperfection that was present in the test specimen and that promoted buckling in the manner shown. In spite of this difference, the location and length of local buckling are consistent with the test data. Therefore, the validation results provide confidence that the employed modeling techniques can reasonably simulate the cyclic behavior and failure modes of HSS members.

- Displaced end
- Translation X and Z are free
- Translation Y is restrained
- All rotations are restrained
- Lateral motion in X-direction

- Displaced end (cantilever end)
- Lateral motion in X-direction

- All translations are restrained
- Rotation about Y is controlled by vertical springs

Vertical Springs

- Fixed end
- All translations and rotations are restrained

(a)

(b)
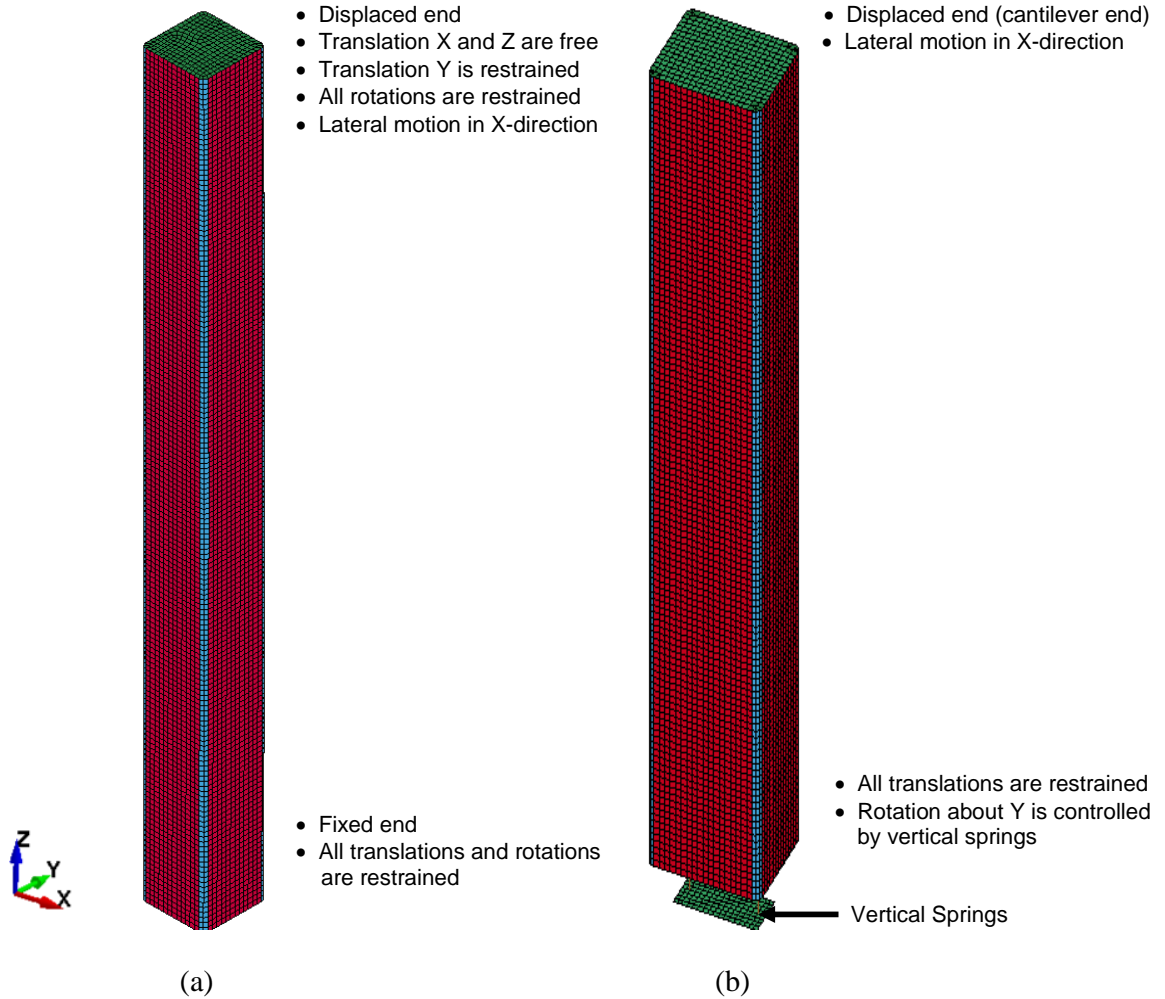
Figure 2-26 Mesh and boundary conditions used in finite element models of columns in: (a) the parametric study and (b) validation
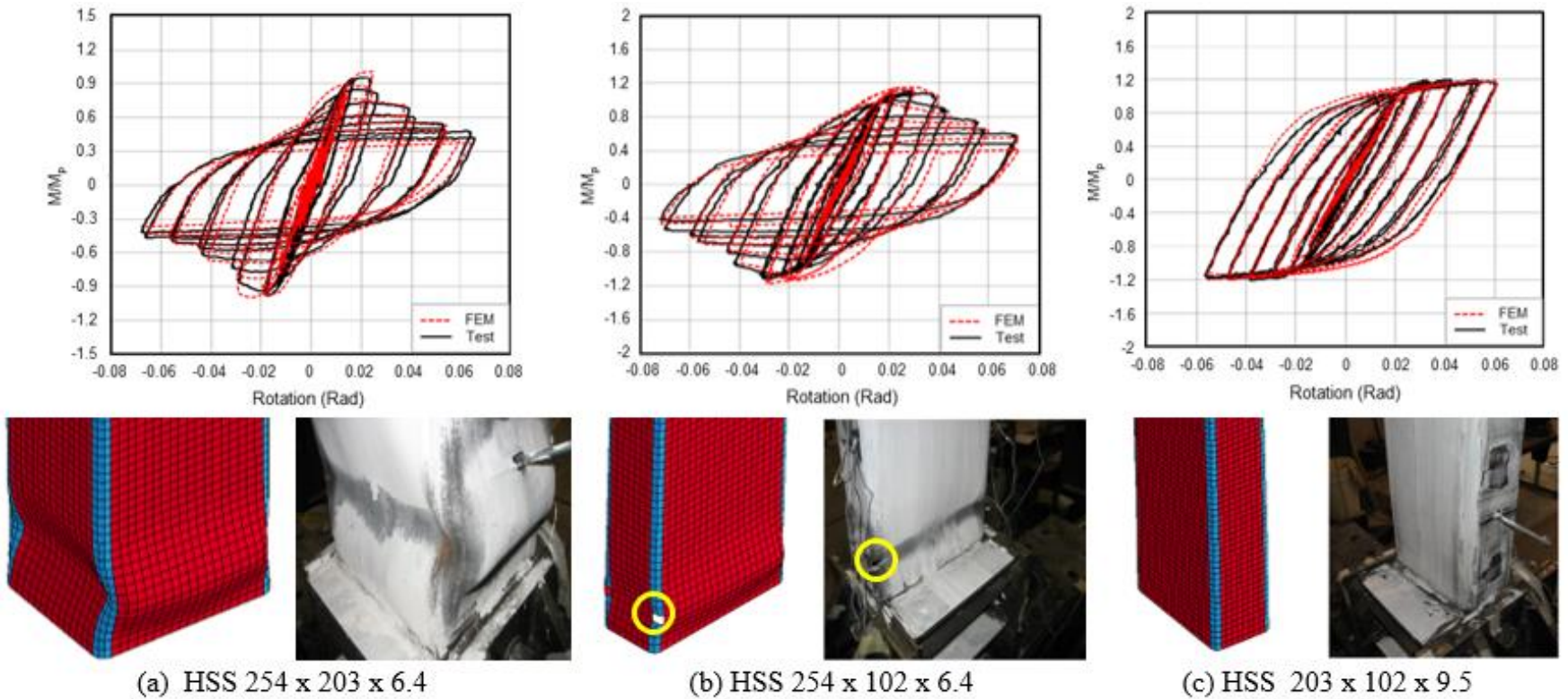
Figure 2-27 Comparison of moment-rotation behavior and hinge region shape at the end of the test of validated HSS beams: (a) HSS 254 × 203 × 6.4, (b) HSS 254 × 102 × 6.4 and (c) HSS 203 × 102 × 9.5 (all data is from Fadden and McCormick 2012)

2.4.5 Simulation Results

The studied HSS columns are investigated under both the SC and CR2 loading protocols. The results with respect to the considered performance parameters, CCALR and PDSR, are listed in Table 2-13 and Table 2-14, respectively. In order to facilitate discussion of the considered parameters, columns under specific loading protocols are designated as H-X-Y-Z, where "H" is the HSS profile, "X" is the global slenderness ratio, "Y" is the lateral drift protocol and "Z" is the initial axial load percentage. For example, HSS 356×254×16-60-CR2-20 is the HSS 356×254×16 column with a global slenderness ratio equal to 60 subjected to the CR2 lateral loading protocol and an initial axial load ratio of 0.20 P_y.

Failure Mode

Two failure modes are observed from the range of studied columns. The first mode is the global failure mode (GF) described earlier for DSW columns (i.e., the column does not experience significant local buckling near the plastic hinge zone prior to excessive flexural buckling, as shown in Figure 2-28(a)). The second mode is the local failure mode (LF) described earlier for DSW columns (i.e., the column ends experience severe local buckling leading to a local crushing mechanism and eventual failure of the column, as shown in Figure 2-28(b)).

Investigating the behavior of the studied columns, the failure mode is controlled mainly by web depth-to-thickness ratio (h/t) and the level of initial applied axial load (P/P_y). For relatively high width-to-thickness ratios (b/t) and low initial axial load levels (P/P_y), increasing h/t results in severe local buckling in the plastic hinge region that alters the failure mode from global to local, e.g., the HSS 356×254×16-60-CR2-20 (h/t=21.2, b/t=14.2) column versus the HSS 356×152×9.5-60-CR2-20 (h/t=37.2, b/t=14.2) column. This change of failure mode does not occur when both b/t and P/P_y are relatively low, as can be seen with the HSS 203×152×16-60-CR2-20 (h/t=10.8,

b/t=7.33) column versus the HSS 457×152×16-60-CR2-20 (*h/t*=28.1, *b/t*=7.33) column. Furthermore, increasing the initial axial load level (*P/P$_y$*) also changes the failure mode from the global to local, e.g. the HSS 406×203×16-60-CR2-20 column versus the HSS 406×203×16-60-CR2-30 column. As a result, at the CCALR where the initial axial load level (*P/P$_y$*) is high, the dominant failure mode is the local failure mode for both loading protocols. In general, increasing *b/t* or *L/r$_y$* does not change the failure mode.

The post drift strength ratio (PDSR) highly depends on the dominant failure mode of the column. Columns undergoing a global failure mode yield significantly higher PDSR than those undergoing a local failure mode. This is attributed to the plastic hinges formed at the ends of columns undergoing local failure, which changes the boundary conditions of the columns leading to lower post drift axial strength than those undergoing global failure without plastic hinges. The columns that experience a change in failure mode with increasing initial axial load level also experience a significant decrease in PDSR by 50% on average for the same reason. For example, when the HSS 254×127×8-72-CR2 column undergoes an increase of *P/P$_y$* from 0.20 to 0.30, the column maintains a global failure mode and the corresponding PDSR only drops from 0.84*P$_y$* to 0.80*P$_y$*. However, when the *P/P$_y$* further increases to 0.40, the column fails by the local failure mode, which significantly decreases the PDSR to 0.61*P$_y$*. This result implies that high initial axial load ratios are not recommended when considering the seismic design of HSS columns in SMFs.

Table 2-13 CCALR results of studied HSS columns under both loading protocols

HSS Section (mm × mm × mm)	b/t	h/t	L/r_y.	P_y (kN)	SC Protocol		CR2 Protocol	
					CCALR	Failure Mode	CCALR	Failure Mode
HSS 203×152×16	7.33	10.8	60.8	4010	0.7	LF	0.75	G
HSS 203×203×16	10.8	10.8	60.2	4698	0.6	GF	0.8	G
HSS 203×203×16	10.8	10.8	70.2	4698	0.6	GF	0.7	G
HSS 203×152×16	7.33	10.8	71.3	4011	0.65	GF	0.7	G
HSS 203×152×16	7.33	10.8	79.3	4010	0.65	LF	0.7	G
HSS 203×203×16	10.8	10.8	80.2	4698	0.55	GF	0.7	G
HSS 203×102×16	3.89	10.8	99.3	3352	0.65	GF	0.65	G
HSS 305×305×16	17.7	17.7	31.1	7362	0.45	LF	0.6	L
HSS 305×305×16	17.7	17.7	41.5	7362	0.5	LF	0.6	L
HSS 305×203×16	10.8	17.7	60.2	6016	0.45	LF	0.7	G
HSS 305×152×16	7.33	17.7	61.9	5357	0.45	LF	0.65	L
HSS 305×203×16	10.8	17.7	70.2	6016	0.5	LF	0.6	G
HSS 305×102×16	3.89	17.7	80.2	4698	0.45	LF	0.6	G
HSS 305×152×16	7.33	17.7	80.9	5357	0.5	LF	0.6	G
HSS 305×102×16	3.89	17.7	99.3	4698	0.5	LF	0.6	G
HSS 356×254×16	14.2	21.2	60.2	7362	0.35	LF	0.6	L
HSS 406×305×16	17.7	24.6	32.5	8680	0.25	LF	0.4	L
HSS 406×305×16	17.7	24.6	42.5	8680	0.3	LF	0.4	L
HSS 406×203×16	10.8	24.6	60.2	7362	0.35	LF	0.45	L
HSS 406×203×16	10.8	24.6	70.2	7362	0.35	LF	0.5	L
HSS 406×102×16	3.89	24.6	80.2	6016	0.3	LF	0.45	L
HSS 457×152×16	7.33	28.1	60.7	7362	0.25	LF	0.4	L
HSS 254×152×8	17.6	31.4	60.7	2509	0.3	LF	0.35	L
HSS 254×127×8	14.2	31.4	60.8	2340	0.25	LF	0.35	L
HSS 254×152×8	17.6	31.4	70.4	2509	0.25	LF	0.35	L
HSS 254×127×8	14.2	31.4	72.4	2340	0.25	LF	0.4	L
HSS 254×152×8	17.6	31.4	80.1	2509	0.25	LF	0.4	L
HSS 254×127×8	14.2	31.4	81.1	2340	0.25	LF	0.4	L
HSS 254×102×8	10.8	31.4	100.6	2174	0.3	LF	0.45	G
HSS 508×305×16	17.7	31.5	31.6	10026	0.25	LF	0.25	L
HSS 508×305×16	17.7	31.5	41.3	10026	0.25	LF	0.35	L
HSS 356×152×9.5	14.2	37.2	61.9	3781	0.25	LF	0.3	L
HSS 356×152×9.5	14.2	37.2	71.4	3781	0.25	LF	0.3	L
HSS 356×152×9.5	14.2	37.2	80.9	3781	0.25	LF	0.3	L
HSS 305×152×8	17.7	38.1	61.9	2841	0.2	LF	0.3	L
HSS 305×152×8	17.7	38.1	71.4	2841	0.2	LF	0.3	L
HSS 305×152×8	17.7	38.1	80.9	2841	0.2	LF	0.3	L

LF: The dominant failure mode is local failure
GF: The dominant failure mode is global failure

Table 2-14 PDSR of studied columns under CR2 loading protocol

HSS Section (mm × mm × mm)	L/r_y	P_y (kN)	P/P_y=0.20 Failure Mode	PDSR	P/P_y=0.30 Failure Mode	PDSR	P/P_y=0.40 Failure Mode	PDSR
HSS 203×152×16	60.8	4010	GF	1.00	GF	1.00	GF	1.00
HSS 203×203×16	60.2	4698	GF	0.98	GF	0.97	GF	0.95
HSS 203×203×16	70.2	4698	GF	0.89	GF	0.87	GF	0.86
HSS 203×152×16	71.3	4011	GF	1.00	GF	1.00	GF	1.00
HSS 203×152×16	79.3	4010	GF	0.98	GF	0.97	GF	0.95
HSS 203×203×16	80.2	4698	GF	0.90	GF	0.90	GF	0.85
HSS 203×102×16	99.3	3352	GF	0.89	GF	0.89	GF	0.89
HSS 305×305×16	31.1	7362	GF	1.00	GF	1.00	LF	0.96
HSS 305×305×16	41.5	7362	GF	0.98	GF	0.98	GF	0.96
HSS 305×203×16	60.2	6016	GF	0.99	GF	0.99	GF	0.99
HSS 305×152×16	61.9	5357	GF	1.00	GF	1.00	GF	1.00
HSS 305×203×16	70.2	6016	GF	0.94	GF	0.87	GF	0.85
HSS 305×102×16	80.2	4698	GF	1.00	GF	0.99	GF	0.97
HSS 305×152×16	80.9	5357	GF	0.93	GF	0.91	GF	0.89
HSS 305×102×16	99.3	4698	GF	0.91	GF	0.88	GF	0.86
HSS 356×254×16	60.2	7362	GF	0.94	GF	0.94	GF	0.93
HSS 406×305×16	32.5	8680	LF	0.87	LF	0.70	-------	a
HSS 406×305×16	42.5	8680	LF	0.94	LF	0.78	LF	0.61
HSS 406×203×16	60.2	7362	GF	0.97	LF	0.91	LF	0.70
HSS 406×203×16	70.2	7362	GF	0.91	GF	0.91	LF	0.79
HSS 406×102×16	80.2	6016	GF	0.96	GF	0.85	LF	0.62
HSS 457×152×16	60.7	7362	GF	0.91	LF	0.68	LF	0.41
HSS 254×152×8	60.7	2509	GF	0.87	GF	0.81	-------	a
HSS 254×127×8	60.8	2340	LF	0.76	LF	0.67	-------	a
HSS 254×152×8	70.4	2509	GF	0.87	LF	0.67	-------	a
HSS 254×127×8	72.4	2340	GF	0.84	GF	0.80	LF	0.61
HSS 254×152×8	80.1	2509	GF	0.87	LF	0.60	LF	0.42
HSS 254×127×8	81.1	2340	GF	0.84	GF	0.78	LF	0.67
HSS 254×102×8	100.6	2174	GF	0.41	GF	0.40	GF	0.69
HSS 508×305×16	31.6	10026	LF	0.48	LF	0.31	-------	a
HSS 508×305×16	41.3	10026	LF	0.82	LF	0.48	-------	a
HSS 356×152×9.5	61.9	3781	LF	0.63	LF	0.31	-------	a
HSS 356×152×9.5	71.4	3781	LF	0.67	LF	0.46	-------	a
HSS 356×152×9.5	80.9	3781	LF	0.64	LF	0.47	-------	a
HSS 305×152×8	61.9	2841	LF	0.60	LF	0.30	-------	a
HSS 305×152×8	71.4	2841	LF	0.57	LF	0.32	-------	a
HSS 305×152×8	80.9	2841	LF	0.59	LF	0.47	-------	a

[a] The column did not sustain the applied constant axial load till the end of CR2 protocol

LF: The dominant failure mode is local failure

GF: The dominant failure mode is global failure
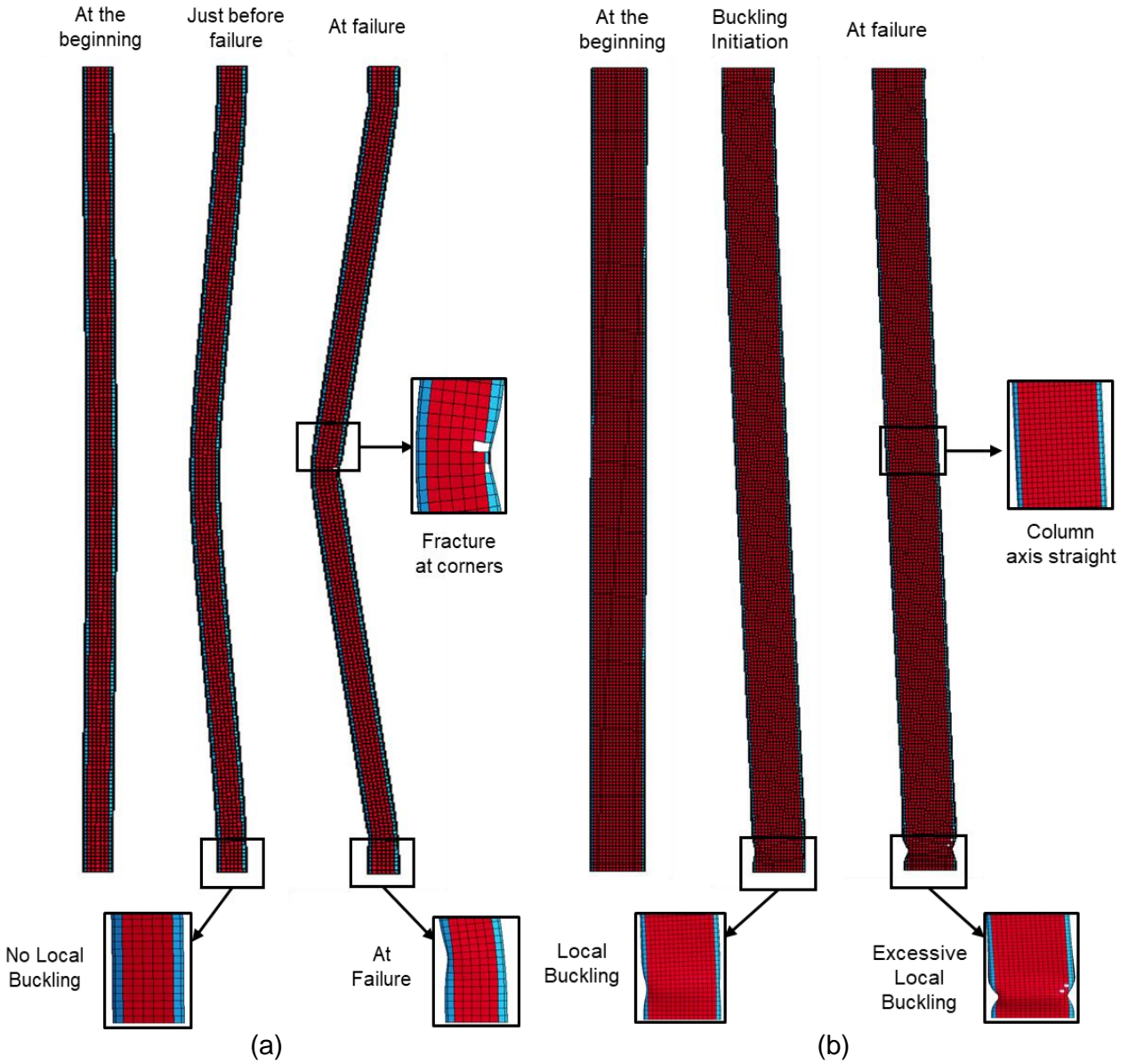
Figure 2-28 Failure modes of HSS columns: (a) global failure mode (HSS 305 x 305 x 16-40-CR2-20); and (b) local failure mode (HSS 254 x 127 x 8-70-CR2-40)

Effect of Local Slenderness Ratios

As shown in Figure 2-29(a), there is a clear negative correlation with minimal scatter between h/t and PDSR for HSS columns under the CR2 loading protocol. Moreover, the influence of h/t is larger at higher initial axial load ratios. For example, increasing h/t from 17.7 to 31.4 for columns (HSS 305×152×16-80-CR2 and HSS 254×152×8-80-CR2) under 0.20 P_y results in a decrease of 7% in PDSR, while the PDSR decreases by 32% and 53% for the same two HSS columns under initial axial loads of 0.30 P_y and 0.40 P_y, respectively. Also, there is a strong negative relationship between h/t and CCALR under both lateral loading protocols as shown in Figure 2-29(b), implying that h/t is an important parameter with respect to both CCALR and PDSR. This finding is consistent with the AISC seismic provisions (2016a), which directly relate the h/t high ductility limit with axial load level.

The correlation between b/t and PDSR for HSS columns under the CR2 loading protocol is also negative, but the amount of scatter in the results is much higher than that seen in h/t (Figure 2-30(a)). This increased scatter is attributed to the fact that the dominant failure mode is controlled mainly by the h/t ratio so the effect of b/t on PDSR is not independent of h/t. Figure 2-30(b) shows the relationship between b/t and CCALR for both lateral loading protocols. There is a clear downward trend with a large amount of scatter between b/t and CCALR. Similar to PDSR, b/t is not a significant parameter in determining CCALR.
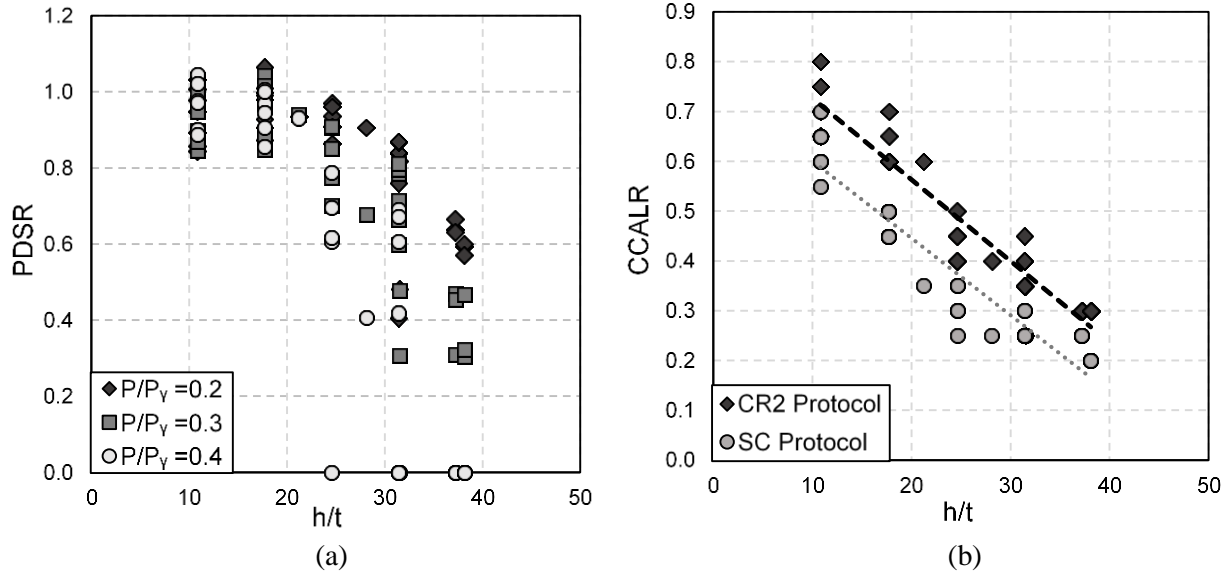
Figure 2-29 Effect of depth-to-thickness ratio (*h/t*) on: (a) PDSR and (b) CCALR
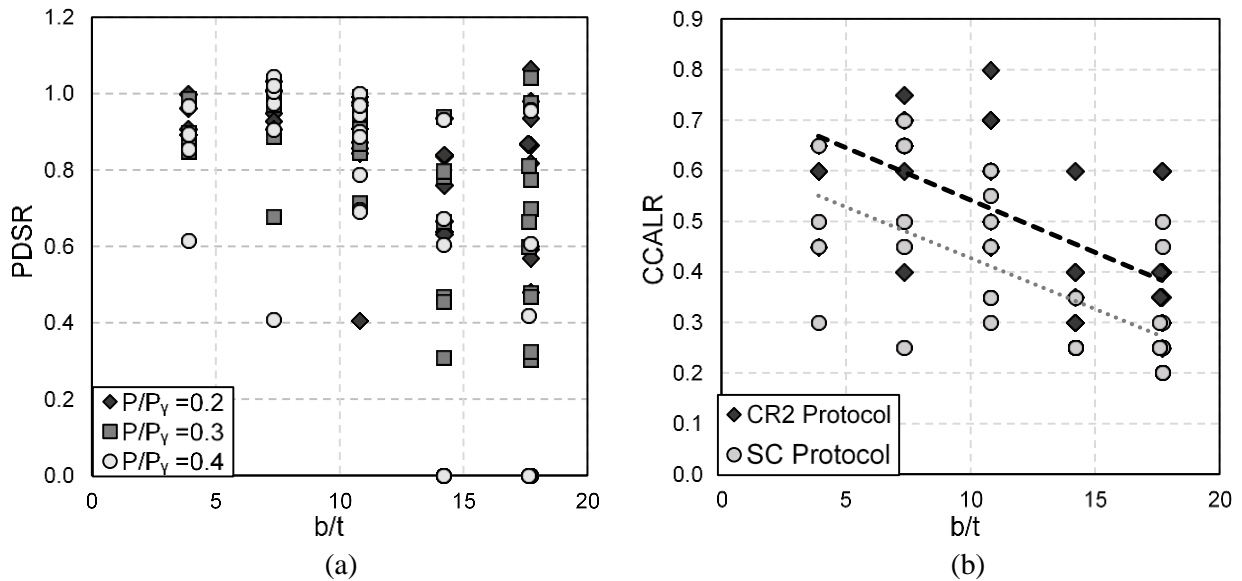
Figure 2-30 Effect of flange width-to-thickness ratio (*b/t*) on: (a) PDSR and (b) CCALR

Effect of Global Slenderness Ratio

The effect of global slenderness ratio (L/r_y) on PDSR under the CR2 loading protocol is

not the same for both failure modes. As shown in Figure 2-31, when the dominant failure mode is

a global failure, there is a negative correlation between L/r_y and PDSR with minor scatter implying

that L/r_y has a significant effect on PDSR under this mode of failure. Furthermore, the slope of the trendline is fairly constant for different initial axial load ratios (P/P_y). When a local failure mode is the dominant mode, there is a negative correlation between L/r_y and PDSR with large amount of scatter implying that PDSR is less dependent on L/r_y as shown in Figure 2-31. This result is again attributed to the fact that PDSR for a local failure mode is controlled mainly by h/t. The slope of trendline also decreases with increasing initial axial load level, leading to a horizontal trend at P/P_y=0.40 for the local failure mode as shown in Figure 2-31(c). CCALR is mainly controlled by the local slenderness ratios h/t and b/t because the dominant failure mode under P/P_y = CCALR is the local mode. Therefore, the global slenderness ratio L/r_y does not have a significant impact on CCALR under both loading protocols within the ranges of studied parameters.
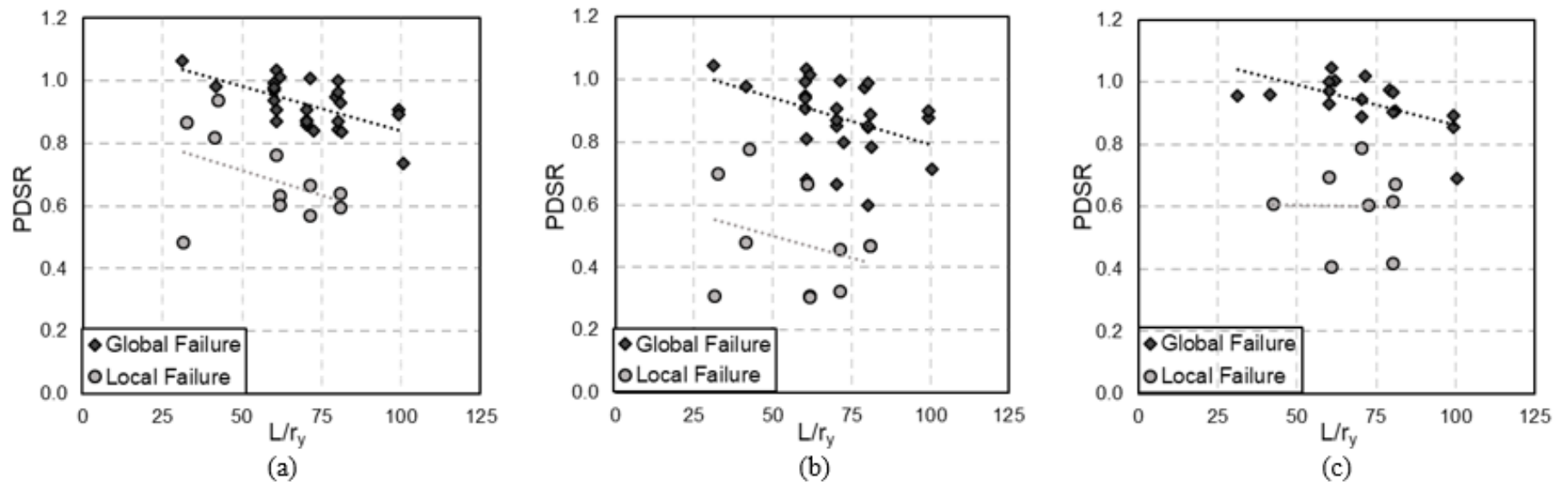
Figure 2-31 Effect of global slenderness ratio (*L/r$_y$*) on PDSR when initial constant axial load ratio (*P/P$_y$*) = (a) 0.20; (b) 0.30; and (c) 0.40

Effect of Axial Load

Finite element results show that the initial axial load ratio (P/P_y) significantly affects the behavior of HSS columns subjected to lateral drift. As shown in Figure 2-29(a), increasing P/P_y results in substantial reduction in PDSR, especially when h/t is high. For example, for the HSS 203×152×16-70-CR2 column with h/t equal to 10.8, increasing the initial axial load level from 0.20 P_y to 0.40 P_y decreased PDSR by only 2%. On the other hand, for the HSS 457×152×16-60-CR2 column with higher h/t of 28.1, increasing initial axial load level from 0.20 P_y to 0.40 P_y significantly decreased PDSR by 55%. This result is attributed to the fact that the failure mode changes from global to local failure when the initial axial load level increases from 0.20 P_y to 0.40 P_y for the HSS 457×152×16-60-CR2 column.

Increasing P/P_y reduces the ductility of HSS columns significantly. Figure 2-32 shows the moment-rotation behavior of the HSS 356×152×9.5-80-SC column. It is clear that the ductility of the HSS 356×152×9.5 column is much higher when subjected to 0.15 P_y than when subjected to 0.30P_y. As shown in Figure 2-32(a), the column sustained an initial axial load level of 0.15 P_y and reached 5% drift. However, as shown in Figure 2-32(d), under an axial load of 0.30 P_y, the column failed to reach the end of the second cycle of 3% drift.

Effect of Loading Protocols

Based on the finite element results listed in Table 2-13, it is clear that the SC loading protocol is more severe than the CR2 loading protocol in regard to the demands placed on HSS columns. This fact can be observed by comparing the common performance parameter considered in both loading protocols (CCALR). It is noted that CCALR evaluated under the SC loading protocol is generally less than CCALR evaluated under the CR2 loading protocol. On average, the SC loading protocol yields a CCALR 25% lower than that for the CR2 loading protocol. For the

HSS 305×152×16-60 column, CCALR decreased from 0.65 under the CR2 loading protocol to 0.45 under the SC loading protocol. The local failure mode is more dominant in the case of the SC loading protocol due to the excessive cycling experienced by the HSS columns. Unlike under the CR2 protocol, where P/P_y and L/r_y are more influential, local slenderness ratios (h/t and b/t) are more significant under the SC loading protocol because of the dominant local behavior.
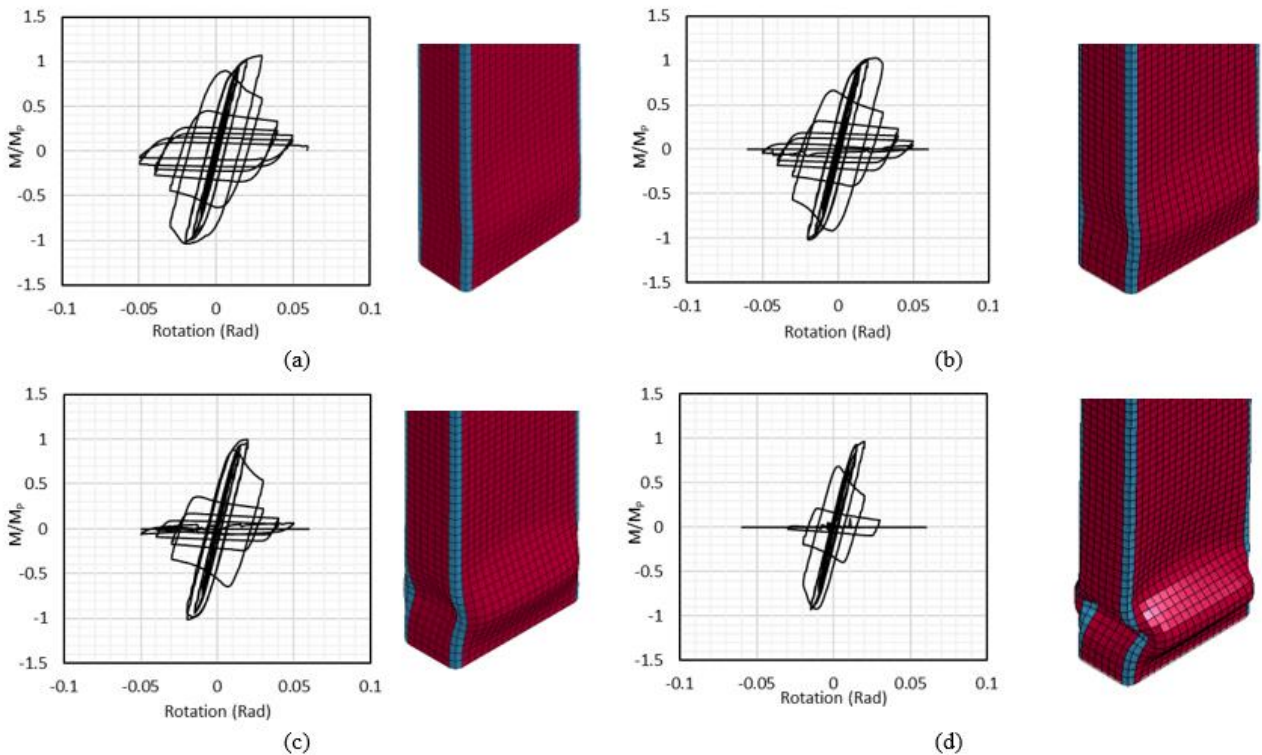
Figure 2-32 Moment-rotation behavior and shape of the plastic hinge region at 3% drift for the HSS 356 x 152 x 9.5-80-SC column under an initial axial load ratio of: (a) 0.15 P_y; (b) 0.20 P_y; (c) 0.25 P_y and (d) 0.30 P_y

Axial Shortening

Finite element results of studied columns show that axially loaded HSS columns subject to cyclic lateral drift experience significant axial shortening due to deformation in the plastic hinge region. However, the amount of axial shortening of all studied HSS columns at a 0.01 rad. base

rotation (i.e., 1% lateral drift), which is commonly associated with immediate occupancy performance objective (ASCE 2006), is minimal under both loading protocols. Also, the amount of axial shortening of the studied HSS columns is much higher under the SC loading protocol than the CR2 protocol. Figure 2-33(a) shows the axial shortening versus base rotation of the HSS 508×305×16-40 column subjected to an initial axial load level of 0.20 P_y for both lateral loading protocols. In this figure, the axial shortening is normalized by the column height. The column experiences the same amount of axial shortening under the effect of both loading protocols at the first elastic cycles (with base rotation less than 0.01). However, the axial shortening of the column accumulates faster under the SC loading protocol than the CR2 protocol at larger inelastic cycles. This finding is attributed to the fact that HSS columns experience more severe local buckling in the plastic hinge region due to the excessive cycling experienced under the effect of the SC loading protocol.

The amount of observed axial shortening for larger cycles is significantly higher for columns subjected to higher initial axial load levels (P/P_y). Figure 2-33(b) shows the axial shortening versus base rotation of the HSS 305×102×16-99-SC column subject to different initial axial load levels, 0.20 P_y and 0.40 P_y. The amount of axial shortening is almost the same under both axial load levels for the first cycles. However, the rate of accumulation of axial shortening is much larger under the effect of higher axial load levels at larger inelastic cycles. The axial shortening at a base rotation of 0.01 rad. is 0.04% and 0.05% when P/P_y =0.20 and 0.40, respectively, while the axial shortening at a base rotation of 0.04 rad. (ii.e.,4% lateral drift), which is commonly associated with the collapse prevention performance objective (ASCE 2006), is 0.33% and 1.64% when P/P_y =0.20 and 0.40, respectively.

Furthermore, the amount of axial shortening is significantly higher for HSS columns with higher depth-to-thickness ratios (h/t). Figure 2-33(c) shows the axial shortening of the HSS

305×102×16-80-CR2-40 (*h/t*=17.7, *b/t*=3.89) column and the HSS 406×102×16-80- CR2-40 (*h/t*=24.6, *b/t*=3.89) column. During later inelastic cycles, the rate of growth of axial shortening of the column with larger *h/t* is higher. This result is attributed to the fact that *h/t* influences the amount of local buckling in the plastic hinge region. To limit the amount of axial shortening of HSS columns, the depth-to-thickness ratio (*h/t*) or the applied axial load level (*P/P_y*) can be reduced.

(a)   (b)   (c)
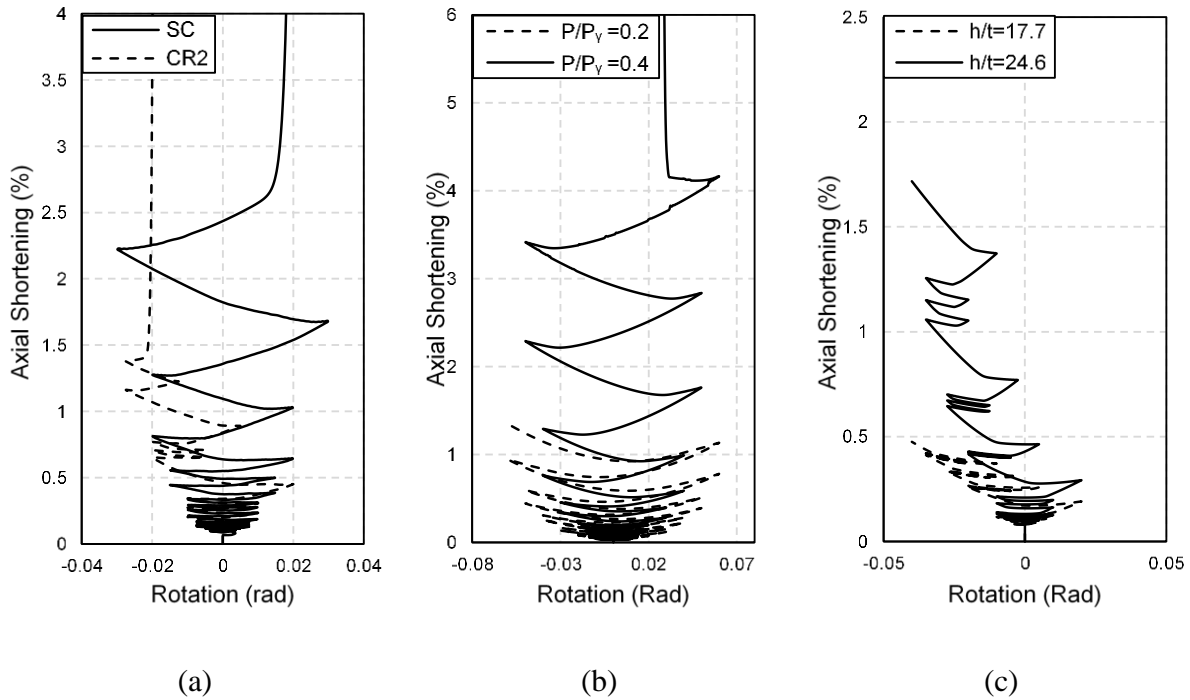
Figure 2-33 Effect on axial shortening of HSS columns of: (a) lateral loading protocol (HSS 508×305×16-40), (b) *P/P_y* (HSS 305×102×16-99-SC) and (c) *h/t* (HSS 305×102×16-80-CR2-40 and HSS 406×102×16-80- CR2-40)

Regression Analysis

The results listed in Table 2-13 and Table 2-14 are used in a linear regression analysis to provide mathematical expressions to calculate the studied performance parameters, CCALR and PDSR, under the CR2 loading protocol. For CCALR, the element slenderness ratios are the most

100

influential parameters that control the axial capacity of HSS columns. Thus, the general response variable (CCALR) is expressed in the following simple model:

$$CCALR = K_1 + K_2\,\frac{h}{t} + K_3\,\frac{b}{t} + K_4\,\frac{L}{r_y} \qquad (2\text{-}28)$$

Backward elimination (Chaterjee et al. 2000) with standard t-test is used until all parameters are statistically significant at the 5% level. At P/P_y = CCALR the dominant failure mode is the local failure. Therefore, not surprisingly, CCALR is controlled by the local slenderness ratios of the column h/t and b/t, while L/r_y is eliminated from the regression analysis based on its statistical significance. CCALR is expressed as follows:

$$CCALR = 0.92 - 0.016\,\frac{h}{t} - 0.003\,\frac{b}{t} \qquad (2\text{-}29)$$

For PDSR, the slenderness ratios are not the only parameters that control the post drift behavior of HSS columns. The initial axial load ratio (P/P_y) also has a significant effect on PDSR as it can change the failure mode. However, P/P_y does not have a significant effect on PDSR when the dominant failure mode is global while it is a strong parameter when the dominant failure mode is local. Similarly, the significance of the effect of the local slenderness ratios is not the same for the global and local failure modes. Width-to-thickness ratio (b/t) does not have a significant effect on PDSR compared to depth-to-thickness ratio (h/t) when the dominant failure mode is local failure. However, it has the same effect as h/t when the global failure mode is the dominant mode. Therefore, it is more adequate to formulate two expressions for PDSR based on the expected failure mode, which depends on the column local slenderness ratios and the initial axial load level.

PDSR$_G$ and PDSR$_L$ are formulated based on the results of columns that experience a dominant global and local failure mode, respectively. Based on the failure modes observed in the finite element models along with the local slenderness ratios of the studied columns, the limits for

101

calculating PDSR using either PDSR$_G$ or PDSR$_L$ are listed in Table 2-15 for different levels of initial axial load ratios. For the sake of simplicity, the limits listed in Table 2-15 are graphically described in Figure 2-34 considering ASTM A500 grade B steel. The appropriate graph is chosen based on the initial axial load level. A designer can enter the graph with *h/t* and *b/t* to determine whether to calculate PDSR using PDSR$_G$ or PDSR$_L$. The points shown in Figure 2-34 represent the columns used in the parametric study.

Table 2-15 Proposed local slenderness ratio limits for calculating PDSR of HSS columns under different initial axial load ratios

P/P_y	Local Slenderness Ratio	Recommended PDSR
0.2	$h/t \leq 1.48\sqrt{E/R_yF_y}$ & $b/t \leq 0.83\sqrt{E/R_yF_y}$	PDSR$_G$
	$h/t > 1.48\sqrt{E/R_yF_y}$ or $b/t > 0.83\sqrt{E/R_yF_y}$	PDSR$_L$
0.3	$h/t \leq 1.48\sqrt{E/R_yF_y}$ & $b/t \leq 0.67\sqrt{E/R_yF_y}$	PDSR$_G$
	$h/t > 1.48\sqrt{E/R_yF_y}$ or $b/t > 0.67\sqrt{E/R_yF_y}$	PDSR$_L$
0.4	$h/t \leq \sqrt{E/R_yF_y}$ & $b/t \leq 0.67\sqrt{E/R_yF_y}$	PDSR$_G$
	$h/t \leq \sqrt{E/R_yF_y} < h/t \leq 1.48\sqrt{E/R_yF_y}$ or $b/t > 0.67\sqrt{E/R_yF_y}$	PDSR$_L$
	$h/t > 1.48\sqrt{E/R_yF_y}$ or $b/t > 0.67\sqrt{E/R_yF_y}$	N/A

N/A The column will not sustain the applied constant axial load till the end of CR2 protocol
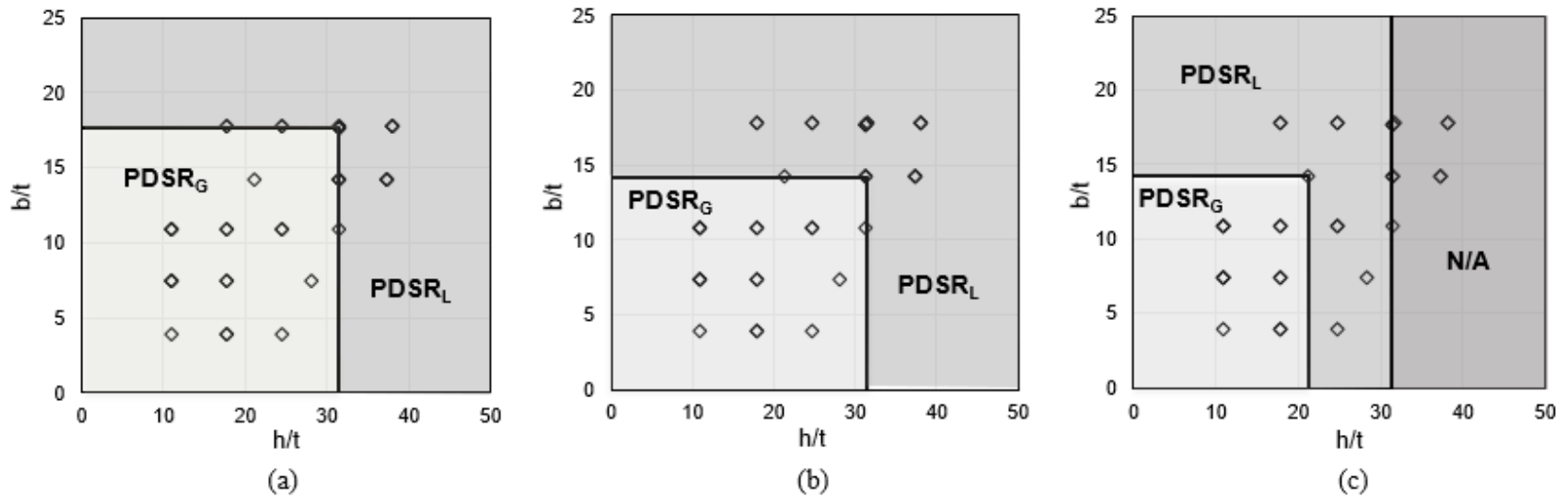
Figure 2-34 Graphical illustration of the boundary between PDSRG and PDSRL for HSS columns under a constant axial load ratio (P/P_y) of: (a) 0.20; (b) 0.30 and (c) 0.40

With the aim of predicting the influence of each parameter on PDSR, the response variable (i.e., PDSR) is calculated in terms of explanatory variables (i.e., h/t, b/t, L/r_y and P/P_y). The general response variable is expressed in the following model:

$$PDSR = K_1 + K_2 \frac{h}{t} + K_3 \frac{b}{t} + K_4 \frac{L}{r_y} + K_5 \frac{P}{P_y} \qquad (2\text{-}30)$$

For PDSR$_G$, column slenderness ratios h/t, b/t and L/r_y are shown to be the main parameters controlling the response variable, while P/P_y is eliminated from the regression analysis based on its statistical significance. On the other hand, for PDSR$_L$, b/t is eliminated from the regression analysis based on its statistical significance, while P/P_y is shown to have a significant influence along with h/t and L/r_y. PDSR$_G$ and PDSR$_L$ are expressed as follows:

$$PDSR_G = 1.42 - 0.012 \frac{b}{t} - 0.003 \frac{h}{t} - 0.0045 \frac{L}{r_y} \qquad (2\text{-}31)$$

$$PDSR_L = 2.04 - 0.039 \frac{h}{t} + 0.0059 \frac{L}{r_y} - 1.93 \frac{P}{P_y} \qquad (2\text{-}32)$$

2.4.6 Design Implication and Recommendation

Proposed Design Guidelines

As mentioned previously, CCALR can be considered as the maximum constant axial load an interior HSS column can sustain and reach 4% lateral drift (i.e., classified as highly ductile). This definition is based on the assumption that interior columns do not experience large variations in axial load during an earthquake. Thus, Equation 2-29 can be rewritten to derive an expression to calculate the maximum design gravity-induced axial load ratio $(P_g/P_y)_{max}$ for interior HSS columns:

$$\left(\frac{P_g}{P_y} \right)_{max} = 0.92 - 0.016 \frac{h}{t} - 0.003 \frac{b}{t} \qquad (2\text{-}33)$$

For the sake of simplicity, a design aid is proposed based on the formulated equation to facilitate the design of interior HSS columns. Figure 2-35 plots the interaction between local slenderness ratios, *h/t* and *b/t*, along with the expected maximum gravity-induced axial load ratio (P_g/P_y) max ranging from 0.20 to 0.70. The circles represent the columns used in the parametric study. A designer can enter the plot with local slenderness ratios, *h/t* and *b/t*, and determine the maximum gravity-induced axial force to design for by selecting the closest line to the right. For example, consider an HSS 254×102×9 where *h/t* is 28.2 and *b/t* is 11.3. Entering the plot with 28.2 along the *x*-axis and 11.3 along the *y*-axis yields a P_g/P_y equal to 0.4. The designer in this case should not select this interior HSS column if it will experience 40% or more of its axial yield strength.
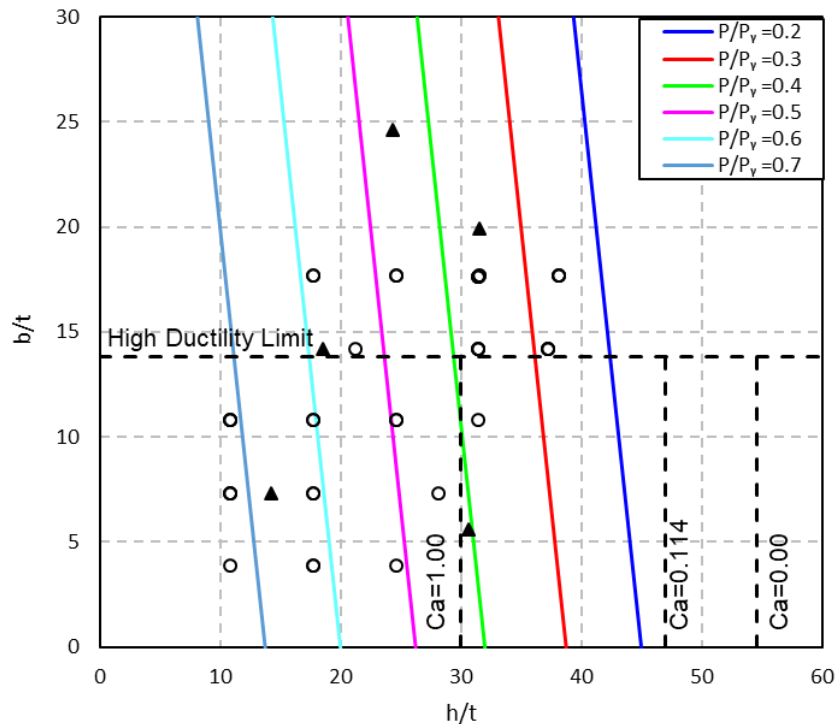
Figure 2-35 Proposed design aid for axial load capacity of interior HSS columns

Rearranging Equation (6) gives:

$$\frac{h}{t} \le 62.5 \left(0.92 - \frac{P_g}{P_y} \right) - 0.18 \frac{b}{t} \qquad (2\text{-}34)$$

The highly ductile limit for h/t of interior HSS columns, $\lambda_{hd,in}$, can then be approximated and reformatted into:

$$\lambda_{hd,in} = 2.945 \sqrt{\frac{E}{R_y F_y}} \left(0.92 - \frac{P_g}{P_y} \right) - 0.18 \frac{b}{t} \qquad (2\text{-}35)$$

For exterior columns, PDSR can be interpreted as the maximum required strength that must be resisted due to gravity loads and overturning moments. Accordingly, Equation 2-31 and Equation 2-32 can be rewritten to derive expressions to calculate the required axial strength of an exterior HSS column, $(P_r/P_y)_{max}$. The designer should choose the appropriate expression to use based on the specified limits for local slenderness ratios along with expected gravity-induced axial load ratio (P_g/P_y) shown in Figure 2-34. The proposed expressions are as follows:

$$\left(\frac{P_r}{P_y} \right)_{G,max} = 1.42 - 0.012 \frac{b}{t} - 0.003 \frac{h}{t} - 0.005 \frac{L}{r_y} \qquad (2\text{-}36)$$

$$\left(\frac{P_r}{P_y} \right)_{L,max} = 2.04 - 0.039 \frac{h}{t} + 0.006 \frac{L}{r_y} - 1.93 \frac{P_g}{P_y} \qquad (2\text{-}37)$$

where P_r is the required axial compressive strength as determined using the over-strength seismic load. Rearranging Equation (2-36) and (2-37) gives:

$$\left(\frac{h}{t} \right)_G \le 333 \left(1.42 - \frac{P_r}{P_y} \right) - 1.5 \frac{L}{r_y} - 4 \frac{b}{t} \qquad (2\text{-}38)$$

$$\left(\frac{h}{t} \right)_L \le 25.6 \left(2.04 - \frac{P_r}{P_y} - 1.93 \frac{P_g}{P_y} \right) + 0.15 \frac{L}{r_y} \qquad (2\text{-}39)$$

The highly ductile limit for h/t of exterior HSS columns, $\lambda_{hd,ex}$, can then be approximated and reformatted based on the expected failure mode into:

$$\lambda_{hd,ex,\mathrm{G}} = 15.7\sqrt{\frac{E}{R_y F_y}}\left(1.42 - \frac{P_r}{P_y}\right) - 1.5\frac{L}{r_y} - 4\frac{b}{t} \qquad (2\text{-}40)$$

$$\lambda_{hd,ex,\mathrm{L}} = 1.21\sqrt{\frac{E}{R_y F_y}}\left(2.04 - \frac{P_r}{P_y} - 1.93\frac{P_g}{P_y}\right) + 0.15\frac{L}{r_y} \qquad (2\text{-}41)$$

The proposed equations for PDSR and CCALR along with the proposed design aid are validated by analyzing five columns that are not included in the parametric study (shown as triangles in Figure 2-35). The same modeling approach used in the parametric study is used for the validation models. The simulation results along with the PDSR and CCALR determined by the proposed equations and design aid are listed in Table 2-16. It is clear that the proposed equations are in good agreement with the finite element results implying that the proposed equations are effective in representing both interior and exterior HSS columns with slenderness ratios and initial axial load ratios within the studied ranges. Also, the expected failure mode using limits proposed in Table 2-15 and Figure 2-34 match the failure modes obtained using finite element simulations implying the effectiveness of the proposed limits to predict the failure mode of exterior HSS columns.

Table 2-16 Verification of proposed equations and design guide for PDSR and CCALR

HSS Section	b/t	h/t	L/r_y	P/P_y	Failure Mode (Expected)	Failure Mode (FEM)	$PDSR_{FEM}$	$PDSR_{eq.}$	$CCALR_{FEM}$	$CCALR_{eq.}$	$CCALR_{aid}$
HSS 254×152×16	7.3	14.2	76.9	0.3	G	G	0.90	0.94	0.60	0.67	0.60
HSS 254×203×12.7	14.2	18.5	60.2	0.2	G	G	0.93	0.92	0.60	0.58	0.50
HSS 406×406×16	24.6	24.6	38.4	0.4	L	L	0.59	0.54	0.45	0.45	0.40
HSS 406×101×12.7	5.6	31.4	90.9	0.2	L	L	0.71	0.77	0.35	0.40	0.40
HSS 305×203×9.5	19.9	31.5	42.9	0.2	L	L	0.67	0.68	0.35	0.36	0.30

Evaluation of Current AISC Specifications

Finite element results show that the maximum CCALR for Type I columns under the effect of the CR2 loading protocol is 0.75 (HSS 203×152×16-60-CR2). This implies that the maximum initial axial load that an HSS 203×152×16 column can sustain to the end of the CR2 lateral loading protocol is 0.75 P_y. However, based on the current AISC highly ductile limits for h/t, Type I columns should be able to sustain axial loads of 0.90 P_y (where the resistance factor for compression Φ_c=0.90). On the other hand, all Type III columns (considered not highly ductile because of b/t) are able to sustain minimum axial loads of 0.20 P_y up to the end of the CR2 lateral loading protocol (i.e., 4% drift). These findings suggest that the current AISC highly ductile limits for HSS columns are conservative for the b/t limit and unconservative for the h/t limit.

To show the difference between the findings in this study and the current AISC Seismic Provisions (AISC 2016a), the proposed highly ductile limit for h/t of interior HSS columns in equation (2-34) is simplified in Figure 2-36 and plotted with current AISC limits for h/t. The width-to-thickness ratio (b/t) in Figure 2-36 is equal to the highly ductile limit in the current AISC provisions. The first zone (highly ductile zone) implies that the columns in this zone are considered highly ductile based on both the proposed high ductility limits and current AISC Seismic Provisions. While the columns in the second zone (unconservative zone) satisfy the current highly ductile limits, they do not exhibit highly ductile behavior based on the regression results. Finally, the third zone (not highly ductile zone) represents the columns that are not highly ductile according to either limits.
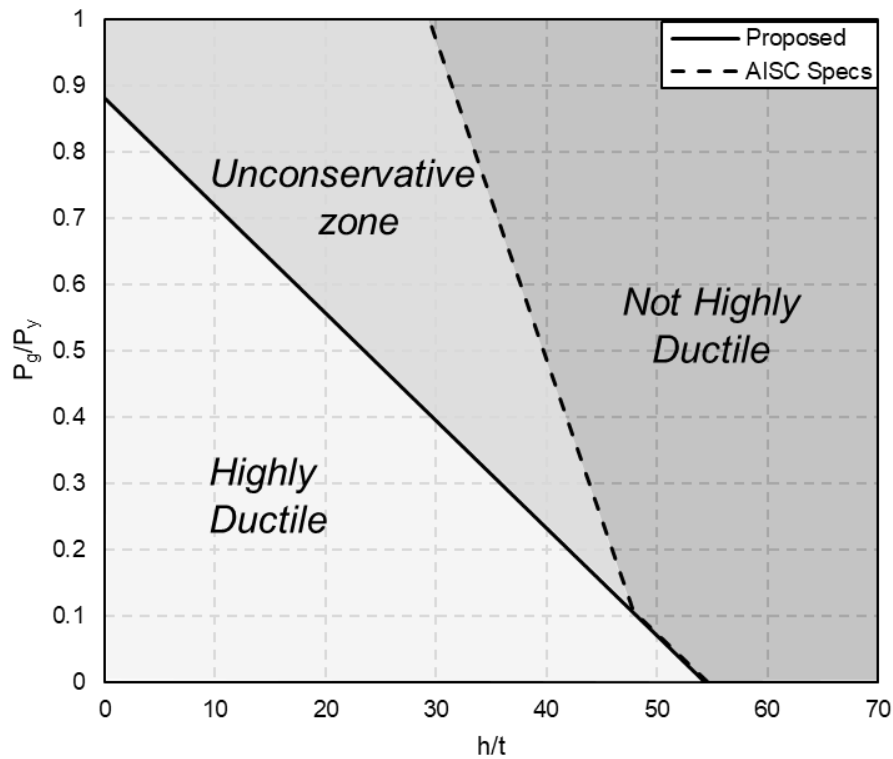
Figure 2-36 Evaluation of current AISC high ductility limits of web depth-to-thickness ratio (*h/t*) for interior HSS columns with width-to-thickness ratio (*b/t*) equal to the highly ductile limit in the current AISC provisions

Comparison between W-shape and HSS columns

The performance of HSS columns evaluated in this study is compared to the performance of similar W-shape columns evaluated by Wu et al. (2018a). Both types of columns are subjected to the combined axial and CR2 lateral loading protocol. All columns are assumed to have a height of 4 m to represent typical first floor columns. Constant critical axial load ratio (CCALR) is used to assess the capacity of both types of columns because it is a common performance parameter considered in both studies. The proposed equations for CCALR in this study and by Wu et al. (2018a) are used to calculate CCALR for all commercially available sections for both types of columns. Figure 2-37 shows the relationship between the weight of the column and CCALR to represent the strength-to-weight ratio.

110

For columns with a weight less than 150 kg/m, HSS columns provide higher strength (CCALR) than W-shape columns. This finding is attributed to the fact that W-shape columns with lower weight typically have smaller thicknesses resulting in higher local and global slenderness ratios. For columns with a weight larger than 150 kg/m, W-shape columns provide higher strength than HSS columns. This result is attributed to the fact that HSS columns with higher weights typically have larger depths resulting in larger local slenderness ratios unlike W-shapes, which have larger thicknesses leading to lower slenderness ratios. Consequently, HSS columns can be a more efficient alternative to W-shape columns in low to mid-rise SMFs with columns having weights smaller than 150 kg/m.
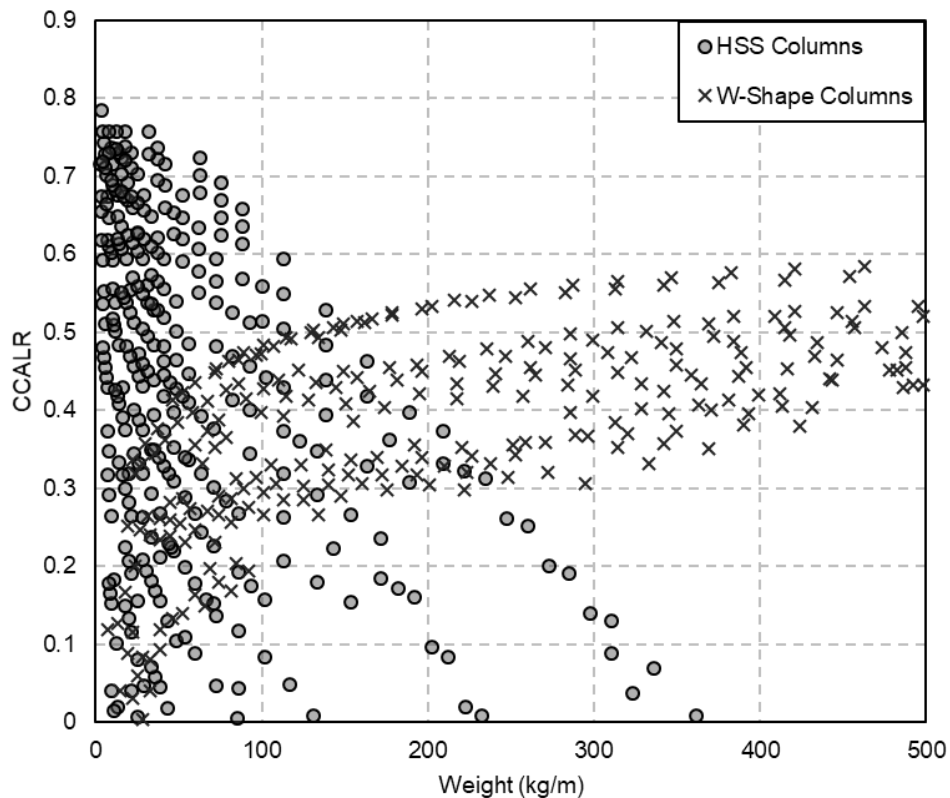
Figure 2-37 Comparison between W-shape and HSS columns under combined axial and CR2 lateral loading protocol

2.5 Summary and Conclusions

This chapter presented three studies focused on the seismic collapse behavior of steel deep W-shape and HSS columns as part of special moment frames.

2.5.1 Initial Geometric Imperfections in Wide-Flange Steel Members

In the first study, the IGIs in steel W-shape members were measured using a 3D noncontact laser scanning technique. A spectral approach that models the IGIs in each plate of the W-shape member as a 2D random field, which is commonly used to model random vibrations, was used to characterize the measured IGIs. Although it is more convenient to implement the traditional modal approach in modeling IGIs, it does not relate to the physical reality of IGIs, i.e., there is no evidence for assuming that IGI's must be constrained to follow specific buckling mode shapes. The 2D Fourier transforms of the measured IGI profiles revealed the existence of periodicity in the measured fields. Therefore, the average 2D Fourier transforms of the measured IGI profiles were used to introduce the concept of "idealized imperfection spectrums" that could be used to generate new normalized IGI profiles (i.e., having a unit maximum amplitude) for different specimens based on actual imperfection data. The measured data was used in a regression analysis to propose expressions for the maximum amplitude of IGIs in W-shape steel members.

The proposed spectral approach and the traditional modal approach were used to study the sensitivity of computational models to IGIs at the member level (i.e., single column). It was shown that there is weak correlation between the two approaches and, generally, the effect of IGIs on the results of computational models of W-shape steel columns is quite small, within 3% on average, for initial axial load levels of P/P_y of 0.4. It was noted that although geometric imperfections can, in certain situations, influence column buckling behavior, their effect on nonlinear cyclic behavior was generally inconsistent, in addition to being small. Based on this finding, it was recommended

that initial geometric imperfections need not be incorporated in high fidelity numerical models of W-shape members subjected to combined axial and cyclic lateral loads. This was conditioned upon the use of an analysis platform with sufficient numerical precision to capture early small deformations that promote geometric nonlinearity in the response. This result is of significance because introducing IGIs can be a complex and time-consuming endeavor for system-level studies depending on the approach taken and complexity of the structure.

2.5.2 Prediction of Seismic Collapse Behavior of DSW Columns Using Machine Learning Methods

In the second study, the prediction of the seismic collapse behavior of deep steel W-shape (DSW) columns experiencing axial and lateral demands as part of special moment frames (SMFs) was explored using different machine learning (ML) classification and regression methods. Steel Column Net (SCNet), a dataset of more than nine hundred experimental and numerical results of DSW columns with different attributes was assembled. The seismic collapse behavior of the W-shape columns was identified by two characteristics: failure mode and rotation capacity. Three types of failure modes were distinguished in this study: local, global, and coupled modes. The rotation capacity of the columns was expressed in terms of their cumulative inelastic rotation until failure (CIR). An exploratory data analysis (EDA) of SCNet was performed to evaluate the relationships between the different attributes and output parameters or categories. EDA revealed that the decision surfaces or boundaries between the failure modes are complex and nonlinear, which emphasizes the need for ML methods to predict the seismic collapse behavior of steel DSW columns.

SCNet was divided randomly into two subsets: training (70%) and test (30%) sets. Twenty percent of the training set was used as validation to optimize the hyperparameters of the machine

113

learning algorithms. The efficiency of five machine learning classification methods was explored to identify the failure mode of the entries in the test set. The machine learning methods are linear discriminant analysis (LDA), K-nearest neighbor (KNN), support vector machine (SVM), Naïve Bayes (NB), and classification decision trees (CDT). It was shown that SVM and CDT have the best performance amongst all of the explored machine learning methods (test accuracy of 89%). The performance of the trained ML models was compared with the performance of the classification criteria available in literature and found to provide superior performance due to the ability to capture the highly nonlinear and complex decision surfaces between the different failure modes.

The efficiency of four ML regression methods was also explored to predict CIR of the entries in the test set. The predicted CIR was then used to identify the highly ductile behavior of the entries (i.e., identify whether the columns reached plastic rotation of 0.04 rad or not). The explored ML methods are stepwise linear regression (SLR), regression decision trees (RDT), support vector regression (SVR), and gaussian process regression (GPR). It was shown that GPR has the best performance amongst all the explored methods. The performance of the ML regression models was compared with the current AISC highly ductile limits for W-shape columns and found to provide a 30% improvement in classification accuracy with respect to the number of correctly classified highly and non-highly ductile columns in the test set. Based on these results, it is argued that machine learning algorithms that are continually updated with new experimental and computational data could inform future generations of design specifications.

2.5.3 Collapse Behavior of HSS Columns as part of SMFs

In the third study, the response of HSS columns under combined axial and lateral loading was investigated using a validated computational model. Two lateral loading protocols were

considered: symmetric cyclic loading protocol (SC) up to story drift of 6% to simulate a far field type earthquake and CR2 loading protocol to represent realistic drift demands of a column in a system during seismic collapse. The studied columns were selected to cover a wide range of parameters including local and global slenderness ratios. Two performance parameters were considered to evaluate the behavior of HSS columns namely, constant critical axial load ratio (CCALR) and post drift strength ratio (PDSR). Finite element results were used in a regression analysis to formulate the two performance parameters under the effect of the CR2 protocol.

Within the limits of the parameters studied HSS columns experience two modes of failure. Global failure implies that the column does not experience significant local buckling near the plastic hinge region. Local buckling failure indicates that the column experiences severe local buckling near the support. When the dominant failure mode is a global mode, width-to-thickness ratio (b/t), depth-to-thickness ratio (h/t) and global slenderness ratio (L/r_y) are significant parameters affecting the behavior of HSS columns. When the dominant failure mode is a local mode, h/t and initial axial load ratio (P/P_y) are the most influential parameters on the axial capacity of HSS columns under combined axial and lateral loading.

Based on finite element results, the SC loading protocol results in a higher demand (i.e., more conservative) than the CR2 protocol. CCALR for the studied HSS columns is significantly smaller under the SC loading protocol than the CR2 protocol implying that the axial capacity of HSS columns under the SC protocol is much smaller. Local failure mode dominates in the case of the SC loading protocol due to the excessive cycling experienced by the column. The amount of axial shortening of HSS columns is much higher under the SC loading protocol as well. Also, axial shortening of HSS columns is mainly controlled by the depth-to-thickness ratio (h/t) and initial axial load level (P/P_y). The amount of axial shortening of HSS columns is significantly higher for columns with higher h/t and P/P_y. The amount of column shortening at 1% drift, which is

commonly associated with the design performance level for immediate reoccupation of buildings after major earthquakes, is minimal for all studied columns. This finding suggests good serviceability performance of HSS columns when used in SMFs.

Generally, HSS columns provide higher axial strength than W-shape columns for column weights less than 150 kg/m because W-shape columns with lower weight typically have smaller thicknesses resulting in larger local and global slenderness ratios. Consequently, HSS columns can be a more efficient alternative to W-shape columns in low to mid-rise SMFs. The finite element results are also used to propose a guide for designing both interior and exterior HSS columns under combined axial and lateral loading. New highly ductile limits for h/t of interior and exterior HSS columns are proposed. The proposed expressions are formulated in a familiar format to facilitate their adoption into future design provisions. The results of the parametric study suggest that the current AISC high ductility limits for HSS columns are conservative for the b/t limit and unconservative for the h/t limit.

CHAPTER 3

Seismic Debris Field for Collapsed RC Moment Resisting Frame Buildings

3.1   General

This chapter focuses on estimating the extent of debris generated around collapsed reinforced concrete (RC) moment frame buildings using a validated computational approach that explicitly models the building collapse process and subsequent formation of the debris field. A set of RC moment resisting frame structures with different heights is modeled under different ground motion records scaled up until they induce collapse of the building to assess the seismic debris field under different ground motion histories and building heights. The collapse modes are classified using a deep neural network (DNN) based on ground motion parameters and building height. The extent of debris around the collapsed buildings is modeled in a probabilistic manner and then characterized using linear regression analysis. The effect of building code on debris field extent is also investigated.

3.2   Background

Building collapse is one of the most catastrophic consequences of an earthquake. In addition to injuring or killing their inhabitants, collapsed buildings also produce large amounts of debris, severely hindering first response and hampering the eventual recovery operation. Historical examples of this abound around the world. The 2010 Haiti earthquake produced 13 million cubic yards of debris that severely delayed emergency and recovery processes (UNDP 2010). The 1995

117

Kobe earthquake, which destroyed more than 250,000 dwellings, created 20 million tons of debris, while the 2011 Great East Japan earthquake and resulting tsunami destroyed 1.1 million dwellings, causing 28 million tons of debris (Tabata et al. 2019).

The debris produced by earthquake-induced collapsed buildings is typically characterized by two attributes: quantity and extent. The former refers to the amount of structural and nonstructural debris in tons, while the latter describes the area and shape of the debris field around the collapsed building. Techniques exist to estimate the quantity of debris resulting from collapsed buildings (in tons) of which the method used in HAZUS (FEMA 2003) is the most prominent example. It computes the quantity of debris generated at each collapsed building site based on an empirical approach calibrated to data from previous earthquakes. The debris is classified into two types: debris that falls in large pieces (e.g., structural elements) and debris that falls in smaller pieces (e.g., brick, glass, wood, etc.).

3.3   Motivation and Objectives

Few studies have addressed the extent of debris around collapsed buildings (Nishino et al. 2012, Quagliarini 2016 et al., and Ravari et al. 2016). Hirokawa and Osaragi (2016) integrated a street blockage model into a city-wide simulation to model how debris from collapsed buildings blocks adjacent roadways. Their model assumed that the amount of debris generated by a collapsed building is equal on all sides, which is not a realistic assumption for many types of buildings where a ratcheting type collapse mechanism has been shown to occur (Wu et al. 2018b). Castro et al. (2019) applied an agent-based model to simulate the evacuation process of the population for a tsunami scenario following an earthquake. In the simulation, traffic flow constraints imposed by the debris produced by collapsed buildings were considered. They used the empirical approach in

HAZUS (FEMA 2003) to evaluate the weight of debris generated by collapsed buildings. Then, using conversion factors developed by the U.S Army Corps of Engineers (USACE), they converted a building's debris weight to volume and used that to estimate the extent of debris assuming it to be a triangular prism. Domaneschi et al. (2019) proposed a more detailed methodology to evaluate debris generation from collapsed masonry buildings based on validated computational simulations of different building collapse scenarios. A simplified analytical formula was proposed to predict the extent of debris generated by collapsed masonry buildings with respect to the original area of the building. The proposed formula was then used in a case study of a virtual city district to demonstrate the capabilities of the proposed methodology.

Of the studies surveyed above, the Hirokawa and Osaragi (2016) and Castro et al. (2019) studies are based on empirical approaches, while the Domaneschi et al. (2019) study is based on a more rational approach. However, the Domaneschi et al. (2019) study only focused on masonry structures and not reinforced concrete moment frame buildings, which are generally taller and therefore have a greater potential for blocking adjacent roadways. Given the above limitations and dearth of research results, this chapter focuses on estimating the extent of debris generation around reinforced concrete (RC) moment frame buildings using a validated computational approach that explicitly models the building collapse process and subsequent formation of the debris field.

A set of RC moment resisting frame structures with different heights is modeled under different ground motion records scaled up until they induce collapse of the building to assess the seismic debris field under different ground motion histories and building heights. The collapse modes are classified using a deep neural network (DNN) based on ground motion parameters and building height. The extent of debris around the collapsed buildings is modeled in a probabilistic manner and then characterized using a linear regression analysis. The effect of building code on debris field extent is also investigated.

3.4 Modeling Methodology

Numerous studies over the past two decades have addressed progressive collapse of buildings. As summarized in El-Tawil et al. (2014) and Kunnath et al. (2018), many of the recent studies employed three dimensional (3D) finite element analysis. As noted in El-Tawil et al. (2014) and evident in Grunwald et al. (2018), traditional finite element analysis (FEM) is computationally expensive, primarily because the explicit dynamic analysis scheme used for modeling progressive collapse behavior necessarily utilizes a small-time step to ensure computational stability.

The Applied Element Method (AEM) developed by Meguro and Tagel-Din (2000) and Meguro (2001) is a discrete element variant that models a structure using rigid elements connected at their adjacent faces via zero length normal and shear springs. The springs model transfer of shear and normal stresses and strains between adjoining elements through uniaxial relationships. The characteristics of AEM permit implicit dynamic analysis to be employed, resulting in a larger time step and, hence, a faster dynamic analysis than a comparable explicit FEM. Grunwald et al. (2018) reported that the computational time for simulating the partial collapse of the PGC building after the 6.3 magnitude Christchurch earthquake using AEM was 3.5 hours on a standard personal computer with six cores and 32 GB RAM. A comparable FEM model ran for twelve days on a high-performance cluster with 64 cores.

The use of springs in AEM introduces limitations that are naturally addressed in FEM. For example, it is not straightforward, if at all feasible, to model certain types of multi-axial phenomena, e.g., associated plasticity or the effect of triaxiality on the fracture strain of steel (Chao et al. 2006 and El-Tawil et al. 2000). The tradeoff between accuracy and expediency is assessed through validation studies and found to be favorable, based on the objective of the current chapter, which is capturing the general collapse behavior of a building as well as the generated debris field

around it, as detailed later. As such, AEM is adopted in the study presented in this chapter. Other studies that have utilized AEM for collapse analysis can be found in Khalil (2012), Dinu et al. (2016), Zerin et al. (2017), Fathalla and Salem (2018), and Grunwald et al. (2018).

3.4.1 Modeling Scheme

In AEM, structural elements are discretized into rigid cubes connected together using one set of normal and two sets of orthogonal shear springs distributed along element faces as shown in Figure 3-1. The displacements are evaluated at the spring locations unlike with FEM, where the displacements are evaluated at integration points within the elements. Each group of springs in a set models a specific material. For reinforced concrete elements, two groups of springs are used: concrete springs and reinforcement springs as shown in Figure 3-1. The connecting springs are generated and distributed automatically in the AEM software Extreme Loading for Structures (ASI 2018) that was used in the study presented in this chapter.

Compression behavior of the concrete is simulated using the Maekawa compression model shown in Figure 3-1 (Maekawa et al. 1983). The tensile behavior of concrete is assumed to be linear until cracking after which the tensile stress drops to zero. The stress-strain relationship for shear springs is assumed to be linear until cracking of the concrete occurs, after which the shear stress decreases (see Figure 3-1). The magnitude of decrease in the shear stress depends on aggregate interlocking and friction at the crack surface. The cyclic behavior of the reinforcement bars is simulated using the material model presented by Ristic et al. (1986) shown in Figure 3-1. The elements are assumed to be connected together as long as the average absolute strain on their adjacent faces is smaller than a defined fracture strain. However, the effect of low cycle fatigue of steel reinforcing bars is not considered in AEM. After the separation of the elements, they are assumed to behave as separate rigid bodies that may collide with other elements in which case new

springs are generated at the contact points between the collided elements to simulate the collision behavior between them.
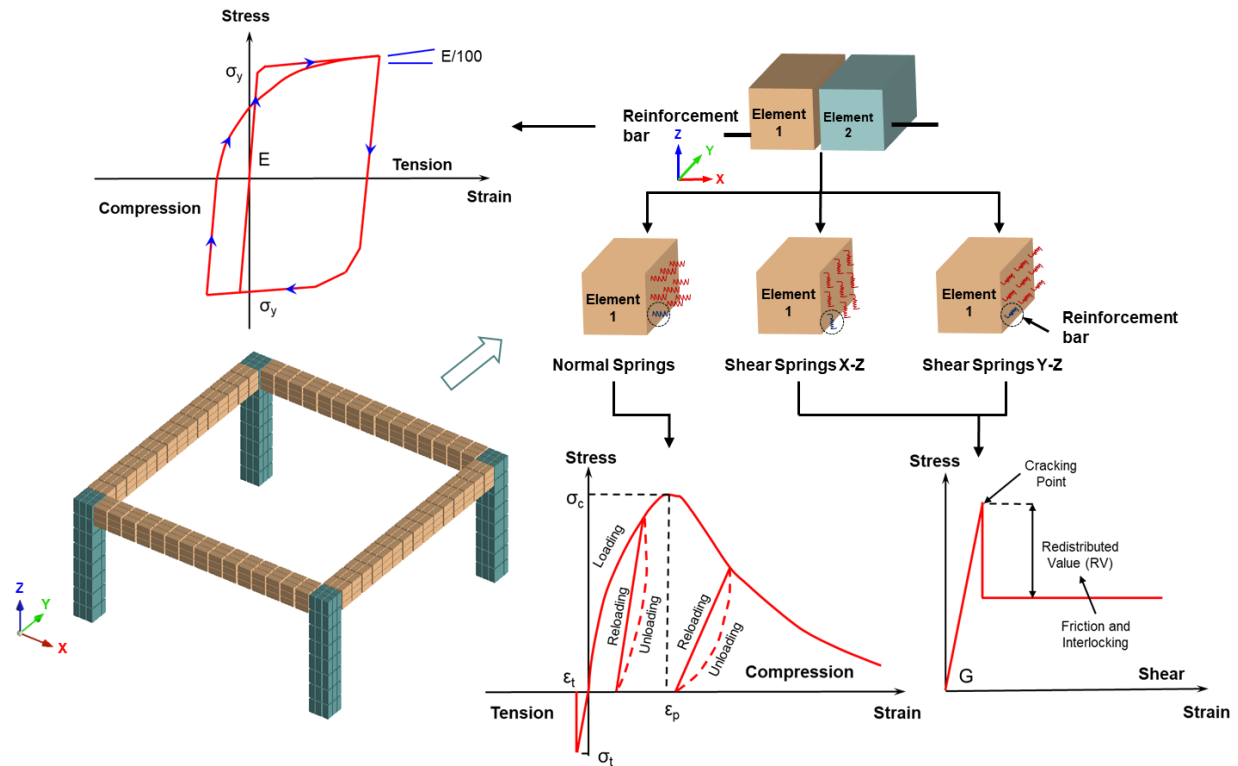
Figure 3-1 Applied element model discretization and cyclic material models

3.4.2 Model Validation

Due to lack of available experimental data for seismic collapse of full-scale buildings, the ability of the AEM approach to reasonably model collapse behavior is validated against a shake table collapse test of a typical scaled multi-story RC frame building conducted by Xu et al. (2017). However, as discussed earlier, AEM has been successfully validated on the building full scale level by Grunwald et al. (2018) against the partial collapse of the PGC building after the 6.3 magnitude Christchurch earthquake. The test building is a scaled version of a building that nearly collapsed

during the 2010 Mw 7.1 Yushu earthquake in China. The prototype building is a 4-story RC frame constructed in 2009 and located at the epicenter of the Yushu earthquake. Severe damage, including massive concrete spalling and reinforcement buckling at most column ends, was observed in the first story of the building after the earthquake. Due to limitations on shake table capability, only three bays from the original building were designed and tested at scale of 1:5. The design drawings of the test building are shown in Figure 3-2(a).

The influence of exterior walls on the behavior of the building was not considered in the shake table test. However, the contribution of the wall mass was simulated by adding cast iron blocks on each floor of the test building. Also, a total of 6 tons of cast iron blocks were added equally on each floor of the test building to ensure that the predicted response from the test reliably simulated the behavior of the prototype building. The mechanical properties of the concrete and reinforcement of the test building are listed in Table 3-1 and Table 3-2, respectively. The El Centro ground motion record (PGA = 0.35 g and Duration = 53.7 sec) was applied in one direction (X direction) considering seven different cases where the ground motion history was scaled to have PGAs ranging from 0.08 g to 1.0 g.

A detailed AEM of the described test building was created using the modeling scheme presented in the previous section. Figure 3-2(b) shows the AEM of the test building. Both the tested and simulated building models survived the initial cases scaled to PGAs of 0.08g and 0.26g with only slight cracking (simulated by failure of connecting springs in the AEM). After case 3 (PGA = 0.46 g), further cracking appeared in both experimental and numerical models at the column ends. After case 5 (PGA = 0.66 g), the columns of the first two stories were severely damaged as a result of the formation of plastic hinges.

Collapse occurred during case 7 (PGA = 1 g) in both the test and the applied element model as shown in Figure 3-3. The moment designated as 0 s is defined as the moment that the building

started to exhibit a collapse response (i.e., sudden large lateral displacement of the building). As shown in Figure 3-3(a), plastic hinges formed at the top and bottom of the first story columns leading to a loss of stability. At 0.858 s (see Figure 3-3(b)), the first story formed a mechanism and collapsed. After this point, progressive collapse of the rest of the building initiated as shown in Figure 3-3(c) and (d). A comparison of the results from the experimental test and model shows that the AEM is able to reasonably simulate the general collapse behavior of the building as well as the generated debris field around it.

(a)

(b)
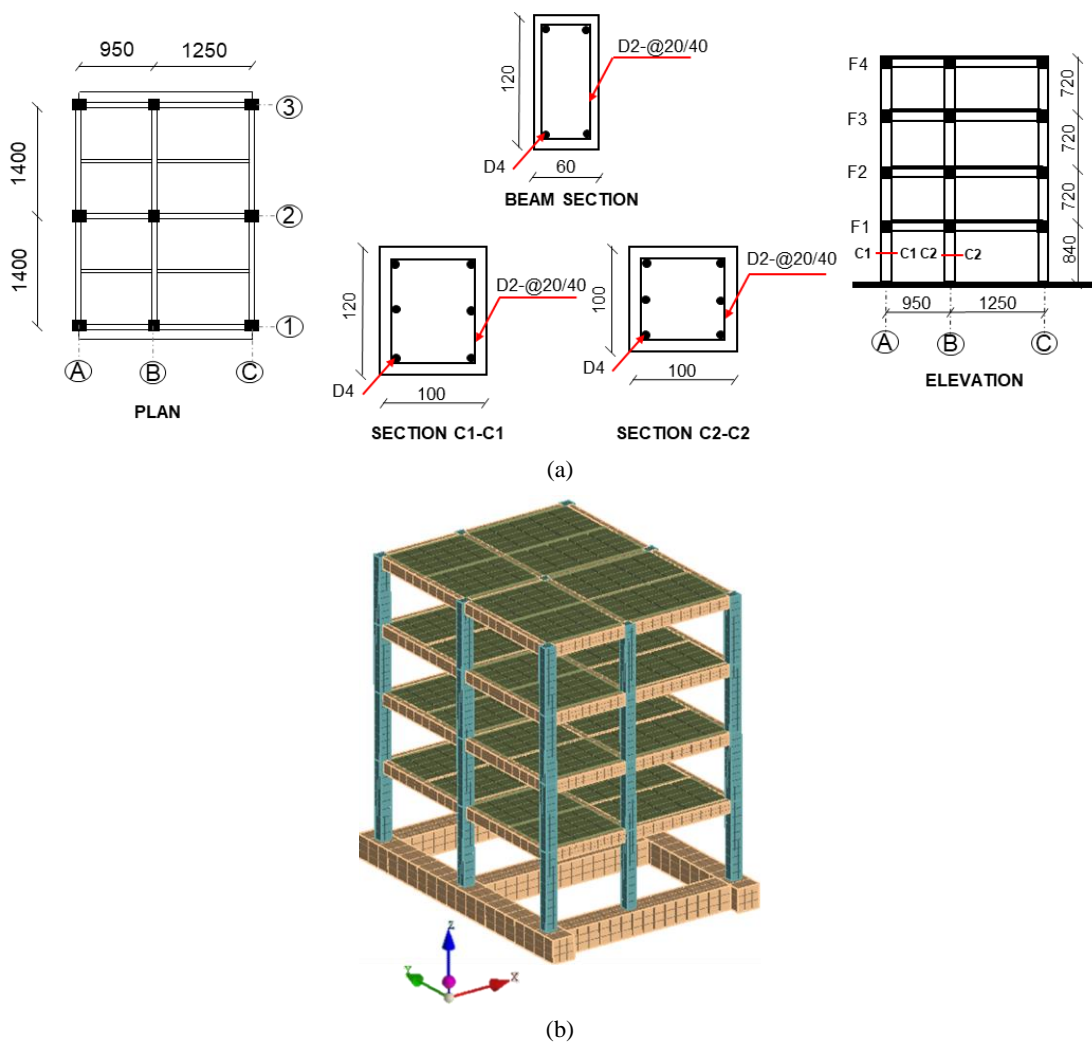
Figure 3-2 Illustration of : (a) design drawings; and (b) Applied element model of the test building (dimensions in mm)

Figure 3-3 Comparison between experimental and numerical collapse progress at: (a) 0 s; (b) 0.858 s; (c) 1.155 s; and (d) 1.188 s (photos from Xu et al. 2017)

Table 3-1 Mechanical properties of concrete for the test building (Data from Xu et al. 2017)

Story	Elastic Modulus (MPa)	Compressive Strength (MPa)
First story	14070	13.5
Second story	18230	16.4
Third story	14930	13.2
Fourth story	15230	12.7

Table 3-2 Mechanical properties of reinforcement for the test building (Data from Xu et al. 2017)

Type	Diameter (mm)	Yield Strength (MPa)	Ultimate Strength (MPa)
Main reinforcement	4	360	422
Stirrup	2	254	382

3.4.3 Prototype Building

The space frame building outlined and designed in Haselton (2006) is used as the prototype structure to study the debris field of collapsed RC moment frame structures. Figure 3-4(a) shows the plan of the building. It consists of four RC special moment resisting frames in each direction, which are assumed to resist all the seismic demands on the building. Three building heights are considered: 4, 8 and 12 stories. The bay width of the typical RC special moment resisting frame varies from 6.1 m (20 ft) for the 8 and 12 story buildings to 9.1 m (30 ft) for the 4-story building. For all building heights, the first story height is 4.57 m (15 ft), and the typical upper story height is 3.96 m (13 ft). The building is designed for a general high seismic site in California (Design category D, soil class D, $S_{ms} = 1.5$g, and $S_{m1} = 0.9$g). All the design details are in accordance with the IBC (2003) and ACI 318-05 (2005) code requirements. The concrete compressive strength is 35 MPa (5 ksi) for both the beams and columns. The longitudinal rebar diameters commonly used

in the beams and columns are 25 mm (#8) and 28 mm (#9) with yield strength of 400 MPa (60 ksi). The design dead and live loads are 8 kN/m^2 (175 psf) and 2.4 kN/m^2 (50 psf), respectively. Further design details can be found in Haselton (2006).

Detailed AEMs for the prototype buildings are created using a meshing scheme that entails discretizing the 4, 8, and 12-story buildings into a total of 2.1×104, 3.4×104, and 4.9×104 elements, respectively. Figure 3-4(b) shows a typical 8-story model. The material models discussed earlier are used to simulate the behavior of the different reinforced concrete elements in the buildings based on the properties specified in Haselton (2006). The simulation time to model 30 s of the ground motion record is around 2.8, 6.1, and 7.5 hours for the 4, 8, and 12-story buildings, respectively, on a personal computer with four cores and 32 GB RAM.

Based on the fact that the seismic debris produced from the collapse of RC buildings is not exclusive to structural elements, the exterior walls of the buildings are included in the AE models as shown in Figure 3-4(b). The micro-modeling approach for masonry walls described by Domaneschi et al. (2019) is implemented for the exterior walls where the properties of bricks and mortar are taken as given in Aref and Dolatshahi (2013). The brick pattern (staggered) and mortar are explicitly considered as shown in Figure 3-4(b). The bricks are connected by interface springs with mortar properties. This modeling approach allows different material properties to be defined for the brick and mortar. It should be noted that the staircases are not considered for simplicity. A typical distribution of windows is considered at each floor of the building as shown in Figure 3-4(b). The prototype building is assumed to be fully fixed at its base. The self-weight of the structure, floor weight, and live loads are applied to the prototype building based on the values specified earlier and in Haselton (2006). The load combination of $1.05D + 0.25L$ per FEMA P695 (FEMA 2009) is used where D and L are the dead and live loads of the structure, respectively.

The twenty-two ground motion records (each comprised of two orthogonal components) specified in the Far-Field record set of FEMA P695 (FEMA 2009) are applied to each building and scaled up until they induce total collapse of the building. Table 3-3 lists the properties of the ground motion records employed. Each record is applied twice: aligned and skewed with respect to the primary axes of each building. The former assumes that the earthquake strikes the building such that its components are aligned with the main axes of the building as shown in Figure 3-4. The latter assumes that the earthquake approaches the building at an angle of 45 degrees with respect to the primary axes of the building. This combination of ground motion records and building heights yields 132 different collapse scenarios (3 prototype buildings × 2 orientations × 22 records) to study the variability in the collapse behavior and debris field of RC moment resisting frame buildings with respect to the building height, ground motion histories, and ground motion orientations.

(a)   (b)
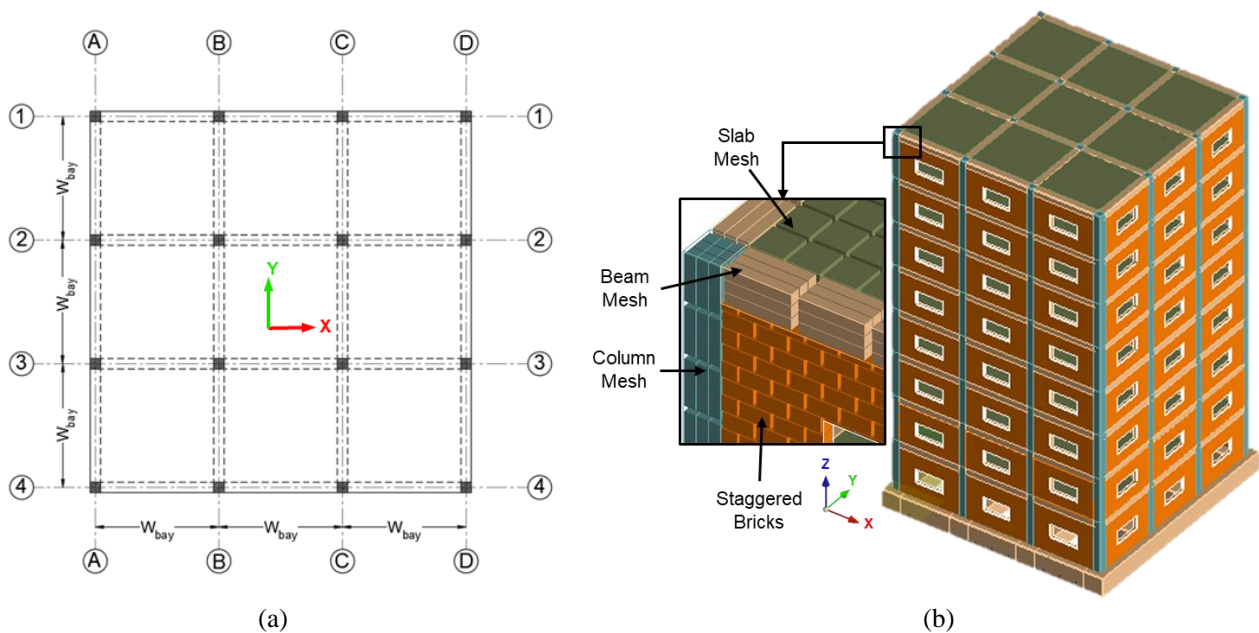
Figure 3-4 Illustration of: (a) Plan of the prototype building; and (b) AEM of the prototype building (8-story)

Table 3-3 Ground motion records used in this study

No.	Event	Year	Magnitude (M_w)	Recording Station	PGA (g) (Unscaled)
1	Northridge	1994	6.7	Beverly Hills-Mulhol	0.52
2	Northridge	1994	6.7	Canyon County-WLC	0.48
3	Düzce, Turkey	1999	7.1	Bolu	0.82
4	Hector Mine	1999	7.1	Hector	0.34
5	Imperial Valley	1979	6.5	Delta	0.35
6	Imperial Valley	1979	6.5	El Centro Array # 11	0.38
7	Kobe, Japan	1995	6.9	Nishi-Akashi	0.51
8	Kobe, Japan	1995	6.9	Shin-Osaka	0.24
9	Kocaeli, Turkey	1999	7.5	Düzce	0.36
10	Kocaeli, Turkey	1999	7.5	Arcelik	0.22
11	Landers	1992	7.3	Yermo Fire Station	0.24
12	Landers	1992	7.3	Coolwater	0.42
13	Loma Prieta	1989	6.9	Capitola	0.53
14	Loma Prieta	1989	6.9	Gilory Array # 3	0.56
15	Manjil, Iran	1990	7.4	Abbar	0.51
16	Superstition Hills	1987	6.5	El Centro Imp. Co.	0.36
17	Superstition Hills	1987	6.5	Poe Road	0.45
18	Cape Mendocino	1992	7.0	Rio Dell Overpass	0.55
19	Chi-Chi, Taiwan	1999	7.6	CHY 101	0.44
20	Chi-Chi, Taiwan	1999	7.6	TCU045	0.51
21	San Fernando	1971	6.6	LA-Hollywood Stor.	0.21
22	Friuli, Italy	1976	6.5	Tolmezzo	0.35

3.5 Simulation Results

The collapse behavior and debris field of each prototype building are computed for each ground motion and earthquake incidence angle. The generated debris is characterized by three types of data: 1) the collapse mode of the building (i.e., aligned or skewed as discussed later), 2) the collapse direction of the building (positive or negative direction), and 3) the extent of debris in

each direction around the collapsed building. To facilitate the discussion of the results, the ground motion records are labeled as GM_X_Y where X is the number of the ground motion from the first column of Table 3-3 and Y is the earthquake incidence angle (0° or 45°).

3.5.1 Categorization of Collapse Modes

The collapse modes of the studied RC frame buildings can be categorized into 4 distinct groups. Figure 3-5 shows the collapse modes and final debris field of the 4-story prototype building while the final debris field for all the studied cases can be found in Appendix B. Modes 1 and 2 are "aligned" collapse modes meaning that most of the building debris is aligned along the X axis of the building for mode 1 and Y axis for mode 2. Modes 3 and 4 are "skewed" modes where the building collapses at an angle to its primary axes but with the majority of debris skewed towards one of the two axes (X axis for mode 3 and Y axis for mode 4). Another mode of collapse that has been previously observed and discussed (e.g., in Gu et al. 2014) but not observed in the current study due to the symmetry of the building shown earlier is the "revolving" mode of collapse where the building experiences significant twisting prior to failure due to its irregularity. This mode can be studied stochastically using the developed AE model by changing the location of the center of mass of the building to be away from its centroid or changing the stiffness of the structural elements to break the symmetry of the structure.
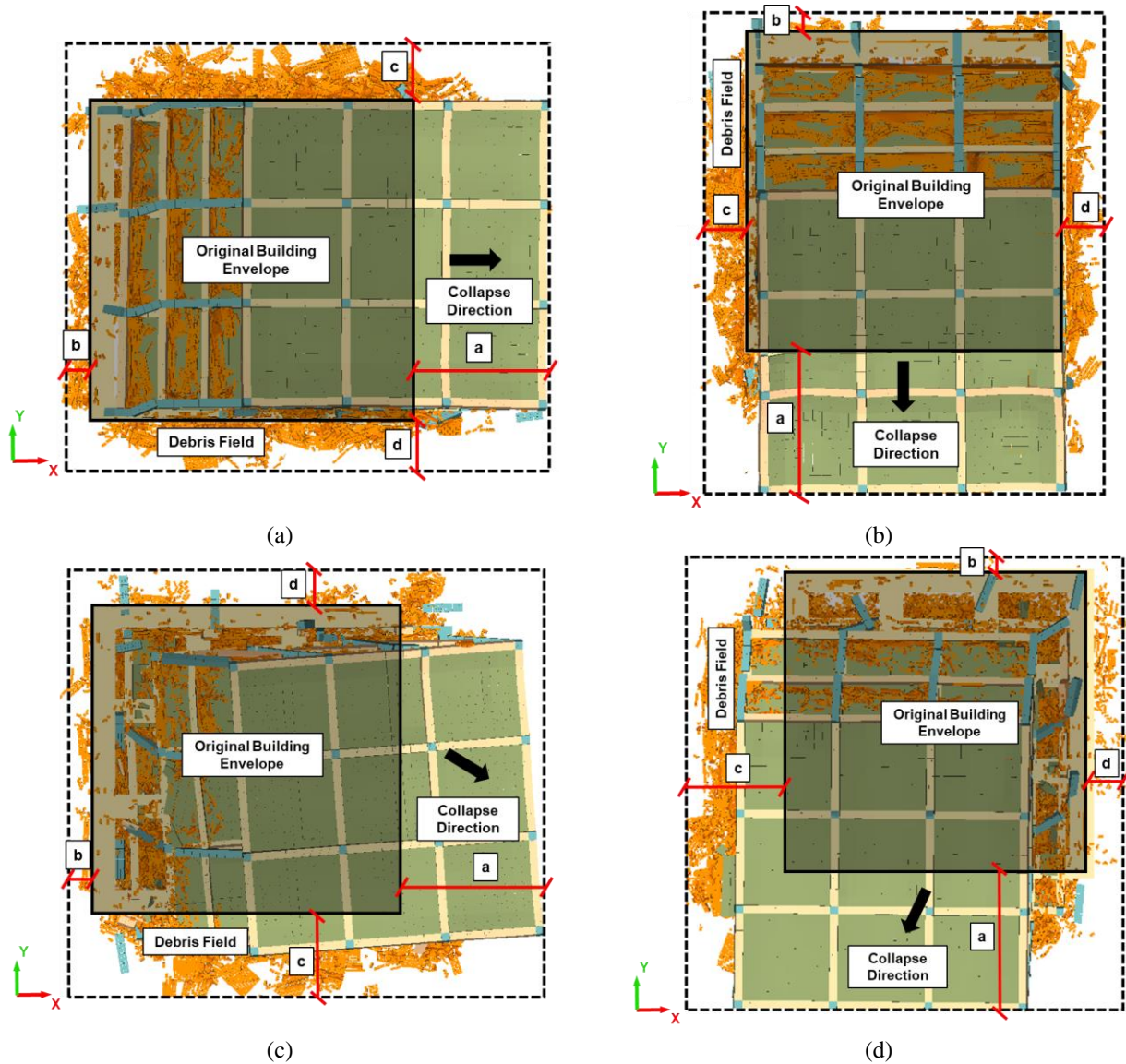
Figure 3-5 Final collapse shape for: (a) mode 1 (aligned in X-direction), (b) mode 2 (aligned in Y-direction), (c) mode 3 (skewed towards X), and (d) mode 4 (skewed towards Y)

The collapse modes of the prototype buildings are summarized in Table 3-4 and Figure 3-6. As shown, the aligned collapse modes (i.e., mode 1 and mode 2) are more dominant for low-rise buildings (i.e., 4-story building) while the skewed collapse modes (i.e., mode 3 and mode 4) occur more frequently in the taller buildings.

Table 3-4 Collapse mode of studied buildings subjected to the employed ground motion records

No. of Stories	GM Orientation	Ground motion record																					
		1	2	3	4	5	6	7	8	9	10	11	12	13	14	15	16	17	18	19	20	21	22
4	0	2	2	2	2	2	1	2	1	3	2	1	2	1	1	1	2	2	1	2	4	1	2
	45	1	2	2	2	1	1	1	3	4	4	3	1	3	1	2	1	1	4	4	2	1	2
8	0	1	3	3	2	1	1	1	1	2	4	1	1	3	3	4	2	2	3	3	1	3	3
	45	2	2	2	3	2	1	2	4	1	4	2	3	1	1	3	1	4	1	4	3	4	2
12	0	2	4	1	4	3	1	2	3	4	2	3	1	2	3	1	2	2	1	1	1	1	4
	45	2	4	1	3	4	4	4	3	1	4	2	4	1	1	2	1	3	1	4	3	1	4
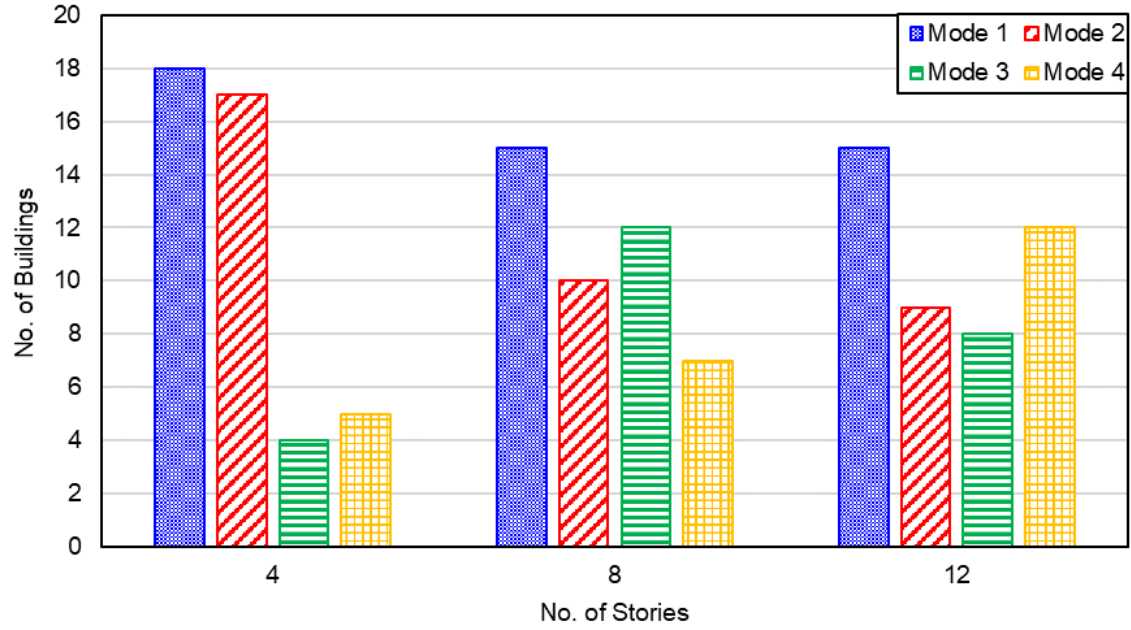
Figure 3-6 Distribution of collapse modes for different building heights

3.5.2 Classification of Collapse Modes

A deep neural network (DNN) approach is used to classify the mode of collapse of a building based on the ground motion and building height. DNN has been widely used as a robust machine learning tool for separating "classifying" classes that are not linearly separable (Cireşan et al. 2012, Sladojevic et al. 2016, and Chatterjee and Poullis 2019). A DNN consists of a set of layers containing one input layer, one output layer, and hidden layers. The number of hidden layers depends on the level of complexity of the problem and the properties of the dataset. Each hidden layer consists of a set of neurons as shown in Figure 3-7.

Each neuron is considered as a computational unit that is associated with a scalar valued function called the "activation function" having the following form.

$$g_n(X, W, b) = f_a(W^T X + b) \tag{3-1}$$

where $g_n(X, W, b)$ is the output of the neuron (i.e., activation function), W is the weights matrix, X is the input of the neuron, and b is the bias. The neurons of successive hidden layers are cross connected together through the weights W and biases b meaning that the output of one layer is input to the next layer. This type of DNN is of the feed-forward type, as the data moves in only one direction, i.e., forward, from the input neurons, through the hidden neurons and to the output neurons. The performance of the neural network is evaluated based on the error between the predicted output of the DNN and the ground truth using a cost function. The training process of a DNN entails finding the optimal W's and b's that minimize the cost function through different automated optimization algorithms.

Five attributes are used as input parameters to the DNN. They are chosen by examining the influence of each of them on the collapse mode of the studied buildings. These include four ground

motion attributes and building height in terms of number of stories. The input ground motion parameters are the ratio between the peak ground accelerations, PGA_x/PGA_y; peak ground velocities PGV_x/PGV_y; peak ground displacements PGD_x/PGD_y; and arias intensities I_{Ax}/I_{Ay} of the orthogonal (X and Y) components of the seismic records. The arias intensity of the ground motion is a measure of the energy of its acceleration signal proposed by Arias (1970) and can be expressed mathematically as follows:

$$I_A = \frac{\pi}{2g} \int_0^T a^2(t)dt \qquad \text{(3-2)}$$

where I_A is the arias intensity of the ground motion, $a(t)$ is the acceleration of the ground motion at time t, and T is the duration of the ground motion.

The size of the input dataset is an important attribute that affects the performance of DNNs. The present dataset is generated artificially using a relatively expensive computational tool (i.e., AEM), which limits the size of the set. One way to overcome this challenge is to use the symmetry of the problem to artificially increase the size of the input dataset to the DNN as shown in Figure 3-7. For example, the collapse mode of the 4-story prototype building subjected to GM_1_0 is mode 2. Symmetry entails that GM_1_90 will cause a mode 1 collapse. Taking advantage of symmetry doubles the size of the data points from 132 to 264.

The architecture of the implemented DNN is shown in Figure 3-7 and consists of one input layer, one output layer, and two hidden layers each containing 10 neurons. A hyperbolic tangent (tanh) activation function is implemented in the input and hidden neurons, while a linear activation function is used for the output layer. The Pareto principle (80/20 rule) is used to split the dataset into a training set representing 80% of the dataset (212 data points) and a test set representing 20% of the dataset (52 data points). The output classes (i.e., collapse modes) are expressed in probability

135

vector form in the training dataset where each class i is mapped to e_i (the ith unit vector where its ith component is one and all others are zero). A softmax layer is used with the output layer to return the probability vector of any real-valued vector x. It is common to use the cross-entropy function to measure the distance between probability vectors in a way that is more natural than the mean-squared error between the vectors, which does not consider the fact that vectors are probability vectors (Simard et al. 2003). Therefore, the cross-entropy function is used as the cost function in the implemented DNN.

The first-order gradient-based optimization algorithm, ADAM (Kingman and Ba 2017) is used to find the optimal weights, W's, and biases, b's. The presented architecture and parameters of the DNN are database dependent and cannot be generalized to any database (i.e., different structural system or ground motion type). The performance of the DNN is measured through its accuracy, which is the percentage of the correctly predicted classes with respect to the database size. The training accuracy is 92% meaning that the designed DNN is able to correctly predict the collapse mode of 196 out of 212 scenarios in the training dataset while the test accuracy is 82% meaning that designed DNN is able to correctly predict the collapse mode of 43 out of 52 scenarios in the test dataset. The presented results provide a measure of confidence in the ability of the designed DNN to predict the collapse modes of RC frame buildings with different heights and subjected to different ground motion records.
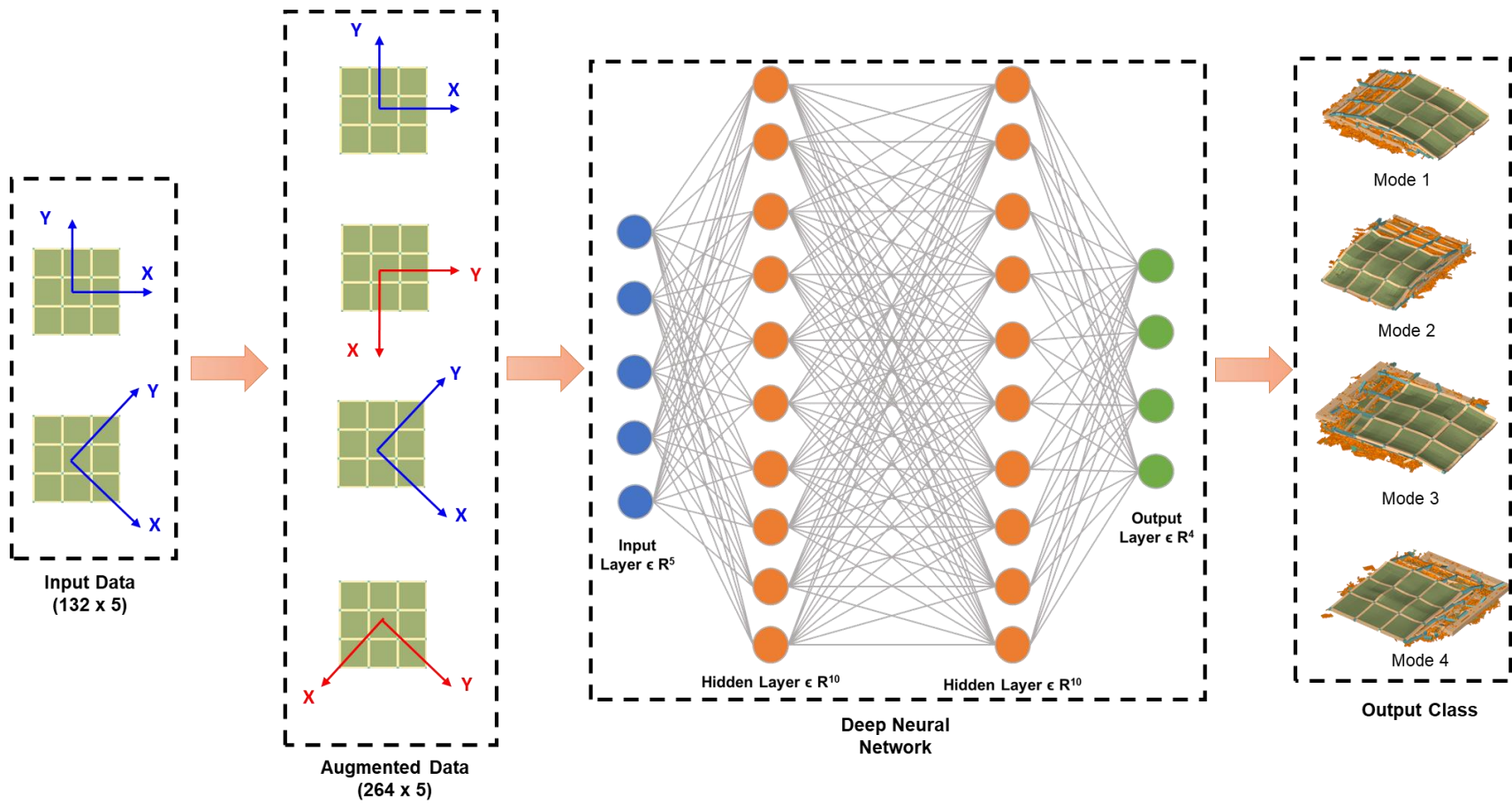
Figure 3-7 Deep neural network training process to classify the mode of collapse

The labels within the figure read:

Input Data (132 x 5)

Augmented Data (264 x 5)

Input Layer ϵ R^5

Hidden Layer ϵ R^{10}

Hidden Layer ϵ R^{10}

Output Layer ϵ R^4

Deep Neural Network

Mode 1

Mode 2

Mode 3

Mode 4

Output Class

3.5.3 Collapse Direction

The direction of the collapse of the studied buildings (i.e., positive or negative) depends on the direction of the ground acceleration at the onset of collapse. For aligned collapse modes, the building can collapse in one of the two directions shown in Figure 3-8(a). Whereas, for skewed collapse modes, the building can collapse in one of the four directions shown in Figure 3-8(b). The direction of the collapse of the building is considered as a random variable with uniform distribution. It can be modeled (for different collapse scenarios) by generating a random number (RN in Figure 3-8) having a uniform distribution between 0 and 1 and using the criteria shown in Figure 8.

(a)   (b)
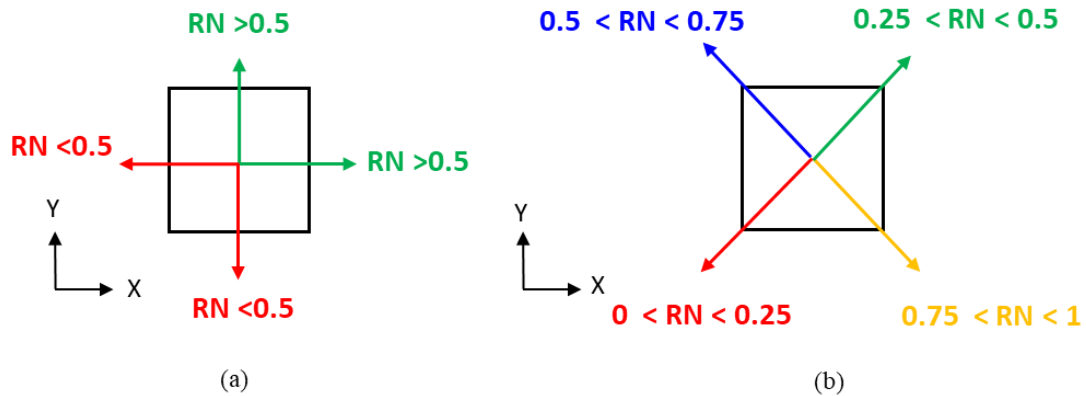
Figure 3-8 Prediction of collapse direction for: (a) modes 1 and 2; and (b) modes 3 and 4

3.5.4 Extent of Debris Field

The footprint of the debris field is defined as the smallest rectangle that fits the debris area as highlighted in Figure 3-5. The dimensions of the debris field in each of the four directions around the collapsed prototype buildings are listed in Table 3-5 and Table 3-6. The debris footprint

is larger than the original footprint by the dimensions *a, b, c*, and *d*, where *a* is always assigned the largest dimension. The collapse scenarios are first categorized into two groups based on the building collapse mode: group 1 contains buildings with aligned collapse modes (i.e., modes 1 and 2) while group 2 contains buildings with skewed collapse modes (i.e., modes 3 and 4). In group 1, *a* (larger) and *b* (smaller) are measured along the direction of collapse, whereas *c* and *d* are measured orthogonal to the collapse direction (see Figure 3-5). In group 2, *a* and *c* are measured in the direction of collapse while *b* and *d* are opposite to the direction of collapse (see Figure 3-5). In this case, *a* and *c* are larger than *b* and *d*, respectively. The variables are normalized with respect to the building height and shown in Figure 3-9. Two trends are evident from Figure 3-9. First, debris is generally strewn in one primary direction as evinced by the fact that *a* is significantly larger than the other variables for aligned collapse (modes 1 and 2), while *a* and *c* are larger than the other two variables for skewed collapse (modes 3 and 4). Second, the larger dimensions (*a* for aligned collapse and *a* and *c* for skewed collapse) become more dominant than the other dimensions as the buildings become taller.

Variability of the footprint of the seismic debris field is considered probabilistically by fitting the results to a log-normal distribution as shown in Figure 3-10. The median and dispersion of each dimension are listed in Table 3-7 for each of the collapse scenario groups described earlier.

Table 3-5 Dimensions of the seismic debris field for the prototype buildings subjected to the first eleven ground motion records

No. of stories	Ground motion record	Earthquake Incidence Angle							
		0°				45°			
		X - Direction (m)		Y - Direction (m)		X - Direction (m)		Y - Direction (m)	
		+ ve	- ve	+ ve	- ve	+ ve	- ve	+ ve	- ve
4	1	8.3	7.9	12.0	5.3	16.3	3.2	3.2	7.7
	2	6.5	6.3	11.6	5.8	8.3	6.1	2.5	13.5
	3	6.3	5.7	0.2	13.6	6.4	7.6	15.0	0.0
	4	6.8	5.6	0.4	13.2	7.8	6.0	13.9	2.7
	5	7.8	7.0	0.3	12.8	13.7	4.1	4.5	6.7
	6	4.7	13.3	6.6	7.1	3.1	13.7	5.4	7.4
	7	5.3	4.8	13.5	3.6	12.8	4.5	5.8	4.9
	8	13.7	2.3	10.9	6.0	14.2	4.0	3.9	9.8
	9	13.4	2.2	2.5	9.2	5.2	12.2	6.3	7.5
	10	5.2	10.2	3.0	14.8	11.0	9.3	4.1	9.6
	11	16.2	0.5	5.4	7.2	11.8	3.9	8.7	5.5
8	1	25.3	3.7	9.7	5.2	25.2	3.2	8.8	4.9
	2	19.8	4.2	18.1	5.5	9.7	5.7	5.7	23.7
	3	21.7	3.9	4.6	17.5	3.5	10.4	26.6	3.4
	4	3.3	12.6	2.8	23.3	3.3	22.9	7.9	5.5
	5	20.0	5.8	7.5	4.3	6.1	6.7	5.3	16.1
	6	3.9	25.5	5.0	11.1	3.5	26.8	8.7	6.1
	7	27.8	2.9	8.4	4.9	4.4	7.0	7.1	17.9
	8	3.2	23.6	5.2	8.4	3.6	19.0	5.5	15.5
	9	7.1	11.2	8.4	22.0	5.0	16.0	5.0	10.4
	10	4.1	14.7	1.8	23.5	2.4	18.3	4.7	20.4
	11	24.1	2.5	4.2	12.6	4.3	8.5	22.5	5.0
12	1	4.3	12.7	38.9	3.0	12.4	2.7	4.7	35.9
	2	4.1	17.4	39.8	2.7	21.3	3.7	4.1	36.9
	3	38.4	2.7	16.5	5.6	39.9	3.4	4.6	13.5
	4	28.7	4.2	3.5	34.2	23.4	5.1	7.3	20.3
	5	3.8	34.5	21.1	3.8	10.7	4.6	5.6	31.7
	6	5.0	37.1	7.9	7.5	5.4	20.2	2.8	25.8
	7	4.1	10.6	3.8	38.7	4.0	31.7	4.7	19.6
	8	5.5	26.6	18.4	4.7	3.2	32.2	14.9	6.0
	9	16.7	6.9	8.7	26.7	4.8	30.7	7.0	10.8
	10	6.5	6.8	2.3	45.9	7.2	11.3	30.5	2.5
	11	36.6	2.6	3.3	20.7	7.2	5.1	40.9	2.9

Table 3-6 Dimensions of the seismic debris field for the prototype buildings subjected to the second eleven ground motion records

No. of stories	Ground motion record	Earthquake Incidence Angle							
		0°				45°			
		X - Direction (m)		Y - Direction (m)		X - Direction (m)		Y - Direction (m)	
		+ ve	- ve	+ ve	- ve	+ ve	- ve	+ ve	- ve
4	12	8.2	4.4	14.0	4.2	13.7	2.8	4.7	9.1
	13	13.5	2.9	6.7	6.4	3.1	10.5	5.6	7.8
	14	14.1	3.1	4.6	7.0	14.8	0.7	7.9	4.2
	15	14.2	0.4	4.3	8.6	6.2	3.2	14.0	0.5
	16	3.6	8.5	0.8	15.8	15.3	2.8	4.5	6.7
	17	5.1	7.4	4.2	13.6	3.1	13.8	5.6	7.7
	18	15.0	0.7	5.7	5.8	6.9	6.7	13.7	2.6
	19	7.7	6.1	1.7	14.2	3.5	10.0	2.7	13.2
	20	5.8	12.8	6.0	6.9	4.8	6.3	13.9	4.1
	21	2.9	16.0	3.8	8.0	4.9	13.7	6.6	6.9
	22	6.8	5.4	2.0	13.9	13.7	3.0	4.5	4.7
8	12	7.8	18.2	8.3	7.6	21.6	4.4	4.6	13.4
	13	5.1	27.3	14.3	8.1	5.6	35.5	7.5	15.6
	14	20.0	5.1	17.0	3.7	25.6	3.9	5.4	10.9
	15	17.7	2.7	2.8	18.4	3.5	23.3	13.3	2.5
	16	4.7	6.7	22.2	6.0	3.3	20.2	7.7	7.4
	17	9.3	4.9	3.4	24.7	2.3	19.0	3.8	21.7
	18	23.5	2.4	12.8	2.7	27.5	2.2	9.0	3.0
	19	18.2	4.3	10.9	8.1	5.6	10.9	3.9	24.9
	20	3.5	27.1	7.2	5.9	4.7	23.8	15.5	4.7
	21	3.1	24.0	11.2	3.8	11.6	4.4	17.7	3.4
	22	15.6	7.1	7.3	13.0	7.6	7.7	24.4	3.3
12	12	35.5	8.7	9.2	7.8	17.9	5.2	4.5	38.5
	13	3.4	17.2	4.3	37.5	4.8	30.9	6.8	14.0
	14	34.1	3.8	19.5	3.6	37.8	2.5	2.5	8.4
	15	34.2	4.1	3.2	13.0	5.8	4.3	37.4	4.6
	16	7.2	9.3	29.6	7.4	32.7	7.4	5.0	7.1
	17	4.9	8.1	2.8	4.3	25.2	9.1	3.7	24.9
	18	47.4	1.6	8.8	4.6	44.3	2.1	6.2	9.7
	19	3.9	38.7	5.5	14.2	4.6	16.3	27.9	3.5
	20	3.7	42.9	6.4	15.8	3.7	30.8	16.6	4.6
	21	37.9	3.0	7.0	6.4	6.9	24.2	5.6	10.0
	22	4.8	12.4	7.8	19.3	4.6	29.6	21.7	5.1
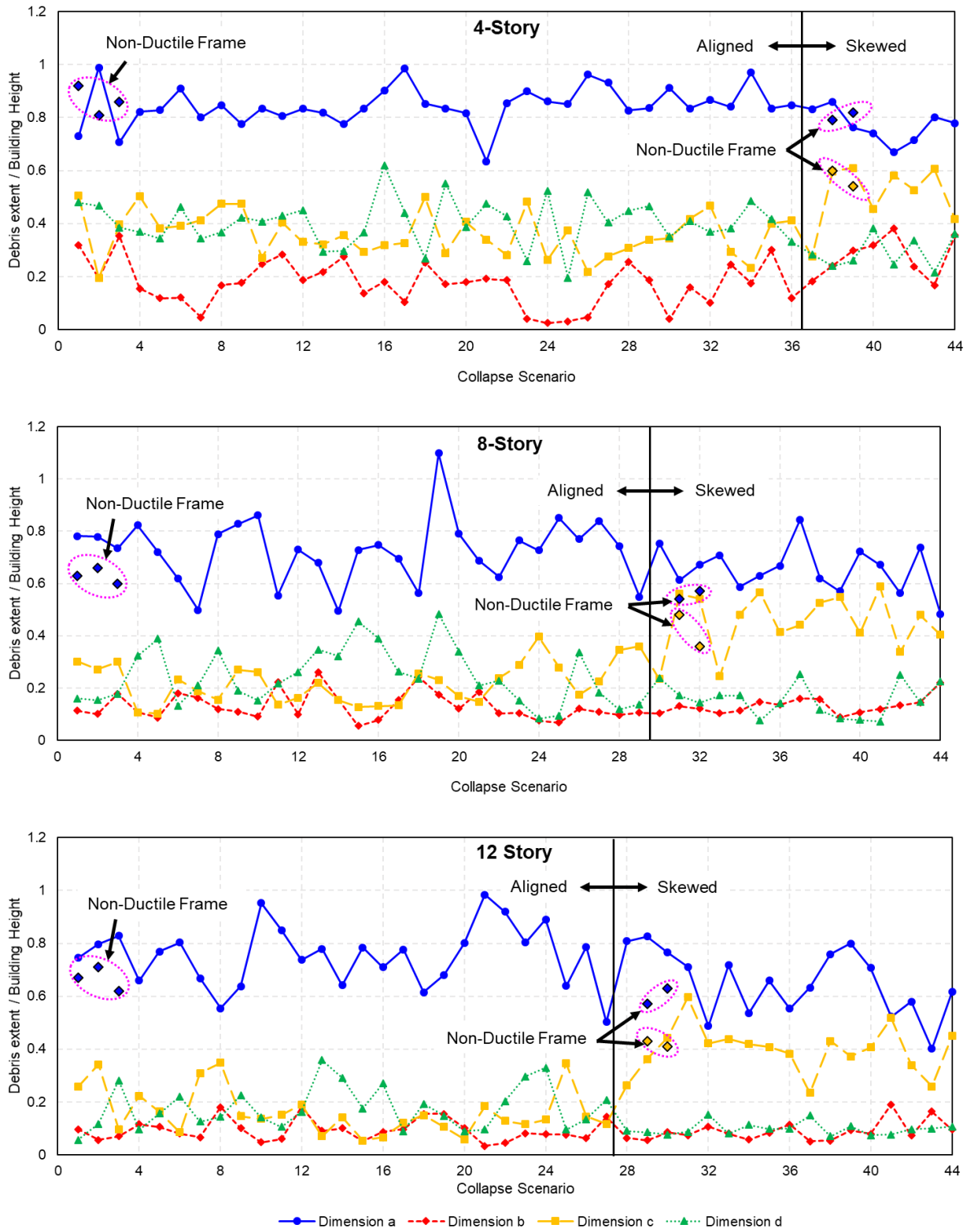
Figure 3-9 Normalized extent of seismic debris field in the studied collapse scenarios
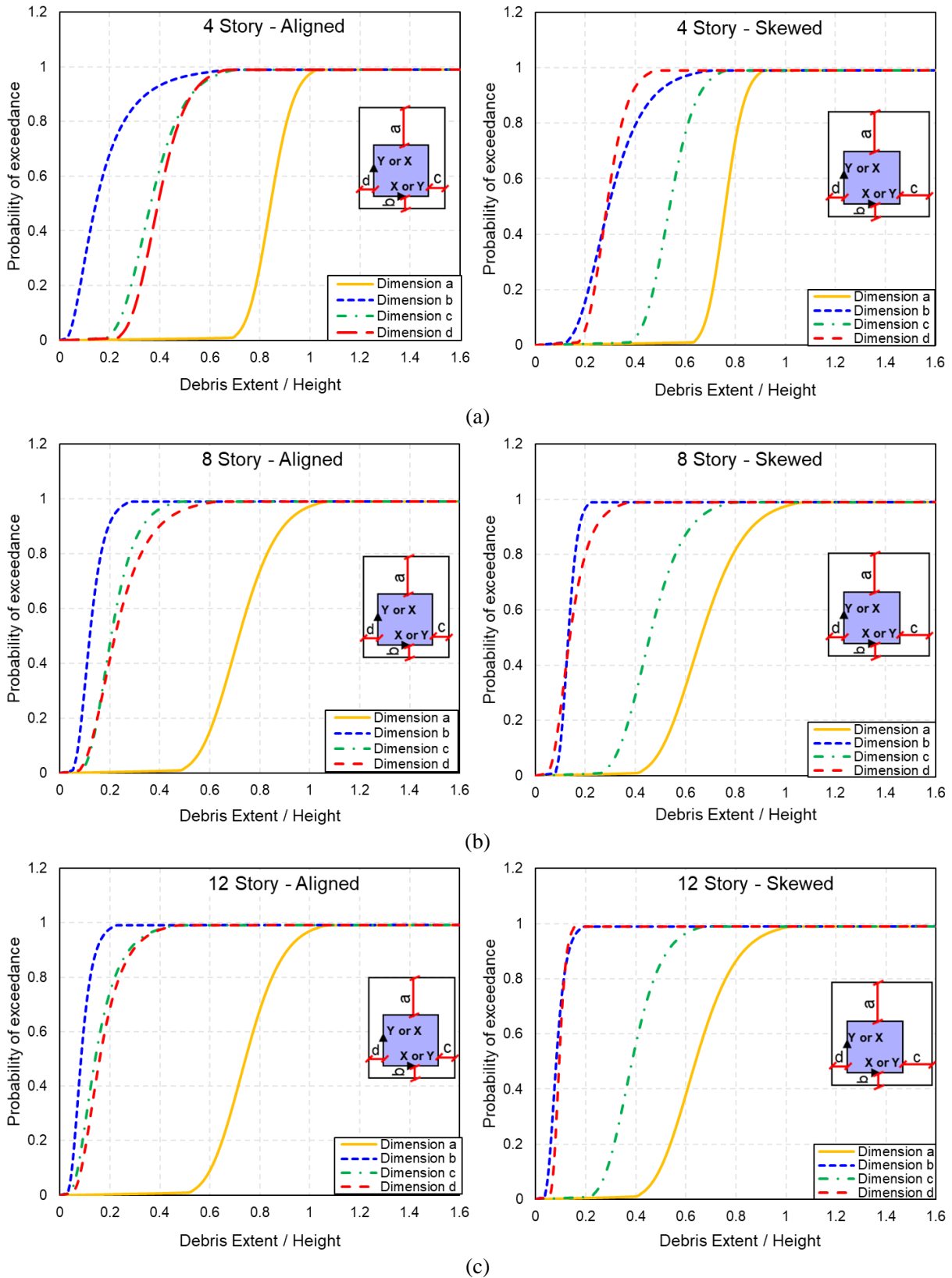
Figure 3-10 Fitted log-normal cumulative density functions of the debris extent of: (a) 4 story,(b) 8 story, and (c) 12 story buildings with different collapse modes

143

Table 3-7 Parameters of fitted log-normal cumulative density functions of the debris extent of the studied buildings

Collapse Mode	No. of Stories	Dimension a		Dimension b		Dimension c		Dimension d	
		Median	Dispersion	Median	Dispersion	Median	Dispersion	Median	Dispersion
	4	0.84	0.09	0.14	0.68	0.36	0.29	0.39	0.23
Aligned	8	0.74	0.17	0.12	0.38	0.21	0.37	0.22	0.46
	12	0.72	0.16	0.09	0.43	0.14	0.52	0.16	0.48
	4	0.76	0.081	0.29	0.38	0.54	0.15	0.29	0.23
Skewed	8	0.66	0.21	0.13	0.23	0.46	0.24	0.14	0.44
	12	0.64	0.20	0.08	0.37	0.39	0.24	0.10	0.22

3.5.5 Effect of Design Code

The space frame building outlined and designed in Liel (2008) is used to study the effect of design code on the maximum extent of the debris field of collapsed RC frame structures. Similar to the studied prototype building, it consists of four RC frames in each direction, which are assumed to resist all the seismic demands on the building except that the frames are non-ductile instead of ductile special moment frames. Three variants (4-story, 8-story and 12-story) of the building are considered. The bay width, first story height and upper story height are 7.6 m (25 ft), 4.57 m (15 ft), and 3.96 m (13 ft), respectively, for all three building heights. The frames are designed according to the requirements of the 1967 Uniform Building Code (UBC) to represent older, non-ductile, RC frame structures in California designed between 1950 and 1975 (IBCO 1967). The buildings are designed for seismic zone 3, which was the highest seismic zone at the time. Further design details can be found in Leil (2008).

Detailed AEMs for the outlined buildings are created using the modeling scheme described earlier for the prototype buildings. The first five ground motion records (aligned orientation only) listed in Table 3-3 are applied to each building and scaled up until they induce total collapse of the building. The maximum extent of the debris field resulting from each of the studied collapse

scenarios of the non-ductile frame buildings are shown by the circled diamonds in Figure 3-9. As shown in Figure 3-9 and observed from the collapse modes, the extent of the debris field for the older building designs is quite similar to that for newer designs. Therefore, it is reasonable to assume that the fitted lognormal distributions shown in Figure 3-10, which were developed for newer designs, can be used to model the variability of the maximum extent of debris of older, non-ductile frames. As expected, the scaled peak ground acceleration (PGA) that induces the collapse of the ductile prototype buildings are larger than those for the non-ductile frame buildings.

3.6   Urban Planning Implications and Recommendations

The maximum extent of the seismic debris field can be characterized by *a* for aligned collapse and *a* and *c* for skewed collapse. These values are useful for estimating whether a collapsed building could block an adjacent roadway and thus be of importance to urban disaster planning officials interested in assessing potential roadway blockage during severe seismic events. Estimates of debris field extent can therefore play a key role in assessing the resilience of communities.

There are numerous situations in past earthquakes where building collapse blocked adjacent roadways. Figure 3-11(a) shows an aerial view of the seismic debris field associated with the collapse of RC buildings caused by the Izmit earthquake (Turkey, 1999, Mw 7.6). The figure shows two buildings completely blocking a road and a third partially blocking an adjacent road. The arrows on the buildings show the actual direction of collapse of the buildings. Figure 3-11(a) also shows the computed seismic debris field of the 4-story prototype building using the applied element model and the material properties values described earlier. While not a rigorous validation

145

exercise because the structural details of the buildings are not known, the comparison provides some measure of confidence that the computational methodology yields reasonable results.

Figure 3-11(b) shows the interaction between the collapsed 4-story prototype building subjected to GM_13_0 and a three-lane road. The lane width is 3.7 m (12 ft), and the building setback is 3.0 m (10 ft), numbers that are typical of many US cities. As shown, more than 50% of the road is blocked due to the collapse of the 4-story building. Taller buildings can lead to greater roadway blockages.

(a)

(b)
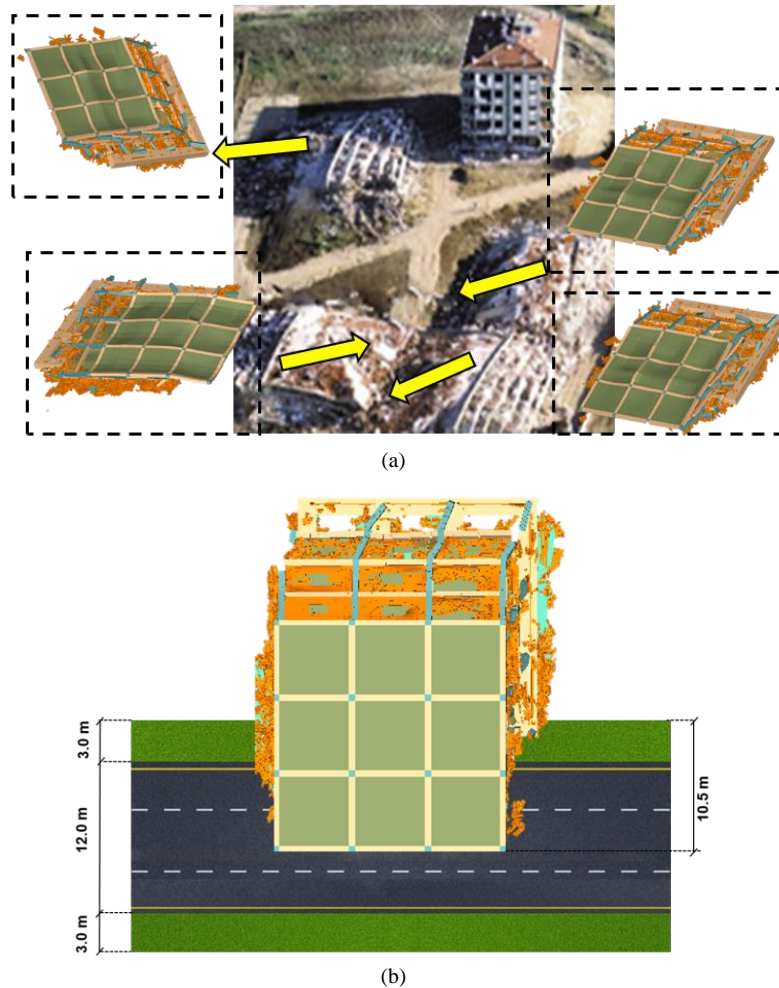
Figure 3-11 Illustration of : (a) comparison between real debris field of collapsed RC frame buildings caused by the Izmit earthquake and debris field of collapsed prototype building (the photograph is from Rodkin and Korzhenkov 2019), and (b) interaction between the collapsed prototype building (4-story under GM_13_0) and adjacent road

3.6.1 Expressions for the Maximum Extent of the Debris Field

Using the data in Figure 3-9, three expressions are derived and shown in Figure 3-12 for each of the maximum extent dimensions: the median, 10th percentile, and 90th percentile. The general response variable (normalized dimensions $\tilde{a}$ or $\tilde{c}$) is expressed in the following linear regression model:

$$\tilde{a} \text{ or } \tilde{c} = K_1 N_s + K_2 \qquad\qquad (3\text{-}3)$$

where N_s is the number of building stories. Linear regression analysis is used to find the parameters shown in Equation 3-3 (k_1 and k_2). The resulting parameters are listed in Table 3-8. It is reasonable to assume that the proposed expressions for the maximum extents of debris are valid for both special moment and non-ductile frame RC buildings based on the earlier discussion, which showed that the design code era had little effect on the maximum extent of the debris field of collapsed RC frame structures.

Table 3-8 Parameters of the proposed linear model for the median and range of the maximum debris extents for different collapse modes

Dimension		k_1	k_2
$\tilde{a}$ aligned case	Median	-0.015	0.89
	10th Percentile	-0.020	0.81
	90th Percentile	-0.007	0.97
$\tilde{a}$ skewed case	Median	-0.015	0.81
	10th Percentile	-0.024	0.75
	90th Percentile	-0.005	0.88
$\tilde{c}$ skewed case	Median	-0.019	0.61
	10th Percentile	-0.020	0.52
	90th Percentile	-0.015	0.73
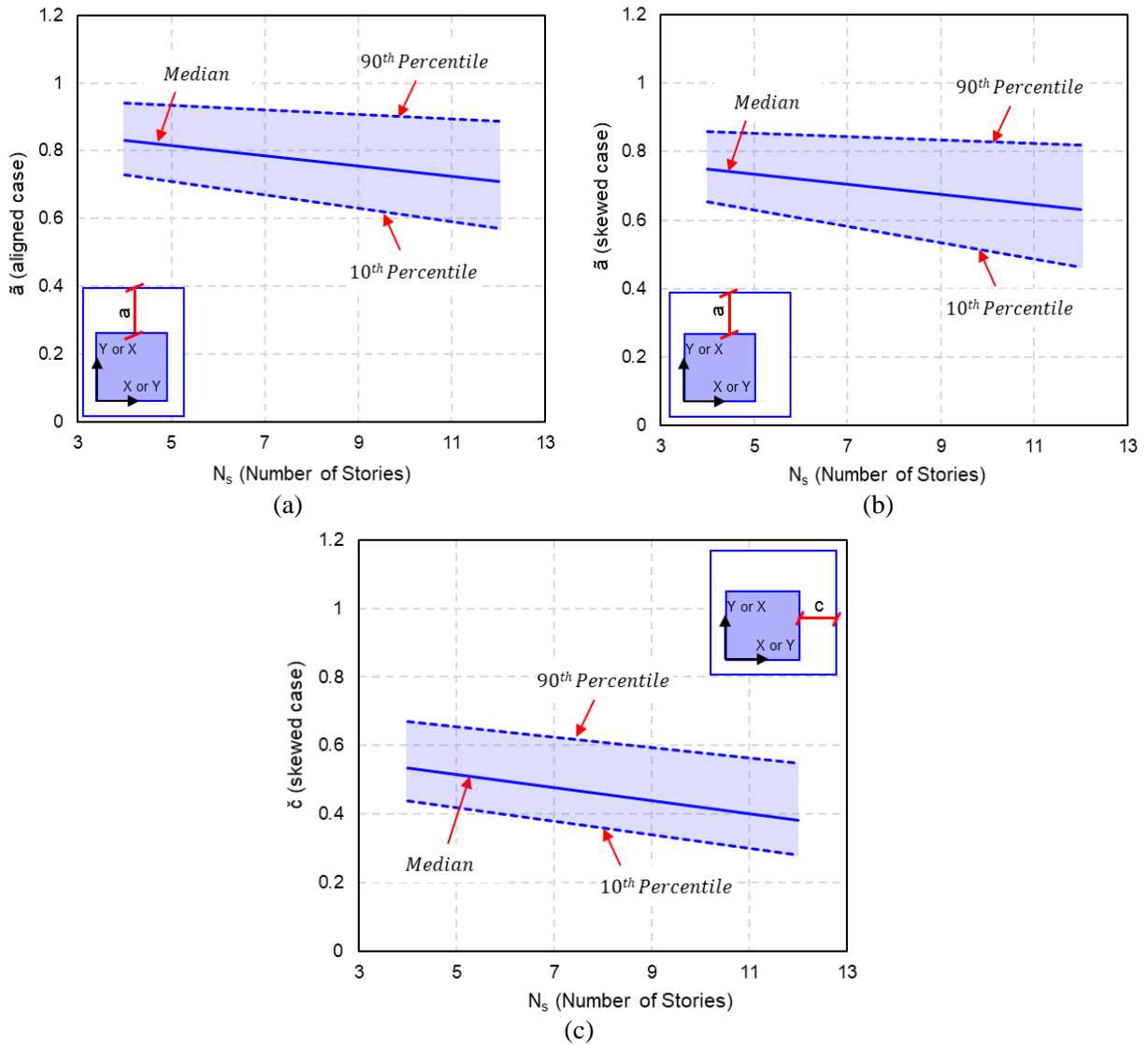
Figure 3-12 Proposed median and range for: (a) normalized dimension *a* for aligned collapse, (b) normalized dimension *a* for skewed collapse, and (c) normalized dimension *c* for skewed collapse

3.7   Summary and Conclusions

The characteristics of the seismic debris field caused by the collapse of RC moment resisting frame buildings were investigated and characterized using applied element method simulations. The simulation technique was validated against available shake table test results.

Four-, eight- and twelve-story prototype buildings designed to contemporary codes were investigated. Each building model was subjected to a set of twenty-two ground motion records scaled up until they induced collapse. Each ground motion record was applied twice, aligned and skewed with respect to the primary axes of the building. The debris field generated from each model was characterized using three types of data: 1) the collapse mode of the building (i.e., aligned or skewed), 2) the collapse direction of the building (positive or negative), and 3) the debris extent in each direction around the collapsed building.

Four collapse modes were identified. Two of the collapse modes were aligned, i.e., the debris was aligned along one of the two orthogonal axes of the building, while the others were skewed, i.e., the majority of debris was skewed towards one of the two axes of the building. The results suggest that the aligned modes were more dominant for low-story buildings (4-story building) while the skewed modes were more dominant for taller buildings (8 and 12 story buildings). It was shown that a deep neural network (DNN) could be trained to accurately classify the mode of collapse of the buildings based on a set of input parameters related to the properties of the ground motion record and building height. The DNN was successfully able to predict the collapse mode of the studied prototype buildings with an accuracy of 92% for the training data and 82% for the test data.

The dimensions of the debris field were characterized using a lognormal distribution as a function of building height and measured dimensions. Although the scaled peak ground acceleration (PGA) that induces collapse of the special moment frame considered in this work was larger than that for the non-ductile frame building, it was shown that the extent of the debris field is quite similar. A linear regression analysis of the simulation data was used to propose estimates for the extent of the debris field as a function of building height. The proposed expressions were

obtained through a limited number of simulations for prototype structural systems under idealized conditions. Additional studies should be conducted on a broader range of frames and building designs to generalize the results.

The results of this chapter are important for modeling the interdependencies between the building portfolios (through the collapse of buildings) and transportation networks (through the extent of debris) in the resilience of communities vulnerable to seismic risk. In particular, use of the proposed expressions for the maximum extent of debris and developed DNN and similar machine learning techniques can enable rapid assessment of roadway blockage in disaster planning exercises.

CHAPTER 4

A Scalable Model for In-Event Interdependencies in Community Resilience

4.1   General

This chapter describes a scalable model that employs a simulation-based dynamic analysis, which models the behavior of the community at each time step as the seismic event occurs (time step in seconds) and as the community recovers after the event (time step in days). As such, it permits explicit consideration of in-event interdependencies (i.e., during the hazard as well as the recovery stage) that can arise between the physical (i.e., buildings-related) and social (i.e., injured people-related) systems of the community and provides detailed information about the temporal and spatial distribution of injuries/fatalities during the seismic hazard. The capability of the proposed model to support hazard mitigation planning is demonstrated through a case study that highlights the tradeoff between the physical and social costs of different mitigation strategies.

4.2   Background

Early models for assessment of earthquake impact on a community computed loss as a function of high-level parameters. For example, Chen et al. (1997) proposed an earthquake loss estimation method based on population distribution and gross domestic product. As it became clear that economic and social losses were highly dependent on the physical damage caused by an

extreme event, the state-of-the-art evolved towards more realistic and detailed loss models that explicitly accounted for structural response.

A prominent example of damage-based loss estimation methods is the HAZUS methodology (FEMA 2003). HAZUS computes direct and indirect social and economic losses based on building fragility functions. However, it treats a building as a single-degree-of-freedom (SDOF) system, which limits the granularity of the methodology. In particular, losses are assessed at the entire building level and not the story level. This limitation has been solved by the FEMA P-58 (FEMA 2012a) methodology by quantifying the performance of each structural and nonstructural component in the building separately (i.e., different fragilities) in terms of repair time, repair cost and casualties.

A number of researchers have developed computational frameworks using available damage and loss estimation models to assess earthquake loss and, more broadly, community resilience (Burton et al. 2016 & 2017, Vona et al. 2018, Sutley et al. 2017, Cimellaro et al. 2016, and Kammouh et al. 2018). Miles and Chang (2003, 2006) proposed a conceptual framework for community recovery, which was extended into a numerical model implemented in ResilUS (Miles and Chang 2011). Cimellaro et al. (2010) simplified the recovery process by defining three types of recovery functions (linear, exponential and trigonometric) depending on community preparedness. Other notable frameworks on community resilience can be found in Lin and Wang (2019 & 2017) and Masoomi et al. (2018).

4.3   Motivation and Objectives

Most available frameworks for assessing resilience have key limitations. Many are based on generic loss estimation models (e.g., HAZUS) where each building is simplified to a fragility

152

curve. Even when finer granularity is taken into account to permit computation of repair time at the component level (e.g., based on FEMA P-58), there is frequently insufficient information about the required number of workers, repair sequences and delay times needed for accurate and realistic recovery computations. Most of the available recovery models do not accurately consider the availability of resources and the interdependencies between the different infrastructure systems of society during the recovery stage. In addition, the majority of existing frameworks are fully integrated platforms, which makes it difficult to extend them, add new features or expand their capabilities to address new situations.

Two recent frameworks have been proposed to address the above-mentioned shortcomings: IN-CORE, which is being developed by the Center of Excellence for Risk-Based Community Resilience Planning (Ellingwood et al. 2016) and the platform developed in Lin et al. (2019). The former is a modular platform while the latter is also modular and based on a publish-subscribe data management model implemented within a distributed computing simulation environment. Distributed computing enables executing different models (simulators) across multiple processors (or computers) connected through a communication network. The proposed simulation model herein has architectural similarities to these two platforms.

Departing from most previous approaches, the proposed model employs a simulation-based dynamic analysis that models the behavior of the community at each time step as the seismic event occurs (time step in seconds) and as the community recovers after the event (time step in days). As such, it permits explicit consideration of in-event interdependencies (i.e., during the hazard as well as the recovery stage) that can arise between the physical (i.e., buildings-related) and social (i.e., injured people-related) systems of the community and provides detailed information about the temporal and spatial distribution of injuries/fatalities during the seismic

hazard. This sort of data allows emergency teams to better optimize the utilization of their resources, which results in more realistic modeling of recovery trajectories.

Another key innovation in this work is the combination of the FEMA P-58 (FEMA 2012a) methodology for loss estimation, which provides detailed information about the spatial distribution of the seismic losses at the component level, and the REDi model (Almufti and Willford 2013) for assessment of downtime, repair schedule and required number of workers to repair the damaged buildings at the community level. This combination permits evaluation of the recovery path of the community based on realistic repair schedules as well as the availability of workers in the community.

The objective of this chapter is to describe the new scalable simulation model and showcase how it can be used to explicitly model in-event interdependencies that arise between the physical (i.e., buildings-related) and social (i.e., injured people-related) systems of the community. The capability of the proposed model to support hazard mitigation planning is demonstrated through a case study that highlights the tradeoff between the physical and social costs of different mitigation strategies.

4.4   Simulation Model Overview

The proposed simulation model (outlined in Figure 4-1 and Figure 4-2) connects different simulators that model different aspects of the studied scenario including the city layout, seismic hazard, community losses, and physical and social recovery path simulation. Each simulator can be replaced by another of higher or lower fidelity as long as it takes input and provides output in the same format as the original simulator. For example, the *structural analysis simulator* computes the structural responses of the buildings (i.e., output) using the ground motion parameters from the

ground motion simulator (i.e., input) regardless of the fidelity of the structural model implemented in the *structural analysis simulator*. It can be as simple as a 2D elastic representation of the building or as detailed as a 3D inelastic model.

There are two types of connectivity between the simulators: sequential and interdependent connectivity. In sequential connectivity, the simulators are connected in such a way that the data flows in one direction during each time step. In the latter, the data flows in two directions between the simulators meaning that both simulators update each other within a time step in order to account for mutual interdependencies. As shown in Figure 4-2, there are four types of simulators based on how they are connected to the model: (1) a simulator that runs once at the beginning of the hazard event and broadcasts initial required data (i.e. *city simulator*), (2) simulators that run at every time step during the earthquake (time step in seconds), (3) simulators that run once at the end of the hazard event to estimate the initial conditions for the recovery stage (e.g. economic and social losses), and (4) simulators that run at each time step during the recovery stage (time step in days).
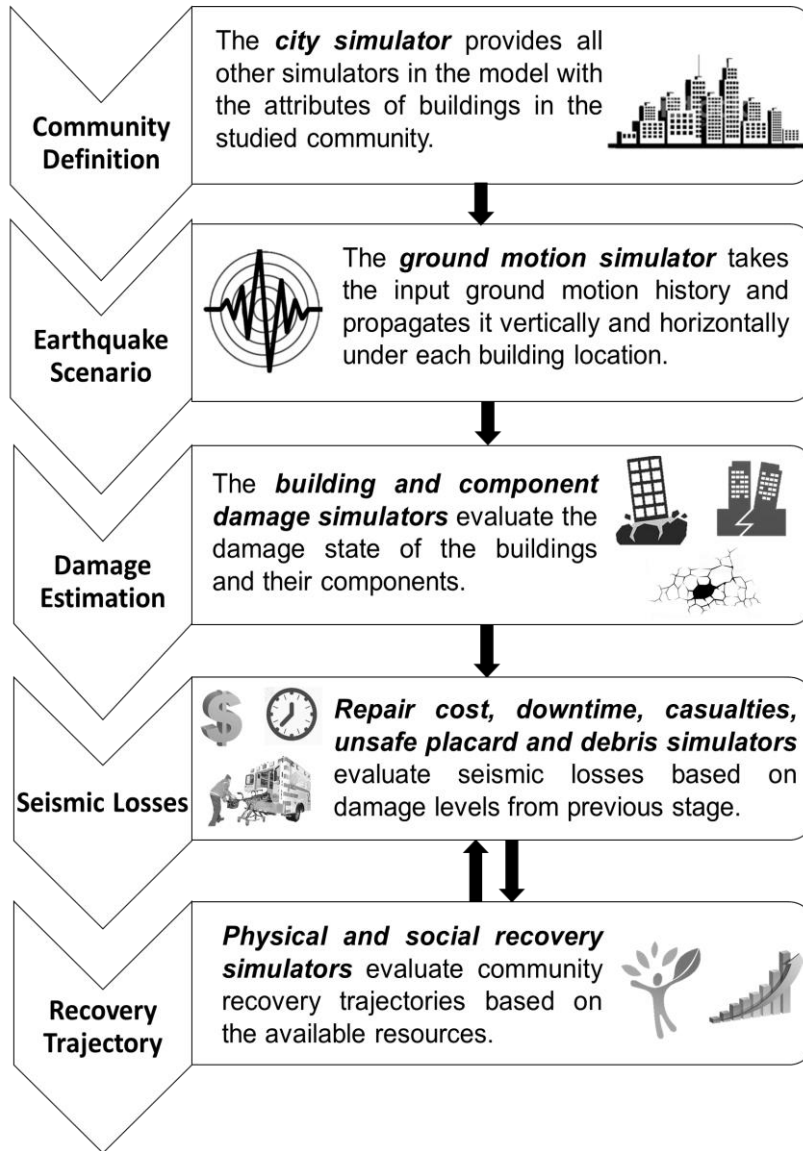
Figure 4-1 Proposed simulation model overview
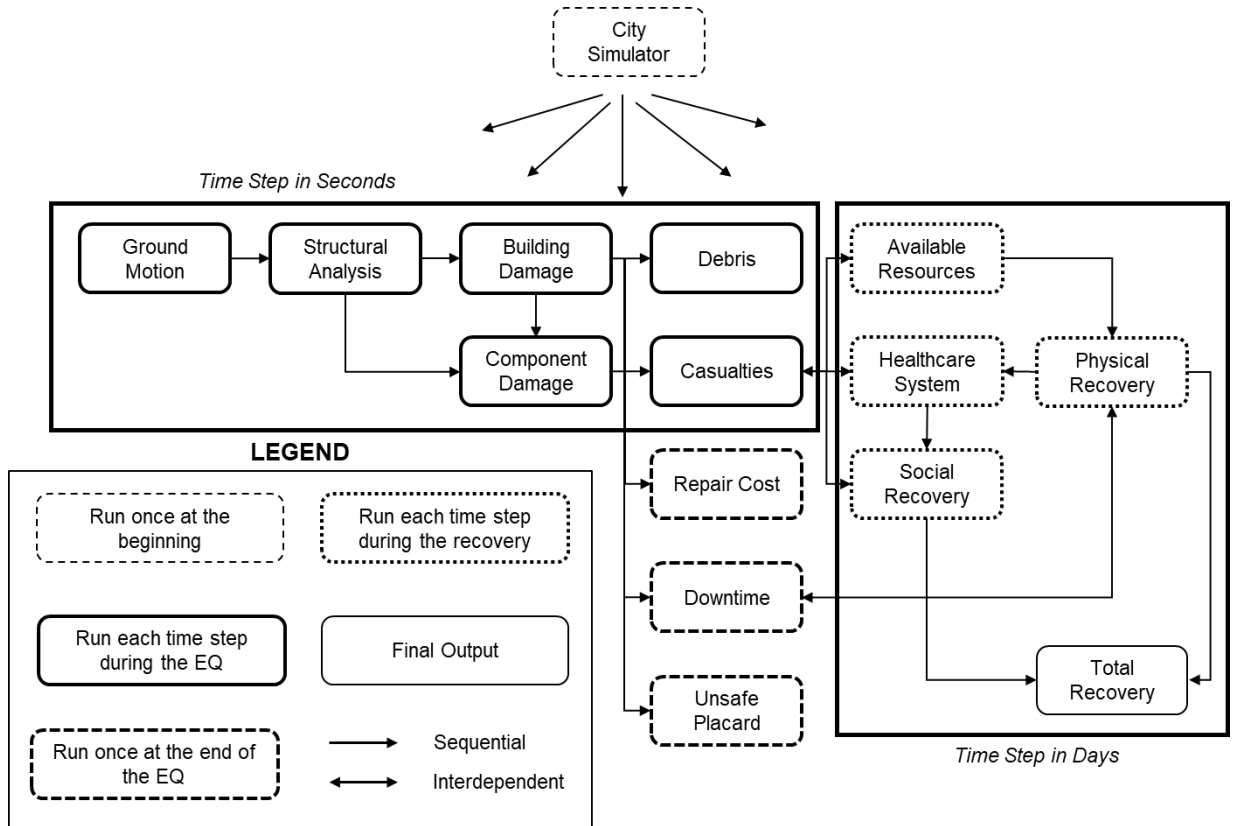
Figure 4-2 Schematic diagram of the proposed simulation model

4.5 Methodology

4.5.1 Problem Setup and Naming Scheme

The *city simulator* broadcasts information about the community including coordinates, elevation, occupancy, material, structural system, structural and nonstructural component specifications and quantities of all the buildings to all other simulators. It reads this information from a MATLAB database providing flexibility in studying any existing, new, or virtual community given that the attributes are modeled properly in the MATLAB database. The description of the city variables in the MATLAB database can be found in Appendix C. In order to facilitate the interpretation of building attributes in the studied community, the buildings are

designated as ABC-D-E, where "A" is the material, "B" is the structural system, "C" is the design code, "D" is the number of stories and "E" is the occupancy of the building. For example, "SFC-2-1" is a steel moment frame, old code (Pre-1973) 2-story commercial building. The naming scheme used by the *city simulator* is listed in Table 4-1.

Table 4-1 Naming scheme of buildings used by the *city simulator*

Material "A"		Structural System "B"		Design Code "C"		Occupancy "E"	
Label	Description	Label	Description	Label	Year	Label	Description
S	Steel						
C	Concrete	B	Braced Frame	A	>1994	1	Commercial
						2	Elementary Schools
						3	Middle Schools
WS	Small Wood (Area < 465 m^2)					4	High Schools
		F	Moment Frame	B	1973-1994	5	Healthcare
WL	Large Wood (Area > 465 m^2)					6	Hospitality
						7	Residential Buildings
RM	Reinforced Masonry					8	Research Laboratories
		S	Shear Wall	C	<1973	9	Retail
URM	Unreinforced Masonry					10	Warehouse

4.5.2 Demand and Capacity Computations

The *ground motion simulator* takes the ground motion history at the underlying rock or "rocklike" layer of a recording station as input. It then performs site response analysis by propagating the ground motion in both directions (i.e., vertically and horizontally) at each time step during the earthquake. In order to propagate the ground motion vertically through different soil layers, the lumped mass-spring analysis formulated by Idriss and Seed (1968) is used by assuming linearly elastic soil layers. Then, a Newmark-Beta scheme is used to solve the formulated equations of motion. The ground motion history is scaled using the attenuation relationship

proposed by Campbell and Bozorgnia (2008) to propagate the ground motion horizontally under each building in the community.

The *structural analysis simulator* evaluates the dynamic response of each building in the community using nonlinear dynamic analysis in OpenSees (McKenna et al. 2000) based on the ground motion history provided by the *ground motion simulator*. The structural responses evaluated by the *structural analysis simulator* are then used to evaluate the damage state of each building in the community at each time step during the earthquake based on the damage state limits obtained from HAZUS (FEMA 2003). These limit states are based on building attributes such as total height, building area, lateral force resisting system and the design year. HAZUS categorizes the building damage into four limit states: slight, moderate, extensive, and complete. More details about the description of each damage state can be found in FEMA (2003).

The structural responses evaluated by the *structural analysis simulator* are also used by the *component damage simulator* to evaluate the damage state of each structural and nonstructural component in each building in the community at each time step during the earthquake (for the non-collapsed buildings) based on the fragility curves specified in the FEMA P-58 database (FEMA 2012b). The fragility curves of FEMA P-58 are defined using different engineering demand parameters, *edp*, including inter-story drift, floor acceleration or floor velocity. The seismic fragility functions of all the components in FEMA P-58 are described by a lognormal cumulative distribution function (CDF) defined by Equation 4-1:

$$F_R(x) = \Phi[ln(^x/_{m_R})/\beta_R] \qquad (4\text{-}1)$$

where $F_R(x)$ is the fragility function; x is the *edp*; m_R is the median capacity; β_R the logarithmic standard deviation; and Φ is the standard normal probability integral.

A random number having a uniform distribution between 0 and 1, N_{ij}, is generated at the first time step of the simulation for the jth component of building i. Then, the maximum *edp* for each damage state is computed using Equation (4-1) as shown in Figure 4-3. The expected damage state of the jth component of building i is evaluated at each time step during the earthquake for each of the conducted simulations based on the structural response edp_{ij}, using the following criteria:

$$
\begin{aligned}
&\text{No Damage if } edp_{ij} < edp_{DS1} \\
&\text{Damage state 1 if } edp_{DS1} \leq edp_{ij} < edp_{DS2} \\
&\text{Damage state 2 if } edp_{DS2} \leq edp_{ij} < edp_{DS3} \\
&\text{Damage state 3 if } edp_{ij} \geq edp_{DS3}
\end{aligned}
\tag{4-2}
$$
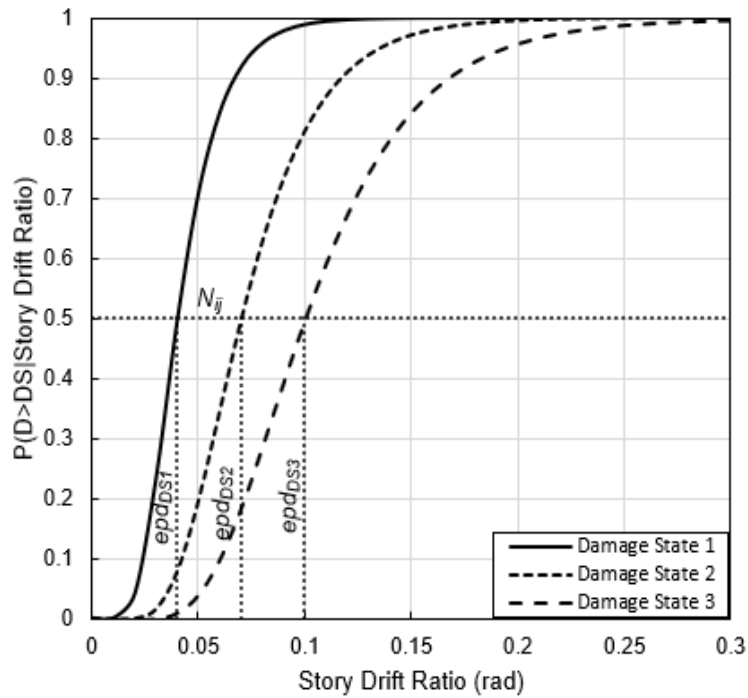
Figure 4-3 Fragility curves for steel column base plates specified by FEMA P-58 (B1031.011a)

4.5.3 Seismic Losses

Seismic losses of buildings are classified into two types: economic and social losses. Economic losses are expressed in terms of downtime, repair cost, unsafe placarding status and amount of debris resulting from damaged components. Social losses are expressed in terms of potential injuries and fatalities resulting from the collapse of buildings or damaged structural and non-structural components of the buildings. The casualties and debris are evaluated at each time step during the earthquake in the *casualties* and *debris* simulators, respectively, while the downtime, repair cost, and unsafe placard simulators evaluate the economic seismic losses once at the end of the earthquake (initial conditions for the recovery stage). The amount of debris generated at each building is calculated based on the empirical approach described in FEMA (2003).

The repair cost and unsafe placarding status of each building in the community are calculated probabilistically using the consequence functions specified in the FEMA P-58 database for all structural and non-structural components of buildings. The *downtime simulator* evaluates the downtime of each building in the community using the REDi methodology (Almufti and Willford 2013), which relates the damage state of structural and non-structural components evaluated using FEMA P-58 to actual downtime of buildings including both the repair time evaluated by FEMA P-58 and impeding factors, which delay the initiation of repairs to the buildings. The impeding factors considered by the REDi methodology are inspection, financing, contractor mobilization and permitting, and engineering mobilization and review/re-design. These factors are typically evaluated probabilistically and are influenced by the degree of building damage. The *downtime simulator* constructs an initial repair schedule for each building in the community considering the aforementioned impeding factors, the sequence of repairs that will be undertaken as shown in Figure 4-4, the number of workers required to perform repairs of each

component type in the building and the maximum number of workers that are able to work on-site simultaneously.

The casualties defined in FEMA P-58 are either fatalities or injuries (requiring hospitalization) that occur inside the building envelope. Minor injuries and outdoor casualties are not considered in the scope of this study. The population distribution in each building is based on its occupancy (i.e., commercial, schools, etc.) as specified in FEMA P-58. Thus, the time of day and day of the week of the occurrence of the earthquake are important to accurately evaluate the casualties. In the case of building collapse, the number of injuries and fatalities is calculated based on the casualty rates specified in HAZUS for casualty severity levels 3 and 4, respectively, and the population present in the building at the time of the earthquake. Casualty severity level 3 is a life threatening injury that requires hospitalization while level 4 is a fatality. If collapse does not occur, the number of injuries and fatalities at each time step during the earthquake is calculated probabilistically using the consequence functions specified in the FEMA P-58 database where each damage state of the structural and nonstructural components includes a description of potential life safety hazards and the corresponding affected area.
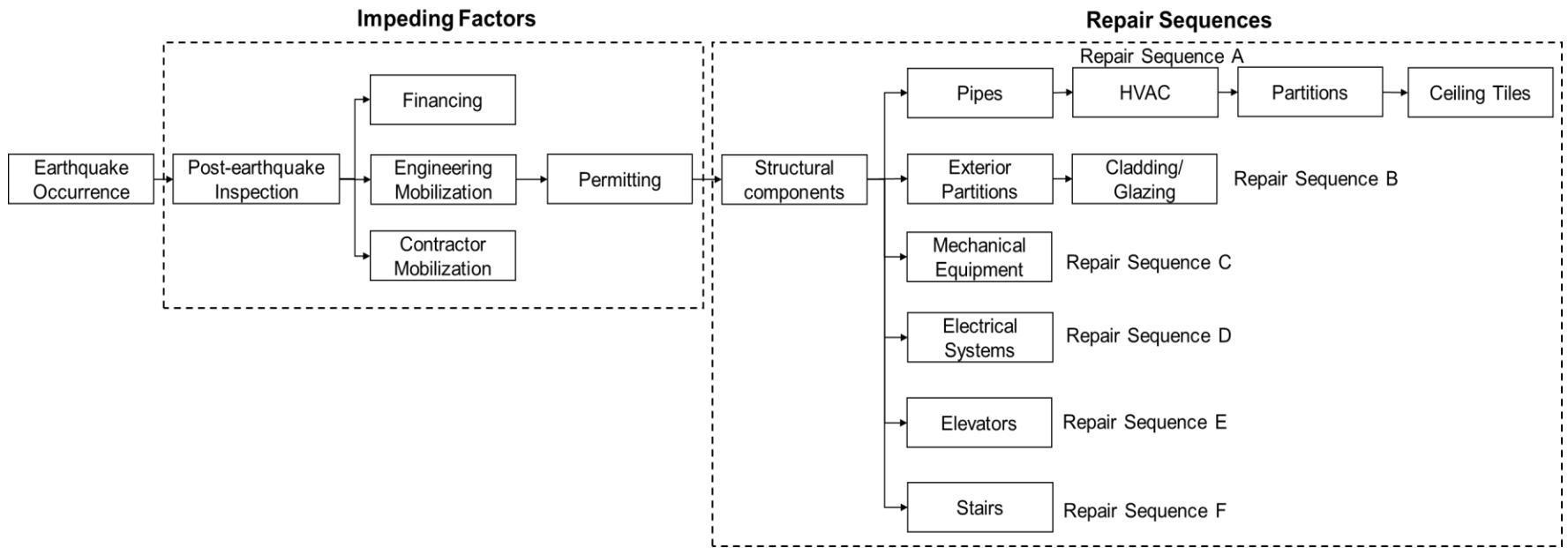
Figure 4-4 Repair schedule of buildings including impeding factors proposed in the REDi methodology (Almufti and Willford 2013)

4.5.4 Physical Recovery

It is important to differentiate between two types of community recovery efforts: physical and social. Physical recovery is defined as the ability of buildings to recover from the physical damage caused by the earthquake and return back to full functionality. Social recovery is defined in this work as the ability of injured people to return back to normal health. In the proposed simulation model, each type of recovery is simulated by different simulators based on the factors affecting the recovery process.

The first step to simulate the physical recovery of a community is to evaluate the initial functionality of each building in the community immediately after the earthquake. Therefore, the components of the buildings are classified into three groups based on their importance and effect on the functionality of the building: (1) structural components (S), (2) nonstructural essential components (NE), and (3) nonstructural nonessential components (NN). The first group (S) are the components that directly affect the stability of the building (e.g., columns, beams, connections, etc.). The second group (NE) are those that impede reoccupying a building (i.e., sequence B, C, D, F and pipes from sequence A defined in the REDi repair sequences shown in Figure 4-4). The third (NN) are components that do not prevent re-occupancy of the building (i.e., sequence A, except pipes, and sequence E defined in the REDi repair sequences).

The damage states (*DS*) of structural and nonstructural components in FEMA P-58 are expressed in discrete states, which are not the same for all components (e.g., bolted shear tabs have three damage states while concrete roof tiles have only two damage states). In order to relate the *DS* of the different components of the building to the functionality of the building, it is important to have a unified scale to express the damage of the components. Thus, the repair time required to recover from each *DS* of the components is normalized to the repair time required to recover from

the maximum damage state of the component (designated %*RT*). Then, Equation (4-3) is used to map the *DS* of the components to a unified scale of 3 damage states. The limits shown in Equation (4-3) are based on the average %*RT* considering each *DS* for components that can be classified into 3 different damage states according to FEMP-58 (FEMA 2012b).

$$
\begin{aligned}
&DS1: 0 < \%RT \le 30\\
&DS2: 30 < \%RT \le 75\\
&DS3: 100 < \%RT \le 100
\end{aligned}
\tag{4-3}
$$

Four functionality states of a building are considered: (1) not functional (NF), (2) re-occupancy (RO), (3) basic functionality (BF), and (4) full functionality (FF). NF implies that the building suffers from extensive structural or nonstructural damage that threatens life safety. An NF state prevents the building from providing its intended service. The RO state implies that the building suffers from minor to moderate structural or nonstructural damage that does not prevent the occupation of the building. However, RO prevents the building from providing its full intended service. The BF state implies that the building suffers from slight structural or nonstructural damage that does not prevent it from providing its essential intended services. However, the building does not provide its full intended services as before the occurrence of the earthquake due to the ongoing repairs that partially hinder this ability. The FF state implies that the building does not suffer any damage after the earthquake, and it can provide its full intended service as before the occurrence of the earthquake. In order to quantify the seismic resilience of the community, each physical functionality state, $Q_p(t)$, is quantified as 0, 50, 80, or 100 % for the NF, RO, BF, or FF states, respectively based on the definition of each functionality state described earlier. The initial functionality of each building in the community is related to the level of damage of the three

aforementioned components (S, NE, and NN) in the *physical recovery simulator* using the

combinations shown in Figure 4-5.
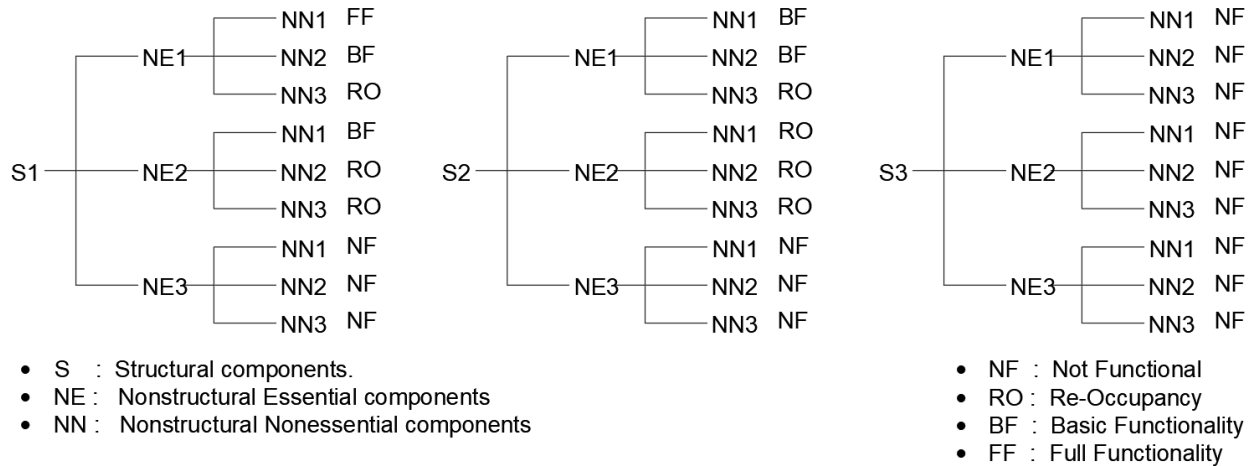
Figure 4-5 Combinations used to evaluate the initial functionality of buildings in the
physical recovery simulator **(the appended number is** *DS***)**

The *available resources simulator* evaluates the available number of workers in the

community at each time step during the recovery stage based on the number of casualties obtained

from the *healthcare system simulator*. It is assumed that the percentage of total casualties in the

population of the community is the same as the percentage of casualties in the population of

workers. Thus, the available number of workers increases during the simulation due to recovery

of workers from earthquake-induced injuries. The *physical recovery simulator* allocates the limited

number of workers available in the community calculated by the available resources simulator to

repair the damaged buildings using the repair schedule and required number of workers evaluated

by the *downtime simulator*. The number of workers is allocated to buildings based on the priority

of the building in the community where the buildings are prioritized based on their usage and

occupancy level. Usage priority used in this research is as follows: hospitals, schools, residential houses, commercial buildings, retail and other occupancies.

After allocating the available workers to repair the damaged buildings in the community, the *physical recovery simulator* sends back a list of buildings that have not been repaired at the current time step, due to the limited number of available workers, to the *downtime simulator* to update their repair schedule. The *downtime simulator* sends back the updated schedules to the *physical recovery simulator* to be used in the next time step.

The physical functionality of each building in the community is updated at each time step during the recovery stage based on the functionality in the previous step and the damage state of different components in the building. For a building in the NF state, the physical functionality is restored in two stages. The first stage is to return to the RO state after finishing the repairs of the components specified as schedule B, C, D, F and pipes from sequence A in the REDi methodology. The repair sequence of the different components adopted in the REDi methodology is summarized in Figure 4-4. The second stage is to return back to the FF state after finishing all the required repairs in the building. However, for a building in the RO or BF state, the physical functionality is restored in one stage only by returning back to the FF state after finishing all the repairs in the building. Figure 4-6 shows a schematic diagram of the physical functionality restoration process. The total physical functionality of the community $Q_p(t)$ is evaluated at each time step during the recovery stage as the weighted average of all the physical functionalities of the buildings in the community at this time step based on the importance of each building in the community as follows:

$$\%Q_p(t) = \frac{\sum_{i=1}^{n} I_i * \%Q_i(t)}{\sum_{i=1}^{n} I_i} \tag{4-4}$$

where $\%Q_i(t)$ is the functionality of building i in the community at time step t, I_i is the seismic importance factor of building i based on its occupancy as specified in ASCE 7-16 (ASCE 2016) and n is the total number of buildings in the community.
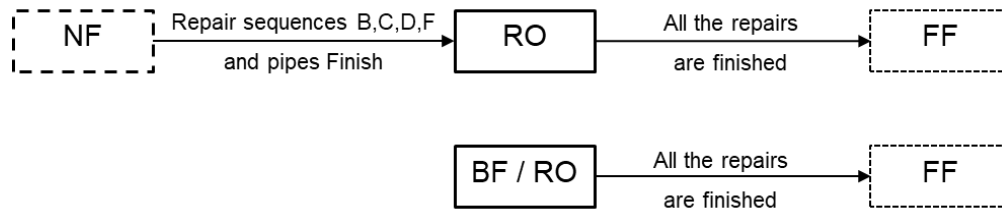
Figure 4-6 Restoration of building functionality at each time step during the recovery stage

4.5.5 Social Recovery

The social recovery of the community is a measure of the number of casualties in the community with respect to the total population. Therefore, the first step to simulate social recovery of the community is to evaluate the number of injuries that need treatment at each time step during the recovery stage. At the end of the earthquake (i.e., the initial time step of the recovery stage), the *casualties simulator* evaluates the total number of injuries and fatalities at each building in the community. Some of the injured will be trapped in damaged or collapsed buildings (i.e., they cannot be assigned to hospitals until they are rescued). In the proposed model, 60% of the injured people are assumed to be trapped and need to be rescued during the recovery stage as modeled by Fawcett and Oliveira (2000). The rate at which the trapped, injured people are rescued during the recovery stage depends on the emergency response capabilities of the community and is an important characteristic of resilient communities. In the proposed simulation model, the daily rate of rescue of injured people is assumed to be constant. However, it can be adapted to any other assumption as discussed in Fawcett and Oliveira (2000). The other 40% of injured people will be

168

waiting to receive treatment by the hospital system in the community. The *healthcare system simulator* assigns the waiting injured people to hospitals in the community based on the closest hospital to the building where the injury occurs and the available number of beds in the hospital, which is calculated as follows:

$$B(t) = Q_p(t) * B_t - B_b(t)$$

(4-5)

where *B(t)* is the available number of beds at time *t* during the recovery stage, $Q_p(t)$ is the physical functionality of the hospital building evaluated by the *physical recovery simulator*, B_t is the total number of beds in the hospital before the earthquake and $B_b(t)$ is the number of filled beds at time *t*. During the first days after the earthquake, there is a high mortality rate, which is about 20-25% according to Coupland (1994). The proposed simulation model considers a constant mortality rate of 3% per day for untreated injuries as modeled by Fawcett and Oliveira (2000). The remaining 97% of untreated injured people will continue to the next time step to be assigned to hospitals if open beds are available.

Rescued people with injuries are added to the waiting injured to be assigned to hospitals in the next time step. Also, it is assumed that 20% of the waiting injured people that are not assigned to hospitals at the current time step will be mobilized to hospitals in nearby zones to model the fact that injured people are usually distributed to nearby health care facilities after a seismic event in cases where no beds are available in the hospitals in their zone. Figure 4-7 shows a schematic diagram of the injury treatment process during the recovery stage performed in the *healthcare system simulator*. The social functionality of the community is evaluated at each time step during the recovery stage by the *social recovery simulator* as follows:

$$\%Q_s(t) = 100 * (1 - \sum_{i=1}^{n} C_i(t)/P)$$

(4-6)

169

where $C_i(t)$ is the total number of injuries and fatalities at building i at time step t and P is the total population in the community. The social functionality of the community will not return back to 100% if fatalities occur.
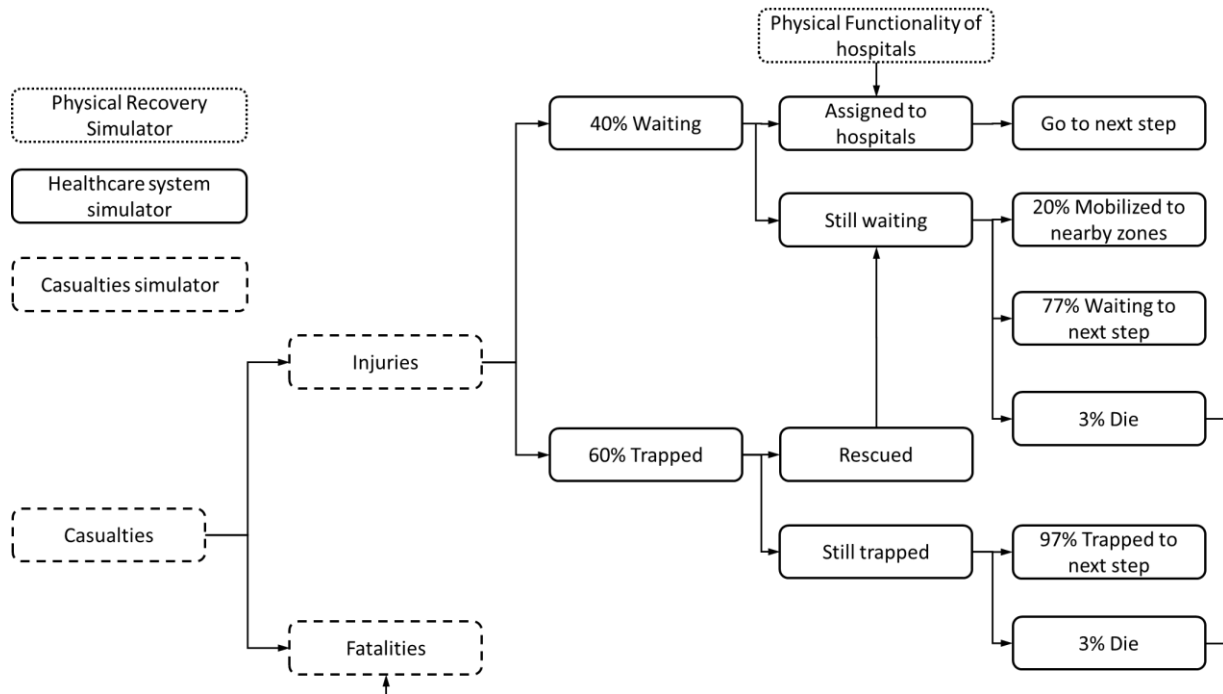
Figure 4-7 Schematic diagram for the injury treatment process performed in the *healthcare system simulator*

4.5.6 Quantifying Seismic Resilience of Communities

The total functionality of the community is calculated at each time step during the recovery stage by the *total recovery simulator* as the product of the physical and social functionalities as follows:

$$\%Q_t(t) = Q_p(t) * Q_s(t) \qquad (4\text{-}7)$$

170

The seismic resilience index of the community (%R) is evaluated as the area under the total recovery path during the recovery time as shown in Figure 4-8, which can be represented mathematically as follows (Bruneau and Reinhorn 2004,2007):

$$\%R = \frac{\int_{t_{oE}}^{t_{oE}+T_{RE}} Q_t(t)}{T_{RE}} \tag{4-8}$$

where t is the time during the recovery stage, t_{oE} is the time when the earthquake occurs, T_{RE} is the time required by the community to restore full functionality after the earthquake and $Q_t(t)$ is the total functionality of the community calculated by equation (4-7).
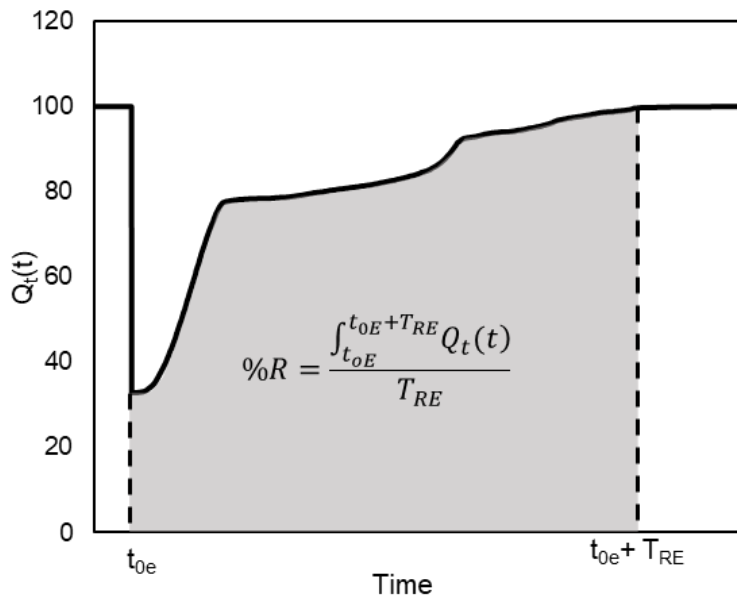
Figure 4-8 Evaluation of seismic resilience of a community

4.6   Case Study: Seismic Resilience of An Archetype Community

4.6.1 Building Portfolio

The proposed simulation model and its capabilities are demonstrated through a case study that focuses on a part of Shelby County, Tennessee, as shown in Figure 4-9. It is a typical mid-

171

size community with a population of approximately 40,000 (Statistical Atlas 2018) and is approximately 14 km^2 (5.4 square miles) in area. It consists of about 8600 buildings with different occupancies, structural systems, heights and design codes. The data for the buildings is extracted from the database provided in the Ergo-EQ software (NCSA 2018). The buildings are mapped to 100 different developed archetype buildings. Table 4-2 lists the archetype buildings designated according to the naming scheme described earlier and the total number of each archetype. Most of the buildings are wooden houses that are typical of U.S. communities.
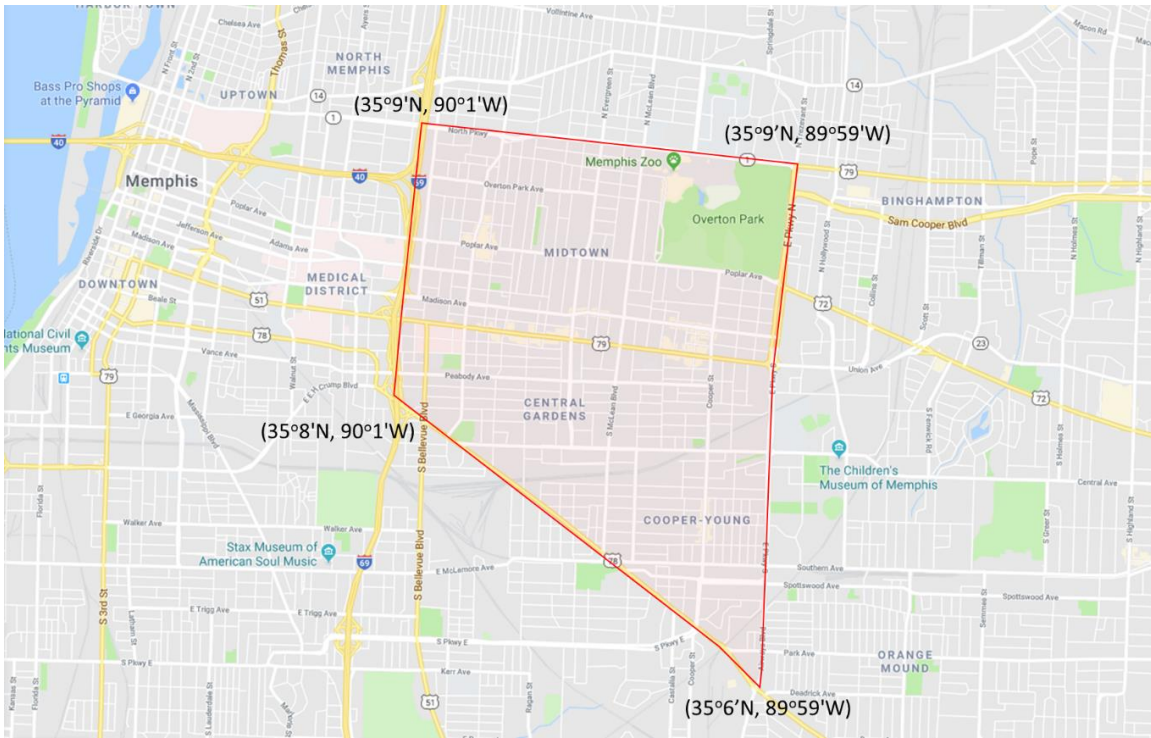
Figure 4-9 Archetype community location

Table 4-2 List of building archetypes and total number of each archetype in the studied community

Model	Total	Model	Total	Model	Total	Model	Total	Model	Total
CFB-2-1	2	CSC-20-1	1	RMC-2-2	1	SFC-2-1	5	WLC-2-9	5
CFB-2-10	1	CSC-20-8	1	RMC-2-7	1	SFC-4-1	1	WLC-2-7	177
CFB-2-9	4	CSC-2-1	1	RMC-2-9	3	URMB-2-7	1	WLC-3-1	4
CFB-6-1	2	CSC-2-2	1	SBA-2-1	1	URMC-2-6	1	WLC-3-7	2
CFB-8-1	1	CSC-2-7	1	SBA-2-10	14	URMC-2-1	220	WSA-1-7	11
CFC-12-10	1	CSC-2-9	4	SBA-2-9	2	URMC-2-7	105	WSA-2-7	93
CFC-12-7	1	CSC-4-2	3	SBA-4-9	5	URMC-2-10	60	WSA-3-7	209
CFC-2-1	7	CSC-4-7	2	SBB-2-1	1	URMC-2-2	1	WSB-1-1	1
CFC-2-10	4	CSC-6-1	1	SBB-2-10	9	URMC-2-9	64	WSB-1-10	8
CFC-2-7	29	CSC-6-7	1	SBB-2-9	7	URMC-4-7	139	WSB-1-7	1
CFC-2-9	2	CSC-8-1	1	SBC-2-1	8	URMC-4-10	15	WSB-1-9	60
CFC-4-1	3	CSC-8-7	3	SBC-2-10	51	URMC-4-2	4	WSB-2-7	3
CFC-4-7	1	RMA-2-1	1	SBC-2-9	8	URMC-4-1	2	WSC-1-9	172
CFC-6-1	1	RMA-2-7	3	SBC-4-1	40	URMC-4-9	6	WSC-1-10	25
CFC-6-7	2	RMA-2-9	2	SBC-4-10	6	URMC-6-1	11	WSC-1-1	1
CFC-8-7	1	RMA-4-1	10	SBC-4-9	4	URMC-6-10	1	WSC-1-7	4671
CSA-12-5	1	RMB-2-1	1	SFA-2-5	1	WLA-2-7	2	WSC-2-1	5
CSA-2-9	1	RMB-2-9	2	SFA-4-5	1	WLB-2-1	3	WSC-2-9	1
CSB-20-1	1	RMB-4-1	11	SFB-2-1	1	WLB-2-7	4	WSC-2-7	2156
CSC-12-7	2	RMC-2-1	1	SFB-2-7	1	WLC-2-1	4	WSC-3-7	1

There are three hospitals that are 2, 4 and 12 stories high (SFA-2-5, SFA-4-5 and CSA-12-5, respectively). The total number of beds in the hospitals before the earthquake is taken as 140, 223, and 326 for SFA-2-5, SFA-4-5, and CSA-12-5, respectively, based on data for hospitals located in Tennessee from the American Hospital Directory (AHD 2018). The total number of construction workers available in the community before the earthquake is taken as 1400, which is approximately 3.5% of the community's population representing the same percentage of construction workers in the U.S. population as per data from the Bureau of Labor Statistics (BLS 2018). The buildings are prioritized as mentioned previously and the buildings with the same priority are repaired starting from the Midtown area (North side of the community).

Moment resisting and braced frame steel structures are assumed to be the same as the archetype buildings designed in NIST (2010). The seismic demands on the moment resisting frame buildings are assumed to be resisted by the three-bay special moment frames (SMFs) on the buildings' perimeter. The behavior of the moment resisting frame buildings is modeled using 2D concentrated plasticity beam-column elements in OpenSees (McKenna et al. 2000). The modified Ibarra-Medina-Krawinkler deterioration model (Ibarra et al. 2005) is used to represent the strength and stiffness deterioration properties due to cyclic loading where the material model parameters are quantified using the experimental database of Lignos and Krawinkler (2012).

The seismic demands on the braced frame buildings are assumed to be resisted by one-bay special concentrically braced frames (SCBF) located on the buildings' perimeter. The behavior of the SCBFs is modeled using 2D concentrated plasticity models (McKenna et al. 2000) in OpenSees. Due to its modular nature, the proposed simulation model supports the use of detailed structural models of all of the buildings in the inventory. However, for the sake of simplicity and to showcase the ability of the proposed simulation model to accommodate different modeling

methods of the buildings in the community, the other types of buildings are represented using the fragility curves provided in HAZUS (FEMA 2003). The Normative Quantity Estimation Tool provided in volume 3 of FEMA P-58 (FEMA 2012b) is used to evaluate the non-structural component quantities and distributions in the buildings. This tool provides an estimate of the quantities of the components likely to be in a building with a specific occupancy on a gross square foot basis.

4.6.2 Seismic Hazard

The seismic event is the first horizontal component of the ground motion record RSN 1961 (PEER 2018), which was recorded at the Lepanto station near the studied community. The epicenter is located at 35°18'N, 90°18'W and the peak ground acceleration (PGA) is scaled at each building location to meet the PGA for a M_w 7.7 earthquake scenario specified by the United States Geological Survey (USGS 2018) for the studied region. The spatial distribution of the PGA at the buildings location in the studied community is shown in Figure 4-10. The earthquake event is assumed to occur on a weekday at 8:00 PM. For the sake of simplicity, vertical propagation of the ground motion is not considered in the demonstrated case study.
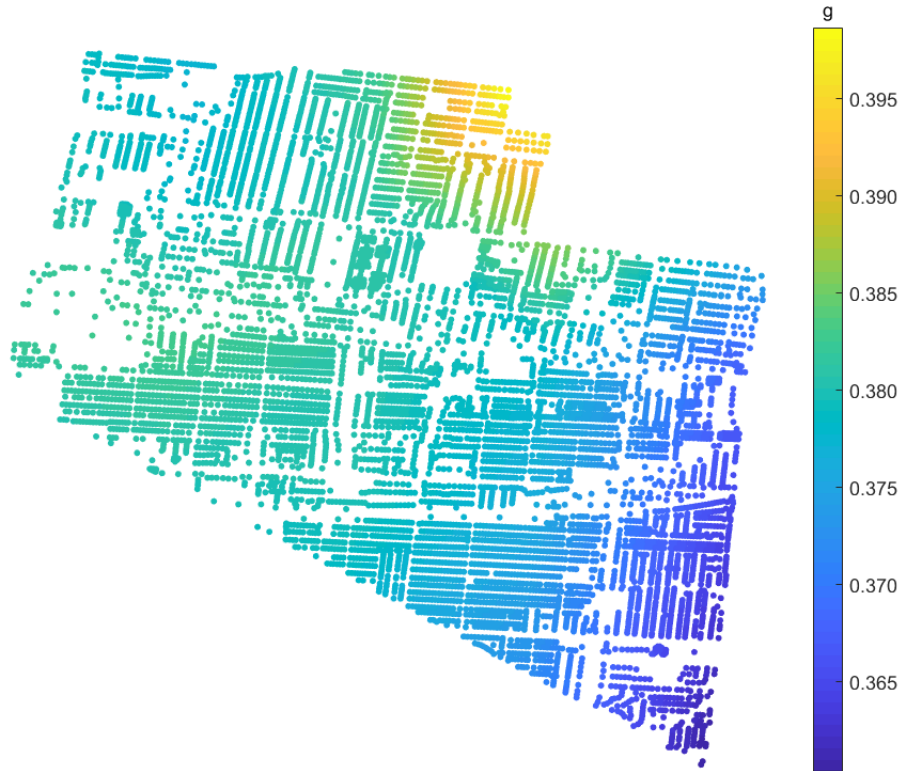
Figure 4-10 Spatial distribution of the PGA at the buildings location in the studied community

4.6.3 Results and Discussion

To account for the many uncertainties inherent in the factors affecting the different types of losses after a seismic event, the FEMA P-58 methodology (FEMA 2012a) and thus the proposed model uses a Monte Carlo procedure to perform loss calculations. The proposed simulation model is computationally demanding and was therefore implemented and run within a parallel computing environment. The computational time for running 100 Monte Carlo simulations for the presented case study is around 10 hours on a personal computer with four cores and 32 GB RAM. The number of Monte Carlo simulations is selected based on a sensitivity study where the number of simulations is progressively increased until convergence occurs (after 150 simulations). Convergence is deemed to occur when changes in the range, mean and standard deviation of the

recovery time (T_{RE}) and resilience index ($\%R$) do not exceed 10%. The sampling is performed based on the distribution properties of each component specified in the FEMA P-58 methodology (FEMA 2012a). Figure 4-11 shows the evolution of trapped and free individuals with injuries during the earthquake for an arbitrary Monte Carlo simulation in two areas of the studied community, namely Midtown and Central Gardens (see Figure 4-9). No injuries occurred in either areas during the first few seconds. However, by 30 seconds into the simulation, around 150 people were trapped and had injuries in Midtown. By 60 seconds, the number increased to 1100. Dynamic analysis implemented in the proposed simulation model provides step-by-step information about injuries, which can help rescue and medical teams better plan their first response efforts during simulation exercises. For longer duration events (such as hurricanes), where actual models are being used during the event itself, data of this sort can be used to optimize first response operations emphasizing the importance of dynamic analysis.
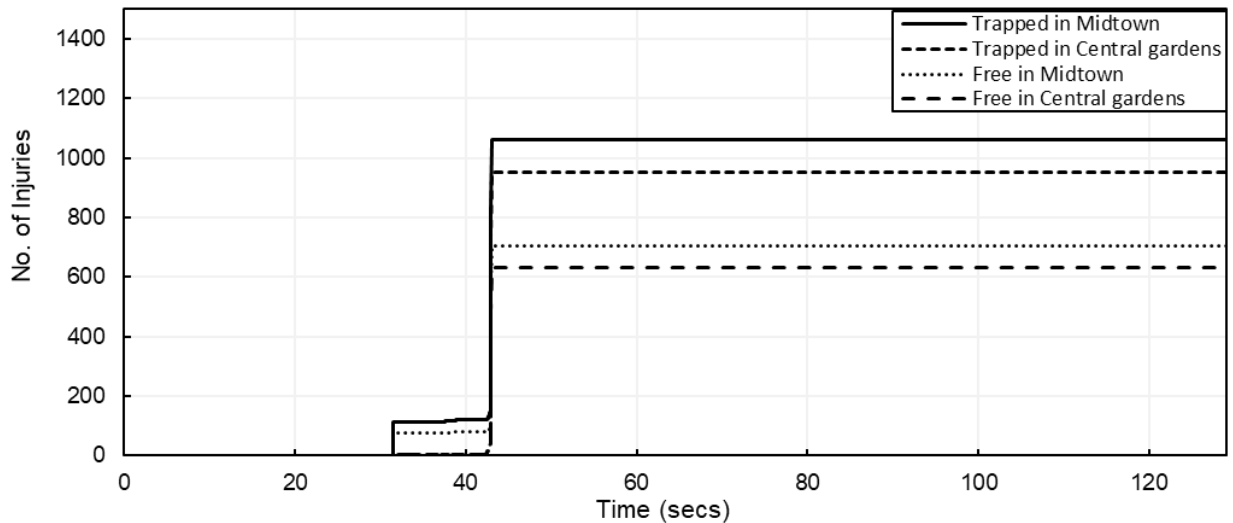
Figure 4-11 Evolution of trapped and free injuries during the earthquake for an arbitrary Monte Carlo simulation in two areas of the studied community

Most of the buildings fall into the none to moderate damage states (75.6%), which indicates that the studied community is performing relatively well under the seismic event. About 9.5% of the buildings suffer from complete collapse. Table 4-3 lists the mean percentage of collapsed buildings with respect to building material, design code and building occupancy. Most of the collapsed buildings are wood buildings (67.1%), which represent the majority of the buildings in the studied community. No steel buildings collapsed during the studied earthquake, while 3.2% of the collapsed buildings are reinforced concrete buildings. Almost all of the collapsed buildings are those designed according to old codes (pre-1973 buildings) emphasizing the relatively high vulnerability of older, unretrofitted buildings in modern communities. Most of the collapsed buildings are residential buildings, which represent the majority of the building inventory.

Table 4-3 Distribution of building collapse and casualties with respect to building characteristics in the studied community

	Building Characteristics	Collapsed buildings (%)	Casualties (%)
Building Material	Reinforced concrete	26 (3.2)	715 (19.1)
	Reinforced Masonry	3 (0.4)	22 (0.6)
	Unreinforced Masonry	239 (29.3)	655 (17.5)
	Wood	546 (67.1)	2352 (62.8)
Design Code	New (code A)	2 (0.2)	11 (0.3)
	Moderate (code B)	9 (1.1)	82 (2.2)
	Old (code C)	803 (98.7)	3651 (97.5)
Building Occupancy	Commercial	56 (6.9)	15 (0.4)
	Residential	670 (82.4)	3426 (91.5)
	Retail	61 (7.5)	300 (8.0)
	Warehouse	27 (3.2)	3 (0.1)

The majority of the casualties associated with earthquakes result from the collapse of buildings. As reported by Nobuhara et al. (2000), about 90% of the casualties that resulted from the 1995 Kobe earthquake were due to collapsed buildings. This observation is in accord with the results of the proposed model, where 93% of the casualties in the studied community occur in collapsed buildings while the other 7% are caused by falling components inside the non-collapsed buildings. Another observation from Table 4-3 is that the percentage of casualties in reinforced concrete buildings is relatively high compared to that in wood buildings. Approximately 98% of the casualties occur in buildings designed according to old codes (pre-1973 buildings) again emphasizing the higher vulnerability of older, unretrofitted buildings in modern communities. As noted earlier, the earthquake event is assumed to occur on a weekday at 8:00 PM, which implies that most of the population is in residential buildings rather than other types of buildings. Consequently, most of the casualties (91.5%) are located in residential buildings.

Figure 4-12 shows the spatial distribution of the physical functionality of the buildings during the recovery stage immediately after the earthquake and at three different points in time for one arbitrary Monte Carlo simulation. A significant number of buildings regain their functionality in the first 60 weeks (~ 1.2 years) after the earthquake. This relatively rapid recovery in functionality is attributed to the fact that buildings with high repair priority and lower damage states have relatively low delay time. However, after the first 60 weeks, repair of the buildings with lower priority and higher damage states (thus requiring longer repair times) starts, contributing to the plateau in the recovery trajectory shown in Figure 4-13. The mean restoration period of full physical functionality for the studied community, T_{RE}, is approximately 240 weeks (~ 4.6 years). The "recovery clouds" in Figure 4-13 show the range of possible recovery

trajectories taking into consideration the inherent uncertainties in the proposed methodology. In order to improve the recovery of the studied community in response to earthquakes, several mitigation actions are considered and evaluated as discussed later.
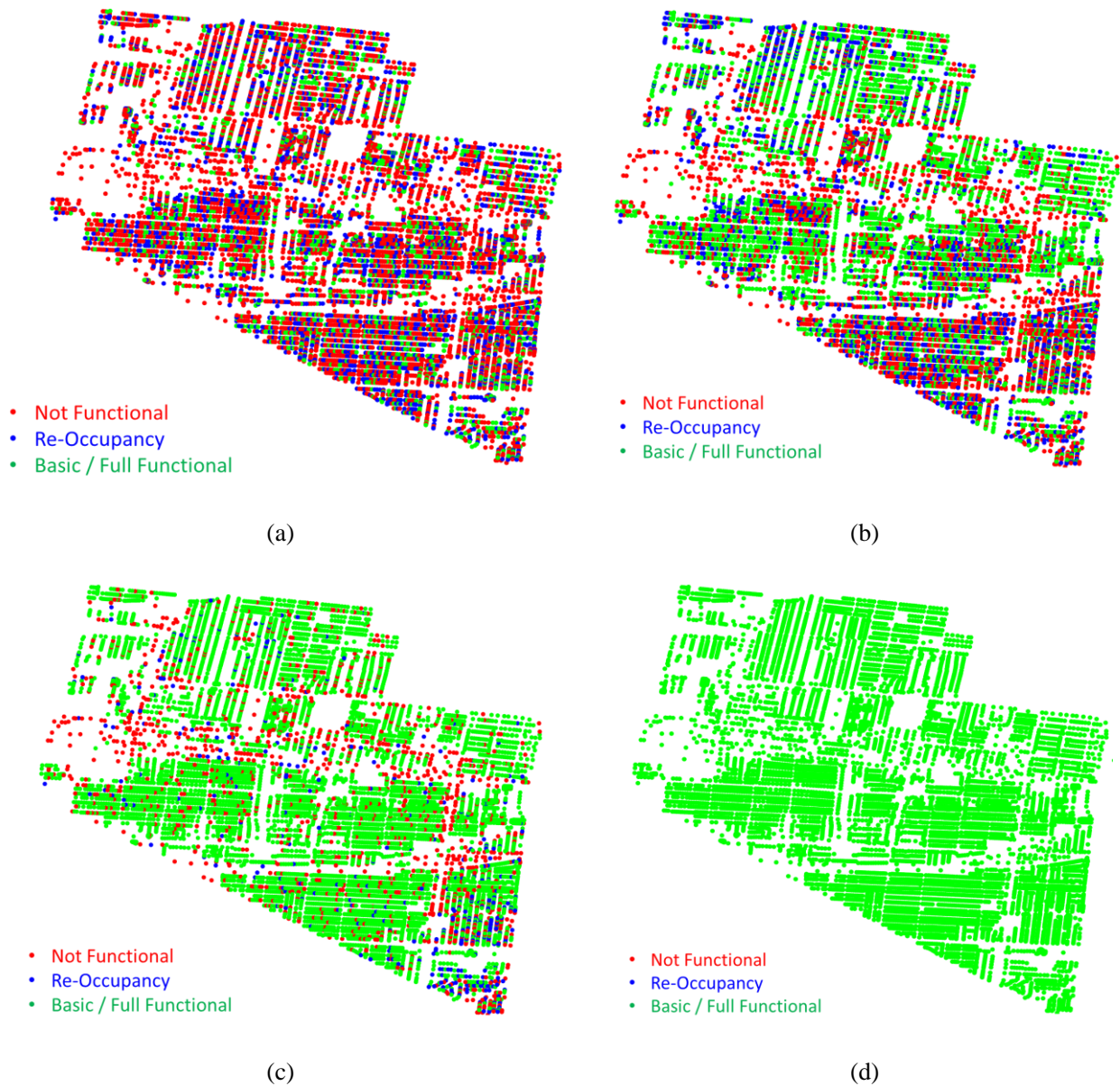
Figure 4-12 Spatial distribution of the functionality of the buildings in the studied community for one arbitrary Monte Carlo simulation: (a) Immediately after the earthquake; (b) after 30 weeks; (c) after 60 weeks; and (d) after 240 weeks
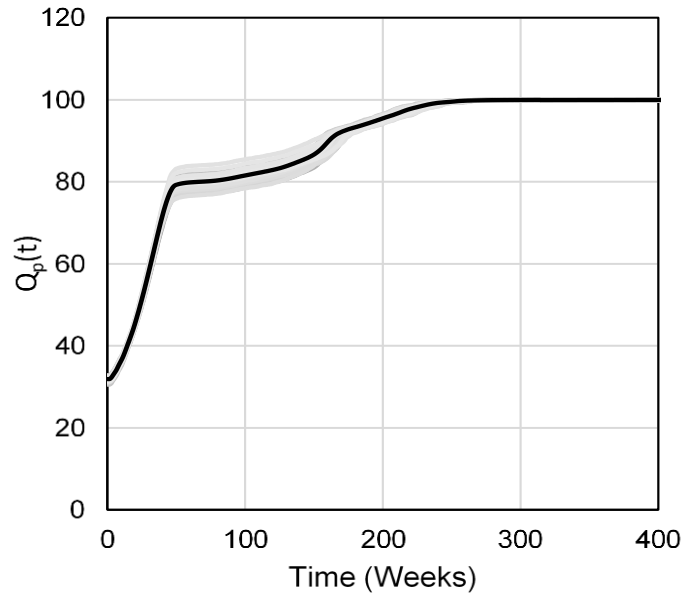
Figure 4-13 Physical recovery trajectories for conducted Monte Carlo simulations and the mean recovery trajectory for the studied community (the gray area represents the recovery clouds)

A key design feature of the proposed simulation model is that it operates in a plug and play sense to facilitate studying the effects of interdependencies between the different systems of the community. To showcase this important capability, Figure 4-14 plots the mean total recovery trajectory of the community without considering the interdependency between physical recovery and available number of workers in the community. This simulation is achieved by simply unplugging the available resources simulator from the model (no interdependency) compared to the normal case where all the interdependencies are considered (interdependency). Considering the interdependency between the physical recovery and available number of workers in the community delays the recovery of the community and shifts the recovery trajectory to the right, which reduces the resilience index of the community from 90% to 81% (10% reduction). This reduction in community resilience index is demonstrated by the shaded area under the recovery trajectory shown in Figure 4-14. It should be noted that it is required to have a fixed time frame in

181

equation (4-8) to be able to use the computed community resilience index (%R) as a metric to compare resilience for different cases. Thus, T_{RE} used in equation (4-8) is the maximum recovery time between the two compared trajectories (i.e., 240 weeks). Also, the mean restoration period of full functionality for the community, T_{RE}, decreased from 240 weeks (~ 4.6 years) when considering the interdependency to only 150 weeks (~ 2.9 years) when neglecting the interdependency, which is a substantial difference in recovery time (~ 38%).
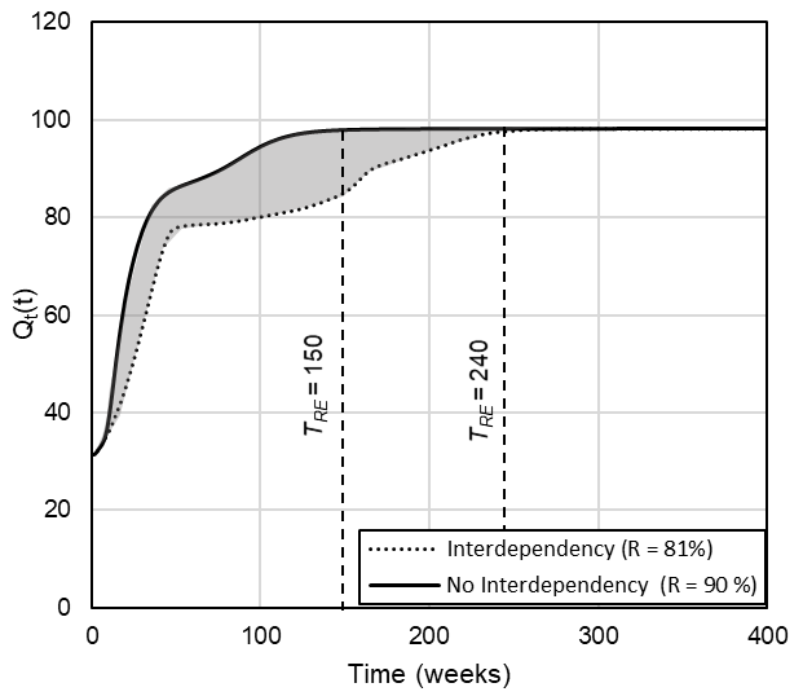
Figure 4-14. Effect of the interdependency between physical recovery and availability of resources in the community during the recovery stage

4.6.4 Effectiveness of Hazard Mitigation Plans

To further demonstrate the capability of the proposed simulation model to support hazard mitigation planning, a sensitivity study is performed to look at the effect of pre-hazard and post-

hazard mitigation actions on the response of the studied community to earthquakes. Pre-hazard mitigation actions are defined as those taken before an extreme event to mitigate the effect of the hazard. Post-hazard mitigation actions are those taken at certain times during the recovery process to provide a better recovery trajectory. Accordingly, three mitigation actions are considered in this study and applied to the studied community through the proposed model. The selected actions are representative of a multitude of actions that could be taken and are designed to showcase the capability of the developed simulation model.

- Action A: a pre-hazard mitigation action through a community-wide residential building retrofit plan that entails upgrading the seismic resistance of all residential buildings that were built according to design codes prior to 1973 (code C buildings) to a current design level (code A buildings).

- Action B: a post-hazard mitigation action that entails increasing the number of workers to 3000 (i.e., requesting more workers from a nearby state) starting 2 months after the earthquake (60 days).

- Action C: both actions A and B.

Figure 4-15(a) shows the mean number of buildings in different damage states under normal conditions and after applying action A. It is clear that upgrading the seismic design of residential buildings reduces the mean number of collapsed buildings from 814 to 298 collapsed buildings (64% reduction). The mean number of buildings in the none to moderate damage states increases from 6473 to 7921 buildings (22% increase). The mean number of collapse-related casualties drops significantly from 3700 to 1500 (a 59% reduction) as shown in Figure 4-15(b). Clearly action A is quite effective in reducing earthquake losses.

Figure 4-16(a) plots the mean total recovery trajectory of the studied community before and after applying the mitigation actions. Considering action, A, the initial total functionality of the community immediately after the earthquake increases significantly from 31% to 50%. The mean restoration period to maximum total functionality, T_{RE}, decreases from 240 weeks (~ 4.6 years) to 160 weeks (~ 3.0 years). Applying action B does not affect the initial total functionality of the community immediately after the earthquake. However, the mean restoration period to maximum total functionality, T_{RE}, decreases from 240 weeks (~ 4.6 years) to 170 weeks (~ 3.2 years). Action C leads to both an increase in the initial total functionality and decrease in the mean restoration period to maximum total functionality for the studied community, T_{RE}, from 240 weeks (~ 4.6 years) to 120 weeks (~ 2.3 years), which is the best among all the considered mitigation actions.

Figure 4-16(b) shows the resilience index (%R) for different cases of the studied community. The recovery time, T_{RE}, used in equation 4-8 to evaluate %R is the maximum recovery time between the compared trajectories as discussed earlier (i.e., 240 weeks). As shown, applying the pre- and post-hazard mitigation actions improves the resilience of the studied community. For action A, %R increased from 81% to 92%, which is a 13% improvement in community resilience. For action B, %R increased from 81% to 89%, which is a 9% improvement in community resilience. For action C, %R increased from 81% to 94%, which is a 16% improvement in community resilience.
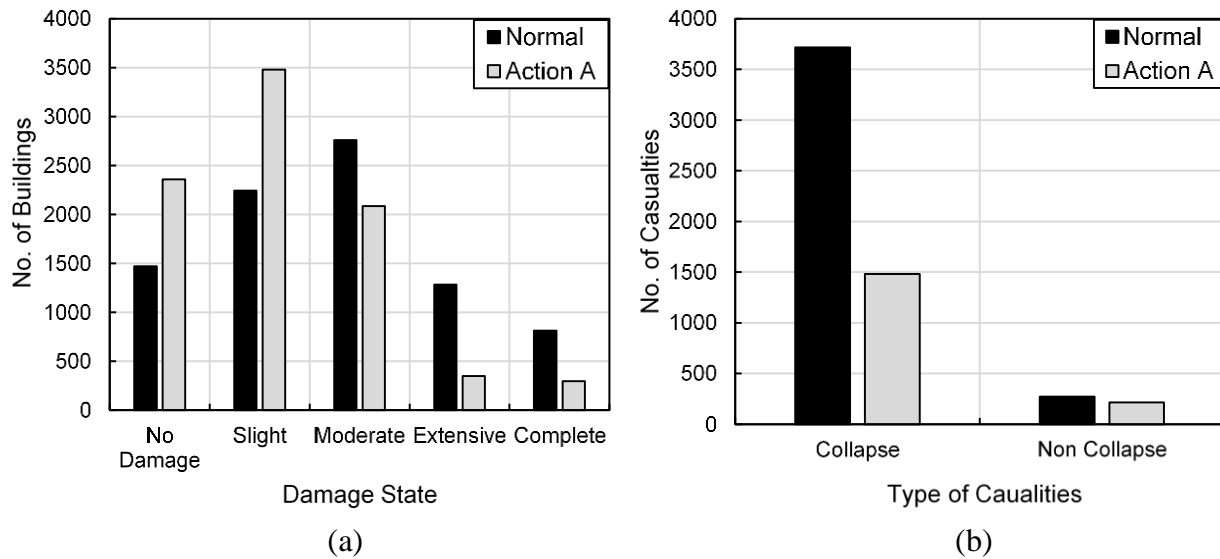
Figure 4-15 Effect of mitigation action A on: (a) the mean number of buildings in different damage states; and (b) the mean number of casualties resulting from collapsed and non-collapsed buildings
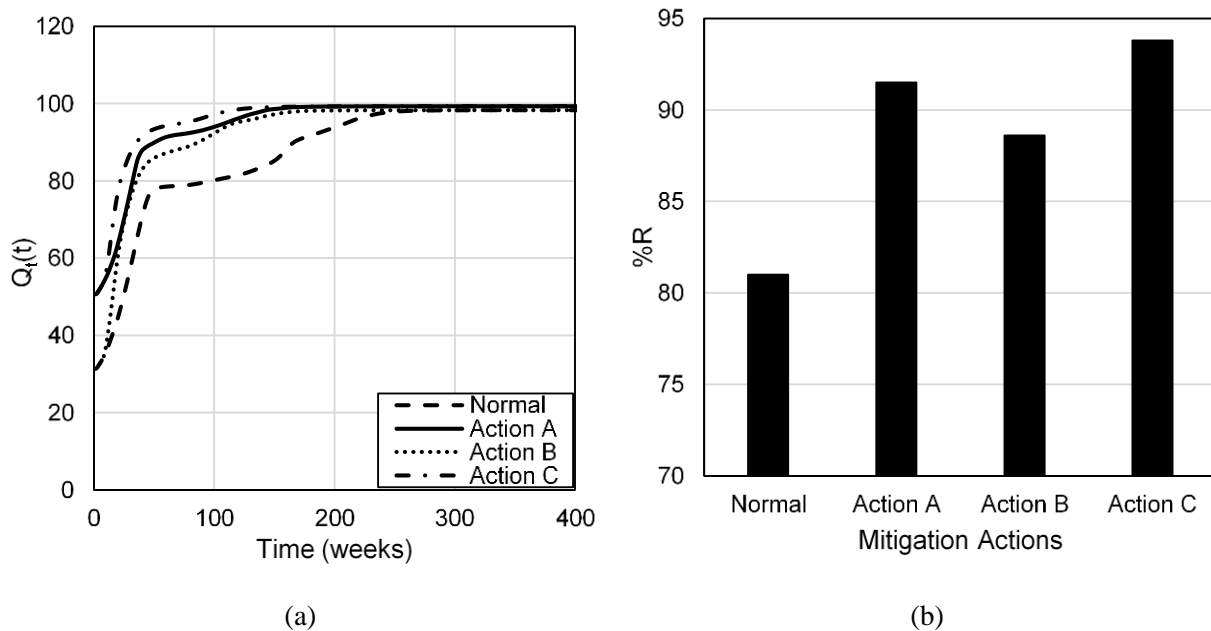
Figure 4-16 Effect of the proposed mitigation actions on: (a) The recovery trajectory of the studied community; and (b) Resilience index (%*R*) of the studied community

Choosing the appropriate mitigation strategy depends on many factors, which are community specific beyond just the resilience index (%*R*). One of these factors is the initial

185

investment required for each plan (e.g., the cost of upgrading the design of current buildings versus repairing them after a seismic event). Another factor is the social aspect of the problem. For example, action B provides a comparable enhancement to action A in regard to the resilience index (%R) of the community. However, it produces more casualties than action A, which may motivate decision makers to choose action A or action C.

4.7   Simulation Model Limitations

Although the proposed simulation model combines the physical aspect of community resilience (related to the buildings) with the social aspect (related to the injuries/fatalities), there are other critical dimensions of community resilience that have not been accounted for in this chapter but will be considered in later chapters. For example, bridge and transportation network damage can affect traffic flow and, therefore, access to healthcare facilities. Also, the social vulnerability is expressed in terms of injuries and fatalities only. However, there are other short and long term social vulnerability indicators that affect the resilience of communities (e.g., household relocation) that are out of scope of the current chapter. These aspects of community resilience will be accounted for in the next chapters through the addition of relevant simulators. Furthermore, the presented results and mitigation strategies are based on the assumptions discussed earlier related to the building portfolio, components and ground motion scenario. Clearly, the results (i.e., building collapse, injuries and recovery outcomes) will change when using different points for fault rupture or a different city. However, the proposed model allows for the ability to evaluate multiple scenarios and strategies providing the necessary data to make informed decisions as will be shown in later chapters.

4.8   Summary and Conclusions

This chapter proposed a simulation-based model for the assessment and quantification of seismic resilience of communities. The proposed model is modularized into independent simulators, each representing an aspects of the overall problem. The system is designed to step through time as the seismic event occurs (time step in seconds) and as the community recovers after the event (time step in days). Due to its modularized nature, the proposed simulation model can combine two different aspects of community recovery to quantify the seismic resilience of communities: physical and social recovery.

The proposed model is demonstrated through a case study in which a part of Shelby County, Tennessee, is subjected to a M_w 7.7 earthquake located northwest of Memphis. In order to demonstrate the capability of the proposed simulation model in supporting hazard mitigation planning, a study is performed to look at the effect of different mitigation strategies on community resilience. Three different mitigation actions are studied and applied through the proposed model. The results of the case study show that upgrading the seismic resistance of residential buildings to current codes improved the seismic resilience of the studied community by 10%, while increasing the number of workers from 1,400 to 3,000 during the recovery stage improved the seismic resilience of the studied community by 7.5%.

The proposed simulation model has a number of key advantages that make it well suited for community resilience computations. First, it provides fine granularity by allowing for separate treatment of each building in the community. Building seismic performance is used to calculate economic and social losses, both of which are handled in an integrated manner within the model. Second, due to its modularized nature, the proposed model is scalable and adaptable. It is designed to operate within a plug and play environment and, as such, facilitates the improvement/substitution of any discipline-specific simulator without affecting the other

simulators. Third, the ability to conduct in-event simulation (by explicitly stepping through time) allows for full consideration of the interdependencies that arise between the different systems of society. For instance, without in-event simulation, it is not possible to consider the effect of the physical recovery of the hospitals on social recovery as pertains to injuries. Also, increasing the number of workers at a certain time during the recovery stage is straightforward using the current configuration. The proposed simulation model is a key step forward towards quantifying the seismic resilience of communities based on detailed loss estimation models as well as recovery models that consider the effect of multiple interdependencies between different systems of the community as will be shown in next chapters.

CHAPTER 5

Modeling Interdependencies Between the Building Portfolio, Transportation Network, and Healthcare System in Community Resilience

5.1 General

This chapter employs the scalable simulation model described in Chapter 4 to model the mutual interdependencies between the building portfolio, transportation network, and healthcare system in a community. The transportation network model accounts for the capacity reduction attributed to bridge damage and links blocked by debris from collapsed buildings. It also addresses the increased demand from ambulance trips ferrying injured people to healthcare facilities and trucks hauling away debris. The transportation network model is incorporated into a discrete event simulation environment that models the response of the healthcare system as well as the debris removal process in the aftermath of a seismic event. Measures are proposed to quantify and improve the seismic resilience of each individual system as well as the whole community considering the three systems' mutual interdependencies. The capability of the proposed model to support hazard mitigation planning is demonstrated through a case study that highlights the effects of interdependencies between the three systems under consideration. Mitigation strategies to improve seismic resilience of a prototype community are proposed and assessed.

5.2 Background

Severe earthquakes generate complex interactions between the building portfolio, transportation network and healthcare system of a community. The interdependencies between the three systems profoundly influence first response activities and extend into the long-term recovery effort. Building collapse produces debris piles that may block or reduce the capacity of adjacent roadways, thereby impairing the capacity of the transportation network. The transportation network's capacity may be further compromised by seismic damage to the bridges within the network. The healthcare system, which itself may see damage to its buildings during a seismic event and hence has a reduced capacity, contributes traffic to the impaired transportation network in the form of ambulance trips. Post-earthquake casualties in the community affect the availability of the workforce (i.e., construction labor) in the community, which in turn affects the recovery of the building portfolio. The effort to haul away debris piles places additional demands on the transportation network, which at the same time, is called upon to also handle day-to-day traffic as the community strives to recover from the disruption. These complex interactions are shown in Figure 5-1.

Previous studies have focused on the behavior of one of these infrastructure systems. For example, Lin and Wang (2017) and Burton et al. (2017) studied the response of the building portfolio. Kirsch et al. (2010), Mitrani-Reiser et al. (2012), and Hassan and Mahmoud (2020) focused on the response of the healthcare system, while Vishnu et al. (2018), Zhang et al. (2019) and Feng et al. (2020) analyzed the transportation network.

Moving away from a focus on a single system, some studies have investigated the effect of the seismic debris field generated by damaged structures on the transportation network, e.g., Hirokawa and Osaragi (2016), Castro et al. (2019), and Feng et al. (2020). These studies used empirical approaches for modeling the debris field. A more rational approach for modeling the

debris field can be found in Domaneschi et al. (2019) and in Chapter 3 where a computational technique, the Applied Element Method (AEM), is used to model building collapse and the extent of the debris piles. However, Domaneschi et al. (2019) and Chapter 3 did not explicitly consider the interdependency between the building system and transportation network.
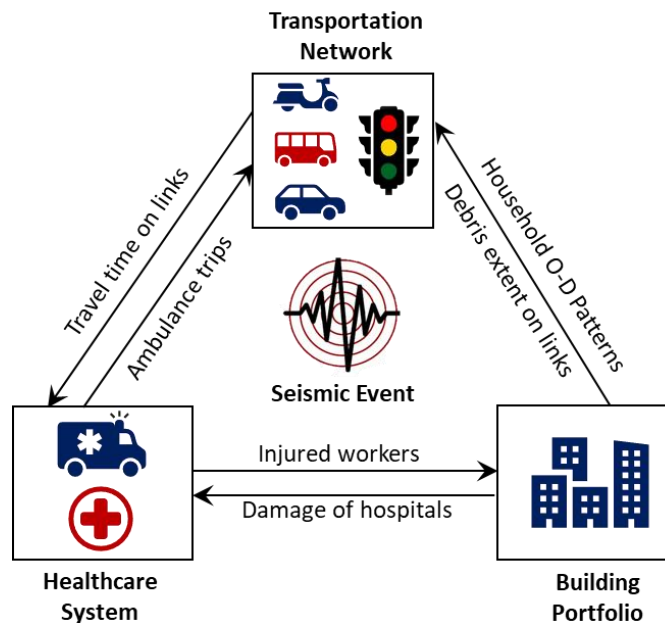
Figure 5-1 Interdependencies between community sectors

Buildings that collapse or are damaged during seismic events are no longer able to provide their intended service. In chapter 4, the damage of the components of the buildings were mapped to their post-earthquake functionality. A reduced post-earthquake functionality of buildings affects the origin-destination (O-D) travel patterns since community residents who use those buildings as homes or for work will not travel to or from these locations. Shiraki et al. (2007) related the O-D reduction rates to the seismic intensity of the event. However, use of a constant reduction rate is not realistic because the level of building damage, and hence functionality loss, can greatly vary across the community.

The effect of post-earthquake traffic (i.e., travel time) on the transportation network controls the number of ambulance trips that can be made. Fawcett and Oliveira (2000) proposed a regional simulation model for casualty treatment after earthquake disasters. In their model, they used the pre-earthquake travel times between all pairs of zones in the community to estimate the number of injuries that can be mobilized in each time interval. However, travel times can be impacted by the state of the transportation network. Ceferino et al. (2020) proposed a methodology to evaluate emergency response of the healthcare system based on a model that assesses the loss of hospital functionality and quantifies multi-severity injuries (i.e., injuries with different levels of severity) as a result of earthquake damage. However, their model did not consider the effect of the transportation network on the healthcare system.

Unlike the Fawcett and Oliveira (2000) and Ceferino et al. (2020) studies, Cimellaro et al. (2013) used agent-based models to evaluate the functionality and resilience of healthcare facilities after seismic events taking into account the functionality of the roadway system. While the Cimellaro et al. (2013) study went farther than others by considering the condition of the roadway system on the healthcare system, it did not consider the opposite effect, i.e., the effect of the healthcare system on the transportation network. The trips made by ambulances in the first few days after the earthquake between the locations of the injured and the hospitals in the community affects the travel time and flow on the links of the transportation network.

5.3   Motivation

Based on the studies surveyed above, there are key limitations in the available models for assessing community resilience especially when dealing with mutual interdependencies between different infrastructure systems. Given these limitations and the dearth of research results, this

192

chapter employs the simulation model presented in Chapter 4 to model the mutual interdependencies outlined in Figure 5-1 between the building portfolio, transportation network, and healthcare system in a community.

The proposed model simulates the capacity of the transportation network as a function of the combined effect of bridge damage and the accumulation of debris resulting from the collapse of buildings. The transportation network model is then incorporated into a discrete event simulation environment that accounts for the response of the healthcare system as well as the debris removal process to model the aftermath of a seismic event. The capability of the proposed model to support hazard mitigation planning is demonstrated through a case study that highlights the mutual interdependencies between the three studied systems.

5.4   Simulation Model Overview

Figure 5-2 shows an overview of the proposed simulation model. The modular design implemented in Chapter 4 is used to connect the models (termed simulators) representing different aspects of the community. As shown in Figure 5-2, each of the simulated systems (i.e., building portfolio, transportation network, and healthcare system) is represented by a set of simulators. The ability to account for the interdependencies between the different systems is achieved through the connection between the individual simulators. The simulators are connected through the same two types of connections described in Chapter 4: sequential and interdependent as shown in Figure 5-2.

Similar to the simulation model in Chapter 4, the proposed model runs in four stages, each with a different time scale. The model starts with the pre-earthquake stage where the community setup is loaded and broadcast to all the simulators in the simulation model through the *city* simulator. The pre-earthquake behavior of the transportation network is evaluated in the *pre-*

earthquake traffic simulator. The second stage is during the earthquake, where the time step is taken in seconds After the earthquake, there is a transition stage where the *bridge* and *building downtime* simulators are executed in a single step to evaluate seismic losses. The final stage is the recovery stage, where the time step is taken in days in all the simulators except for the *healthcare* and *post-earthquake traffic* simulators. The *healthcare* simulator described earlier in Chapter 4 is refined to take the time step in hours (i.e., 2 hours for each time step) to rigorously simulate the emergency response of the healthcare system in the community after the earthquake, as will be discussed later. For the *post-earthquake traffic* simulator, the time step is taken as 10 days after the first 30 days as discussed later. During the recovery stage, the recovery trajectory of the different systems in the community is evaluated with explicit modeling of the interdependencies between them.

More details about the implementation of the *city*, *ground motion*, *structural analysis*, *building damage*, *component damage*, *casualties*, *buildings downtime*, *building recovery*, and *available resources* simulators can be found in Chapter 4. The implementation of the *pre-earthquake traffic*, *debris*, *bridge damage*, *bridge downtime*, *bridge recovery*, *healthcare*, *debris removal*, *post-earthquake traffic*, and *network recovery* simulators is discussed later on in this chapter.
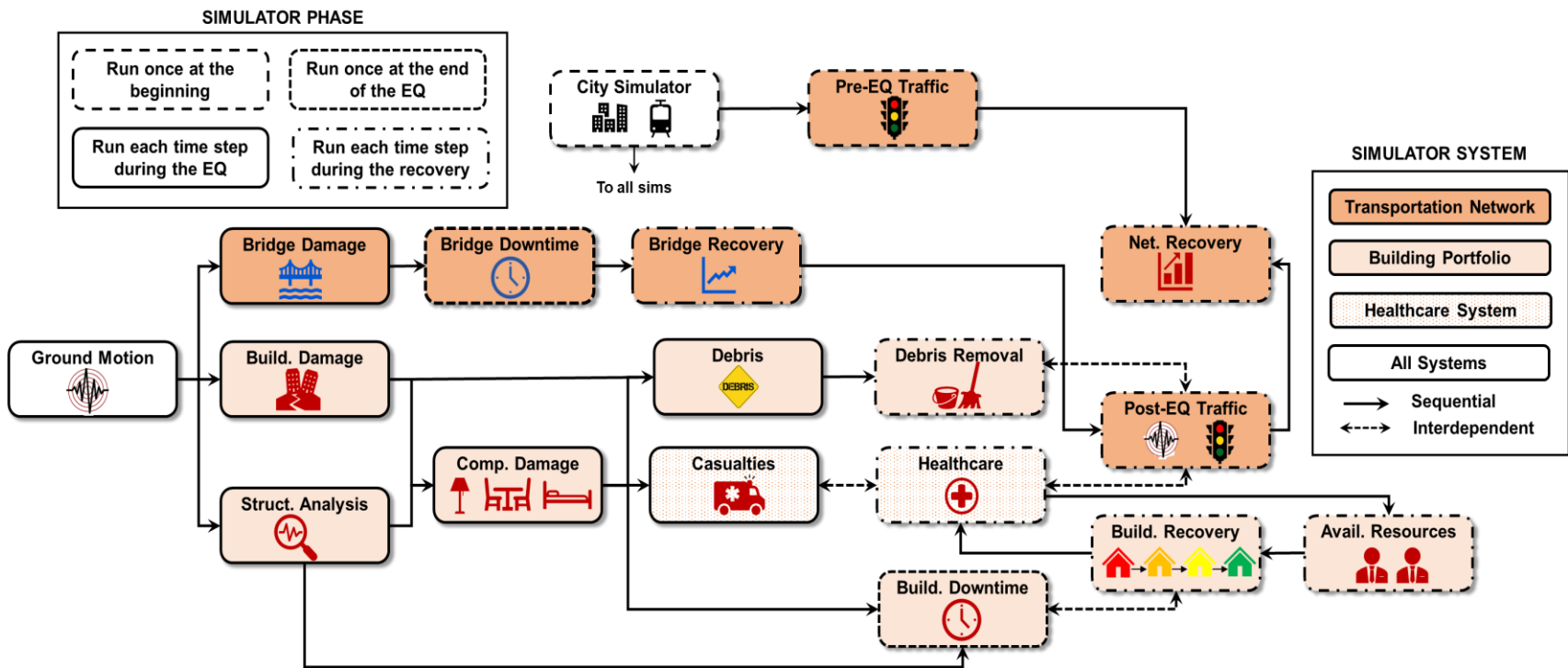
Figure 5-2 Simulation model overview

5.5   Methodology

5.5.1 Pre-Earthquake Traffic Simulation

As shown in Figure 5-2, the *pre-earthquake traffic* simulator receives information about the transportation network in the community under consideration from the *city* simulator. Transportation networks usually are comprised of two main components: roads and bridges. These networks are often represented mathematically using graph theory (Biggs et al. 1986). In graph theory, a network is represented by vertices (called nodes) connected together using edges (called links). In transportation networks, the nodes represent the intersection between the roads whereas the links are the roadways between these nodes. The level of detail included in the modeled transportation network (i.e., links represent only highways or every road in the region) depends on the available computational resources and the purpose of the simulation. Information about the transportation networks in the U.S. and around the world (i.e., node locations, links connecting nodes, capacity and maximum speed on roads, etc.) is publicly available in many open-source platforms (e.g., OpenStreetMap, OSM).

The normal pre-earthquake traffic conditions of the transportation network (i.e., travel time, flow on links, and route choice of each vehicle) are evaluated in the *pre-earthquake traffic* simulator using a four-step model, which has been developed and widely used since the 1950s (see Weiner 1997). The four steps are: trip generation, trip distribution, mode choice, and route assignment. Before applying the four-step model, the studied community is divided into smaller traffic analysis zones (TAZ). TAZs are geographic areas with relatively similar land use and activity. They represent the origins and destinations of travel activity within the studied community. Trip generation is performed to predict the trip productions and attractions between

196

the different TAZs for different purposes (i.e., home-based, work-based, etc.). A cross-classification model is adopted in the present study because it is based on data from real cities (e.g., the travel demand model used by Memphis Urban Area Metropolitan Planning Organization [MPO]).

Trip distribution is performed to distribute the predicted production and attractions between the different TAZs as origin-destination (O-D) pairs. A widely used gravity model (Isard 1956), based on Newton's Theory of Gravity, is adopted to perform this step. Mode choice is performed to distribute the O-D pairs between the different modes of transportation available in the city (i.e., vehicles, bus, bike, etc.). A trip end model is adopted to perform this step in the current study based on data from real cities. The final step in the four-step model is route assignment, which uses the O-D pairs developed by the mode choice step to assign the routes for each O-D pair based on the state of the transportation network (i.e., capacity and maximum speed of the links in the network). The most widely used method to perform this step is the static user equilibrium (UE) model proposed by Evans (1976), which is used herein. In this methodology, the transportation network is assumed to reach equilibrium when the cost of travel (i.e., travel time) on any route for any traveler in the O-D pair cannot be improved by choosing another route (Wardrop 1952).

5.5.2 Debris Generation

The *debris* simulator receives the damage state of each structural and nonstructural component in the building from the *building* and *component damage* simulators to characterize the seismic debris field in the community. As outlined in Chapter 3, the seismic debris is characterized by two attributes: quantity and extent. The debris quantity is the amount of debris generated in tons, whereas the debris extent is the size of the footprint of the debris field around

the damaged building. In the current study, the debris quantity is estimated using the methodology described in HAZUS (FEMA 2003).

The extent of debris generated from the collapse of each building in the community is evaluated based on its type (i.e., RC, steel, ...etc.) using different approaches as summarized in Figure 5-3. For RC frame buildings, the approach developed in Chapter 3 is adopted. For masonry buildings, the approach developed by Domaneschi et al. (2019) is adopted. In this approach, the area of the seismic debris field is assumed to be larger than the original building area by an amplification factor, ε, as shown in Figure 5-3(b). The amplification factor is evaluated as:

$$\varepsilon = 1.228 + 0.0787\left(\frac{L}{W}\right) + 0.0563\left(\frac{A_f h_b^2}{V_b L}\right) \tag{5-1}$$

where L and W are the building length and width, respectively, A_f is the footprint area of the building, h_b is the building height, and V_b is the total masonry volume of the building.

For other types of buildings in the community, the debris around the collapsed building is assumed to form a triangular prism with the long side adjacent to the collapsed building as shown in Figure 5-3(c) (Argyroudis et al. 2015). Per Argyroudis et al. (2015), the width of debris outside the building envelope (W_d) is evaluated as:

$$W_d = \sqrt{W^2 + \frac{2k_v WH}{\tan\theta}} - W \tag{5-2}$$

where W is building width perpendicular to the road's axis, k_v is the proportion of the volume of debris with respect to the original volume, and θ is the angle of collapse. k_v and θ are assumed to be statistically independent random variables with normal distribution, where: $\mu_{kv} = 0.5$, $\sigma_{kv} = 0.15$, $\mu_\theta = 45°$, and $\sigma_\theta = 13.5°$ (Argyroudis et al. 2015). For all buildings, the percentage of roadway blockage adjacent to the collapsed buildings due to seismic debris is estimated by subtracting the building setback from the debris extent in the direction of the roadway.
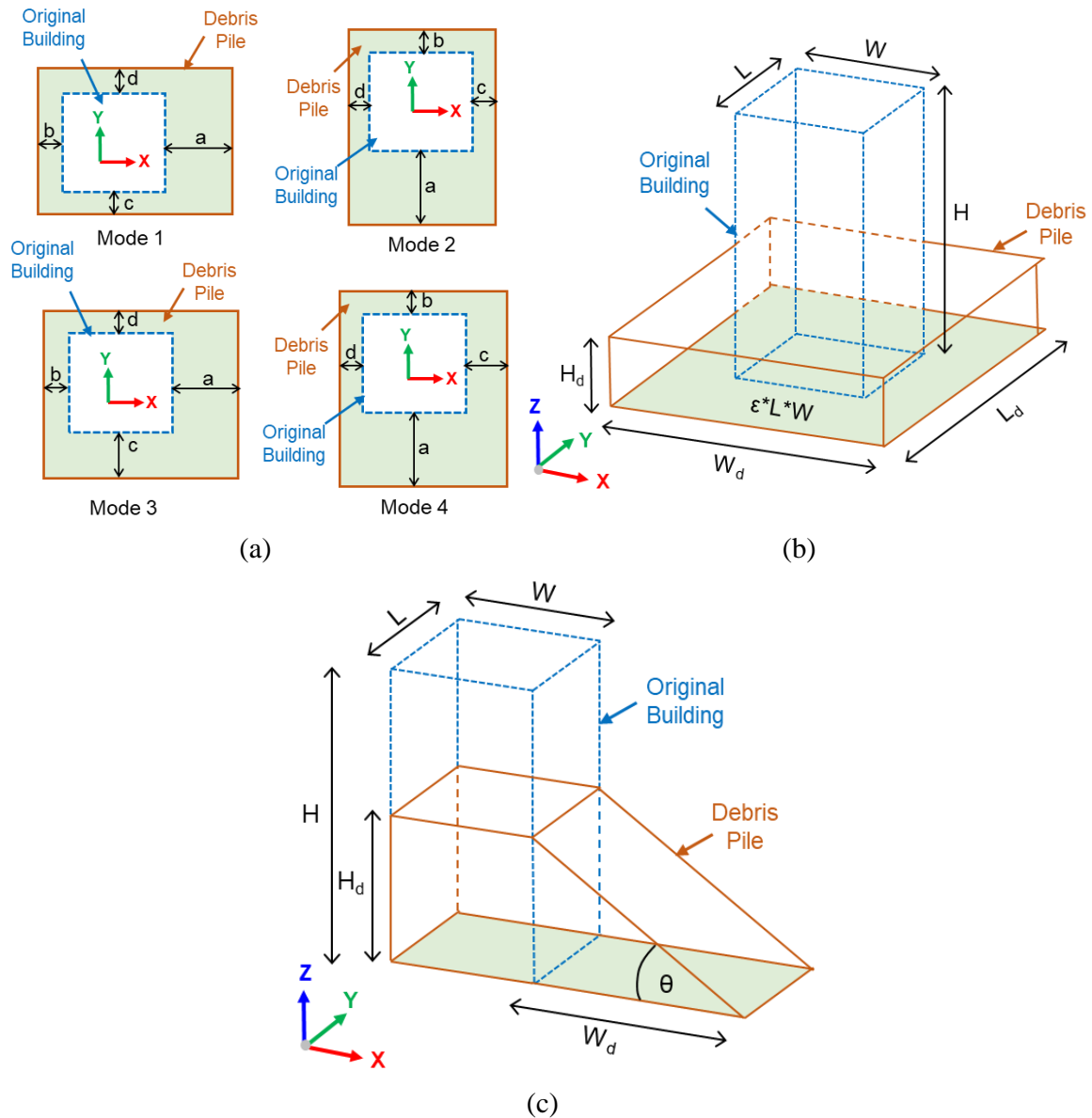
Figure 5-3 Assumed shape of seismic debris pile resulting from the collapse of: (a) RC frame; (b) masonry; and (c) other types of buildings in the community

5.5.3 Bridge Damage and Recovery

The *bridge damage* simulator receives the ground motion parameters from the *ground motion* simulator to evaluate the damage state of each bridge in the transportation network based on the fragility curves specified in HAZUS (FEMA 2003). Five damage states are differentiated

in HAZUS: no damage, slight, moderate, extensive, and complete damage. Two types of links are attached to each bridge in the network: major and minor links. Major links are those links that are directly connected to and affected by damage to a bridge. Minor links are those links that are indirectly connected to and affected by damage to a bridge (i.e., the roadway under the bridge). For a major link, it is assumed that any damage to the bridge will cause complete closure of that link. For a minor link, only extensive and complete damage to the bridge are assumed to cause complete closure of that link based on the definition of extensive and complete damage states in HAZUS (FEMA 2003).

The recovery process of the bridge is assumed to be discrete as per Padgett and DesRoches (2007) where the bridges are assumed to open when they reach either partial (e.g., 50%) or full (100%) functionality. Thus, three levels of bridge functionality are differentiated: closed (0%), partially open (50%), and open (100%). The partial functionality (i.e., 50%) of the bridge is interpreted as half capacity with a free flow speed of the major link attached to the bridge in the pre-earthquake condition. The repair time for these levels of functionality is taken as per Padgett and DesRoches (2007).

5.5.4 Post-Earthquake Traffic Simulation

The travel time and flow on each link in the transportation network are evaluated in the *post-earthquake traffic* simulator based on the updated conditions of the transportation network. The *post-earthquake traffic* simulator runs once every 10 time steps (i.e., 10 days) after the first 30 days during the recovery stage as discussed earlier due to the computational cost of the traffic analysis. It is assumed that the behavior of the transportation network is constant between these time steps after the first 30 days. During the first 30 days, the *post-earthquake traffic* simulator

runs each time step to rigorously model the post-earthquake emergency response of the community.

The four-step model is adopted once again to perform the traffic analysis. The second and third steps in the model (i.e., trip distribution and modal split) are assumed to be the same as before the seismic event. However, the first and fourth steps are updated to consider the effect of the seismic event and the interdependencies discussed earlier. The trip productions and attractions between the TAZs are reduced based on the reduction in the functionality of each building in the TAZ. The reduction values are adopted from Chapter 4 based on the functionality state of each building (i.e., not functional, re-occupancy, basic functionality, and full functionality).

A mutual interdependency that has not been previously studied in any significant depth but is considered in the current study is the interaction between the *healthcare* and the *post-earthquake traffic* simulators (see Figure 5-1 and Figure 5-2). The trips made by ambulances between the locations of injured people (i.e., produced) and hospitals in the community (i.e., attracted) and vice versa are added to the productions and attractions in the trip generation step. Another mutual interdependency exists between the *debris removal* and the *post-earthquake traffic* simulators (see Figure 5-2). The trips made by trucks to remove the generated debris from the locations of building collapse (i.e., produced) to the debris management sites and final disposal locations (i.e., attracted) and vice versa are also added to the productions and attractions in the trip generation step.

Route assignment is performed using the static user equilibrium (UE) model discussed earlier. However, the capacity and free flow speed of each link in the network are updated based on the bridge functionality and extent of debris that encroaches onto surrounding roadways. The reduction of the capacity and free flow speed of a link in the transportation network is assumed to be the maximum of the reduction due to bridge damage and debris extent. The reduction due to

201

debris extent on a link is assumed to be the maximum percentage of road blockage due to seismic debris generated from all the collapsed buildings adjacent to that link. The reduction due to bridge damage is assumed to be the maximum reduction in functionality of all the bridges attached to a link. Both reductions are updated each time step during the recovery stage as the debris is removed and bridges recover. The dynamic nature of the simulation model allows straightforward consideration of such complex interdependencies.

5.5.5 Discrete-Event Simulation of Healthcare System

Discrete-event simulation (DES) is the process of modeling the behavior of complex systems using an ordered sequence of well-defined events (Robinson 2004). It can be used to study what-if scenarios by changing the input parameters of the simulation and studying the effect of these changes on the modeled system. It has been widely used over the past decade to simulate the behavior of various engineering (e.g., Alvanchi et al. 2011), economic (e.g., Cigolini et al. 2014), and healthcare systems (e.g., Jun et al. 1999, Hamrock et al. 2003, and Hasan et al. 2020). In the present study, DES is used to model the behavior of the healthcare system during the post-earthquake stage. A fixed-increment time progression scheme is adopted where the time after the earthquake is divided into small equal intervals of two hours each and the state of the healthcare system is updated each time interval depending on the events occurring in this time interval.

The *healthcare* simulator described earlier in Chapter 4 is refined to run for the first 360 hours (i.e., 15 days) for a total of 180 time intervals instead of running once each time step during recovery stage (i.e. time step in hours instead of days). Figure 5-4 shows a schematic diagram for the DES implemented in the modified *healthcare* simulator. As shown, the simulation is separated spatially into two locations (i.e., the injuries are assumed to be in one of two locations): traffic analysis zones (TAZs) or hospitals. First, the number of injuries and fatalities in each TAZ is

evaluated during the earthquake stage in the *casualties* simulator. It is assumed that 60% of the injuries in TAZs are trapped inside buildings and need to be rescued during the recovery stage as per Facwett and Oleveria (2000). The rescue rate in each time interval is assumed to follow an exponential decay function (i.e., Ae^{-Bt}) defined by parameters A and B that depend on the emergency response capabilities of the studied community, where t is the time after earthquake.

The other 40% are transported to the hospitals in the community during the recovery stage based on the availability of ambulances and beds in the hospitals. The ambulances are distributed among the hospitals based on the availability of beds in each hospital, which is evaluated in the *physical recovery* simulator described earlier in Chapter 4. The ambulances are distributed among TAZs based on the smallest travel time on the transportation network. The number of injuries that can be mobilized between the TAZs and hospitals using a specific ambulance in a certain time interval depends on the travel time on the transportation network subscribed from the *post-earthquake traffic* simulator and the loading and unloading times of the injured into and out of the ambulances. The loading and unloading times are assumed to be random variables having a triangular (4.36,1.8) + 0.83 minutes and lognormal distributions (-0.49,3.36,5.54) minutes, respectively as per Su et al. (2008).

The admission of the injuries to the hospital depends on the number of beds available in the hospital. Previous earthquakes showed that multiple patients can occupy the space allocated to one bed during post-earthquake emergencies in real hospitals. For example, after the M_w 7.8 Kashmir earthquake, Mulvey et al. (2008) reported that up to 4 patients on average occupied the space allocated for one bed during the first 72 hours in a military hospital in the Forward Kahuta town. Therefore, a multiplier of 4 is assumed for the number of patients that can be admitted to hospitals during the post-earthquake stage. The total number of beds available at any time in the

hospital is proportional to the physical functionality of the hospital (see Chapter 4) as well as the social functionality of the medical staff in the hospital, which is assumed proportional to the number of injuries in the community (i.e., the percentage of injuries in the medical staff is assumed the same as the percentage of injuries in the population of the community). It is also assumed that 5% of the injuries waiting admission to hospitals or waiting mobilization from TAZs each time step (i.e., 2 hours) are taken to a hospital beyond the study region using resources outside the considered community.

The length of stay of an injured person in a hospital is assumed to be a random variable with lognormal distribution having a median of 3 days, dispersion of 0.4 and maximum of 64 days as was observed after the M_w 7.7 2001 Gujarat earthquake (Phalkey et al. 2011). During the first days after the earthquake, there is a high mortality rate, which is about 20-25 % according to Coupland (1994). The proposed simulation model considers a variable mortality rate for untreated injuries based on where the injured person is located (i.e., trapped inside a collapsed building or waiting admission to the hospital) and the number of days after the earthquake as listed in Table 5-1.

Table 5-1 Daily mortality rate assumed in the *healthcare* simulator.

Daily mortality rate	Reference
3% of injuries waiting mobilization in TAZs.	Facwett and Oleveria (2000)
12.1% of trapped injuries in TAZs for first day.	Bruycker et al. (1983)
64.7% of trapped injuries in TAZs for second day.	Bruycker et al. (1983)
91.5% of trapped injuries in TAZs for third day.	Bruycker et al. (1983)
100% of trapped injuries in TAZs after third day.	Bruycker et al. (1983)
1 % of injuries waiting admission in hospitals.	Facwett and Oleveria (2000)
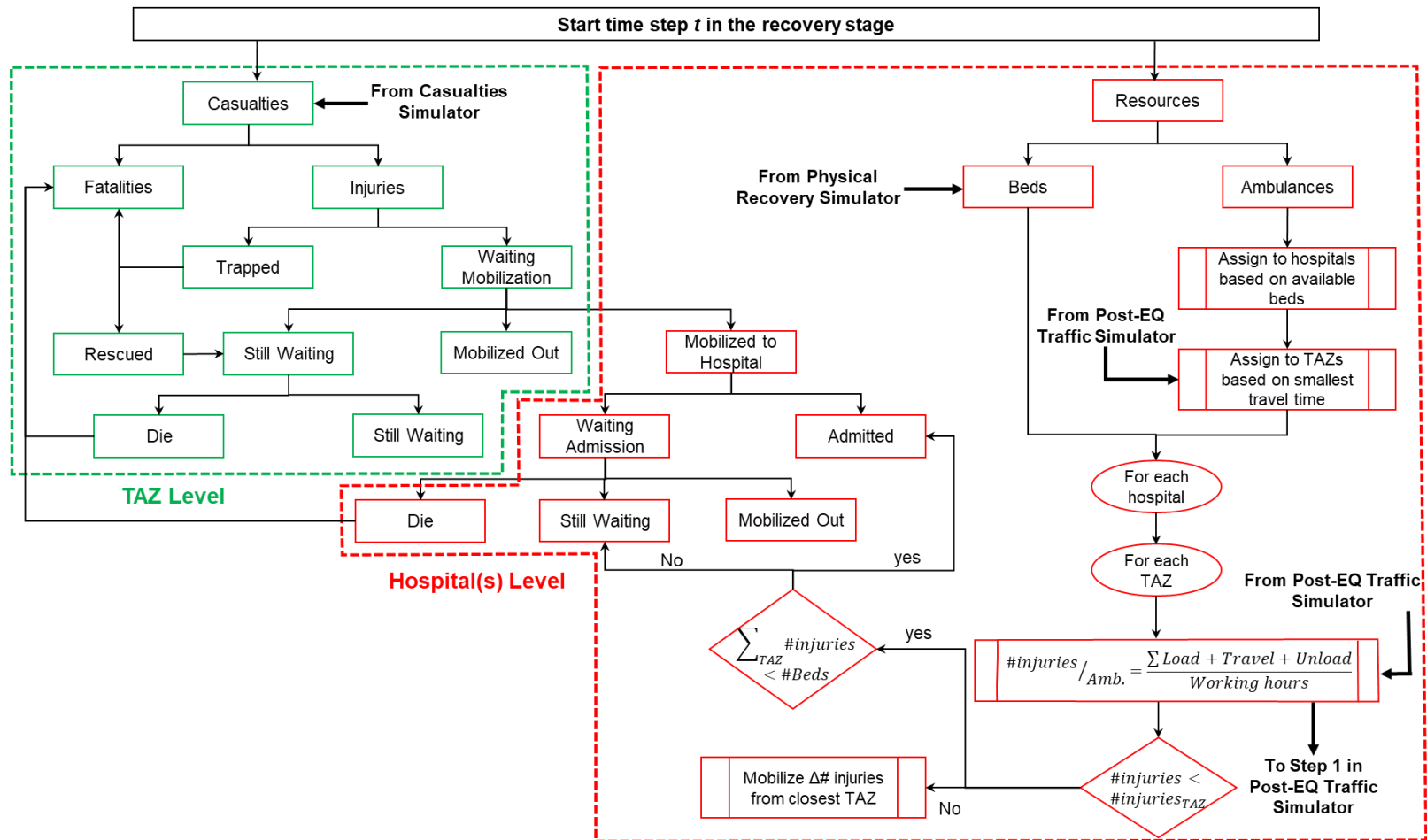
Figure 5-4 Overview of DES implemented in *healthcare* simulator

5.5.6 DES of Debris Removal

Debris removal is generally performed in two stages: (1) clearing emergency routes to expedite rescue operations; and (2) clearing remaining roadways as a means to recovery (FEMA 325 2007). The transition between stage 1 and stage 2 depends on the impact of the seismic debris on the road network as well as the number of trapped people after an earthquake. FEMA-325 (2007) classifies seismic debris into: construction and demolition debris; white goods; hazardous waste; and soil, mud, and sand. Generally, specific procedures are required to remove each debris type. However, FEMA-325 (2007) proposes a general framework for all types of debris as shown in Figure 5-5. The debris is first collected from the building's location to a temporary debris management site (TDMS), where it is sorted, reduced, and recycled before transportation to its final disposal landfill. The location of the TDMS in the community is ideally predefined before the earthquake based on the specifications suggested by the US EPA (U.S. Environmental Protection Agency) and UNEP (United Nation Environment Program). It should be located near the impacted area of the community but away from residential and commercial neighborhoods. The optimal choice of TDMS is an open research question that has been rarely studied (Kim et al. 2018) and outside the scope of the current study.
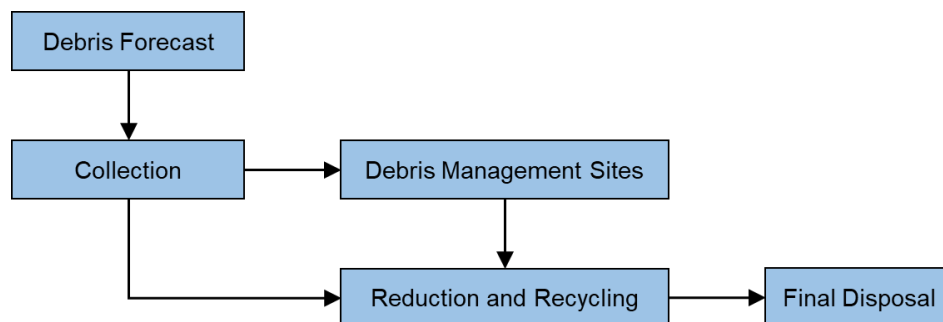
Figure 5-5 Debris removal process outlined in FEMA-325 (2007)

In the *debris removal* simulator, DES is used to simulate the process of debris removal from TAZs to TDMSs and then to landfills (LFs) during the post-earthquake stage. Similar to the healthcare system, a fixed-increment time progression scheme is adopted where the time after the earthquake is divided into small equal intervals of one day each. The *debris removal* simulator runs for the first 365 days (i.e., 1 year) after the earthquake. Figure 5-6 shows a schematic diagram for the DES implemented in the *debris removal* simulator. As shown, the trucks in the community are distributed to transport the debris from the building locations (i.e., TAZs) to TDMSs or from TDMSs to LFs or from TDMSs to recycling facilities in the community. The number of trucks assigned to each task is a decision parameter that can be optimized to enhance the performance of the debris removal system in the community. First, the amount of debris (in tons) evaluated by the *debris* simulator at the location of each building is converted into cubic yards (CY) using a factor of 2 as specified by FEMA (2010) for construction and demolition debris.

The trucks used to transport the debris from the buildings to TDMSs are distributed among the TDMSs based on the available space in the TDMSs. It is assumed that the capacity of each TDMS is 30,000 CY as per Kim et al. (2018). The number and locations of TDMSs in the community is an input parameter to the proposed model and can be optimized to enhance the performance of the debris removal process. The debris is collected from the building locations based on the importance of the adjacent roadway in the transportation network (i.e., main roads then local roads) and the amount of debris at a collapsed building site (i.e., buildings with large amount of debris first). The amount of debris that can be mobilized between the TAZs and TDMSs using a specific truck in a certain time interval depends on the capacity of the truck and the travel time on the transportation network evaluated by the *post-earthquake traffic* simulator and the loading and unloading times of the debris in and out of the trucks.

The loading and unloading times are assumed to be random variables having a lognormal distribution with median of 1hr. and 0.5 hr., respectively and dispersion of 0.4 for both as per Askarizadeh et al. (2016). The capacity of the truck is assumed to be 18 CY as per Kim et al. (2018). The collected debris is sorted at a TDMS into recyclable and non-recyclable debris. The recyclable percentage of construction debris is assumed to be a random variable with a normal distribution, minimum of 0.05, maximum of 0.15, and mean of 0.08 as per Kim et al. (2018). Excess recyclable debris over the daily recycling rate of TDMSs is mobilized to recycling facilities as shown in Figure 5-6. A recyclable rate of 4500 CY/day is assumed at each TDMS as per Kim et al. (2018). The non-recyclable debris is mobilized from TDMS to its final location in landfills (LFs).

Start time step t in the recovery stage

Trucks in the community

Building to TDMS

Assign to TDMS based on free space

Assign to TAZs based on debris quantity

For each TDMS

For each TAZ

From Post-EQ Traffic Simulator

$$Debris/Truck = \frac{\sum Load + Travel + Unload}{Working\ hours}$$

To Step 1 in Post-EQ Traffic Simulator

TAZ to TDMS

$Debris < Debris_{TAZ}$ — yes

No

Mobilize Δ debris from closest TAZ

$\sum_{TAZ} Debris < Capacity_{TDMS}$ — yes

No

Mobilize *Debris from TAZ to TDMS*

Cancel Trips

TDMS to Landfill

Non-recyclable

Recyclable

$$Debris\ to\ LF/Truck = \frac{\sum Load + Travel + Unload}{Working\ hours}$$

To Step 1 in Post-EQ Traffic Simulator

From Post-EQ Traffic Simulator

$Recycable < TDMS_{Rec.Rate}$

No — **To Step 1 in Post-EQ Traffic Simulator**

yes

Recycle Onsite

TDMS to LF

TDMS to Recycling

TDMS to Rec.

$$Debris\ to\ Rec/Truck = \frac{\sum Load + Travel + Unload}{Working\ hours}$$

From Post-EQ Traffic Simulator

Figure 5-6 Overview of DES implemented in *debris removal* simulator

209

5.6   Measuring Community Performance

The first step to enhance the seismic resilience of a community is to quantify in order to measure the effect of different mitigation strategies on the performance of the community. Several parameters are defined to quantify the performance of both the transportation network and healthcare system.

5.6.1 Transportation Network

The performance of the transportation network is quantified using two parameters: network resilience index (%*NRI*) and network performance index (*NPI*). The network resilience index (%*NRI*) is defined as the area under the recovery path of the transportation network until full recovery (i.e., returning back to 100% functionality) as shown in Figure 5-9(a) and expressed mathematically as:

$$\%NRI = \frac{\int_0^{T_{NF}} \%Q_{TN}(t)}{T_{NF}} \tag{5-3}$$

where T_{NF} is the time required for the transportation network to return back to 100% functionality and $\%Q_{TN}(t)$ is the weighted functionality of the transportation network (based on link capacity) at time t during the recovery stage. The weighted functionality of the transportation network is evaluated in the *network recovery* simulator as:

$$\%Q_{TN}(t) = \frac{\sum_{i=1}^{n} C_i \times \%q_i(t)}{\sum_{i=1}^{n} C_i} \tag{5-4}$$

where $\%q_i(t)$ is the functionality of link i at time t during the recovery stage, n is the number of links in the transportation network, and C_i is the capacity of link i. %*NRI* captures the effect of damage and recovery of bridges and buildings on the functionality of the transportation network.

210

NPI is defined as the area under the mean travel time ratio (*MTTR*) curve of the transportation network as shown in Figure 5-9(b). Values closer to one suggest that the post-earthquake behavior of the transportation network is close to that experienced before the earthquake. *NPI* captures the effect of building functionality, debris removal trips, and healthcare trips on the O-D demand in the transportation network. It also captures the effect of bridge damage and building debris on the capacity of the links. *NPI* can be expressed mathematically as:

$$NPI = \frac{\int_0^{T_{NP}} MTTR(t)}{T_{NP}} \tag{5-5}$$

where T_{NP} is the time required to return back to the pre-earthquake travel time on the transportation network and $MTTR(t)$ is the mean travel time ratio of the transportation network at time *t* during the recovery stage. *MTTR* is defined as the ratio between the weighted mean travel time (*MTT*) on the links of the transportation network in the community at any time *t* during the recovery stage and the weighted mean travel time on the links of the transportation network before the earthquake (MTT_o), which can be expressed mathematically as:

$$MTTR(t) = \frac{MTT(t)}{MTT_o} \tag{5-6}$$

$$MTT = \frac{\sum_{i=1}^{n} C_i \times \tau_i}{\sum_{i=1}^{n} C_i} \tag{5-7}$$

where τ_i is the travel time on link *i*.

5.6.2 Healthcare System

Three performance parameters are used to quantify the performance of each mechanism in the healthcare system inside the community: hospital utilization index (%*HUI*), in-community mobilization index (%*IMI*) and waiting admission index (%*WAI*). The hospital utilization index

(%*HUI*) is defined as the area under the normalized treatment curve of the healthcare system (i.e., normalized number of injuries treated in the hospitals during the recovery stage) as shown in Figure 5-10(a). A value of 100% means that the hospitals are working at full capacity (i.e., fully utilized) during the recovery stage. %*HUI* can be expressed mathematically as:

$$\%HUI = \frac{\int_0^{T_H} \hat{I}_{TRE}(t)}{T_H} \times 100 \tag{5-8}$$

where $\hat{I}_{TRE}(t)$ is the number of injuries treated at the hospitals at time t during the recovery stage normalized by the capacity of the hospitals in the community at the same time t. T_H is the time required to discharge the last injury from the hospitals in the community.

The in-community mobilization index (%*IMI*) is defined as the area under the normalized curve of mobilized injuries inside the community (i.e., normalized number of injuries mobilized from buildings to the hospitals during the recovery stage) as shown in Figure 5-10(b). A value of 100% suggests that the available ambulances in the community are able to mobilize all of the injuries waiting mobilization during the recovery stage. %*IMI* can be expressed mathematically as:

$$\%IMI = \frac{\int_0^{T_{MI}} \hat{I}_{MI}(t)}{T_{MI}} \times 100 \tag{5-9}$$

where $\hat{I}_{MI}(t)$ is the number of injuries mobilized inside the community at time t during the recovery stage normalized by the number of injuries awaiting mobilization at the same time t. T_{MI} is the time required to reach zero injuries mobilized inside the community.

Similar to %*HUI*, the waiting admission index (%*WAI*) is defined as the area under the normalized waiting admission curve of the healthcare system (i.e., normalized number of injuries waiting admission to the hospitals during the recovery stage) as shown in Figure 5-10(c). A value

of 0% suggests that the healthcare system is working efficiently without any injuries waiting admission during the recovery stage. %WAI can be expressed mathematically as:

$$\%WAI = \frac{\int_{0}^{T_{WA}} \hat{I}_{WA}(t)}{T_{WA}} \times 100 \qquad (5\text{-}10)$$

where $\hat{I}_{WA}(t)$ is the number of injuries waiting admission to the hospitals at time t during the recovery stage normalized by the capacity of the hospitals in the community at the same time t. T_{WA} is the time required to reach zero injuries waiting admission to the hospitals.

5.7   Illustrative Case Study: Seismic Resilience of Archetype Community

5.7.1 Community Setup

The simulation model and its capabilities are demonstrated through the same case study in Chapter 4 that focuses on modeling the seismic resilience of part of Shelby County, Tennessee (shown in Figure 5-7). The transportation network data is extracted using the open-source platform OpenStreetMap (OSM) and processed to define the traffic analysis zones (TAZs) using the traffic planning software PTV Visum. Only main roads are modeled in the case study (Figure 5-7). Local roadways are beyond the scope of this case study. The studied transportation network consists of 306 nodes, 503 links, and 204 TAZs. The traffic demand model used by Memphis MPO (2016) is adopted to predict the trip productions and attractions and perform modal split for trips with different purposes (i.e., home-based, work-based, etc.) between the different TAZs. Detailed information about the bridges in the studied area is collected from the National Bridge Inventory (NBI 2019), which provides the location of each bridge (Figure 5-7) and representative values for various bridge parameters required for HAZUS (FEMA 2003) fragility curves.
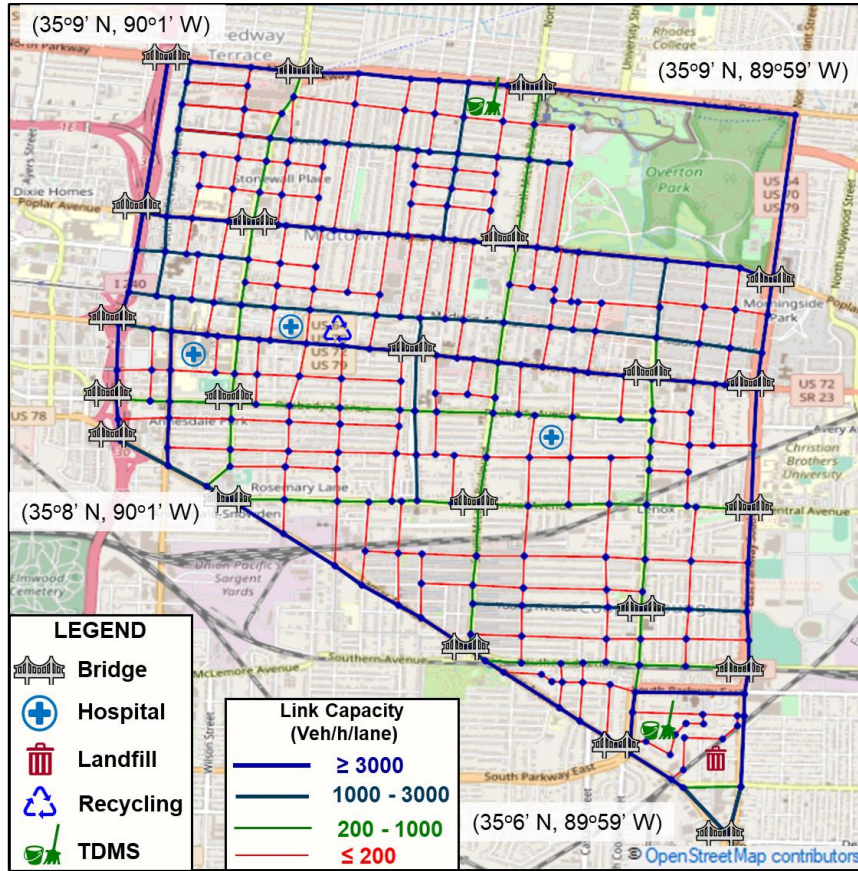
Figure 5-7 Studied community

There are three hospitals in the studied community (Figure 5-7) that are 2, 4, and 12 stories high with a total number of beds during normal operation of 140, 223, and 326, respectively as described in Chapter 4. Braun et al. (1990) reported that cities staff an average of one ambulance per 51,223 people. However, in extreme events as earthquakes this number should be increased. Therefore, it is assumed that 4 ambulances are available in the studied community after the earthquake. This number is an input parameter to the proposed model and can be refined as more data become available from real communities. The rescue rate parameters A and B, defined earlier, are assumed to be 1500 and 1.125 based on a sensitivity study to ensure that all injured are rescued within 24 hours of the earthquake. In real communities, such parameters should be calibrated based on the emergency response capacity of the community. It is also assumed that 10,10, and 5 trucks

are available to transport debris from the building sites to TDMS, transport debris from TDMS to the landfill, and transport debris from TDMS to recycling facilities, respectively. It is assumed that two TDMSs, one landfill, and one recycling facility are available and located in the arbitrary locations shown in Figure 5-7.

5.7.2 Seismic Hazard

Similar to the case study described in Chapter 4, the seismic event is the ground motion record RSN 1961 (PEER 2018), which was recorded at the Lepanto station near the studied community. The epicenter is located at 35°18'N, 90°18'W and the peak ground acceleration (PGA) is scaled at each building location to meet the PGA for a M_w 7.7 earthquake scenario specified by the United States Geological Survey (USGS 2018) for the studied region. The earthquake event is assumed to occur on a weekday at 8:00 PM.

5.7.3 Results and Discussions

To account for the many uncertainties inherent in the factors affecting the behavior of the different systems of the community after a seismic event, the model uses a Monte Carlo procedure to perform loss and recovery calculations. The sampling is performed based on the distribution properties of each component specified in the FEMA P-58 methodology (FEMA 2012a) for evaluation of component losses as well as the distribution properties for each variable discussed earlier related to the healthcare system and debris removal. The proposed simulation model is computationally demanding due to the traffic analysis performed at each time step during the recovery stage as well the adopted Monte Carlo procedure. Therefore, the proposed simulation model is implemented and run within a parallel computing environment. Also, the traffic analysis is performed once every 10 time steps (i.e., 10 days) after the first 30 days as discussed earlier.

The computational time for running a Monte Carlo simulation for the presented case study is approximately 4 hours on a personal computer with four cores and 32 GB RAM. The results shown are for one arbitrary Monte Carlo simulation with a constant seed to be able to demonstrate the capabilities of the proposed model under different conditions (i.e., input parameters for different scenarios). The complete set of parameters and results of the presented case study are documented and publicly available at Sediek et al. (2021b).

Figure 5-8 shows the spatial distribution of the traffic flow along the links of the transportation network during the recovery stage immediately after the earthquake and at three other points in time. As shown in Figure 5-8(a), 55 of the 503 links (~ 11%) in the transportation network lost their functionality (i.e., closed due to debris blockage or bridge damage) immediately after the earthquake. Most of the traffic flow was concentrated around the location of the hospitals due to ambulance trips made to and from hospitals as well as around the location of the landfill and TDMSs due to transportation of debris (Figure 5-8(a)). The functionality of a significant number of links (i.e., 31 out of 55) was restored within 90 days (i.e., 3 months) of the seismic event as shown in Figure 5-8(c) due to removal of seismic debris from collapsed buildings and repair of bridges. This progress is also reflected in the recovery trajectory of the transportation network as shown in Figure 5-9(a) where the functionality of the transportation network increased from 81% immediately after the earthquake to 89% 90 days after the event.

216
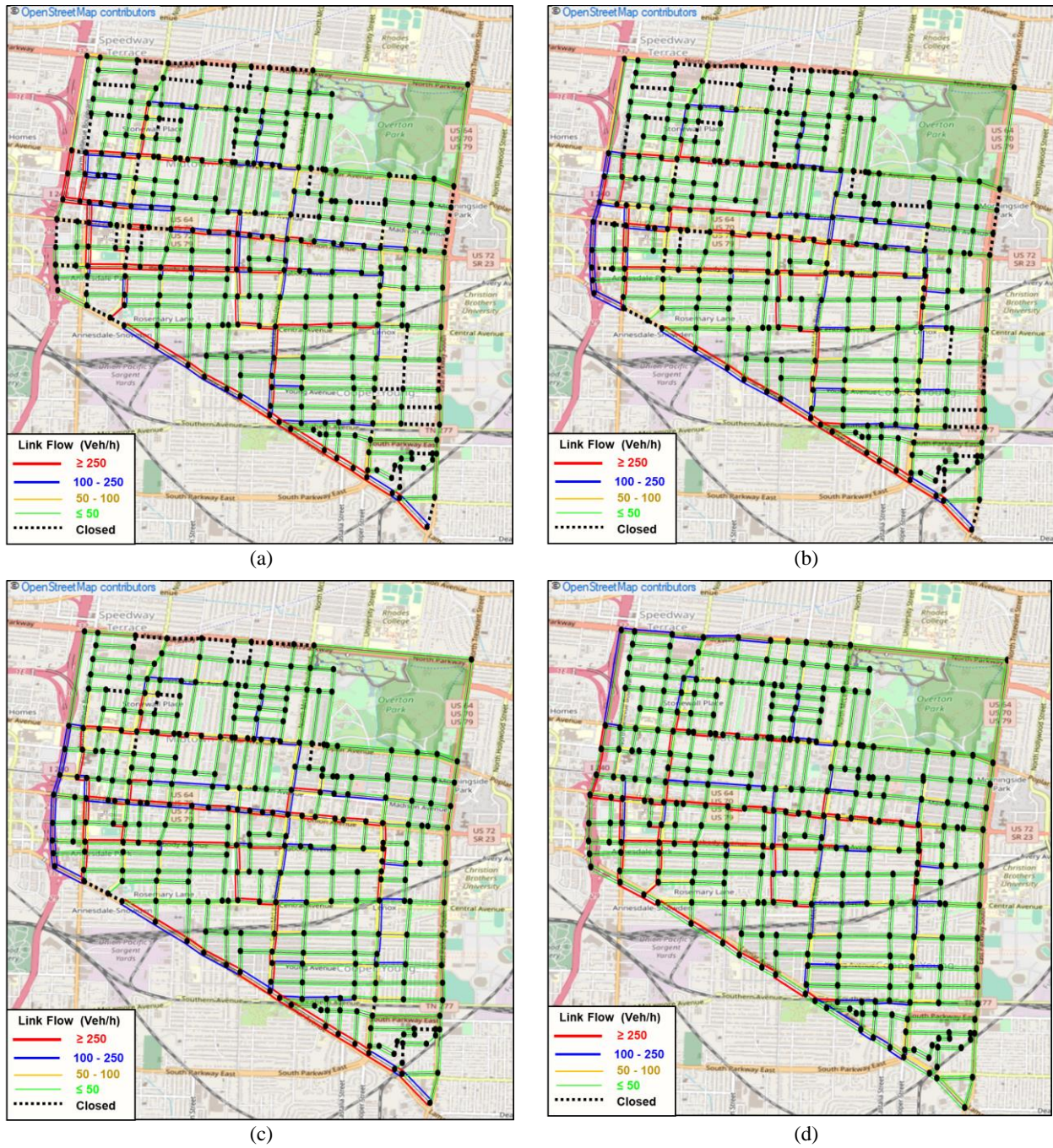
Figure 5-8 Spatial distribution of link flow in the transportation network for one arbitrary Monte Carlo simulation: (a) immediately after the earthquake; (b) after 1 month; (c) after 3 months; and (d) after 12 months

217

The transportation network was restored to full functionality after 1 year (i.e., 365 days) as shown in Figure 5-8(d) and Figure 5-9(a). It should be noted that although the transportation network reached its full functionality, the traffic flow did not return to the pre-earthquake case due to the loss of functionality of some of the buildings. As reported by in Chapter 4, the building portfolio reached its full functionality after 4.6 years, which is much longer than the restoration time for the transportation network. The network resilience index (%NRI) of the transportation network was 90.5% as shown in Figure 5-9(a), which is considered acceptable but can be further enhanced. Figure 5-9(b) shows the mean travel time ratio ($MTTR$) of the studied transportation network during the recovery stage. Immediately after the earthquake, the $MTTR$ of the network was 1.3 due to the loss of functionality of the roads as well as the large number of trips made to mobilize injuries and transport debris. However, the $MTTR$ of the network dropped significantly during the recovery stage due to the decrease in the trips made as well as the increase in the network functionality. The network performance index (NPI) of the studied network was 1.18, which is close to 1 implying good performance of the network after the seismic event.

Figure 5-10 shows the evolution of the social functionality (i.e., injured in the community and healthcare system) during the recovery stage. As noted in Figure 5-10, the time scale is in hours, which is different from the time scale of the previous systems (i.e., building portfolio and transportation network). This ability to use multiple time scales is an important capability of the simulation model, which allows for different spatial and temporal scales even within the same stage (e.g., recovery stage). As shown in Figure 5-10(a), the number of treated injuries in the hospitals increased over the first few hours due to mobilization of injuries from the building locations to the hospitals. Eighteen hours after the earthquake, the capacity of the hospitals in the community was reached and the number of injuries waiting admission increased as shown in

218

Figure 5-10(b). The maximum number of injuries waiting admission was reached after 58 hours from the occurrence of the earthquake as shown in Figure 5-10(b).

As shown in Figure 5-10(c), the normalized number of injuries mobilized inside the community was almost constant over the first 24 hours after the earthquake as the number of injuries waiting mobilization was much more than the capacity of the ambulances due to the continuous rescue of the injured. However, after 24 hours, rescue of those injured stopped but the mobilization of the injured continued causing the sharp increase shown in Figure 5-10(c) until reaching a value of 1 (i.e., all the injuries waiting mobilization are mobilized). The time required to reach zero injuries (i.e., treat all who were injured) was 270 hours (~11 days). As shown in Figure 5-10, %*HUI*, %*IMI*, and %*WAI* were 51%, 15%, and 50% respectively.

(a)   (b)
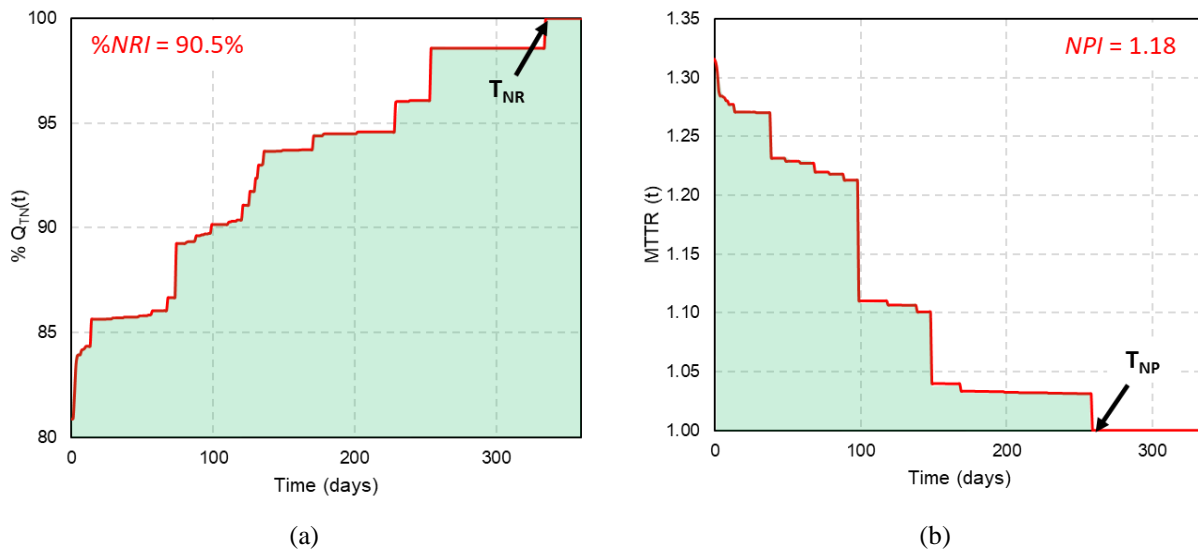
Figure 5-9 Illustration of: (a) recovery trajectory of the transportation network after the earthquake for one arbitrary Monte Carlo simulation; and (b) mean travel time ratio (MTTR) of the studied network during the recovery stage
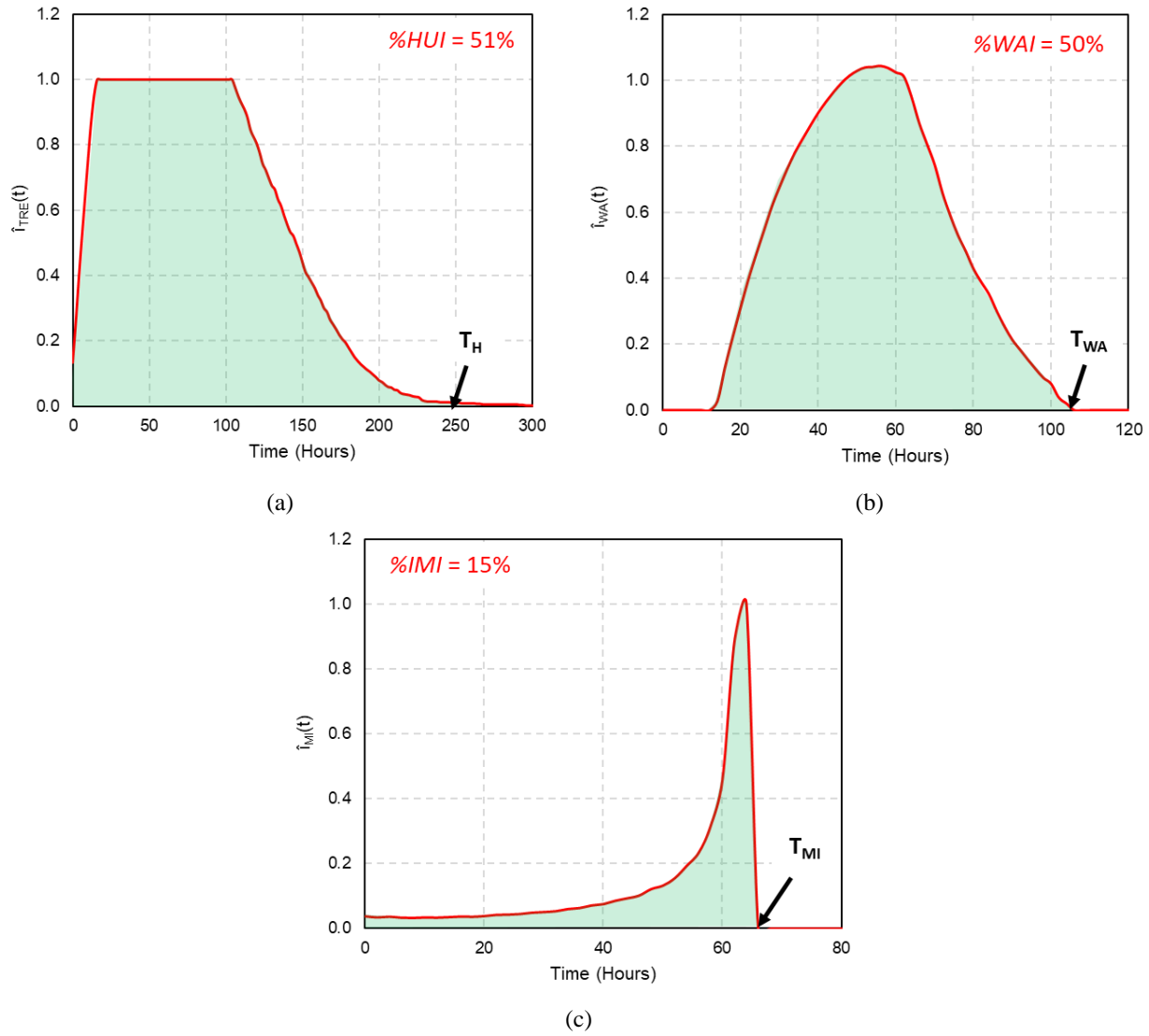
Figure 5-10 Illustration of number of injuries for one arbitrary Monte Carlo simulation: (a) receiving treatment in in the hospitals; (b) mobilized between building locations and the hospitals during the recovery stage; and (c) awaiting admission to the hospitals during the recovery stage

5.7.4 Impact of Interdependencies

The proposed simulation model shown in Figure 5-2 was modified to study the effect of removing or adding interdependencies between the different systems by simply removing or adding the connection (shown by the arrows connecting the boxes in Figure 5-2) between the

220

relevant simulators. Three types of interdependencies were studied: those between the *post-earthquake traffic* simulator and the *bridge recovery* simulator*, debris removal* simulator, and *healthcare* simulator. The first and second interdependencies consider the effect of structural damage of bridges only and debris only, respectively, on the functionality of the links in the transportation network. The lack of considering the third interdependency means that the healthcare system is not affected (i.e., constrained) by the functionality of the transportation network. In this case, all the injured who are rescued are assumed to be mobilized in one time step with no constraint on the number of trips that can be made through the transportation network. This assumption is made by most of the studies available in the literature (e.g., Ceferino et al. 2020).

Figure 5-11(a) shows the recovery trajectory of the studied transportation network with and without considering the first two interdependencies. Considering the interdependency between the *post-earthquake traffic* and *bridge recovery* simulators (indexed as "debris only" in Figure 5-11(a)) had three effects on the recovery trajectory of the transportation network. First, it delayed the recovery of the transportation network due to the time required to restore the functionality of the bridges in the transportation network. The second effect was shifting the recovery trajectory to the right (blue dotted area in Figure 5-11(a)) for the same reason. Lastly, it reduced the initial post-earthquake functionality of the network from 92% to 81% (12% reduction) due to the reduced functionality of the links attached to the damaged bridges in the transportation network.

Considering the interdependency between the *post-earthquake traffic* and *debris removal* simulators (indexed as "bridge only" in Figure 5-11(a)) had two effects on the recovery trajectory of the transportation network. First, it shifted the recovery trajectory to the right (green shaded area in Figure 5-11(a)) due to the time required to remove the debris from the partially and totally

221

blocked links. The second effect was to reduce the initial post-earthquake functionality of the network from 90% to 81% (9% reduction) due to the partial and total blockage of the links affected by the debris resulting from the collapse of the buildings.

(a)

(b)
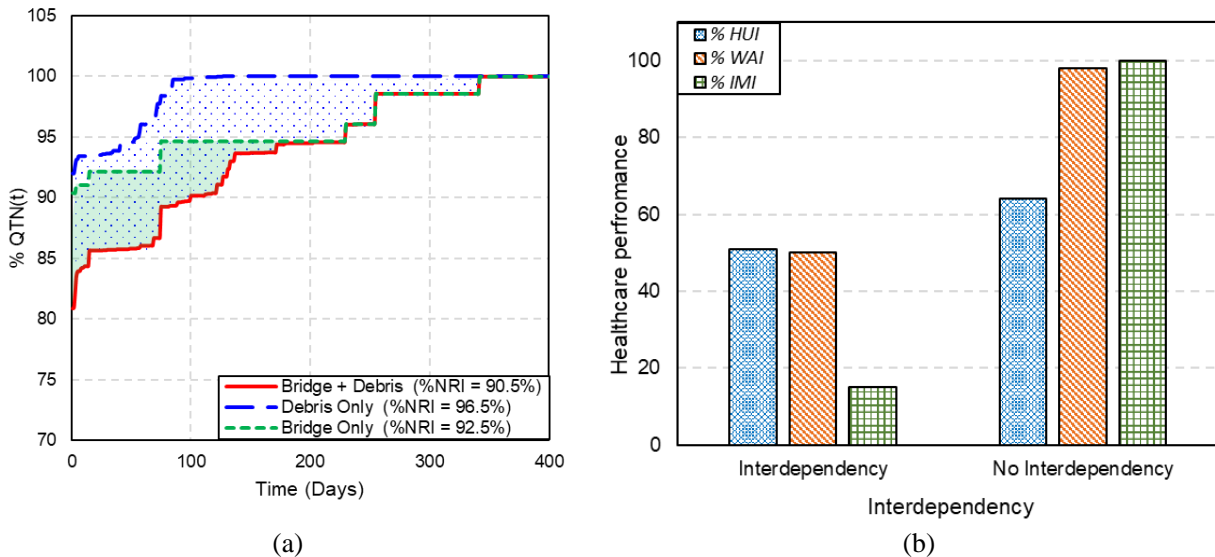
Figure 5-11 Effect of interdependencies between: (a) *post-earthquake traffic* **simulator and** *debris* **and** *bridge recovery* **simulators; and (b)** *post-earthquake traffic* **simulator and** *healthcare* **simulator**

Figure 5-11(b) shows the effect of the interdependency between *post-earthquake traffic* and *healthcare* simulators on the performance of the healthcare system through % *HUI*, %*WAI*, and %*IMI*. As shown, neglecting the interdependency between *post-earthquake traffic* and *healthcare* simulators had a significant effect on %*IMI*, which increased from 15% to 100%. This result is attributed to the assumption that there was no constraint on the number of injured that can be mobilized to the hospitals in the community at any time step. This effect is also reflected in %*HUI* and %*WAI*, which increased from 51% to 64% and from 50% to 98%, respectively, for the same reason. As shown, the novel approach implemented to consider the mutual interdependency between the transportation network and healthcare system in the community has a significant effect

222

(i.e., more realistic) on the predicted behavior of the healthcare system in the community. This approach enables a better understanding of how these systems will function and an improved ability to enhance the behavior of these two systems after seismic events.

5.7.5 Effectiveness of Hazard Mitigation Plans

The capability of the simulation model to support decision makers in studying the effect of different mitigation actions on the behavior of the studied systems (i.e., healthcare, building portfolio, and transportation network) is demonstrated through a sensitivity study that comprises different mitigation actions. For the healthcare system, the studied mitigation action entailed three activities. The first activity was increasing the number of ambulances available after the earthquake from 4 to 8. The second activity was adding a field hospital near to the 12-story hospital (i.e., the same TAZ) with an additional 180 beds. The third activity was enhancing the emergency response of the rescue team in the community after the earthquake (e.g., receiving supporting rescue personnel from nearby zones or states) by changing the rescue rate parameters A and B defined earlier from 1500 to 2000 and from 1.15 to 1.1, respectively.

For the building portfolio, the mitigation action entailed a community-wide building retrofit plan to upgrade the seismic resistance of all buildings that were built according to design codes prior to 1973 to meet current design requirements. For debris removal mitigation action, the number of trucks available to collect debris from the building sites and transport it to TDMS and to transport debris from TDMS to the landfill was increased to 20. The number of TDMSs available in the community was increased to 3 with the same assumed capacity per TDM (i.e., 30,000 CY). All possible combinations of these three mitigation strategies were considered leading to eight different scenarios as defined in Table 5-2.

Table 5-2 Definition of the scenarios that combine the studied mitigation actions for different systems in the studied community

Scenario	Healthcare System	Building Portfolio	Debris Removal
Scenario 1	Original	Original	Original
Scenario 2	Mitigation	Original	Original
Scenario 3	Original	Original	Mitigation
Scenario 4	Original	Mitigation	Original
Scenario 5	Mitigation	Mitigation	Original
Scenario 6	Mitigation	Original	Mitigation
Scenario 7	Original	Mitigation	Mitigation
Scenario 8	Mitigation	Mitigation	Mitigation

Original: input parameters w/o mitigation actions
Mitigation: input parameters w/ mitigation actions

Figure 5-12 shows the effect that the mitigation actions related to debris removal and the building portfolio had on the transportation network. As shown in Figure 5-12(a), upgrading the seismic design of the buildings in the community led to an increase in the initial functionality of the transportation network from 81% to 90% (9% increase), which is attributed to the lower number of collapsed buildings (mainly RC and steel buildings). This increase in initial functionality is also reflected in the initial *MTTR* after the earthquake, which decreased from 1.30 to 1.05 (20% reduction) as shown in Figure 5-12(b), *NPI*, which decreased from 1.18 to 1.02 (14% reduction), and %*NRI*, which increased from 90.5% to 95% (5% increase). The mitigation actions related to debris removal shifted the recovery trajectory of the transportation network to the left due to the expedited clearance of the roadways as shown in Figure 5-12(a). This outcome is also reflected in %*NRI*, which increased from 90.5% to 92% (1.5% increase), and *NPI*, which decreased from 1.18 to 1.1 (7% reduction).

Figure 5-13 shows the effect that the mitigation actions related to the healthcare system and the building portfolio had on the number of injured waiting admission to hospitals as well as the number of injured being mobilized. As shown in Figure 5-13(a), the proposed mitigation

actions had a significant effect on %*WAI*, which decreased from 50% to 12% (76% reduction) due to the increased number of available beds in the community. Also, the number of fatalities in the community significantly decreased from 384 to 278 due to the reduced number of collapsed buildings in the community resulting from the seismic design upgrade. Upgrading the seismic design of buildings along with the mitigation actions for the healthcare system had the most significant effect on %*WAI*, which decreased from 50% to almost 0 (1% as shown in Figure 5-13(a)) due to both the increased number of available beds as well as reduced number of collapsed buildings in the community. Also, these two mitigation strategies had a significant effect on the number of fatalities in the community, which decreased from 384 to 127 for the same reasons.

Increasing the number of ambulances as well as enhancing the emergency response of the rescue team in the community had a significant effect on the time required to mobilize all the injuries waiting mobilization in the community, which decreased from 65 to 38 hours (42% reduction) as shown in Figure 5-13(b). Upgrading the seismic design of the buildings had a similar effect, due to the reduced number of injured resulting from collapsed buildings, where the time required to mobilize all the injuries waiting mobilization in the community decreased from 65 to 45 hours (30% reduction).

Choosing the appropriate mitigation strategy depends on many factors, which are community specific beyond just the performance parameters discussed earlier (e.g., %*NRI*, *NPI*, %*WAI*, %*IMI*, etc.). One of these factors is the initial investment required for each plan (e.g., the cost of upgrading the design of current buildings versus repairing them after a seismic event). Another factor is the social aspect of the problem. For example, the mitigation actions related to the healthcare systems may have a significant economic cost. However, the social gain from such mitigation actions (i.e., reducing number of fatalities or number of injuries mobilized outside the

community) may be much higher than the economic cost. As demonstrated, the proposed simulation model can be used by decision makers in the community to make such tradeoffs and decide on viable mitigation strategies to be executed.

(a)

(b)
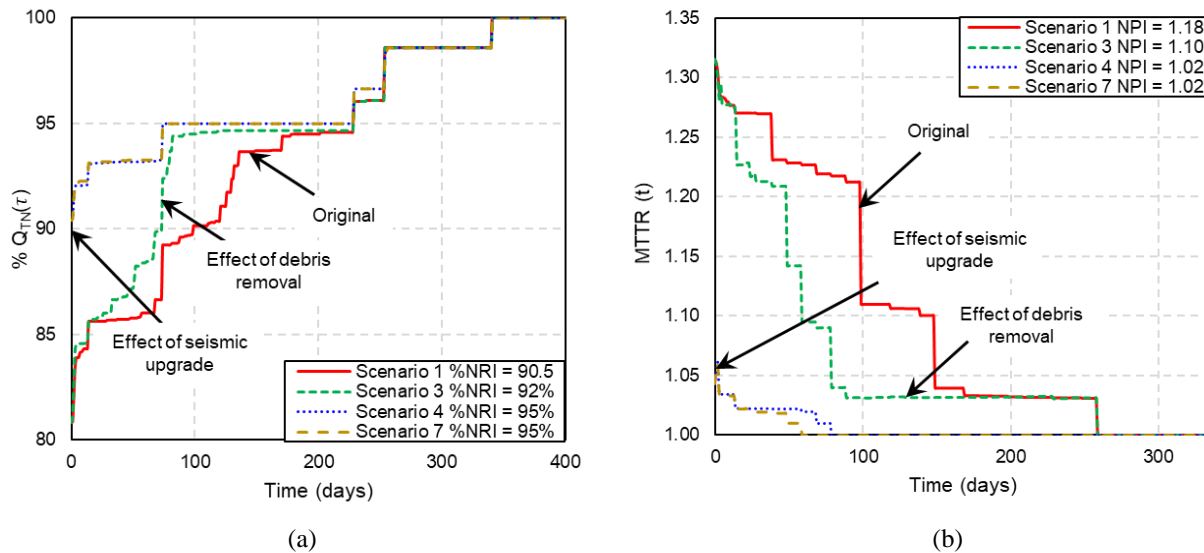
Figure 5-12 Effect of studied mitigation strategies on: (a) transportation network recovery trajectory, and (b) mean travel time ratio (*MTTR*)

(a)

(b)
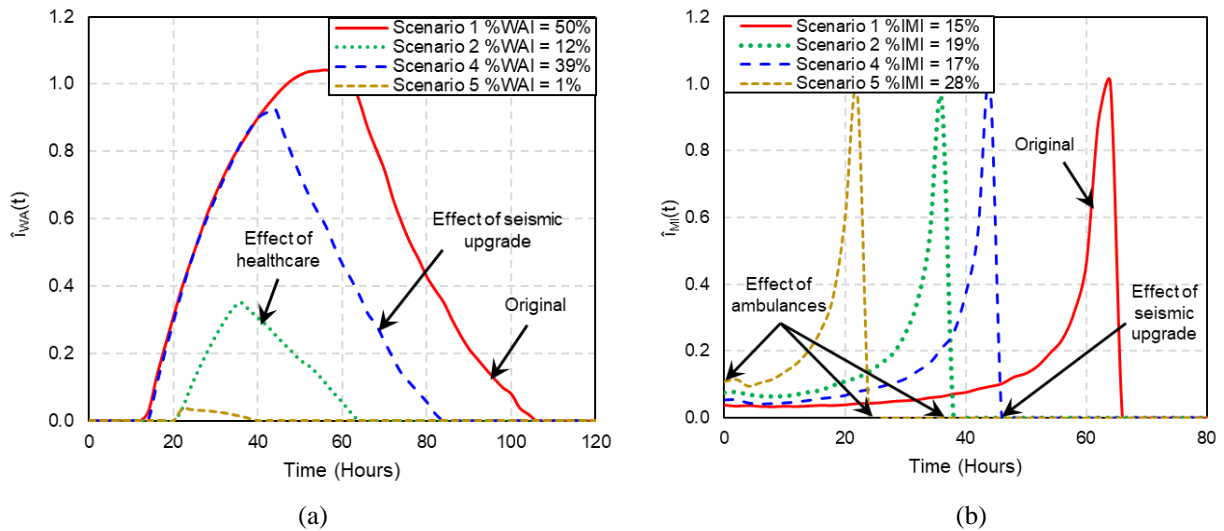
Figure 5-13 Effect of studied mitigation strategies on: (a) number of injuries waiting admission to hospitals, and (b) number of injuries mobilized

226

5.8 Simulation Model Limitations

Although the proposed simulation model considers the interdependencies between the building portfolio, transportation network and healthcare system during and after seismic events, there are still other critical dimensions of community resilience that have not been accounted for in this study. Damage and recovery of lifeline systems is one of these critical dimensions, which deeply influence resilience and the recovery trajectory. Also, social losses are only expressed in terms of casualties, which is not the case in real communities where other short- and long-term social vulnerability indicators affect the resilience of communities including relocation, business disruption, job loss, supply disruption, family stress and neighborhood disruption that are outside the scope of this study. All of these dimensions can be added to the proposed model with the addition of appropriate simulators and their connection with the rest of the system model shown in Figure 5-2. Also, the presented results and mitigation strategies are based on the assumptions discussed earlier related to the building portfolio, transportation network, and healthcare system. Clearly, the results (i.e., building collapse, injuries and recovery outcomes) will change when using different input parameters. However, the proposed model allows for the ability to evaluate multiple scenarios and strategies taking into consideration the effect of interdependencies between the three critical systems discussed earlier, which provides the necessary data to make informed decisions.

5.9 Summary and Conclusions

A simulation-based model is presented in this chapter for the assessment and quantification of seismic resilience of communities while considering the mutual interdependencies between the building portfolio, transportation network, and healthcare system. The model was modularized into independent simulators, each representing an aspect of the overall problem to facilitate

modeling such complex interdependencies. The proposed model combined the effect of bridge damage and accumulation of debris resulting from the collapsed buildings on the transportation network. The post-disaster origin-destination (O-D) patterns of households along with the functionality of the road network were used in a traffic analysis to update the traffic flow and time through the links of the transportation network. The updated traffic flow and time were used in a discrete event simulation (DES) environment to simulate the behavior of the healthcare system as well as the debris removal process in the aftermath of a seismic event.

Resilience measures for each system were proposed to assess and improve the seismic resilience of the individual systems and the community as a whole. The model was demonstrated through a case study in which the building portfolio, transportation network, and healthcare system of a part of Shelby County, Tennessee, was subjected to a M_w 7.7 earthquake located northwest of Memphis. The results of one realization showed that 11% of the links in the studied transportation network lost their functionality due to debris accumulation and bridge damage, which adversely affected the mobilization of injured people as well as debris removal from the community. In order to demonstrate the capability of the simulation model to support hazard mitigation planning, a sensitivity study was performed to investigate the effect of three mitigation actions related to the three studied systems (i.e., healthcare, building portfolio, and debris removal). All possible combinations between the three mitigation actions were considered leading to eight different scenarios. The results of the case study showed that upgrading the seismic design of buildings and increasing the number of ambulances and hospital beds in the community reduced the number of fatalities by 50%. Also, upgrading the seismic design of buildings and increasing the number of trucks used to transport debris in the community improved the seismic resilience of the transportation network by 5%.

228

The proposed simulation model is a key step forward towards quantifying and enhancing the seismic resilience of communities while considering the mutual interdependencies between the different critical systems in a community. Choosing the appropriate mitigation strategy to improve the seismic resilience of a community is a challenging task that depends on many factors beyond just the economic cost. For example, the mitigation actions required for the healthcare systems may have a significant economic cost. However, the social gain from such mitigation actions (i.e., reducing number of fatalities or number of injuries mobilized outside the community) may be much higher than the economic cost. The simulation model can be used by decision makers in the community to make such tradeoffs and decide on viable mitigation strategies to be executed.

CHAPTER 6

Integrating Household Decisions in Quantifying the Seismic Resilience of Communities Subjected to Earthquake Sequences

6.1   General

This chapter employs the scalable simulation model described in Chapter 4 to integrate post-earthquake household decision making when quantifying the seismic resilience of communities subjected to earthquake sequences. A Simple Multi-Attribute Rating Technique (SMART) is used to model post-earthquake household decision making at the building level while earthquake sequences (i.e., aftershocks) are modeled using time-dependent analysis during recovery from the mainshock. Incremental dynamic analysis (IDA) is used to develop fragility curves for mainshock-damaged structures, which are distinguished from the conventional fragility curves of intact structures. The developed simulation model is demonstrated through a case study focused on modeling the seismic resilience of a community that comprises households with different socio-economic characteristics typical of a small U.S. community.

6.2   Background

Severe earthquakes are rare events whose occurrence can lead to catastrophic social and economic losses. The extent of these losses plays a key role in the post-disaster decision of households to stay or abandon their residence within the community. The decision to leave can profoundly influence the recovery trajectory of the overall community since population loss can lead to a reduction in the allocated federal and state disaster funds (Xiao and Van Zandt 2012).

The resulting cycle, whereby population loss leads to a reduction in the influx of disaster funds, slows down recovery and promotes further population loss. This cycle can severely hamper the long term recovery of a community. The process, which is dynamic in nature, is not well understood and provides the general motivation for this research.

The few available studies of post-event household decisions after various types of natural disasters (Brokopp et al. 2015, Nejat et al. 2016, Hikichi et al. 2017, Cong et al. 2018, and Burton et al. 2018) typically focus on three dimensions: 1) the types of decisions made by the households (repair, demolish and rebuild, abandon, etc.); 2) the factors affecting household decision (repair cost, household income, insurance coverage, etc.); and 3) the rules used to predict the decisions made by households. Chandrasekhar and Finn (2015) performed a field study after hurricane Sandy by distributing 100 surveys to homes within the Rockaways Peninsula of New York City. Three types of decisions made by households were reported: stay, undecided, or relocate. Based on the response of households to the survey, three factors were noted to affect the decisions made by households: social interaction (i.e., interaction with different civic groups and organizations), ability to find a job after the hurricane, and ability to find support from organizations to repair their damaged houses. Polese et al. (2018) studied the decisions made by different owners of severely damaged RC buildings after the L'Aquila earthquake in Italy. The study focused on the decision to repair or demolish/rebuild as a function of repair and retrofit costs, construction age, number of stories above ground, floor area, and total area covered. Markhvida and Baker (2018) proposed a framework that combines performance-based engineering with the decisions made by building owners based on real estate investment analysis. Burton et al. (2019) developed a housing recovery model that accounts for the decisions made by the households in the community after seismic events.

6.3 Motivation

None of the above studies accounted for the time-dependent nature of the problem (i.e., household decision may vary during the recovery stage) nor did they consider the influence of aftershocks, which can actually be more catastrophic than the mainshock further exacerbating the previously mentioned vicious cycle. The 2010-11 Canterbury earthquakes (Potter et al. 2015 and Wilson 2013) and the 2011 Tohoku seismic events (Nojima 2012) are prime examples of this situation. To address these limitations, this chapter employs the scalable simulation model presented in Chapter 4 through a distributed computing platform that explicitly solves the problem in a dynamic manner. The platform connects simulators, each of which addresses a particular aspect of the seismic resilience of communities (social, engineering and economic), while stepping through time. Deviating from most of the previous studies, this work incorporates household decisions at the building level rather than in an aggregate manner.

The simulation model used in this chapter employs different structural, social and economic parameters in predicting household decisions based on detailed models of each building, i.e., actual downtime and repair costs evaluated at the component level as discussed earlier in Chapter 4. These decisions are then considered in the recovery behavior of the community. Incremental dynamic analysis (IDA) (Vamvatsikos and Cornell 2002) also is used to develop fragility curves for different archetypes of buildings to accurately account for the reduction in strength of the building set due to the effect of the mainshock. The ability of the simulation model to step through time allows community response to be modeled during the different stages of the disaster, i.e., during the mainshock, recovery from mainshock, aftershocks, and recovery from aftershocks taking into account the actual state of the community at the time of the aftershock.

6.4   Simulation Model Overview

Figure 6-1 shows the simulation model implemented in this chapter, which extends the work presented in Chapter 4. The simulators are connected together through a distributed computing scheme. The simulation model explicitly models the different stages of the disaster (i.e., mainshock and aftershocks) and the recovery of the community. For the sake of simplicity, the first earthquake in the sequence is defined as the "mainshock" regardless of its magnitude, while all the subsequent ground shaking are defined as "aftershocks".

The proposed model is divided into seven different stages (appended numbers in the simulator boxes in Figure 6-1). At stage 0, the *city simulator* broadcasts the attributes of the studied community. During stage 1, *the ground motion*, *structural analysis*, *building damage*, *component damage*, *casualties*, and *debris* simulators step through time (time step in seconds) to simulate real-time seismic damage and losses associated with the mainshock. At stage 2, the *repair cost*, *downtime*, and *unsafe placard* simulators run for one time step to evaluate the final seismic losses resulting from the mainshock. During stage 3, the *available resources*, *physical recovery*, *downtime*, *household decision*, *healthcare system*, *social recovery*, and *total recovery* simulators step through time (time step in days) to simulate the real-time recovery of the community from the mainshock until the first aftershock is triggered by the *ground motion simulator*. During stages 4 and 5, the same procedures are repeated from stages 1 and 2, respectively, for the aftershocks while considering the state of the community and its buildings at the point when the aftershock occurs. The final stage, stage 6, is where the recovery of the community is simulated and the seismic resilience of the community to the mainshock/aftershock scenario is evaluated. More details about the implementation of each simulator can be found in Chapter 4.
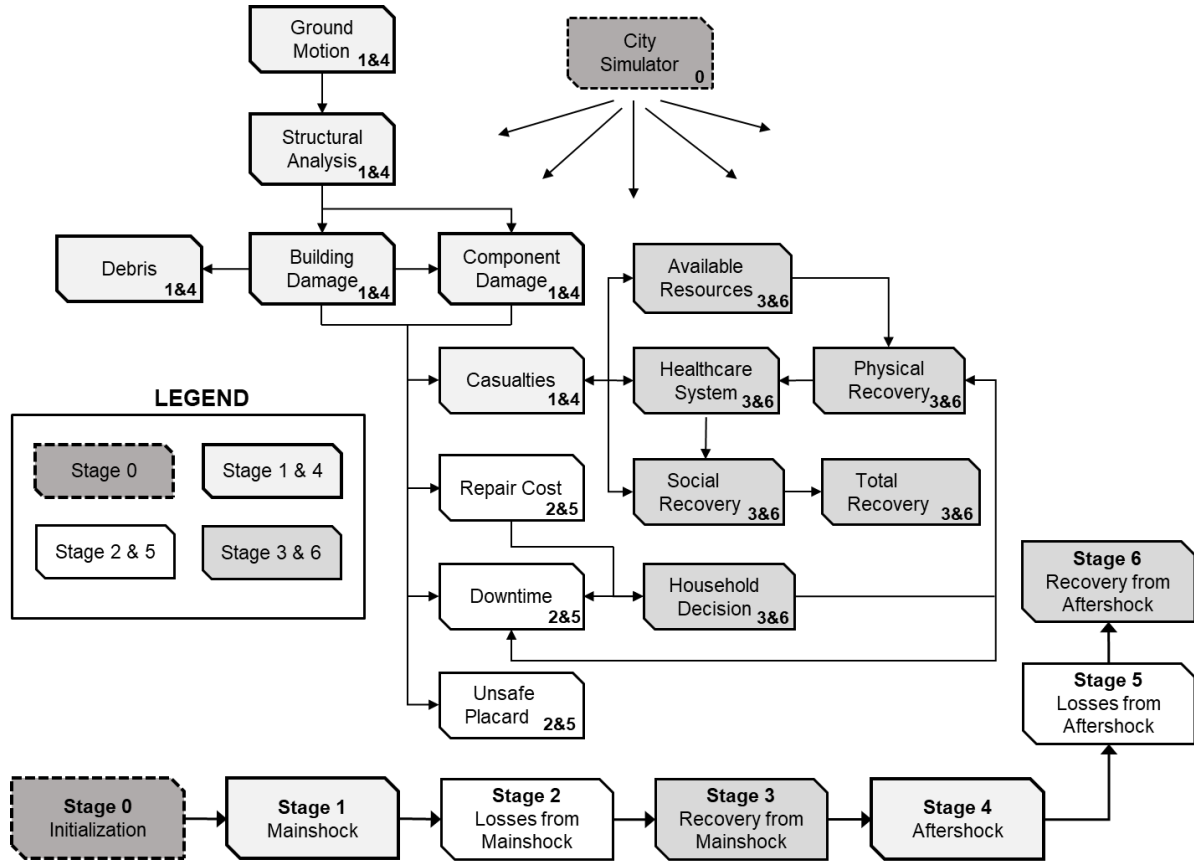
Figure 6-1 Simulation model adopted from Chapter 4 (with modifications)

6.5 Distributed Computing Platform

Distributed computing in the simulation model is enabled by the *Simple Run-Time Infrastructure* (SRTI 2019) developed at the University of Michigan under Project ICoR (Interdependencies in Community Resilience (ICoR 2019)). SRTI (2019) is designed to handle the data traffic between simulators. It ensures that data published by a simulator is directed to the simulator that needs to subscribe to it. This manner of passing data makes the proposed simulation model scalable and expandable. Adding/modifying any simulator in the model is a straightforward task where a user can add/modify any simulator without affecting the other simulators in the system as long as the outputs and inputs remain the same.

SRTI (2019) is based on a client–server structure that uses publish–subscribe techniques for data transmission between the simulators. As discussed in Lin et al. (2019), SRTI consists of three components: the RTI server, the RTI Lib API and the client (the developed simulators). All of the clients (i.e., simulators) are developed in MATLAB while the SRTI is written and pre-compiled in Java. The RTI Lib API is embedded within each simulator to enable connection to the server and enable data publication and subscription. All of the simulators are connected to the RTI server during the simulation. The server handles the message passing between the simulators in the model. First, each simulator publishes its message to the RTI server then the RTI server forwards this message to the simulators subscribed to it. The simulators and the RTI server can run on the same machine or on different machines to allow for the reuse of existing simulation models and distribution of execution cost of complex models to multiple nodes/processors. An interdisciplinary (i.e. engineering and social science) multi-Language (i.e. simulators written in different programming languages) example for using SRTI in the field of natural disasters can be found in Sediek et al. (2020d). Figure 6-2 shows the distributed computing architecture of the proposed simulation model using the SRTI server.

One of the challenges faced in the current implementation is how to handle time progression, which stems from the vastly different time scales across the various phases of the problem being modeled, i.e., time step is seconds during the earthquake and days during the recovery stage. Managing the time stepping between the simulators during the different stages of the analysis is not a straightforward task using the RTI API. The problem was solved by adding another simulator named "*Time Manager*" as shown in Figure 6-2 that is connected to the SRTI server and to each simulator in the model. The *Time Manager simulator* controls time stepping and the order of execution of the simulators within each time step.
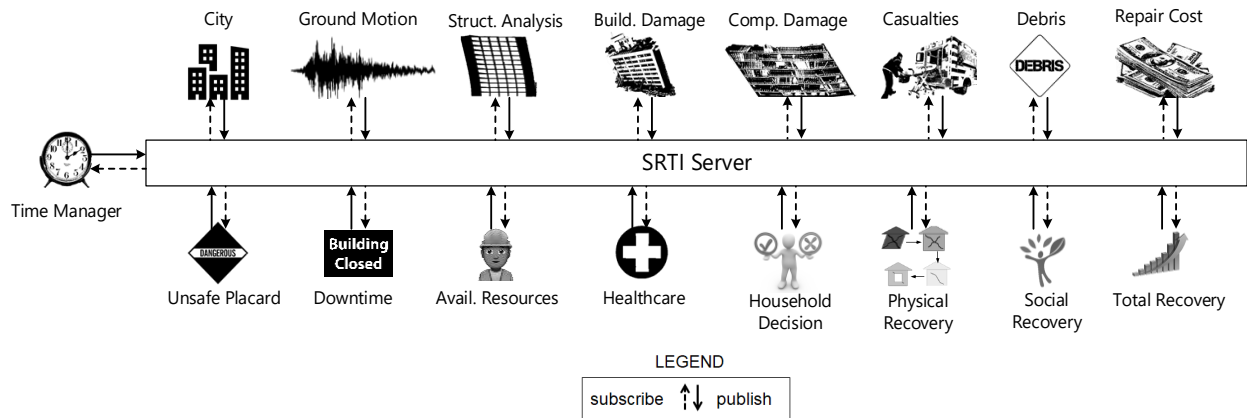
Figure 6-2 Distributed computing architecture of the proposed simulation model

6.6 Modeling Post-Earthquake Decisions of Households

The *household decision simulator* models the decision making process of a household; it (1) defines the possible decisions that can be made by the household in the wake of the earthquake, (2) defines and quantify the attributes that affect the household decision, and (3) formulates appropriate decision rule to predict household behavior. For the sake of simplicity, the simulator is limited to decisions made by those residing in single-family homes (one family per building). Decisions made by commercial building owners and residence of multifamily homes are outside the scope of this study but could conceivably be included using a similar methodology to that adopted here.

Each household in the community is assumed to make one of three possible decisions after an earthquake. The first decision is "repair", which means that the household will do all the repairs required to restore the house to full functionality as specified in FEMA P-58 (FEMA 2012a). The second alternative is "demolish", which means that the household will demolish and rebuild the house according to current seismic provisions (code A as specified earlier in Chapter 4). The last

decision is "abandon", which means that the household will leave the community without doing the first two options. In that case, the house is removed from the repair list in the *physical recovery simulator* and the functionality of that building is set to zero during the recovery stages (i.e., stage 3 and 6). Also, the population of the community is reduced by the number of persons in that house, i.e., population loss.

The decision made by households are evaluated each time step during the recovery stage (stages 3 and 6 shown in Figure 6-1) as the conditions change. However, a demolish or abandon decision is irreversible. This means that households that made a "repair" decision at a given time step will have three options in the next time step (repair, demolish or abandon). On the other hand, households that made a "demolish" decision will only have two options (demolish or abandon). Households that made an "abandon" decision cannot return to either "repair" or "demolish" decisions as their houses are removed from the repair list in the *physical recovery simulator*.

Decisions are based on the set of structural, economic and social attributes listed in Table 6-1 and are related to the socioeconomic characteristics of the household and the extent of damage the building suffered during the earthquake. Structural attributes include the construction age of the house and expected downtime, which is computed during the recovery stage by the *downtime simulator* as discussed earlier in Chapter 4. Economic attributes include the repair cost evaluated by the *repair cost simulator*, insurance coverage, household income, post-earthquake employment status, and disaster relief support received from organizations such as FEMA. Social attributes include social interaction of the household with the surrounding community, length of residence in the community, full-time residency, immigration status, racial and ethnic minority status, and affected students in the household evaluated based on the functionality of the surrounding schools in the community subscribed from the *physical recovery simulator*.

Table 6-1 Attributes and sign of weights matrix implemented in the *household decision simulator.*

Classification	Attribute	Type	Household Decision		
			Repair	Demolish	Abandon
Structural	Construction Age	Continuous	- ve	+ ve	+ ve
	Downtime	Continuous	- ve	+ ve	+ ve
Economic	Repair Cost	Continuous	- ve	+ ve	+ ve
	Insurance Coverage	Binary	+ ve	+ ve	- ve
	Household Income	Continuous	+ ve	+ ve	- ve
	Employment	Binary	+ ve	+ ve	- ve
	Support from organizations	Binary	+ ve	+ ve	- ve
Social	Social Interaction	Continuous	+ ve	+ ve	- ve
	Length of Residence	Continuous	+ ve	+ ve	- ve
	Full-time Residency	Binary	+ ve	+ ve	- ve
	Immigrants and racial and ethnic minority	Binary	- ve	- ve	+ ve
	Affected Student	Binary	- ve	- ve	+ ve

As shown in Table 6-1, the attributes affecting the decisions made by households can be classified into two types: binary or continuous. Binary attributes have only two possible values while continuous attributes can have any value within a specific range. For instance, the post-earthquake employment status of the household is a binary attribute where the possible values are employed or unemployed. However, household income is a continuous attribute that can take any value between the minimum and maximum household income in the community. A unified scale is necessary to add the effects of different types of attributes on the decisions made by households. To do so, continuous attributes, except downtime and repair cost, are first normalized using the following equation:

$$Z_i = \frac{Y_i - Y_{i,min}}{Y_{i,max} - Y_{i,min}} \tag{6-1}$$

where, Z_i is the normalized attribute i, Y_i is the value of attribute i before normalization, and $Y_{i,min}$ and $Y_{i,max}$ are the minimum and maximum values of attribute i in the studied community, respectively. The downtime and repair cost of the house are normalized with respect to the replacement time and cost of the house, respectively. For binary attributes, two values are used (1 for yes and -1 for no). For example, insurance coverage is 1 if the building is insured and -1 if uninsured. The second step is to map the normalized continuous attributes to corresponding binary values. To do so, the following formula is used:

$$X_i = \begin{cases} 1 & Z_i \geq 0.5 \\ -1 & Z_i < 0.5 \end{cases} \tag{6-2}$$

where, X_i is the mapped binary value of attribute i and Z_i is the normalized attribute i evaluated from Eq.(6-1).

The attractiveness of a decision is evaluated using the Simple Multi-Attribute Rating Technique (SMART) (Edwards 1971), which is widely used in decision problems due to its efficiency and simplicity in modeling human decisions. The SMART technique is based on a linear additive model where the overall value of a specific decision k is evaluated using the total sum of the performance score of each attribute multiplied by the weight of that attribute. The SMART technique is modified to consider both the combination of different types of attributes (i.e., continuous and binary attributes) and the different effect of each attribute on different decisions (i.e., one attribute may possess a positive effect on a decision while it possesses a negative effect on another decision). For instance, high repair cost (i.e., $X_3 = 1$) has a positive effect on "demolish" and "abandon" decisions, while it has a negative effect on the "repair" decision. The first challenge is addressed by mapping all of the attributes to an equivalent binary value (X_i),

which is used as the performance score of each attribute. The second challenge is addressed by the sign of the weights in the weight's matrix shown in Table 6-1. The key idea of the SMART technique is that the higher the total score of a specific decision, the higher expectation of the household to make that decision, and vice versa. The total score associated with each type of decision can be represented mathematically as follows:

$$U_k(t) = \sum_{i=1}^{12} w_{ik} * X_i(t) \quad \forall \, K \epsilon \{1,2,3\} \tag{6-3}$$

where $U_k(t)$ is the total score for decision k at time step t, k is an index for the available decisions (1 for repair, 2 for demolish and 3 for abandon), $X_i(t)$ is the binary value of attribute i evaluated from Eq.(6-2) at time step t, and w_{ik} is the weight that represents the effect of attribute i on decision k.

The uncertainty in the influence of the considered attributes on different decisions is considered by assuming $w_{ik}'s$ to be random variables having lognormal distributions with median of 1 and dispersion of 0.4. However, due to the scalability and adaptability of the proposed model, these values can be refined as more data becomes available from real communities (i.e., surveys from real households). After evaluating $U_k(t)$ for each decision k at time step t, the household will choose the decision with maximum $U_k(t)$. Table 6-2 shows the attributes of three different hypothetical example households in the same community (hypothetical community for illustration purposes) and Table 6-3 shows the evaluation of their post-earthquake decision to showcase the realism of the proposed model and its potential to simulate the behavior of households in the wake of earthquakes.

Table 6-2 Attributes of example households and community to showcase the realism of the proposed decision rule

Attribute	Household 1	Household 2	Household 3	Min.	Max.
Construction Age (Years)	20	40	80	5	95
Downtime (Days)	90	380	480	--	--
Replacement time (Days)	380	450	580	--	--
Repair Cost (USD)	15,000	100,000	150,000	--	--
Replacement Cost (USD)	200,000	150,000	200,000	--	--
Insurance Coverage	Yes	No	Yes	--	--
Social Interaction (%)	32%	12%	80%	5%	95%
Length of Residence (Years)	13	6	40	5	45
Household Income (USD)	60,000	80,000	120,000	30,000	200,000
Full-time Residency	Yes	Yes	Yes	--	--
Immigrants and racial and ethnic minority	No	Yes	No	--	--
Employment	Yes	No	Yes	--	--
Support from organizations	No	No	No	--	--
Affected Student	Yes	Yes	Yes	--	--

The shown data is for hypothetical households and community for illustration purposes

Table 6-3 Example of evaluating post-earthquake decisions of households using the proposed decision rule at arbitrary time t during the recovery stage.

Attribute	Household 1		Household 2		Household 3	
	Z	X	Z	X	Z	X
Construction Age (Years)	0.167	-1	0.389	-1	0.833	1
Downtime (Days)	0.237	-1	0.844	1	0.828	1
Repair Cost (USD)	0.075	-1	0.667	1	0.750	1
Insurance Coverage	--	1	--	-1	--	1
Social Interaction (%)	0.300	-1	0.078	-1	0.833	1
Length of Residence (Years)	0.200	-1	0.025	-1	0.875	1
Household Income (USD)	0.176	-1	0.294	-1	0.529	1
Full-time Residency	--	1	--	1	--	1
Immigrants and racial and ethnic minority	--	-1	--	1	--	-1
Employment	--	1	--	-1	--	1
Support from organizations	--	-1	--	-1	--	-1
Affected Student	--	1	--	1	--	1
U_1	**2.91**		-10.73		2.23	
U_2	-6.80		-3.64		**9.54**	
U_3	-2.04		**8.45**		-2.51	

Final Decision at arbitrary time t	Repair	Abandon	Demolish

The shown data is for hypothetical households and community for illustration purposes

6.7 Modeling the Aftershocks

The effect of the aftershock on the studied community is considered in the simulation model by running the same simulators from stage 1 shown in Figure 6-1 (i.e., *ground motion*, *building damage*, etc.) with updated building capacities (i.e., fragilities) to reflect damage to a building from the previous mainshock. To this end, incremental dynamic analysis (IDA: Vamvatsikos and Cornell 2002) is used to develop fragility curves for the mainshock-damaged structures in the community, which are distinguished in the presented study from the fragility curves associate with the undamaged structures. Three different building materials are considered: steel, RC, and wood buildings to simulate the distribution of building archetypes at the community level.

6.7.1 Building Models

Steel buildings are assumed to be the same as the special moment frame prototype buildings designed in NIST (2010) with four different heights: 2, 4, 8, and 20 stories. The buildings' seismic demands are assumed to be resisted by the perimeter three-bay steel special moment frames (SMFs). Thus, the behavior of the steel archetype buildings is represented by 2D concentrated plasticity *OpenSees* (McKenna et al. 2000) models of the perimeter SMFs. The modified Ibarra-Medina-Krawinkler deterioration model (Ibarra et al. 2005) is used to simulate the strength and stiffness deterioration properties due to cyclic loading while the parameters are quantified using the experimental database of Lignos and Krawinkler (2012).

RC buildings are assumed to be the same as the space special moment frame prototype buildings designed in Haselton and Deierlein (2007) and FEMA P695 (2009) with four different heights: 4, 8, 12, and 20 stories. The same abovementioned modeling approach is used to simulate the behavior of the RC archetype buildings except that the parameters of the modified Ibarra-Medina-Krawinkler deterioration model (Ibarra et al. 2005) are quantified using the equations proposed by Haselton and Deierlein (2007) based on calibration to previous flexural column tests.

The seismic demands of the wood-framed buildings are assumed to be resisted by wood shear walls. The behavior of the wood archetype buildings is represented by 3D *OpenSees* (McKenna et al. 2000) models of a conventional 2 ft × 6 ft (609.6 mm × 1828.8 mm) shear wall with overall dimensions of 8 ft × 8 ft (2438.4 mm × 2438.4 mm). The wood shear wall consists of an Oriented Strand Board (OSB) attached to horizontal and vertical framing members through equally spaced nails that provide the lateral strength to the wood shear walls. The wood framing members are modeled using elastic beam columns while the OSB is modeled using shell elements (ShellMTC4 in *OpenSees*). The nails that connect the OSB to the framing members are modeled using zero length elements. The cyclic behavior of the sheathing-to-framing connectors (i.e., the nails) is modeled using the *SAWS* material model developed by the CUREE-Caltech Wood frame Project (Folz and Filliatrault 2001) and implemented in *OpenSees* (McKenna et al. 2000). The nonlinear nailing parameters are calibrated to physical data by Kong (2015). More details about the modeling approach of wood shear walls can be found in Kong (2015).

6.7.2 Ground Motions

A suite of 22 far field ground motions (FEMA 2009) is used for both the mainshock and aftershock records. However, the aftershock records are selected randomly from the 22 ground motions to represent the variability between the mainshock and the aftershock records. The

mainshock-aftershock sequences are applied to the *OpenSees* models by applying the mainshock record, then waiting 20 seconds (i.e., applying a zero magnitude ground motion acceleration for twenty seconds of the time history) and then applying the aftershock record. The spectral acceleration at the fundamental period of each building archetype with a damping ratio of 5% (Sa (T_1, 5%)) is used as the ground motion intensity measure for the mainshock and aftershock.

6.7.3 Fragility of Intact Buildings

Incremental dynamic analysis (IDA) is performed using a total of 44 ground motion records (two components for each earthquake). The resulting IDA curves of one representative building archetype (steel 8-story SMF) are shown in Figure 6-3(a). Four damage states are defined in the developed fragility curves based on the HAZUS methodology (FEMA 2003): slight, moderate, extensive, and complete. The description of each damage state for each building archetype can be found in FEMA (2003). The engineering demand parameter (*edp*) used to define each damage state is the average inter-story drift ratio, which is defined in FEMA (2003) as the roof displacement divided by the building height. The peak *edp* for each damage state for each design code (i.e., code A, B, and C defined in Chapter 4) is defined also in FEMA (2003) and shown for the representative building archetype (with code A) in Figure 6-3(a). The resulting fragility curves for the intact steel 8-story SMF archetype are shown in Figure 6-3(b).
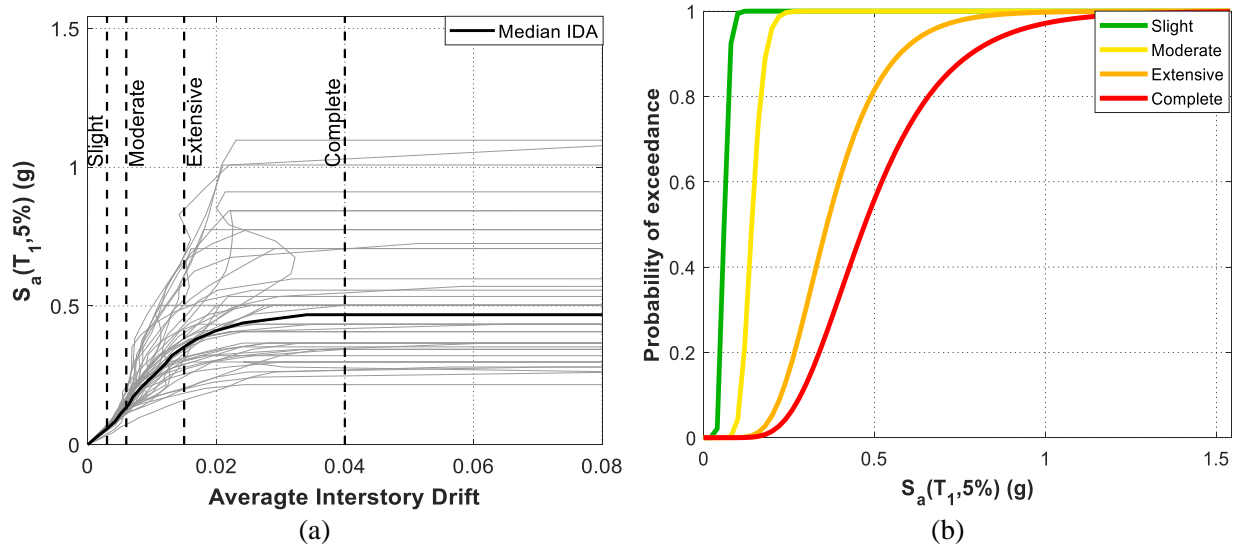
Figure 6-3 (a) IDA curves; and (b) Fragility curves of intact steel 8-story SMF building archetype

6.7.4 Fragility of Mainshock-damaged Buildings

Three different IDAs are performed for each mainshock-damaged building based on the post-mainshock damage state (i.e., slight, moderate, or extensive). The post-mainshock damage state is associated with the peak mainshock response, which is assumed to be uncertain for each damage state (Ryu et al. 2011). The peak mainshock response is assumed to have a lognormal distribution with a median equal to the median threshold for each damage state based on the limits defined in FEMA (2003) and a dispersion of 0.4 (Ryu et al. 2011). The mainshock record is scaled so that the peak mainshock response is equal to the target response. The IDA is then performed using sequences of mainshock-aftershock records where the aftershock is scaled up to collapse. Due to residual deformation resulting from the mainshock, the direction of the aftershock plays an important role in the response of the buildings. Thus, the aftershock responses are computed by applying both positive and negative scaling factors to the aftershock records and considering the larger response. These procedures are then repeated for each building archetype (total of 9), design

code (3 for each archetype) and post-mainshock damage state (3 for each archetype) resulting in a total set of 108 fragility curves (intact and damaged). The total results of the 9 considered building archetypes with latest and most stringent design code (code A) are summarized in Figure 6-4.
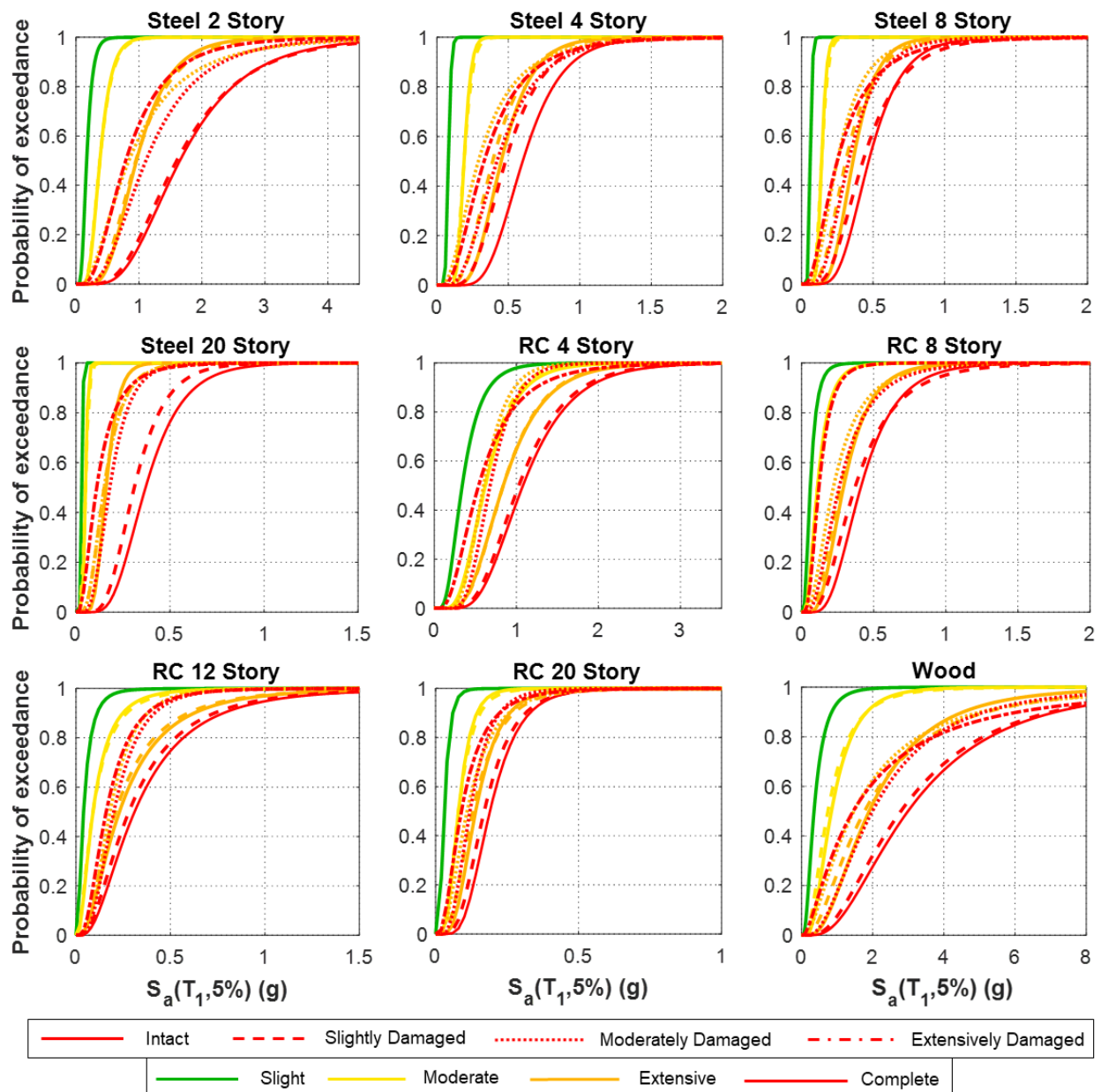
Figure 6-4 Fragility curves for intact and mainshock-damaged structures for the 9 considered archetype buildings with latest and most stringent design code

6.7.5 Fragility of Mainshock-damaged Buildings

The *building damage simulator* evaluates the new damage states of the buildings during the aftershock using the ground intensity measure at each building subscribed from the *ground motion simulator* (i.e., $S_a(T_1, 5\%)$). The new capacities of the buildings (limits of different damage states) are evaluated using the developed fragility curves based on the flowchart shown in Figure 6-5. The *component damage simulator* subscribes to the building damage states and the structural responses from the *building damage* and *structural analysis* simulators, respectively, where the new damage states of all the components are evaluated using the log-normal fitted responses (engineering demand parameters) from the IDAs described earlier based on the post-mainshock damage state of the building.

The damage states of buildings and their components during and after the aftershock stage depend on the damage states resulting from the mainshock and the repair status of the buildings at the time of the aftershock (obtained from stage 3 shown in Figure 6-1), which demonstrates the necessity of using time-dependent analysis. The *casualties simulator* subscribes to the building and component damage states in the community from the *building damage* and *component damage simulators*, respectively, to evaluate the casualties resulting from the aftershock in buildings that are in the re-occupancy functionality state (RO) (obtained from the *physical recovery simulator* at the end of stage 3 (see Figure 6-1)). Casualties in temporary shelters after the mainshock are not considered in the scope of this study. The debris, repair cost and unsafe placard status of the buildings are evaluated based on the new damage states of the buildings and their components after the aftershock (i.e., after stage 4 shown in Figure 6-1). The downtime of the building after an aftershock, DT_{AS}, is calculated using the flowchart in Figure 6-6 and:

$$DT_{AS} = T_{AS} + T_{imp}^{AS} + T_{rep}^{AS} \tag{6-4}$$

where DT_{AS} is the downtime of the building after the aftershock defined from the beginning of stage 3 (see Figure 6-1), T_{AS} is the time of the aftershock defined from the beginning of stage 3, T_{imp}^{AS} is the delay time due to the impeding factors after the aftershock defined from the beginning of stage 6 (see Figure 6-1), and T_{rep}^{AS} the time required to repair all the components in the building after the aftershock.

Based on the new seismic losses evaluated in stages 4 and 5 (see Figure 6-1), the *physical recovery simulator* evaluates the new functionality of the buildings. Then, all the simulators in stage 6 continue evaluating the recovery paths of the community considering both the mainshock and aftershock.
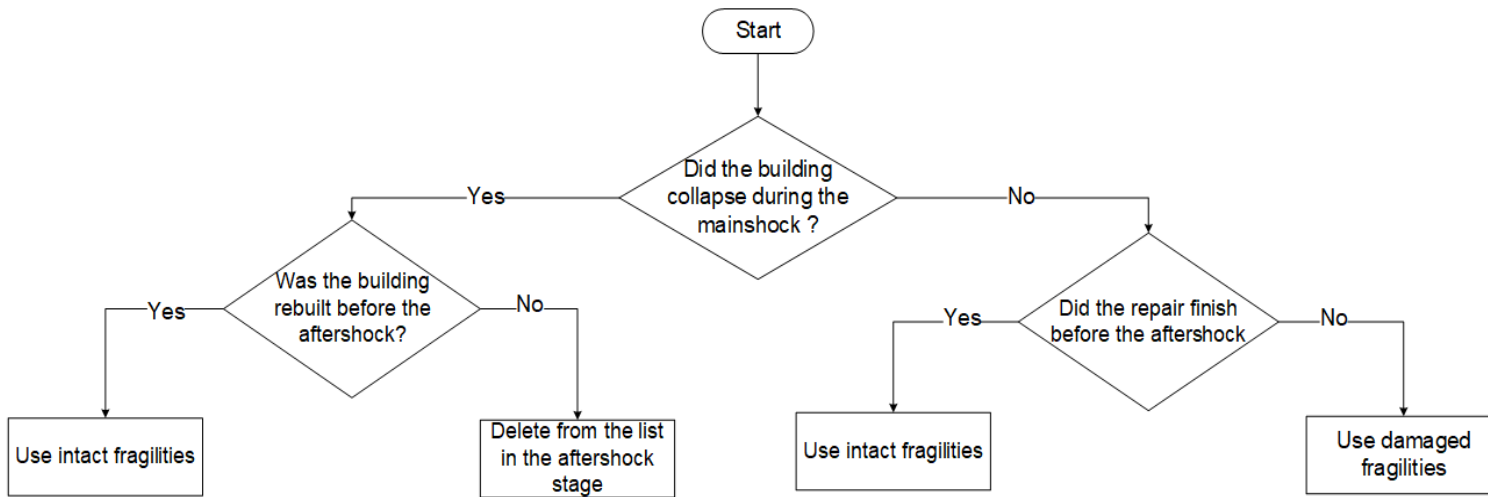
Figure 6-5 Flowchart for evaluating building capacities in the aftershock stage
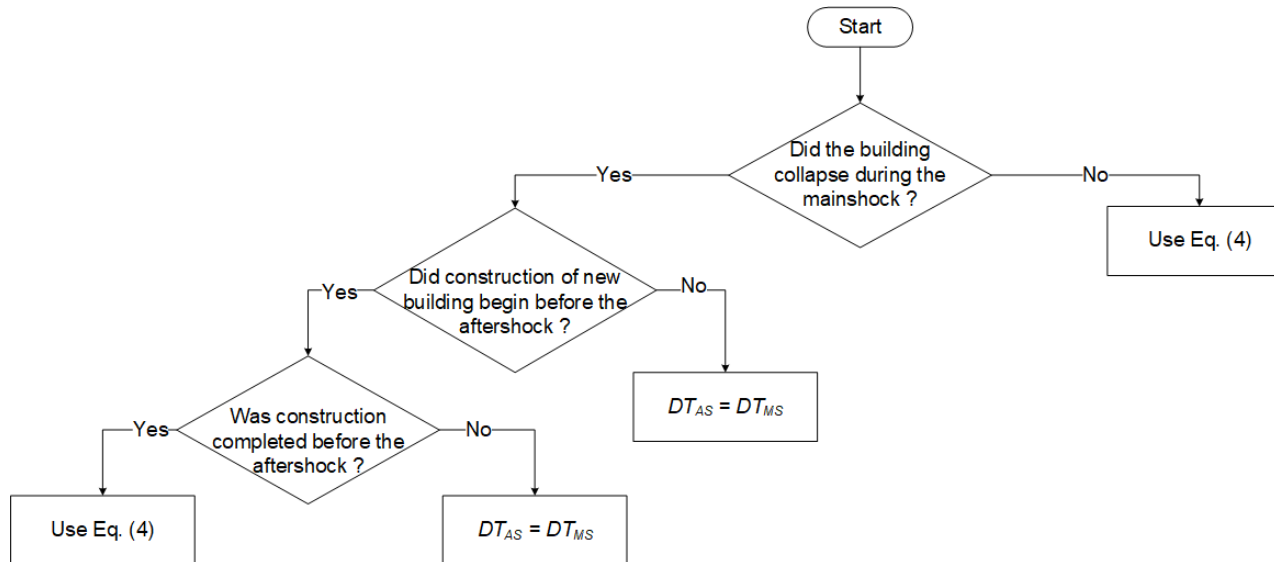
Figure 6-6 Flowchart for evaluating downtime of buildings in the aftershock stage

249

6.8   Case Study: Seismic Resilience of Pseudo City

6.8.1 Building Portfolio

A simplified community named "*Pseudo City*" is developed and modeled in order to demonstrate the capabilities of the simulation model. Figure 6-7 shows the spatial distribution of the buildings in *Pseudo City*. It consists of nine blocks or zones with a total of 1094 buildings and a population of approximately 8,000. Each zone represents households with different socioeconomic characteristics. The buildings have different occupancies, structural systems, heights and design codes leading to a total of 29 different archetypes that are listed in Table 6-4 and designated according to the naming described earlier in Chapter 4. Most of the buildings are wooden residential buildings designed according to old codes, which are typical of U.S. communities. The distribution of construction age and building type in *Pseudo City* (i.e., numbers listed in Table 6-4) is taken as the same as in Shelby county (NCSA 2018).

There are two hospitals that are 4 and 12 stories high (SFA-4-5 and CFA-12-5, respectively). The total number of beds in the hospitals before the earthquake is taken as 200 and 300 for SFA-4-5 and CFA-12-5, respectively. These numbers are chosen based on the expected injuries from an M_w 7.7 earthquake according to FEMA P-58 (FEMA 2012a). SFA-4-5 hospital is located in zone 1 while CSA-12-5 hospital is located in zone 6. Also, there are four public schools in *Pseudo City*. Two of them are elementary schools located in zone 2 and zone 5, while the other two are middle and high schools located in zone 6 and zone 1, respectively. The total number of construction workers available in *Pseudo City* before the earthquake is taken as 300, which is approximately 3.5% of the community's population representing the same percentage of construction workers in the U.S. population as per data from the Bureau of Labor Statistics (BLS

2019). Table 6-5 lists the distribution of different skilled laborers associated with repair of building infrastructure in *Pseudo City* based on the demand for each skill set evaluated using the REDi methodology (Almufti and wilford 2013). The proposed model deals with the availability of construction workers in a rigorous manner where the availability of construction workers with different skills is considered separately in the *Available Resources simulator*. The repair of the buildings is prioritized as in Chapter 4. Repair priority used in this research is as follows: hospitals, schools, residential houses, commercial buildings, retail and other occupancies.
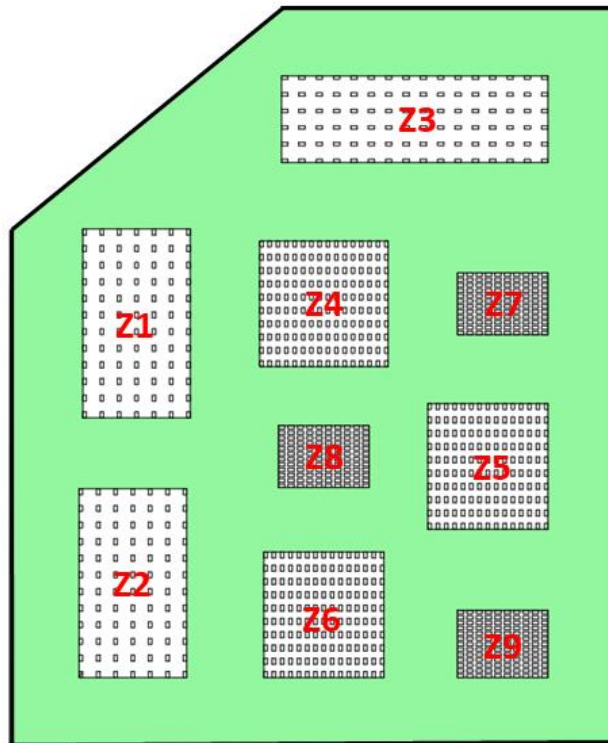
Figure 6-7 Spatial distribution of buildings in *Pseudo City*

Table 6-4 List of building archetypes and total number of each archetype in *Pseudo City*

Model	Total	Model	Total	Model	Total	Model	Total	Model	Total
CFA-12-5	1	CFB-4-1	8	SFA-4-5	1	SFC-8-1	9	WSA-2-7	11
CFA-12-9	5	CFB-8-1	9	SFA-8-1	12	SFC-8-9	4	WSB-1-7	23
CFA-20-1	8	SFA-20-1	5	SFC-20-9	2	WLA-2-7	3	WSB-2-7	12
CFA-4-9	4	SFA-2-1	9	SFC-2-1	5	WLB-2-7	3	WSC-1-7	537
CFA-8-9	3	SFA-4-1	10	SFC-4-1	6	WLC-2-7	93	WSC-2-7	272
CFB-12-1	7	SFA-4-2	4	SFC-8-1	3	WSA-1-7	25		

Table 6-5 Distribution of construction workers by skills assumed in *Pseudo City*

Worker Skill		Number of workers
Structure	RC	20
	Steel	20
	Wood	110
	Masonry	10
Exterior partitions + glazing		20
Mechanical + HVAC		10
Electrical + Elevators		10
Plumbing (pipes)		50
Partitions + Ceiling		50
Total		300

6.8.2 Socioeconomic characteristics of households

Each zone of *Pseudo City* is defined by a median household income (high income *HI*, moderate income *MI*, and low income *LI*) and the social interaction of the households within the community (high social *HS*, moderate social *MS*, and low social *LS*). The density of the buildings in each zone is assumed to be proportional to the household income level as shown in Figure 6-7. The median annual household income in *Pseudo City* is around $60,000, which is close to the national median (US Census Bureau 2017(a)). According to Pressman (2015), the income of middle class households is between 67 percent and 200 percent of the national median. Thus, low income (*LI*) is defined as below $40,000, moderate income (*MI*) is defined between $40,000 and $120,000, and high income (*HI*) is defined as above $120,000. The distribution of household income in *Pseudo City* is taken the same as the 2017 distribution of household income in the U.S. (US Census Bureau 2017 (a)).

The social interaction of a household within the community is defined by the social network possessed by the household, neighborhood civic interaction, and engagement in community activities. It is quantified by an index that describes the degree of engagement of the household in the community. In real cities, this index can be measured through surveys. For *Pseudo City*, the social interaction index of the households in the community is randomized between the different zones to have low interaction (*LS*) below 33%, moderate interaction (*MS*) between 33% and 67%, and high interaction (*HS*) above 67%. Table 6-6 shows the distribution of building occupation, household income and social interaction in different zones of *Pseudo City*.

The damage caused by earthquakes is not typically covered by a standard homeowner insurance policy in the U.S. According to the Insurance Information Institute (I.I.I 2018), only 8% of homeowners who responded to a poll in May 2016 said they have earthquake insurance. In the

Western US, this percentage can be as high as 14%. Based on these numbers, it is assumed that 10% of households in *Pseudo City* have earthquake insurance. It is also assumed that 90% of the households without insurance will receive government support after the earthquake. Modeling the interaction between the households and the government to receive disaster assistance after the earthquake is not within the scope of this study.

The length of residence of a household in *Pseudo City* is randomized with a lognormal distribution having a mean of 13 years, which is the average length of residence of households in U.S. communities (Emrath 2013). Around 25% of households in *Pseudo City* are considered racial minorities, which is the same percentage of racial minorities in the U.S. (US Census Bureau 2017 (b)). Only 41.4% of households in *Pseudo City* are assumed to have children in school (i.e., under 18 years old) matching the national average (NCES 2019). Based on national average data, 29% of these households have children in elementary or middle schools and 12.4% have children in high schools (NCES 2019). The students are assigned to the nearest school in *Pseudo City* based on the location of their home.

Table 6-6 Distribution of building occupation, household income and social interaction in different zones of *Pseudo City*

Zone	No. of Buildings	No. of Residential	No. of Commercial	No. of Schools	No. of Hospitals	No. of Retail
Z1 (*HI/HS*)	84	74	5	1	1	3
Z2 (*HI/MS*)	84	73	8	1	--	2
Z3 (*HI/LS*)	96	83	10	--	--	3
Z4 (*MI/HS*)	150	134	15	--	--	1
Z5 (*MI/MS*)	150	135	12	1	--	2
Z6 (*MI/LS*)	160	151	4	1	1	3
Z7 (*LI/HS*)	120	112	4	--	--	4
Z8 (*LI/MS*)	120	112	7	--	--	1
Z9 (*LI/LS*)	130	126	2	--	--	2

6.8.3 Seismic Hazard

Pseudo city is assumed to be located in the New Madrid seismic zone. The scenario earthquakes are assumed to have an epicenter at 35°18'N, 90°18'W as per Adachi and Ellingwood (2009). Two ground motion records are used to represent feasible seismic activity at this location: RSN 1961 (designated as EQ1) and RSN 5223 (designated as EQ2) from PEER (2019) recorded by the Lepanto Station. The ground motion records are scaled at each building location to meet the PGA for a M_w 7.7 (for EQ1) and M_w 6.3 (for EQ2) earthquake scenario specified by USGS (2018) for this location. EQ1 is assumed to occur on a weekday at 11:00 AM while EQ2 is assumed to occur also on a weekday but at 8:00 PM. Figure 6-8 shows the scaled ground motion history for the two earthquakes at the location of one arbitrary building in *Pseudo City*.
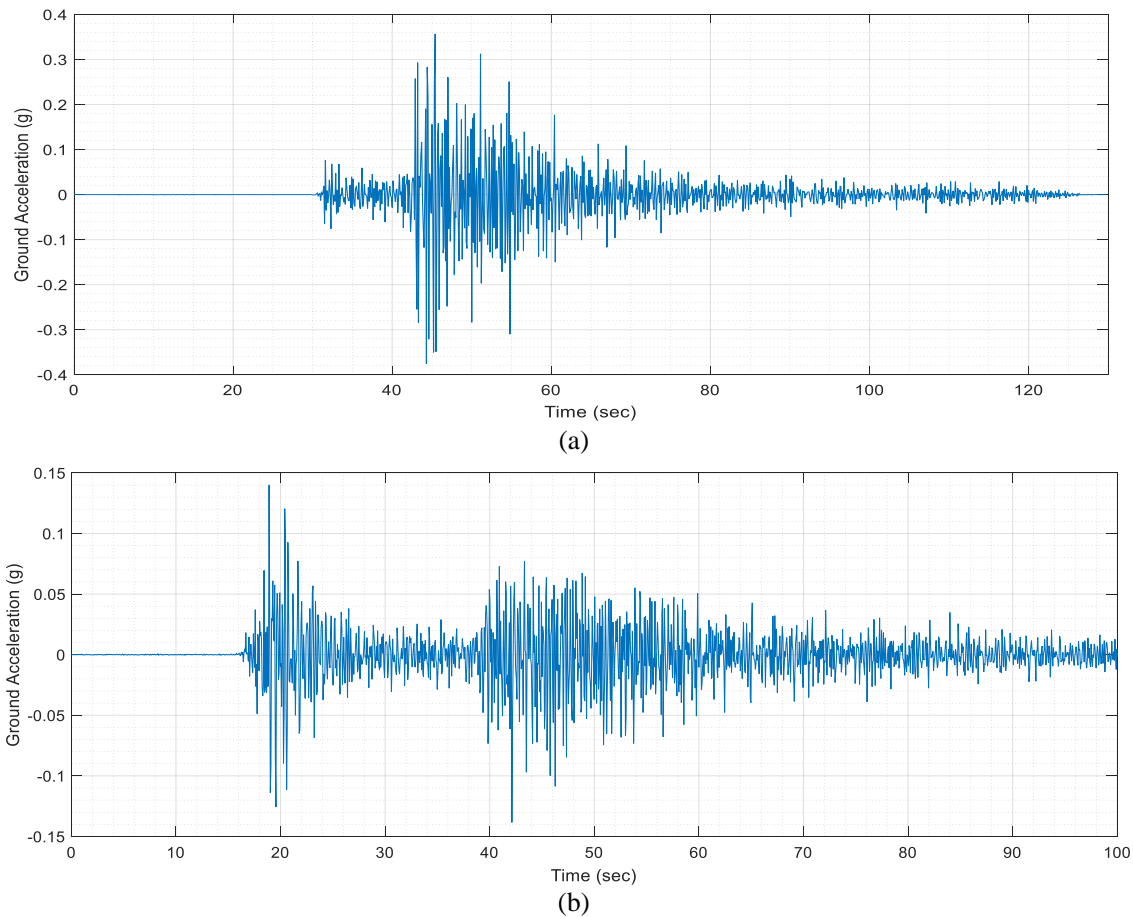
Figure 6-8 Scaled ground motion history for: (a) EQ1, and (b) EQ2

6.8.4 Effect of Post-Earthquake Household Decisions

To account for the many uncertainties in the proposed methodology (i.e., damage, loss, and household decision assessment), the proposed model uses a Monte Carlo procedure to perform seismic resilience assessment. The sampling is performed based on the distribution properties of each component specified in the FEMA P-58 methodology (FEMA 2012a) as well as the distribution of household decision weights matrix described earlier. All results presented are based on 500 realizations for each earthquake (i.e., EQ1 and EQ2). Figure 6-9(a) and (b) show the evolution of the physical recovery of *Pseudo City* after EQ1 and EQ2, respectively for the conducted Monte Carlo simulations "recovery clouds" as well as the mean recovery trajectory. The term "recovery clouds" was previously used by Burton et al. (2019) and in Chapter 4 to show the full range of possible recovery trajectories taking into consideration the inherent uncertainties in the proposed methodology. As shown, EQ1 and EQ2 reduced the functionality of the *Pseudo City* to 42% and 81% on average, respectively.

Figure 6-9(c) and (d) show the spatial distribution of post-earthquake household decisions in *Pseudo City* just after either EQ1 or EQ2 for one arbitrary Monte Carlo simulation. As shown, the percentage of households that decided to leave the community is significantly higher in zones with low to moderate household income for both earthquakes, which emphasizes the importance of considering the socioeconomic characteristics of the households in the community. Also, the percentage of households that decided to leave the community is significantly lower in zones with high social interaction for both earthquakes. After EQ1, only 2.5% of households decided to leave the community in zone 7 (*LI/HS*) while 14% of households decided to leave the community in zone 9 (*LI/LS*). Whereas, for EQ2, only 0.8% of households decided to leave the community in zone 7 (*LI/HS*) while 6.9% of households decided to leave the community in zone 9 (*LI/LS*). It

should be noted that these results are for demonstration purposes and can be refined as more data

is available.
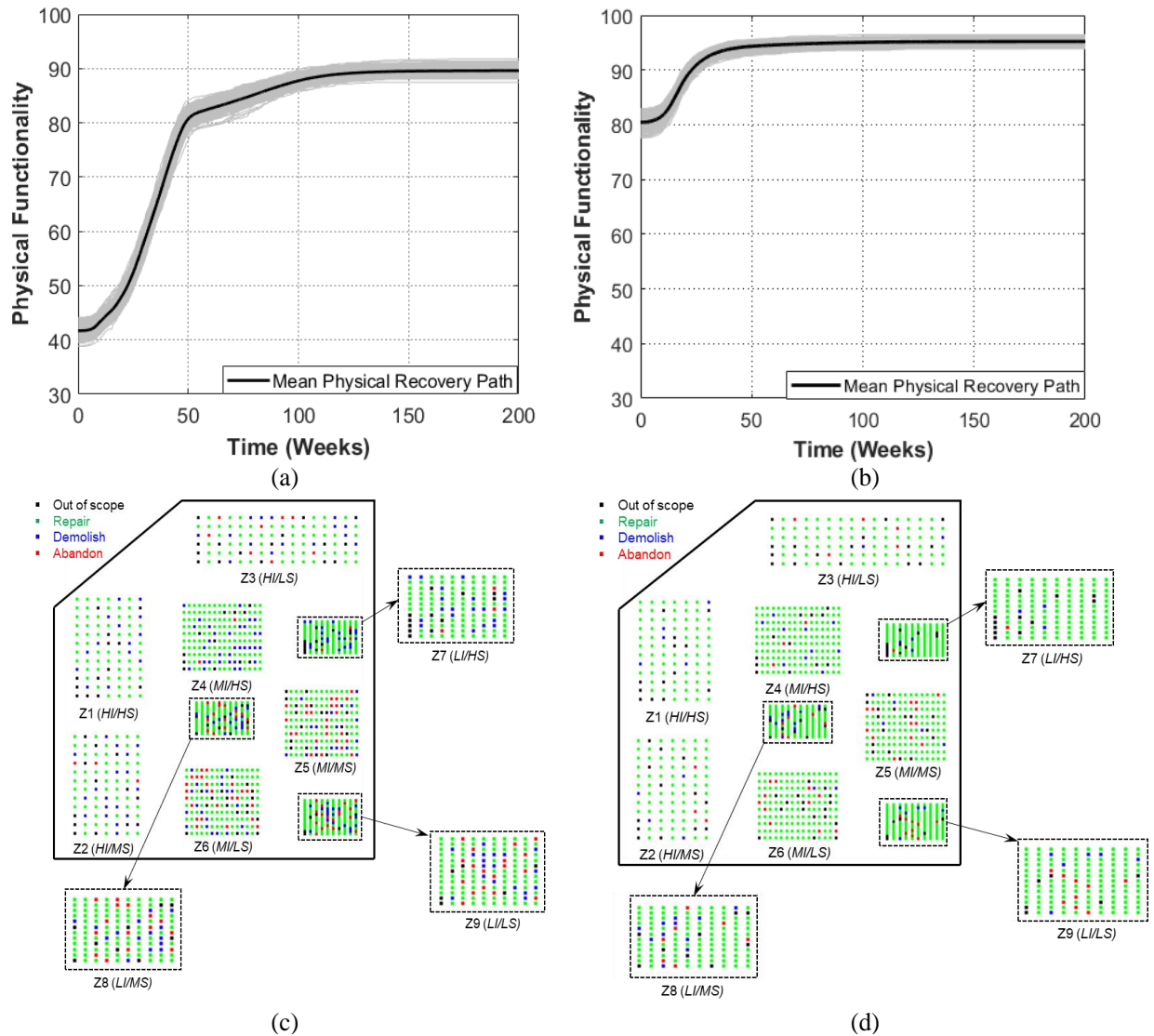
Figure 6-9 Illustration of: (a) Physical recovery trajectories for Pseudo City after EQ1, (b) Physical recovery trajectories for Pseudo City after EQ2, (c) spatial distribution of post-earthquake household decisions in Pseudo City after EQ1, and (d) spatial distribution of post-earthquake household decisions in Pseudo City after EQ2

To demonstrate the significance of considering households decisions in quantifying the

seismic resilience of communities, Figure 6-10 compares the physical recovery trajectory of

Pseudo City with and without considering the effect of household decisions on the functionality of the community for either earthquake (i.e., EQ1 and EQ2). The recovery of the community is affected in three ways: the final restored functionality ($\%Q_{max}$), the recovery time to maximum functionality (T_{RE}), and the physical resilience index defined as the normalized area under the physical recovery trajectory ($\%R_p$). *Pseudo City* recovered only 90% and 95% of its full functionality due to the abandoned houses for EQ1 and EQ2, respectively.

The recovery time (T_{RE}) decreased when considering the effect of household decisions from 160 weeks (~3.1 years) to 140 weeks (~2.7 years) and from 90 weeks (~1.7 years) to 75 weeks (~1.4 years) for EQ1 and EQ2, respectively. This decrease is attributed to the number of abandoned houses, which are removed from the repair list in the *physical functionality simulator* thereby increasing the availability of resources for repair of other buildings (i.e., availability of construction workers in the community). Finally, the physical resilience index ($\%R_p$) decreased from 93% to 85% when considering the effect of household decisions for EQ1, which is about a 10% reduction (demonstrated by the shaded area in Figure 6-10(a)) suggesting the importance of considering the interdependency between the decisions made by households after the earthquake and the functionality of communities. For EQ2, the reduction in the resilience index is only 4% (from 98% to 94%) suggesting that the effect of household decisions is only significant in the case of larger magnitude seismic events (i.e., EQ1).
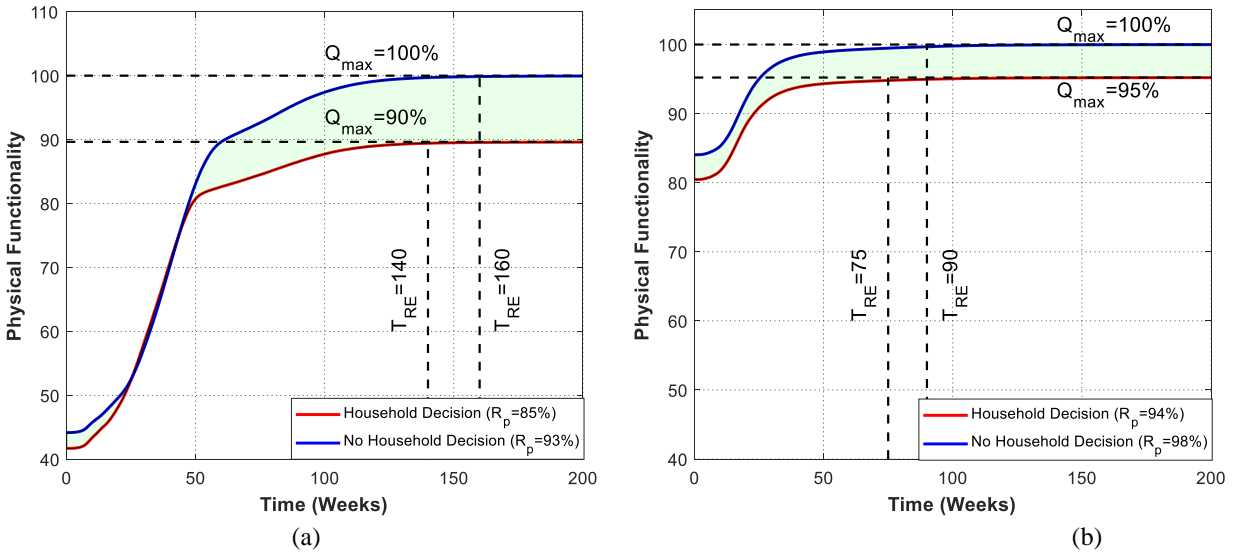
Figure 6-10 Effect of post-earthquake household decisions on the seismic resilience of *Pseudo City* for: (a) EQ1, and (b) EQ2

6.8.5 Effect of Aftershock

Two seismic scenarios are implemented to quantify the effect of aftershocks on the seismic resilience of communities. Scenario 1 includes EQ1 as a mainshock and EQ2 as an aftershock that strikes the community 5 months after the mainshock (i.e., mainshock is larger than the aftershock). Whereas scenario 2 includes EQ2 as a mainshock and EQ1 as an aftershock that strikes the community 5 months after the mainshock (i.e., aftershock is larger than the mainshock). Figure 6-11(a) and (b) show the effect of scenario 1 and 2, respectively, on the building damage states in *Pseudo City*. The mean number of buildings in the complete damage state increased dramatically due to the effect of the aftershock from 82 to 163 and from 4 to 98 in the case of scenario 1 and 2, respectively.

Scenario 1 (i.e., larger mainshock than the aftershock) has a more severe effect on the damage to buildings in *Pseudo City* (in terms of number of buildings in the complete damage state after the aftershock). Also, for scenario 1, the influence of the aftershock is more severe than the

mainshock even though the magnitude of the aftershock is smaller, which agrees with the case of the 2010-2011 Canterbury sequences (Potter et al. 2015 and Wilson 2013). This result is attributed to the reduced capacity of the damaged buildings in *Pseudo City* after the mainshock (see Figure 6-4) and the time of the aftershock (i.e., repairs are not completed on the moderately and extensively damaged buildings prior to the aftershock). Figure 6-11(c) and (d) show the decisions made by the households of *Pseudo City* after both the mainshock and the aftershock for scenario 1 and 2, respectively. For both scenarios, the mean number of households deciding to leave the community or deciding to demolish and rebuild their houses increased after the aftershock due to severe damage.

Figure 6-12 shows the recovery clouds of *Pseudo city* for the two implemented scenarios. As shown, scenario 1 has a more severe impact on the initial damage and overall recovery of *Pseudo city* than scenario 2. This result is attributed to the fact that *Pseudo city* regained most of its functionality after the lower magnitude mainshock in scenario 2 prior to the occurrence of the aftershock (most of the buildings are intact). Whereas only 50% of the cities functionality is restored after the mainshock in scenario 1 at the time of the aftershock. Thus, the recovery time increased from 200 weeks (~ 3.8 years) in scenario 2 to 270 weeks (~ 5.1 years) in scenario 1. This increase in recovery time led to a decrease in the resilience index from 82% in scenario 2 to 73% in scenario 1. It can be concluded that the effect of the aftershock is more dependent on the magnitude of the mainshock than the magnitude of the aftershock. Larger mainshock scenarios result in more damage than smaller mainshock scenarios regardless of the magnitude of the aftershock. The effect of the aftershock is also dependent on its time (i.e., percentage of buildings that regained their functionality prior to the occurrence of the aftershock).
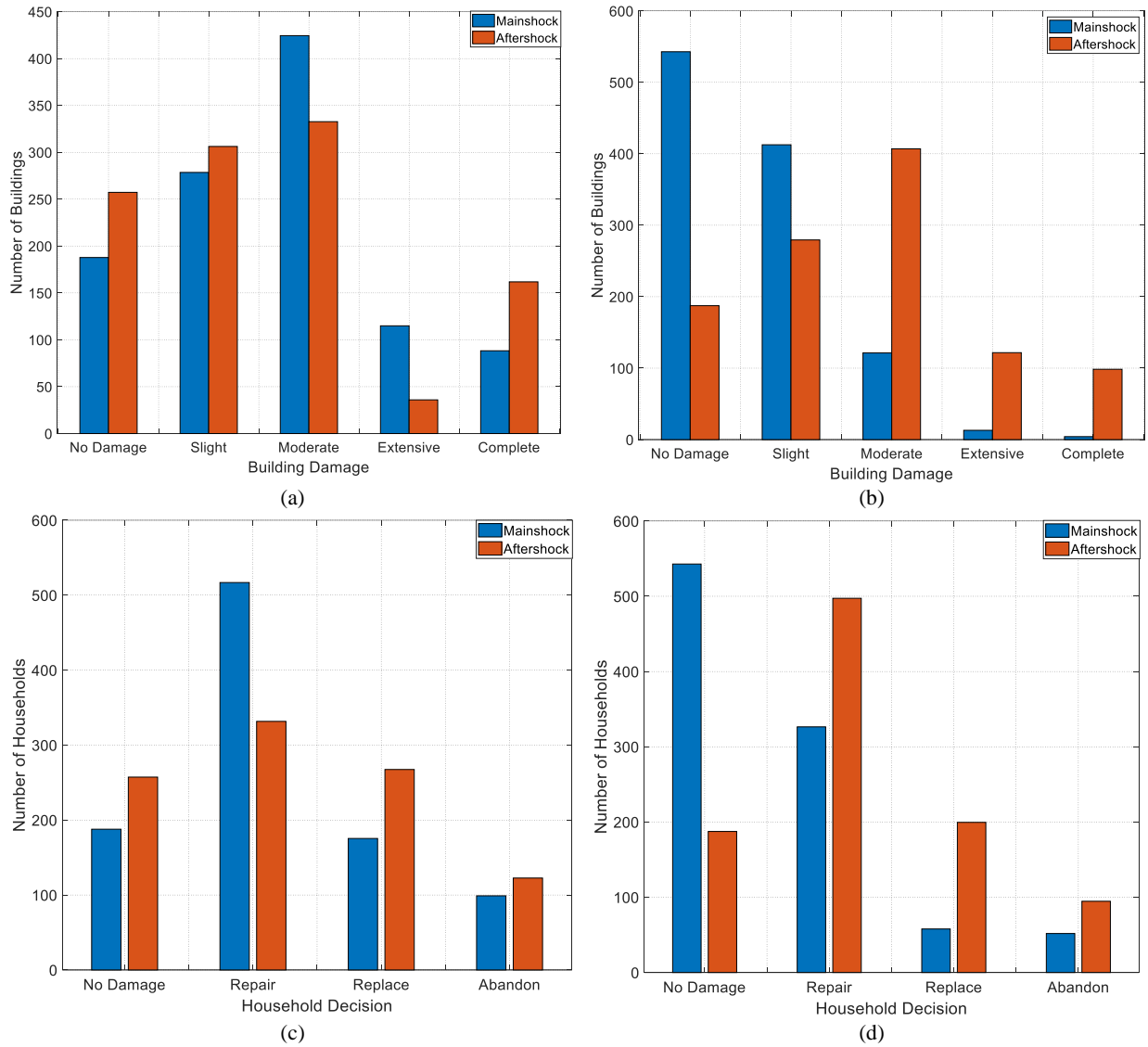
Figure 6-11 Effect of aftershock on: (a) Damage of buildings in scenario 1, (b) Damage of buildings in scenario 2, (b) Post-earthquake household decisions in scenario 1, and (b) Post-earthquake household decisions in scenario 2

To demonstrate the significance of considering the fragility curves for the mainshock-damaged building archetypes (developed earlier) in the aftershock stage, the simulation model is modified to use the fragility curves for undamaged buildings during both the mainshock and the aftershock for the two previously described scenarios. Figure 6-13 shows the mean physical recovery trajectories for both scenarios. For scenario 1, the physical resilience index decreased

261

from 82% when using the fragility curves for undamaged buildings to 73% when using the fragility curves that consider damage (12% reduction shown as the shaded area in Figure 6-13(a)). For scenario 2, the physical resilience index decreased from 84% when using the undamaged building fragility curves to 82% when using the damaged building fragility curves (only 3% reduction shown as the shaded area in Figure 6-13(b)). The presented results suggest that accurate fragility curves for the damaged buildings are important when evaluating community resistance for the case of a large mainshock scenarios. For small mainshock scenarios, the fragility curves for undamaged buildings can be used with little change in the physical recovery trajectory.

(a)   (b)
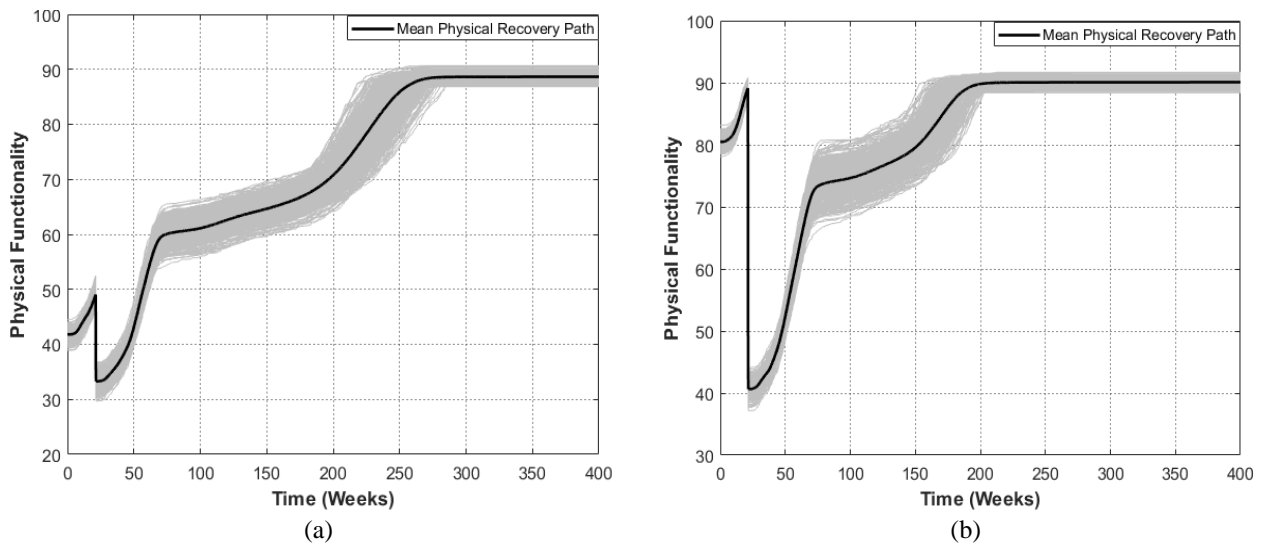
Figure 6-12 Recovery clouds for *Pseudo city* for: (a) Scenario 1, and (b) Scenario 2
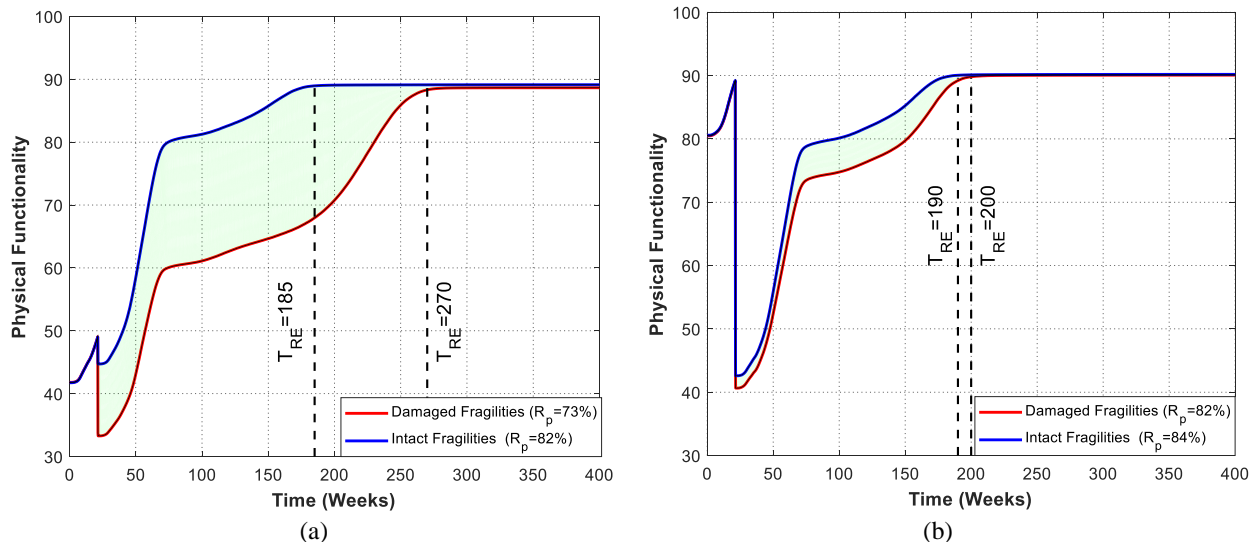
Figure 6-13 Effect of fragility curves used to represent the mainshock damaged buildings on the physical recovery trajectory of *Pseudo city* for: (a) scenario 1, and (b) scenario 2

6.9   Summary and Conclusions

This chapter presents a distributed computing simulation model that integrates post-earthquake household decisions into quantifying the seismic resilience of communities subject to earthquake sequences. Distributed computing allows simulation models (i.e., simulators) from different disciplines to "talk" to each other regardless of the background of each model. The simulation models utilize different time scales (i.e., seconds during the earthquake and days during the recovery) as they step through time during the seismic event and during the recovery process. Time management is accomplished independently in a simulator that works as a middleware between the distributed computing server and the other simulators to control the time stepping and the order of the execution of the simulators within a time step.

Post-earthquake household decision making is modeled using a Simple Multi-Attribute Rating Technique (SMART) based on a set of structural, economic and social attributes for each household in the community. Three possible decisions for each household are considered: repair the house, demolish and rebuild the house, or abandon the house. The aftershock is modeled

263

explicitly during the recovery stage from the mainshock by switching from the recovery stage (time step in days) to the earthquake stage (time step in seconds) in the *Time Manager simulator*. Incremental dynamic analysis (IDA) is used to develop fragility curves for the mainshock-damaged buildings, which are distinguished from the conventional fragility curves of undamaged buildings. The effect of the aftershock on the buildings is modeled by modifying their capacity based on the extent of damage resulting from the mainshock and the status of repairs performed during the recovery from the mainshock.

The proposed simulation model is demonstrated through a case study in which a small virtual community named "*Pseudo City*" is developed and modeled. *Pseudo City* is divided into nine zones with different socioeconomic characteristics of households. The studied community is subjected to two earthquakes with M_w 7.7 and M_w 6.3. The results show that households with low to moderate income are more likely to decide to abandon the community after an earthquake event. Also, considering the effect of the household decisions on the recovery of the community is more important in the case of large seismic events. After the M_w 7.7 event, considering the effect of the household decisions reduced the maximum restored functionality of the community by 10% on average and also reduced the resilience index by the same percentage.

The results further suggest that the developed fragility curves for damaged buildings have more significant effect on a communities recovery and resilience in large mainshock scenarios (more damaged buildings at the aftershock stage). For small mainshock scenarios, the fragility curves of undamaged buildings can be used with only small changes in the resulting recovery path and resilience. The simulation model can further be adapted to any available data from real communities to simulate and improve the performance of communities subjected to earthquakes. Applying the model to real communities will provide an efficient way to engage decision makers

264

from the government, households, and any organization concerned with improving the seismic resilience of communities.

CHAPTER 7

Summary, Conclusions and Future Research

7.1   Summary

Quantifying the seismic resilience of communities requires rigorous modeling of their behavior at disparate temporal and spatial scales, e.g., component (meters) versus system level (kilometers), or during the seismic event (seconds) versus during recovery (months). Typical communities consist of different social, engineering, and economic systems with different scales. The interdependencies between these different systems are difficult to model and therefore frequently ignored. Motivated by these needs, this dissertation investigated the seismic behavior of components with heterogeneous scales in the community (i.e., member, building, and community level studies), and further explored the effect of their behavior on the seismic resilience of communities. It also investigated the mutual interdependencies between the different systems of the community during the disaster (i.e., the seismic event) and the post-disaster recovery stages.

7.1.1 Member Level Studies

The measurements obtained from a 3D noncontact laser scanning technique for initial geometric imperfections (IGIs) in steel W-shape members were first used to propose a spectral approach that modeled the imperfections in each plate of the W-shape member as a 2D field of random vibrations. The proposed modeling approach along with the traditional modal approach were used to study the sensitivity of numerical models to initial geometric imperfections. The

studies were conducted at the member level using a set of deep steel wide flange (DSW) columns suitable for SMFs under combined axial and lateral cyclic loading.

The capabilities of different machine learning (ML) classification and regression methods were then explored in predicting the seismic collapse behavior of DSW columns based on identifying their failure mode and rotation capacity. A dataset of more than nine hundred experimental and numerical results of DSW columns with different attributes was assembled and compiled. The performance of the explored machine learning methods was compared with available methods in the literature and current specifications to predict the seismic collapse behavior of steel DSW columns that are part of SMFs.

The seismic collapse behavior of hollow structural steel (HSS) columns that are part of SMFs was also studied under combined axial and drift loading. Different HSS profiles were selected to cover a wide range of local and global slenderness ratios. Detailed finite element models of the HSS columns were created and validated against available experimental results. The simulation results were used to propose slenderness limits and design guidelines that incorporated key variables identified in the research to permit HSS columns to achieve highly ductile behavior.

7.1.2 Building Level Studies

The extent of debris generated around collapsed reinforced concrete (RC) moment frame buildings was estimated using a validated computational approach that explicitly modeled the building collapse process and subsequent formation of the debris field. A set of RC moment resisting frame structures with different heights was modeled under different ground motion records scaled to induce collapse of the building to assess the seismic debris field under different ground motion histories and building heights. The collapse modes were classified using a deep neural network (DNN) based on ground motion parameters and building height. The extent of

debris around the collapsed buildings was modeled in a probabilistic manner and then characterized using linear regression analysis. The effect of the era of the building code era in which a building was designed on the debris field extent was also investigated.

7.1.3 Community Level Studies

A scalable model that employs a simulation-based dynamic analysis was first developed. It models the behavior of the community at each time step as the seismic event occurs (time step in seconds) and as the community recovers after the event (time step in days). Iit permits explicit consideration of in-event interdependencies (i.e., during the hazard as well as the recovery stage) that can arise between the physical (i.e., buildings-related) and social (i.e., injured people-related) systems of the community and provides detailed information about the temporal and spatial distribution of injuries/fatalities during the seismic hazard. The capability of the proposed model to support hazard mitigation planning was demonstrated through a case study that highlighted the tradeoff between the physical and social costs of different mitigation strategies.

The developed scalable simulation model was then employed to model the mutual interdependencies between building portfolios, transportation networks, and healthcare systems in the community. The effect of the damage of bridges was combined with the accumulation of debris resulting from the collapse of buildings on the transportation network in the community. The post-disaster origin-destination (O-D) patterns of households along with functionality of the road network in the community were used in a traffic analysis to update the traffic flow and time through the links of the transportation network. The updated traffic flow and time were used in a discrete event simulation (DES) environment to simulate the behavior of the healthcare system as well as the debris removal process in the aftermath of a seismic event. The capability of the developed

model to support hazard mitigation planning was also demonstrated through a case study that highlighted the mutual interdependencies between the three studied systems.

To address broader socio-technical considerations in resilience research, the developed scalable simulation model was employed to integrate post-earthquake household decision making for quantifying the seismic resilience of communities subjected to earthquake sequences. A Simple Multi-Attribute Rating Technique (SMART) was used to model post-earthquake household decision making at the building level, while the earthquake sequences were modeled using time-dependent analysis during the recovery stage from the mainshock. Incremental dynamic analysis (IDA) was used to develop fragility curves for mainshock-damaged structures, which were distinguished from the conventional fragility curves of intact structures. The developed simulation model was demonstrated through a case study focused on modeling the seismic resilience of a model community that comprised households with different socio-economic characteristics to simulate a typical small U.S. community.

7.2 Conclusions

Within the scope of the studies conducted in this dissertation, the following conclusions can be drawn:

7.2.1 Member Level Studies

Initial Geometric Imperfections in Wide-Flange Steel Members

- There is weak correlation between the proposed spectral approach and the traditional approach in modeling IGIs in DSW columns. Generally, the effect of IGIs on the results of computational models of DSW columns was quite small, within 3% on average, for initial axial load levels of P/P_y of 0.4.

- Although geometric imperfections can, in certain situations, influence column buckling behavior, their effect on nonlinear cyclic behavior was generally inconsistent, in addition to being small.

- It was recommended that initial geometric imperfections need not be incorporated in high fidelity numerical models of DSW members subjected to combined axial and cyclic lateral loads. This was conditioned upon the use of an analysis platform with sufficient numerical precision to capture early small deformations that promote geometric nonlinearity in the response. This result is of significance because introducing IGIs can be a complex and time-consuming endeavor for system-level studies depending on the approach taken and complexity of the structure.

Prediction of Seismic Collapse Behavior of DSW Columns Using Machine Learning Methods

- The decision surfaces or boundaries between the failure modes of DSW columns are complex and nonlinear, which emphasizes the need for ML methods to predict the seismic collapse behavior of steel DSW columns.

- Support vector machine (SVM) and classification decision trees (CDT) had the best performance amongst all of the explored machine learning methods for predicting the seismic failure mode of DSW columns (test accuracy of 89%).

- The trained ML models were found to provide superior performance over the classification criteria for the seismic failure mode of DSW columns available in literature due to the ability to capture the highly nonlinear and complex decision surfaces between the different failure modes.

- Gaussian process regression (GPR) had the best performance amongst all of the explored methods for predicting the rotation capacity of DSW columns expressed in terms of their cumulative inelastic rotation until failure (CIR).

- The trained ML regression models were found to provide a 30% improvement in classification accuracy over the current AISC highly ductile limits for W-shape columns with respect to the number of correctly classified highly and non-highly ductile columns.

- Machine learning algorithms that are continually updated with new experimental and computational data can inform future generations of design specifications.

Collapse Behavior of HSS Columns as part of SMFs

- HSS columns experienced two modes of failure. Global failure implied that the column did not experience significant local buckling near the plastic hinge region. Local buckling failure indicated that the column experienced severe local buckling near the support. When the dominant failure mode was a global mode, width-to-thickness ratio (b/t), depth-to-thickness ratio (h/t) and global slenderness ratio (L/r_y) were significant parameters affecting the behavior of HSS columns. When the dominant failure mode was a local mode, h/t and initial axial load ratio (P/P_y) were the most influential parameters on the axial capacity of HSS columns under combined axial and lateral loading.

- The symmetric cyclic (SC) loading protocol resulted in a higher demand (i.e., more conservative) than the cyclic ratcheting (CR2) protocol. The capacity of the studied HSS columns was significantly smaller under the SC loading protocol than the CR2 protocol implying that the axial capacity of HSS columns under the SC protocol is much smaller. The local failure mode dominated in the case of the SC loading protocol due to the

271

excessive cycling experienced by the column. The amount of axial shortening of HSS columns was much higher under the SC loading protocol as well.

- Axial shortening of HSS columns was mainly controlled by the depth-to-thickness ratio (h/t) and initial axial load level (P/P_y). The amount of axial shortening of HSS columns was significantly higher for columns with higher h/t and P/P_y. Also, the amount of column shortening at 1% drift, which is commonly associated with the design performance level for immediate reoccupation of buildings after major earthquakes, was minimal for all studied columns. This finding suggested good serviceability performance of HSS columns when used in SMFs.

- HSS columns provided higher axial strength than W-shape columns for column weights less than 150 kg/m because lighter weight W-shape columns typically have smaller thicknesses resulting in larger local and global slenderness ratios. Consequently, HSS columns can be a more efficient alternative to W-shape columns in low to mid-rise SMFs.

- The finite element results were used to propose a guide for designing both interior and exterior HSS columns under combined axial and lateral loading. New highly ductile limits for h/t of interior and exterior HSS columns were proposed. The proposed expressions were formulated in a familiar format to facilitate their adoption into future design provisions.

- The results of the parametric study suggested that the current AISC high ductility limits for HSS columns are conservative for the b/t limit and unconservative for the h/t limit.

7.2.2 Building Level Studies

- The debris field generated around collapsed RC moment resisting frame buildings was characterized using three types of data: 1) the collapse mode of the building (i.e., aligned

272

or skewed), 2) the collapse direction of the building (positive or negative), and 3) the debris extent in each direction around the collapsed building.

- Four collapse modes were identified. Two of the collapse modes were aligned, i.e., the debris was aligned along one of the two orthogonal axes of the building, while the others were skewed, i.e., the majority of debris was skewed towards one of the two axes of the building. The results suggested that the aligned modes were more dominant for low-story buildings (4-story building), while the skewed modes were more dominant for taller buildings (8 and 12 story buildings).

- It was shown that a deep neural network (DNN) could be trained to accurately classify the mode of collapse of a building based on a set of input parameters related to the properties of the ground motion record and building height. The DNN was successfully able to predict the collapse mode of the studied prototype buildings with an accuracy of 92% for the training data and 82% for the test data.

- Although the scaled peak ground acceleration (PGA) that induced collapse of the considered special moment frame was larger than that for the non-ductile frame building, it was shown that the extent of the debris field was quite similar.

- A linear regression analysis of the simulation data was used to propose estimates for the extent of the debris field as a function of building height.

7.2.3 Community Level Studies

A Scalable Model for In-Event Interdependencies in Community Resilience

The proposed simulation model had several key advantages that make it well suited for community resilience computations:

- It provided fine granularity by allowing for separate treatment of each building in the community. Building seismic performance was used to calculate economic and social losses, both of which were handled in an integrated manner within the model.

- Due to its modularized nature, the proposed model was scalable and adaptable. It was designed to operate within a plug and play environment and, as such, facilitated the improvement/substitution of any discipline-specific simulator without affecting the other simulators.

- The ability to conduct in-event simulation (by explicitly stepping through time) allowed for full consideration of the interdependencies that arose between the different systems of society. For instance, without in-event simulation, it would not be possible to consider the influence of the physical recovery of the hospitals on the social recovery of the community with respect to injuries. Also, increasing the number of workers at a certain time during the recovery stage was straightforward using the current configuration.

- A key step forward was taken towards quantifying the seismic resilience of communities based on detailed loss estimation models as well as recovery models that considered the effect of multiple interdependencies between different systems of the community.

Modeling Interdependencies between Building Portfolios, Transportation Networks, and Healthcare Systems in Community Resilience

The proposed model was demonstrated through a case study in which the building portfolio, transportation network, and healthcare system in a portion of Shelby County, Tennessee, was subjected to a Mw 7.7 earthquake located northwest of Memphis. The results of one realization showed that:

- 11% of the links in the studied transportation network lost their functionality due to debris accumulation and bridge damage, which adversely affected the mobilization of injured people as well as debris removal from the community.

- Upgrading the seismic design of buildings as well as increasing the number of ambulances and hospital beds in the community reduced the number of fatalities by 50%.

- Upgrading the seismic design of buildings and increasing the number of trucks used to transport debris in the community improved the seismic resilience of the transportation network by 5%.

- Choosing the appropriate mitigation strategy to improve the seismic resilience of a community is a challenging task that depends on many factors beyond just the economic cost. For example, the mitigation actions required for the healthcare systems may have a significant economic cost. However, the social gain from such mitigation actions (i.e., reducing number of fatalities or number of injuries mobilized outside the community) may be much higher than the economic cost. The simulation model could be used by decision makers in the community to make such tradeoffs and decide on viable mitigation strategies to be executed.

Integrating Household Decisions in Quantifying the Seismic Resilience of Communities Subjected to Earthquake Sequences

The proposed simulation model was demonstrated through a case study in which a small virtual community named "*Pseudo City*" was developed and modeled. *Pseudo City* was divided into nine zones with different socioeconomic characteristics of households. The studied community was subjected to two earthquakes with M_w 7.7 and M_w 6.3. The results showed that:

- Households with low to moderate income were more likely to decide to abandon the community after an earthquake event.

- Considering the effect of the household decisions on the recovery of the community was more important in the case of large seismic events. After the M_w 7.7 event, considering the effect of the household decisions reduced the maximum restored functionality of the community by 10% on average and also reduced the resilience index by the same percentage.

- The results suggested that the developed fragility curves for damaged buildings have more significant effect on a community's recovery and resilience in large mainshock scenarios (more damaged buildings at the aftershock stage). For small mainshock scenarios, the fragility curves of undamaged buildings could be used with only small changes in the resulting recovery path and resilience.

- Applying the proposed model to real communities will provide an efficient way to engage decision makers from the government, households, and any organization concerned with improving the seismic resilience of communities.

7.3   Recommendations for Future Research

The following future research topics are recommended in the area of community resilience simulation at different spatial scales (i.e., member, building, and community level studies):

7.3.1 Member Level Studies

- Recent advances in machine learning techniques (e.g., long short-term memory (LSTM) networks) can be leveraged to develop new tools for "rapid" and "accurate" modeling of the nonlinear dynamic behavior of different types of members (e.g., columns, beams, braces, etc.) subjected to natural (e.g., seismic, wind etc.) or manmade (e.g., blast) hazards. These techniques can be substituted for classical physics-based methods that are

computationally expensive, which hinders their extensibility to consider the effect of more parameters or stochastic uncertainties of external loads.

- It is important for a resilient community to have an automated tool for rapid assessment of the safety of the buildings and critical infrastructure in the community. Drones and other automated reconnaissance methods can be used to substitute for visual inspection done by engineers after disasters, which may pose risk to their safety. Processing of the captured images can be performed using recent advances in computer vision.

7.3.2 Building Level Studies

- UAV/drone images and multi-temporal very high-resolution satellite images acquired days, weeks and months after previous and future disasters as well as commonly available textural analysis techniques (e.g., Gabor filters, Local Binary Pattern (LBP), Histogram of the Oriented Gradients (HOG), etc.) can be utilized to develop a tool that "rapidly" provides emergency teams in the community with the location and extent of building debris after disasters. This tool can help emergency teams reduce time and effort required to rescue injured and trapped people inside buildings after disasters. It can also help debris removal teams better optimize their resources to clear emergency routes and severely impacted roadways.

7.3.3 Community Level Studies

- Describing the results of community level disaster research to the lay audience (e.g., households buying disaster insurance or decision makers in the community) is challenging. Therefore, extended reality (XR) can be utilized to visualize the results of the developed simulation tools described in this dissertation. The immersive and highly

277

realistic capabilities of XR have a good chance of getting key messages about urban

disasters through to users who experience it. Being in the middle of an earthquake, seeing

buildings collapse, hearing the intense crashing and rumbling noises, observing cars

stopping in the roadways, people freezing and cowering, and seeing the overall damage

across the community can provide an effective educational experience. It can also prompt

the realization that preparedness and disaster planning is critical for rapid recovery.

Appendix A

SCNet Database

Table A-1 Properties of columns in SCNet

ID	Section	Local Slenderness		Global Slenderness	Torsional Slenderness	Boundary Conditions	Constant Axial Load (P/P_y)	Axial loading Protocol	Lateral loading Protocol	Failure Mode	CIR (rad)
		$b_f/2t_f$	h/t_w	L/r_y	$J/(S_x h_o)$						
Simulations performed by Dr. Tung-Yu Wu											
1	W24×55	6.94	54.6	116.4	0.0004	FF	0.20	C	SC	GLF	0.09
2	W24×55	6.94	54.6	116.4	0.0004	FF	0.30	C	SC	GLF	0.03
3	W24×55	6.94	54.6	116.4	0.0004	FF	0.40	C	SC	GLF	0.05
4	W24×55	6.94	54.6	116.4	0.0004	FP	0.20	C	SC	GF	0.09
5	W24×55	6.94	54.6	116.4	0.0004	FP	0.30	C	SC	GF	0.03
6	W24×55	6.94	54.6	116.4	0.0004	FP	0.40	C	SC	GF	0.01
7	W24×55	6.94	54.6	116.4	0.0004	BF	0.20	C	SC	GLF	0.27
8	W24×55	6.94	54.6	116.4	0.0004	BF	0.30	C	SC	GLF	0.22
9	W24×55	6.94	54.6	116.4	0.0004	BF	0.40	C	SC	GLF	0.15
10	W24×55	6.94	54.6	116.4	0.0004	PF	0.20	C	SC	GF	0.27
11	W24×55	6.94	54.6	116.4	0.0004	PF	0.30	C	SC	GF	0.22
12	W24×55	6.94	54.6	116.4	0.0004	PF	0.40	C	SC	GF	0.05
13	W24×55	6.94	54.6	116.4	0.0004	FF	0.20	C	AC	GLF	0.25
14	W24×55	6.94	54.6	116.4	0.0004	FF	0.30	C	AC	GLF	0.13
15	W24×55	6.94	54.6	116.4	0.0004	FF	0.40	C	AC	GLF	0.06
16	W24×55	6.94	54.6	116.4	0.0004	FP	0.20	C	AC	GLF	0.25

17	W24×55	6.94	54.6	116.4	0.0004	FP	0.30	C	AC	GF	0.13
18	W24×55	6.94	54.6	116.4	0.0004	FP	0.40	C	AC	GF	0.06
19	W24×55	6.94	54.6	116.4	0.0004	BF	0.20	C	AC	GLF	0.65
20	W24×55	6.94	54.6	116.4	0.0004	BF	0.30	C	AC	GLF	0.26
21	W24×55	6.94	54.6	116.4	0.0004	BF	0.40	C	AC	GF	0.14
22	W24×55	6.94	54.6	116.4	0.0004	PF	0.20	C	AC	GLF	0.49
23	W24×55	6.94	54.6	116.4	0.0004	PF	0.30	C	AC	GF	0.26
24	W24×55	6.94	54.6	116.4	0.0004	PF	0.40	C	AC	GF	0.14
25	W24×55	6.94	54.6	116.4	0.0004	FF	0.20	C	CR	GLF	0.47
26	W24×55	6.94	54.6	116.4	0.0004	FF	0.30	C	CR	GLF	0.18
27	W24×55	6.94	54.6	116.4	0.0004	FF	0.40	C	CR	GF	0.08
28	W24×55	6.94	54.6	116.4	0.0004	FP	0.20	C	CR	GF	0.08
29	W24×55	6.94	54.6	116.4	0.0004	FP	0.30	C	CR	GF	0.04
30	W24×55	6.94	54.6	116.4	0.0004	FP	0.40	C	CR	GF	0.02
31	W24×55	6.94	54.6	116.4	0.0004	BF	0.20	C	CR	GLF	0.47
32	W24×55	6.94	54.6	116.4	0.0004	BF	0.30	C	CR	GLF	0.18
33	W24×55	6.94	54.6	116.4	0.0004	BF	0.40	C	CR	GLF	0.08
34	W24×55	6.94	54.6	116.4	0.0004	PF	0.20	C	CR	GF	0.33
35	W24×55	6.94	54.6	116.4	0.0004	PF	0.30	C	CR	GF	0.09
36	W24×55	6.94	54.6	116.4	0.0004	PF	0.40	C	CR	GF	0.08
37	W24×55	6.94	54.6	116.4	0.0004	FF	0.20	C	CM	GF	0.49
38	W24×55	6.94	54.6	116.4	0.0004	FF	0.30	C	CM	GF	0.20
39	W24×55	6.94	54.6	116.4	0.0004	FF	0.40	C	CM	GLF	0.06
40	W24×55	6.94	54.6	116.4	0.0004	FP	0.20	C	CM	GF	0.49
41	W24×55	6.94	54.6	116.4	0.0004	FP	0.30	C	CM	GF	0.20
42	W24×55	6.94	54.6	116.4	0.0004	FP	0.40	C	CM	GF	0.06
43	W24×55	6.94	54.6	116.4	0.0004	BF	0.20	C	CM	GLF	0.49
44	W24×55	6.94	54.6	116.4	0.0004	BF	0.30	C	CM	GLF	0.10
45	W24×55	6.94	54.6	116.4	0.0004	BF	0.40	C	CM	GF	0.06
46	W24×55	6.94	54.6	116.4	0.0004	PF	0.20	C	CM	GLF	0.10

47	W24×55	6.94	54.6	116.4	0.0004	PF	0.30	C	CM	GLF	0.01
48	W24×55	6.94	54.6	116.4	0.0004	PF	0.40	C	CM	GF	0.01
49	W24×55	6.94	54.6	116.4	0.0004	FF	0.20	C	M	GF	0.14
50	W24×55	6.94	54.6	116.4	0.0004	FF	0.30	C	M	GF	0.07
51	W24×55	6.94	54.6	116.4	0.0004	FF	0.40	C	M	GF	0.03
52	W24×55	6.94	54.6	116.4	0.0004	FP	0.20	C	M	GF	0.04
53	W24×55	6.94	54.6	116.4	0.0004	FP	0.30	C	M	GF	0.02
54	W24×55	6.94	54.6	116.4	0.0004	FP	0.40	C	M	GF	0.01
55	W24×55	6.94	54.6	116.4	0.0004	BF	0.20	C	M	GLF	0.14
56	W24×55	6.94	54.6	116.4	0.0004	BF	0.30	C	M	GF	0.06
57	W24×55	6.94	54.6	116.4	0.0004	BF	0.40	C	M	GF	0.03
58	W24×55	6.94	54.6	116.4	0.0004	PF	0.20	C	M	GLF	0.09
59	W24×55	6.94	54.6	116.4	0.0004	PF	0.30	C	M	GLF	0.04
60	W24×55	6.94	54.6	116.4	0.0004	PF	0.40	C	M	GF	0.02
61	W24×176	4.81	28.7	52.2	0.0022	FF	0.20	C	SC	LF	0.95
62	W24×176	4.81	28.7	52.2	0.0022	FF	0.30	C	SC	LF	0.70
63	W24×176	4.81	28.7	52.2	0.0022	FF	0.40	C	SC	LF	0.53
64	W24×176	4.81	28.7	52.2	0.0022	FP	0.20	C	SC	LF	0.95
65	W24×176	4.81	28.7	52.2	0.0022	FP	0.30	C	SC	LF	0.48
66	W24×176	4.81	28.7	52.2	0.0022	FP	0.40	C	SC	GLF	0.29
67	W24×176	4.81	28.7	52.2	0.0022	BF	0.20	C	SC	LF	1.33
68	W24×176	4.81	28.7	52.2	0.0022	BF	0.30	C	SC	LF	1.00
69	W24×176	4.81	28.7	52.2	0.0022	BF	0.40	C	SC	LF	0.76
70	W24×176	4.81	28.7	52.2	0.0022	PF	0.20	C	SC	LF	1.79
71	W24×176	4.81	28.7	52.2	0.0022	PF	0.30	C	SC	LF	1.39
72	W24×176	4.81	28.7	52.2	0.0022	PF	0.40	C	SC	LF	0.76
73	W24×176	4.81	28.7	52.2	0.0022	FF	0.20	C	AC	LF	1.24
74	W24×176	4.81	28.7	52.2	0.0022	FF	0.30	C	AC	LF	0.94
75	W24×176	4.81	28.7	52.2	0.0022	FF	0.40	C	AC	LF	0.73
76	W24×176	4.81	28.7	52.2	0.0022	FP	0.20	C	AC	LF	0.92

77	W24×176	4.81	28.7	52.2	0.0022	FP	0.30	C	AC	LF	0.70
78	W24×176	4.81	28.7	52.2	0.0022	FP	0.40	C	AC	GLF	0.44
79	W24×176	4.81	28.7	52.2	0.0022	BF	0.20	C	AC	LF	1.24
80	W24×176	4.81	28.7	52.2	0.0022	BF	0.30	C	AC	LF	0.94
81	W24×176	4.81	28.7	52.2	0.0022	BF	0.40	C	AC	LF	0.97
82	W24×176	4.81	28.7	52.2	0.0022	PF	0.20	C	AC	LF	1.64
83	W24×176	4.81	28.7	52.2	0.0022	PF	0.30	C	AC	LF	1.27
84	W24×176	4.81	28.7	52.2	0.0022	PF	0.40	C	AC	LF	0.97
85	W24×176	4.81	28.7	52.2	0.0022	FP	0.30	C	CR	LF	0.48
86	W24×176	4.81	28.7	52.2	0.0022	FP	0.40	C	CR	GLF	0.25
87	W24×176	4.81	28.7	52.2	0.0022	FP	0.40	C	M	GLF	0.17
88	W24×176	4.81	28.7	52.2	0.0022	FP	0.30	C	CM	LF	0.50
89	W24×176	4.81	28.7	52.2	0.0022	FP	0.40	C	CM	GLF	0.33
90	W24×84	5.86	45.9	80	0.0008	FF	0.20	C	SC	GLF	0.43
91	W24×84	5.86	45.9	80	0.0008	FF	0.30	C	SC	GLF	0.23
92	W24×84	5.86	45.9	80	0.0008	FF	0.40	C	SC	GF	0.17
93	W24×84	5.86	45.9	80	0.0008	FP	0.20	C	SC	GLF	0.29
94	W24×84	5.86	45.9	80	0.0008	FP	0.30	C	SC	GLF	0.13
95	W24×84	5.86	45.9	80	0.0008	FP	0.40	C	SC	GF	0.06
96	W24×84	5.86	45.9	80	0.0008	BF	0.20	C	SC	LF	0.64
97	W24×84	5.86	45.9	80	0.0008	BF	0.30	C	SC	LF	0.47
98	W24×84	5.86	45.9	80	0.0008	BF	0.40	C	SC	LF	0.28
99	W24×84	5.86	45.9	80	0.0008	PF	0.20	C	SC	LF	0.94
100	W24×84	5.86	45.9	80	0.0008	PF	0.30	C	SC	LF	0.69
101	W24×84	5.86	45.9	80	0.0008	PF	0.40	C	SC	GLF	0.28
102	W24×84	5.86	45.9	80	0.0008	FF	0.20	C	AC	LF	0.91
103	W24×84	5.86	45.9	80	0.0008	FF	0.30	C	AC	GLF	0.41
104	W24×84	5.86	45.9	80	0.0008	FF	0.40	C	AC	GLF	0.29
105	W24×84	5.86	45.9	80	0.0008	FP	0.20	C	AC	GLF	0.50
106	W24×84	5.86	45.9	80	0.0008	FP	0.30	C	AC	GLF	0.27

107	W24×84	5.86	45.9	80	0.0008	FP	0.40	C	AC	GF	0.14
108	W24×84	5.86	45.9	80	0.0008	BF	0.20	C	AC	LF	0.91
109	W24×84	5.86	45.9	80	0.0008	BF	0.30	C	AC	LF	0.69
110	W24×84	5.86	45.9	80	0.0008	BF	0.40	C	AC	LF	0.44
111	W24×84	5.86	45.9	80	0.0008	PF	0.20	C	AC	LF	1.23
112	W24×84	5.86	45.9	80	0.0008	PF	0.30	C	AC	LF	0.69
113	W24×84	5.86	45.9	80	0.0008	PF	0.40	C	AC	GLF	0.44
114	W24×84	5.86	45.9	80	0.0008	FF	0.30	C	CR	GLF	0.48
115	W24×84	5.86	45.9	80	0.0008	FF	0.40	C	CR	GLF	0.19
116	W24×84	5.86	45.9	80	0.0008	FP	0.20	C	CR	GLF	0.31
117	W24×84	5.86	45.9	80	0.0008	FP	0.30	C	CR	GLF	0.18
118	W24×84	5.86	45.9	80	0.0008	FP	0.40	C	CR	GLF	0.08
119	W24×84	5.86	45.9	80	0.0008	BF	0.40	C	CR	GLF	0.24
120	W24×84	5.86	45.9	80	0.0008	FF	0.30	C	CM	GLF	0.50
121	W24×84	5.86	45.9	80	0.0008	FF	0.40	C	CM	GLF	0.20
122	W24×84	5.86	45.9	80	0.0008	BF	0.40	C	CM	GLF	0.32
123	W24×84	5.86	45.9	80	0.0008	PF	0.40	C	CM	LF	0.50
124	W24×84	5.86	45.9	80	0.0008	FP	0.20	C	CM	GLF	0.31
125	W24×84	5.86	45.9	80	0.0008	FP	0.30	C	CM	GLF	0.20
126	W24×84	5.86	45.9	80	0.0008	FP	0.40	C	CM	GF	0.06
127	W24×84	5.86	45.9	80	0.0008	PF	0.40	C	CR	LF	0.49
128	W24×84	5.86	45.9	80	0.0008	FF	0.40	C	M	GLF	0.18
129	W24×84	5.86	45.9	80	0.0008	FP	0.20	C	M	GLF	0.20
130	W24×84	5.86	45.9	80	0.0008	FP	0.30	C	M	GLF	0.09
131	W24×84	5.86	45.9	80	0.0008	FP	0.40	C	M	GLF	0.04
132	W24×84	5.86	45.9	80	0.0008	BF	0.40	C	M	LF	0.16
133	W24×84	5.86	45.9	80	0.0008	PF	0.40	C	M	LF	0.19
134	W24×103	4.59	39.2	78.4	0.0012	FF	0.20	C	SC	GLF	0.65
135	W24×103	4.59	39.2	78.4	0.0012	FF	0.30	C	SC	GLF	0.24
136	W24×103	4.59	39.2	78.4	0.0012	FF	0.40	C	SC	GLF	0.17

137	W24×103	4.59	39.2	78.4	0.0012	FP	0.20	C	SC	GLF	0.29
138	W24×103	4.59	39.2	78.4	0.0012	FP	0.30	C	SC	GLF	0.13
139	W24×103	4.59	39.2	78.4	0.0012	FP	0.40	C	SC	GF	0.06
140	W24×103	4.59	39.2	78.4	0.0012	BF	0.20	C	SC	GLF	0.65
141	W24×103	4.59	39.2	78.4	0.0012	BF	0.30	C	SC	LF	0.69
142	W24×103	4.59	39.2	78.4	0.0012	BF	0.40	C	SC	GLF	0.28
143	W24×103	4.59	39.2	78.4	0.0012	PF	0.20	C	SC	LF	1.32
144	W24×103	4.59	39.2	78.4	0.0012	PF	0.30	C	SC	LF	0.69
145	W24×103	4.59	39.2	78.4	0.0012	PF	0.40	C	SC	GLF	0.28
146	W24×103	4.59	39.2	78.4	0.0012	FF	0.20	C	AC	GLF	0.67
147	W24×103	4.59	39.2	78.4	0.0012	FF	0.30	C	AC	GLF	0.41
148	W24×103	4.59	39.2	78.4	0.0012	FF	0.40	C	AC	GLF	0.29
149	W24×103	4.59	39.2	78.4	0.0012	FP	0.20	C	AC	GLF	0.51
150	W24×103	4.59	39.2	78.4	0.0012	FP	0.30	C	AC	GLF	0.27
151	W24×103	4.59	39.2	78.4	0.0012	FP	0.40	C	AC	GF	0.15
152	W24×103	4.59	39.2	78.4	0.0012	BF	0.20	C	AC	LF	1.23
153	W24×103	4.59	39.2	78.4	0.0012	BF	0.30	C	AC	GLF	0.70
154	W24×103	4.59	39.2	78.4	0.0012	BF	0.40	C	AC	GLF	0.44
155	W24×103	4.59	39.2	78.4	0.0012	PF	0.20	C	AC	GLF	1.23
156	W24×103	4.59	39.2	78.4	0.0012	PF	0.30	C	AC	GLF	0.70
157	W24×103	4.59	39.2	78.4	0.0012	PF	0.40	C	AC	GLF	0.44
158	W24×103	4.59	39.2	78.4	0.0012	FF	0.30	C	CR	GLF	0.48
159	W24×103	4.59	39.2	78.4	0.0012	FF	0.40	C	CR	GLF	0.20
160	W24×103	4.59	39.2	78.4	0.0012	FP	0.20	C	CR	GLF	0.47
161	W24×103	4.59	39.2	78.4	0.0012	FP	0.30	C	CR	GF	0.12
162	W24×103	4.59	39.2	78.4	0.0012	FP	0.40	C	CR	GF	0.09
163	W24×103	4.59	39.2	78.4	0.0012	BF	0.30	C	CR	GLF	0.48
164	W24×103	4.59	39.2	78.4	0.0012	FF	0.30	C	CM	GLF	0.50
165	W24×103	4.59	39.2	78.4	0.0012	FF	0.40	C	CM	GLF	0.21
166	W24×103	4.59	39.2	78.4	0.0012	BF	0.30	C	CM	GLF	0.50

167	W24×103	4.59	39.2	78.4	0.0012	BF	0.40	C	CM	GLF	0.33
168	W24×103	4.59	39.2	78.4	0.0012	PF	0.40	C	CM	GLF	0.51
169	W24×103	4.59	39.2	78.4	0.0012	FP	0.20	C	CM	GLF	0.49
170	W24×103	4.59	39.2	78.4	0.0012	FP	0.30	C	CM	GLF	0.11
171	W24×103	4.59	39.2	78.4	0.0012	FP	0.40	C	CM	GF	0.06
172	W24×103	4.59	39.2	78.4	0.0012	BF	0.40	C	CR	GLF	0.33
173	W24×103	4.59	39.2	78.4	0.0012	PF	0.40	C	CR	GLF	0.50
174	W24×103	4.59	39.2	78.4	0.0012	FF	0.40	C	M	GLF	0.16
175	W24×103	4.59	39.2	78.4	0.0012	FP	0.20	C	M	GLF	0.11
176	W24×103	4.59	39.2	78.4	0.0012	FP	0.30	C	M	GLF	0.07
177	W24×103	4.59	39.2	78.4	0.0012	FP	0.40	C	M	GF	0.04
178	W24×103	4.59	39.2	78.4	0.0012	BF	0.40	C	M	GLF	0.17
179	W24×103	4.59	39.2	78.4	0.0012	PF	0.40	C	M	GLF	0.19
180	W24×104	8.5	43.1	54.6	0.0008	FF	0.20	C	SC	LF	0.64
181	W24×104	8.5	43.1	54.6	0.0008	FF	0.30	C	SC	LF	0.47
182	W24×104	8.5	43.1	54.6	0.0008	FF	0.40	C	SC	LF	0.28
183	W24×104	8.5	43.1	54.6	0.0008	FP	0.20	C	SC	LF	0.43
184	W24×104	8.5	43.1	54.6	0.0008	FP	0.30	C	SC	LF	0.23
185	W24×104	8.5	43.1	54.6	0.0008	FP	0.40	C	SC	LF	0.16
186	W24×104	8.5	43.1	54.6	0.0008	BF	0.20	C	SC	LF	0.64
187	W24×104	8.5	43.1	54.6	0.0008	BF	0.30	C	SC	LF	0.69
188	W24×104	8.5	43.1	54.6	0.0008	BF	0.40	C	SC	LF	0.52
189	W24×104	8.5	43.1	54.6	0.0008	PF	0.20	C	SC	LF	0.94
190	W24×104	8.5	43.1	54.6	0.0008	PF	0.30	C	SC	LF	0.69
191	W24×104	8.5	43.1	54.6	0.0008	PF	0.40	C	SC	LF	0.52
192	W24×104	8.5	43.1	54.6	0.0008	FF	0.20	C	AC	LF	0.91
193	W24×104	8.5	43.1	54.6	0.0008	FF	0.30	C	AC	LF	0.53
194	W24×104	8.5	43.1	54.6	0.0008	FF	0.40	C	AC	LF	0.43
195	W24×104	8.5	43.1	54.6	0.0008	FP	0.20	C	AC	LF	0.66
196	W24×104	8.5	43.1	54.6	0.0008	FP	0.30	C	AC	LF	0.41

197	W24×104	8.5	43.1	54.6	0.0008	FP	0.40	C	AC	LF	0.29
198	W24×104	8.5	43.1	54.6	0.0008	BF	0.20	C	AC	LF	0.91
199	W24×104	8.5	43.1	54.6	0.0008	BF	0.30	C	AC	LF	0.94
200	W24×104	8.5	43.1	54.6	0.0008	BF	0.40	C	AC	LF	0.55
201	W24×104	8.5	43.1	54.6	0.0008	PF	0.20	C	AC	LF	1.23
202	W24×104	8.5	43.1	54.6	0.0008	PF	0.30	C	AC	LF	0.94
203	W24×104	8.5	43.1	54.6	0.0008	PF	0.40	C	AC	LF	0.72
204	W24×104	8.5	43.1	54.6	0.0008	FF	0.40	C	CR	LF	0.35
205	W24×104	8.5	43.1	54.6	0.0008	FP	0.30	C	CR	LF	0.48
206	W24×104	8.5	43.1	54.6	0.0008	FF	0.40	C	CM	LF	0.32
207	W24×104	8.5	43.1	54.6	0.0008	PF	0.40	C	CM	LF	0.50
208	W24×104	8.5	43.1	54.6	0.0008	FP	0.30	C	CM	LF	0.50
209	W24×104	8.5	43.1	54.6	0.0008	FP	0.40	C	CM	LF	0.20
210	W24×104	8.5	43.1	54.6	0.0008	FP	0.40	C	CR	LF	0.19
211	W24×104	8.5	43.1	54.6	0.0008	BF	0.40	C	CR	LF	0.49
212	W24×104	8.5	43.1	54.6	0.0008	PF	0.40	C	CR	LF	0.49
213	W24×104	8.5	43.1	54.6	0.0008	FP	0.40	C	M	GLF	0.12
214	W24×131	6.7	35.6	52.5	0.0012	FF	0.20	C	SC	LF	0.95
215	W24×131	6.7	35.6	52.5	0.0012	FF	0.30	C	SC	LF	0.48
216	W24×131	6.7	35.6	52.5	0.0012	FF	0.40	C	SC	LF	0.39
217	W24×131	6.7	35.6	52.5	0.0012	FP	0.20	C	SC	LF	0.65
218	W24×131	6.7	35.6	52.5	0.0012	FP	0.30	C	SC	LF	0.48
219	W24×131	6.7	35.6	52.5	0.0012	FP	0.40	C	SC	GLF	0.29
220	W24×131	6.7	35.6	52.5	0.0012	BF	0.20	C	SC	LF	0.95
221	W24×131	6.7	35.6	52.5	0.0012	BF	0.30	C	SC	LF	0.70
222	W24×131	6.7	35.6	52.5	0.0012	BF	0.40	C	SC	LF	0.53
223	W24×131	6.7	35.6	52.5	0.0012	PF	0.20	C	SC	LF	0.95
224	W24×131	6.7	35.6	52.5	0.0012	PF	0.30	C	SC	LF	1.00
225	W24×131	6.7	35.6	52.5	0.0012	PF	0.40	C	SC	LF	0.76
226	W24×131	6.7	35.6	52.5	0.0012	FF	0.20	C	AC	LF	0.92

227	W24×131	6.7	35.6	52.5	0.0012	FF	0.30	C	AC	LF	0.70
228	W24×131	6.7	35.6	52.5	0.0012	FF	0.40	C	AC	LF	0.56
229	W24×131	6.7	35.6	52.5	0.0012	FP	0.20	C	AC	LF	0.92
230	W24×131	6.7	35.6	52.5	0.0012	FP	0.30	C	AC	LF	0.53
231	W24×131	6.7	35.6	52.5	0.0012	FP	0.40	C	AC	GLF	0.29
232	W24×131	6.7	35.6	52.5	0.0012	BF	0.20	C	AC	LF	1.24
233	W24×131	6.7	35.6	52.5	0.0012	BF	0.30	C	AC	LF	0.94
234	W24×131	6.7	35.6	52.5	0.0012	BF	0.40	C	AC	LF	0.72
235	W24×131	6.7	35.6	52.5	0.0012	PF	0.20	C	AC	LF	1.64
236	W24×131	6.7	35.6	52.5	0.0012	PF	0.30	C	AC	LF	0.94
237	W24×131	6.7	35.6	52.5	0.0012	PF	0.40	C	AC	LF	0.97
238	W24×131	6.7	35.6	52.5	0.0012	FP	0.40	C	CR	LF	0.25
239	W24×131	6.7	35.6	52.5	0.0012	BF	0.40	C	CM	LF	0.51
240	W24×131	6.7	35.6	52.5	0.0012	FP	0.40	C	CM	LF	0.33
241	W24×131	6.7	35.6	52.5	0.0012	BF	0.40	C	CR	LF	0.50
242	W24×131	6.7	35.6	52.5	0.0012	FP	0.40	C	M	LF	0.19
243	W24×162	5.31	30.6	51.1	0.0019	FF	0.20	C	SC	LF	0.96
244	W24×162	5.31	30.6	51.1	0.0019	FF	0.30	C	SC	LF	0.71
245	W24×162	5.31	30.6	51.1	0.0019	FF	0.40	C	SC	LF	0.54
246	W24×162	5.31	30.6	51.1	0.0019	FP	0.20	C	SC	LF	0.66
247	W24×162	5.31	30.6	51.1	0.0019	FP	0.30	C	SC	LF	0.49
248	W24×162	5.31	30.6	51.1	0.0019	FP	0.40	C	SC	GLF	0.29
249	W24×162	5.31	30.6	51.1	0.0019	BF	0.20	C	SC	LF	0.96
250	W24×162	5.31	30.6	51.1	0.0019	BF	0.30	C	SC	LF	0.71
251	W24×162	5.31	30.6	51.1	0.0019	BF	0.40	C	SC	LF	0.76
252	W24×162	5.31	30.6	51.1	0.0019	PF	0.20	C	SC	LF	1.33
253	W24×162	5.31	30.6	51.1	0.0019	PF	0.30	C	SC	LF	1.01
254	W24×162	5.31	30.6	51.1	0.0019	PF	0.40	C	SC	LF	0.76
255	W24×162	5.31	30.6	51.1	0.0019	FF	0.20	C	AC	LF	1.24
256	W24×162	5.31	30.6	51.1	0.0019	FF	0.30	C	AC	LF	0.95

257	W24×162	5.31	30.6	51.1	0.0019	FF	0.40	C	AC	LF	0.73
258	W24×162	5.31	30.6	51.1	0.0019	FP	0.20	C	AC	LF	0.92
259	W24×162	5.31	30.6	51.1	0.0019	FP	0.30	C	AC	LF	0.70
260	W24×162	5.31	30.6	51.1	0.0019	FP	0.40	C	AC	LF	0.44
261	W24×162	5.31	30.6	51.1	0.0019	BF	0.20	C	AC	LF	1.24
262	W24×162	5.31	30.6	51.1	0.0019	BF	0.30	C	AC	LF	0.95
263	W24×162	5.31	30.6	51.1	0.0019	BF	0.40	C	AC	LF	0.98
264	W24×162	5.31	30.6	51.1	0.0019	PF	0.20	C	AC	LF	2.13
265	W24×162	5.31	30.6	51.1	0.0019	PF	0.30	C	AC	LF	1.27
266	W24×162	5.31	30.6	51.1	0.0019	PF	0.40	C	AC	LF	0.98
267	W24×162	5.31	30.6	51.1	0.0019	FP	0.40	C	CR	GF	0.25
268	W24×162	5.31	30.6	51.1	0.0019	FP	0.40	C	CM	GLF	0.33
269	W24×162	5.31	30.6	51.1	0.0019	FP	0.40	C	M	GLF	0.19
270	W24×207	4.14	24.8	50.6	0.0030	FF	0.20	C	SC	LF	1.34
271	W24×207	4.14	24.8	50.6	0.0030	FF	0.30	C	SC	LF	1.02
272	W24×207	4.14	24.8	50.6	0.0030	FF	0.40	C	SC	GLF	0.54
273	W24×207	4.14	24.8	50.6	0.0030	FP	0.20	C	SC	LF	0.96
274	W24×207	4.14	24.8	50.6	0.0030	FP	0.30	C	SC	GF	0.49
275	W24×207	4.14	24.8	50.6	0.0030	FP	0.40	C	SC	GF	0.30
276	W24×207	4.14	24.8	50.6	0.0030	BF	0.20	C	SC	LF	1.34
277	W24×207	4.14	24.8	50.6	0.0030	BF	0.30	C	SC	LF	1.02
278	W24×207	4.14	24.8	50.6	0.0030	BF	0.40	C	SC	LF	0.77
279	W24×207	4.14	24.8	50.6	0.0030	PF	0.20	C	SC	LF	1.34
280	W24×207	4.14	24.8	50.6	0.0030	PF	0.30	C	SC	LF	1.02
281	W24×207	4.14	24.8	50.6	0.0030	PF	0.40	C	SC	LF	0.77
282	W24×207	4.14	24.8	50.6	0.0030	FF	0.20	C	AC	LF	1.65
283	W24×207	4.14	24.8	50.6	0.0030	FF	0.30	C	AC	LF	1.28
284	W24×207	4.14	24.8	50.6	0.0030	FF	0.40	C	AC	GLF	0.73
285	W24×207	4.14	24.8	50.6	0.0030	FP	0.20	C	AC	LF	1.25
286	W24×207	4.14	24.8	50.6	0.0030	FP	0.30	C	AC	GLF	0.70

287	W24×207	4.14	24.8	50.6	0.0030	FP	0.40	C	AC	GLF	0.44
288	W24×207	4.14	24.8	50.6	0.0030	BF	0.20	C	AC	LF	1.65
289	W24×207	4.14	24.8	50.6	0.0030	BF	0.30	C	AC	LF	0.95
290	W24×207	4.14	24.8	50.6	0.0030	BF	0.40	C	AC	LF	0.98
291	W24×207	4.14	24.8	50.6	0.0030	PF	0.20	C	AC	LF	1.65
292	W24×207	4.14	24.8	50.6	0.0030	PF	0.30	C	AC	LF	1.28
293	W24×207	4.14	24.8	50.6	0.0030	PF	0.40	C	AC	LF	0.98
294	W24×207	4.14	24.8	50.6	0.0030	FF	0.40	C	CR	GLF	0.50
295	W24×207	4.14	24.8	50.6	0.0030	FP	0.30	C	CR	GLF	0.49
296	W24×207	4.14	24.8	50.6	0.0030	FP	0.30	C	CM	GLF	0.50
297	W24×207	4.14	24.8	50.6	0.0030	FP	0.40	C	CM	GLF	0.33
298	W24×207	4.14	24.8	50.6	0.0030	FP	0.40	C	CR	GLF	0.25
299	W24×207	4.14	24.8	50.6	0.0030	FP	0.40	C	M	GLF	0.16
300	W24×335	2.73	15.6	48.3	0.0070	FF	0.20	C	SC	LF	1.82
301	W24×335	2.73	15.6	48.3	0.0070	FF	0.30	C	SC	GLF	1.03
302	W24×335	2.73	15.6	48.3	0.0070	FF	0.40	C	SC	GLF	0.56
303	W24×335	2.73	15.6	48.3	0.0070	FP	0.20	C	SC	LF	1.36
304	W24×335	2.73	15.6	48.3	0.0070	FP	0.30	C	SC	GF	0.51
305	W24×335	2.73	15.6	48.3	0.0070	FP	0.40	C	SC	GF	0.31
306	W24×335	2.73	15.6	48.3	0.0070	BF	0.20	C	SC	LF	1.82
307	W24×335	2.73	15.6	48.3	0.0070	BF	0.30	C	SC	LF	1.42
308	W24×335	2.73	15.6	48.3	0.0070	BF	0.40	C	SC	GLF	0.78
309	W24×335	2.73	15.6	48.3	0.0070	PF	0.20	C	SC	LF	1.82
310	W24×335	2.73	15.6	48.3	0.0070	PF	0.30	C	SC	LF	1.42
311	W24×335	2.73	15.6	48.3	0.0070	PF	0.40	C	SC	GLF	1.09
312	W24×335	2.73	15.6	48.3	0.0070	FF	0.20	C	AC	LF	2.15
313	W24×335	2.73	15.6	48.3	0.0070	FF	0.30	C	AC	GLF	1.69
314	W24×335	2.73	15.6	48.3	0.0070	FF	0.40	C	AC	GLF	0.74
315	W24×335	2.73	15.6	48.3	0.0070	FP	0.20	C	AC	LF	1.66
316	W24×335	2.73	15.6	48.3	0.0070	FP	0.30	C	AC	GLF	0.71

317	W24×335	2.73	15.6	48.3	0.0070	FP	0.40	C	AC	GLF	0.45
318	W24×335	2.73	15.6	48.3	0.0070	BF	0.20	C	AC	LF	2.15
319	W24×335	2.73	15.6	48.3	0.0070	BF	0.30	C	AC	LF	1.69
320	W24×335	2.73	15.6	48.3	0.0070	BF	0.40	C	AC	GLF	0.98
321	W24×335	2.73	15.6	48.3	0.0070	PF	0.20	C	AC	LF	2.15
322	W24×335	2.73	15.6	48.3	0.0070	PF	0.30	C	AC	LF	1.69
323	W24×335	2.73	15.6	48.3	0.0070	PF	0.40	C	AC	GLF	1.31
324	W24×335	2.73	15.6	48.3	0.0070	FP	0.30	C	CR	GF	0.49
325	W24×335	2.73	15.6	48.3	0.0070	FP	0.30	C	CM	GLF	0.50
326	W24×335	2.73	15.6	48.3	0.0070	FP	0.40	C	CM	GF	0.33
327	W24×335	2.73	15.6	48.3	0.0070	FP	0.40	C	CR	GF	0.31
328	W24×335	2.73	15.6	48.3	0.0070	FP	0.40	C	M	GLF	0.15
329	W30×148	4.44	41.6	78.9	0.0011	FF	0.20	C	SC	GLF	0.68
330	W30×148	4.44	41.6	78.9	0.0011	FF	0.30	C	SC	LF	0.50
331	W30×148	4.44	41.6	78.9	0.0011	FF	0.40	C	SC	LF	0.31
332	W30×148	4.44	41.6	78.9	0.0011	PF	0.20	C	SC	LF	0.98
333	W30×148	4.44	41.6	78.9	0.0011	PF	0.30	C	SC	LF	0.73
334	W30×148	4.44	41.6	78.9	0.0011	PF	0.40	C	SC	GLF	0.41
335	W30×148	4.44	41.6	78.9	0.0011	FF	0.20	C	AC	LF	0.93
336	W30×148	4.44	41.6	78.9	0.0011	FF	0.30	C	AC	LF	0.71
337	W30×148	4.44	41.6	78.9	0.0011	FF	0.40	C	AC	GLF	0.45
338	W30×148	4.44	41.6	78.9	0.0011	PF	0.20	C	AC	LF	1.25
339	W30×148	4.44	41.6	78.9	0.0011	PF	0.30	C	AC	GLF	0.71
340	W30×148	4.44	41.6	78.9	0.0011	PF	0.40	C	AC	LF	0.57
					Fogarty et al. (2017)						
341	W24×104	8.5	43.1	61.9	0.0008	FP	0.00	M	M	GF	0.04
342	W24×104	8.5	43.1	61.9	0.0008	FP	0.25	M	M	GF	0.04
343	W24×104	8.5	43.1	61.9	0.0008	FP	0.50	M	M	GLF	0.04
344	W24×117	7.53	39.2	61.2	0.0010	FP	0.00	M	M	GF	0.04
345	W24×117	7.53	39.2	61.2	0.0010	FP	0.25	M	M	GF	0.04

346	W24×117	7.53	39.2	61.2	0.0010	FP	0.50	M	M	GLF	0.04
347	W24×131	6.7	35.6	60.6	0.0070	FP	0.00	M	M	GF	0.04
348	W24×131	6.7	35.6	60.6	0.0070	FP	0.25	M	M	GF	0.04
349	W24×131	6.7	35.6	60.6	0.0070	FP	0.50	M	M	GF	0.04
350	W27×146	7.16	39.4	56.3	0.0010	FP	0.00	M	M	GF	0.04
351	W27×146	7.16	39.4	56.3	0.0010	FP	0.25	M	M	LF	0.04
352	W27×146	7.16	39.4	56.3	0.0010	FP	0.50	M	M	GLF	0.04
353	W27×178	5.92	32.9	55.4	0.0015	FP	0.00	M	M	GF	0.04
354	W27×178	5.92	32.9	55.4	0.0015	FP	0.25	M	M	GLF	0.04
355	W27×178	5.92	32.9	55.4	0.0015	FP	0.50	M	M	GLF	0.04
356	W27×194	5.24	31.8	54	0.0018	FP	0.00	M	M	GF	0.04
357	W27×194	5.24	31.8	54	0.0018	FP	0.25	M	M	GF	0.04
358	W27×194	5.24	31.8	54	0.0018	FP	0.50	M	M	GLF	0.04
359	W30×191	6.35	37.7	52	0.0012	FP	0.00	M	M	GF	0.04
360	W30×191	6.35	37.7	52	0.0012	FP	0.25	M	M	GLF	0.04
361	W30×191	6.35	37.7	52	0.0012	FP	0.50	M	M	GLF	0.04
362	W30×211	5.74	34.5	51.6	0.0014	FP	0.00	M	M	GF	0.04
363	W30×211	5.74	34.5	51.6	0.0014	FP	0.25	M	M	GLF	0.04
364	W30×211	5.74	34.5	51.6	0.0014	FP	0.50	M	M	GLF	0.04
365	W30×326	3.75	23.4	50	0.0033	FP	0.00	M	M	GF	0.04
366	W30×326	3.75	23.4	50	0.0033	FP	0.25	M	M	GF	0.04
367	W30×326	3.75	23.4	50	0.0033	FP	0.50	M	M	GF	0.04
368	W36×247	6.11	40.1	48.1	0.0011	FP	0.00	M	M	GF	0.04
369	W36×247	6.11	40.1	48.1	0.0011	FP	0.25	M	M	LF	0.04
370	W36×247	6.11	40.1	48.1	0.0011	FP	0.50	M	M	LF	0.04
371	W36×282	5.29	36.2	47.4	0.0014	FP	0.00	M	M	GF	0.04
372	W36×282	5.29	36.2	47.4	0.0014	FP	0.25	M	M	LF	0.04
373	W36×282	5.29	36.2	47.4	0.0014	FP	0.50	M	M	LF	0.04
374	W36×487	3.19	21.4	45.5	0.0039	FP	0.00	M	M	GF	0.04
375	W36×487	3.19	21.4	45.5	0.0039	FP	0.25	M	M	GF	0.04

376	W36×487	3.19	21.4	45.5	0.0039	FP	0.50	M	M	GF	0.04
377	W36×487	3.19	21.4	45.5	0.0039	FP	0.75	M	M	GF	0.04
Wu et al. (2018a)											
378	W24×55	6.94	54.6	80.6	0.0004	BF	0.30	M	CR	GLF	0.50
379	W24×55	6.94	54.6	80.6	0.0004	BF	0.40	M	CR	LF	0.51
380	W24×55	6.94	54.6	80.6	0.0004	BF	0.50	C	CR	LF	0.05
381	W24×76	6.61	49	81.3	0.0007	BF	0.20	M	CR	GLF	0.45
382	W24×76	6.61	49	81.3	0.0007	BF	0.25	M	CR	GLF	0.46
383	W24×76	6.61	49	81.3	0.0007	BF	0.30	M	CR	LF	0.46
384	W24×76	6.61	49	81.3	0.0007	BF	0.35	C	CR	LF	0.36
385	W24×76	6.61	49	81.3	0.0007	BF	0.40	C	CR	LF	0.36
386	W24×76	6.61	49	87.5	0.0007	BF	0.20	M	CR	GLF	0.44
387	W24×76	6.61	49	87.5	0.0007	BF	0.25	M	CR	GLF	0.45
388	W24×76	6.61	49	87.5	0.0007	BF	0.30	C	CR	GLF	0.34
389	W24×76	6.61	49	100	0.0007	BF	0.20	M	CR	GLF	0.42
390	W24×76	6.61	49	100	0.0007	BF	0.25	M	CR	GLF	0.43
391	W24×76	6.61	49	100	0.0007	BF	0.30	C	CR	GLF	0.21
392	W24×76	6.61	49	112.5	0.0007	BF	0.15	M	CR	GF	0.40
393	W24×76	6.61	49	112.5	0.0007	BF	0.20	M	CR	GF	0.41
394	W24×76	6.61	49	112.5	0.0007	BF	0.25	C	CR	GF	0.30
395	W24×76	6.61	49	112.5	0.0007	BF	0.30	C	CR	GF	0.20
396	W24×84	5.86	45.9	49.23	0.0008	BF	0.20	M	CR	LF	0.50
397	W24×84	5.86	45.9	49.23	0.0008	BF	0.30	M	CR	LF	0.51
398	W24×84	5.86	45.9	49.23	0.0008	BF	0.40	C	CR	LF	0.29
399	W24×84	5.86	45.9	55.38	0.0008	BF	0.20	M	CR	LF	0.49
400	W24×84	5.86	45.9	55.38	0.0008	BF	0.30	C	CR	LF	0.50
401	W24×84	5.86	45.9	55.38	0.0008	BF	0.40	C	CR	LF	0.40
402	W24×84	5.86	45.9	67.69	0.0008	BF	0.20	M	CR	GLF	0.47
403	W24×84	5.86	45.9	67.69	0.0008	BF	0.30	M	CR	LF	0.48
404	W24×84	5.86	45.9	67.69	0.0008	BF	0.40	C	CR	LF	0.50

405	W24×84	5.86	45.9	86.15	0.0008	BF	0.20	M	CR	GLF	0.44
406	W24×84	5.86	45.9	86.15	0.0008	BF	0.25	M	CR	GLF	0.45
407	W24×84	5.86	45.9	86.15	0.0008	BF	0.30	C	CR	GLF	0.46
408	W24×84	5.86	45.9	98.46	0.0008	BF	0.20	M	CR	GF	0.42
409	W24×84	5.86	45.9	98.46	0.0008	BF	0.25	M	CR	GF	0.43
410	W24×84	5.86	45.9	98.46	0.0008	BF	0.30	C	CR	GF	0.21
411	W24×84	5.86	45.9	116.9	0.0008	BF	0.20	M	CR	GF	0.40
412	W24×84	5.86	45.9	116.9	0.0008	BF	0.25	C	CR	GF	0.18
413	W24×103	4.59	39.2	90.46	0.0012	BF	0.20	M	CR	GLF	0.43
414	W24×103	4.59	39.2	90.46	0.0012	BF	0.25	M	CR	GLF	0.44
415	W24×103	4.59	39.2	90.46	0.0012	BF	0.30	C	CR	GLF	0.33
416	W24×103	4.59	39.2	96.74	0.0012	BF	0.20	M	CR	GF	0.43
417	W24×103	4.59	39.2	96.74	0.0012	BF	0.25	M	CR	GF	0.43
418	W24×103	4.59	39.2	96.74	0.0012	BF	0.30	C	CR	GF	0.21
419	W24×103	4.59	39.2	114.88	0.0012	BF	0.20	M	CR	GF	0.40
420	W24×103	4.59	39.2	114.88	0.0012	BF	0.25	M	CR	GF	0.41
421	W24×103	4.59	39.2	114.88	0.0012	BF	0.30	C	CR	GF	0.19
422	W24×131	6.7	35.6	60.57	0.0012	BF	0.20	M	CR	LF	0.44
423	W24×131	6.7	35.6	60.57	0.0012	BF	0.30	M	CR	LF	0.45
424	W24×131	6.7	35.6	60.57	0.0012	BF	0.40	M	CR	LF	0.47
425	W24×131	6.7	35.6	60.57	0.0012	BF	0.45	C	CR	LF	0.36
426	W24×131	6.7	35.6	68.65	0.0012	BF	0.20	M	CR	GF	0.42
427	W24×131	6.7	35.6	68.65	0.0012	BF	0.30	M	CR	LF	0.44
428	W24×131	6.7	35.6	68.65	0.0012	BF	0.40	M	CR	LF	0.45
429	W24×131	6.7	35.6	68.65	0.0012	BF	0.45	C	CR	LF	0.46
430	W24×131	6.7	35.6	80.76	0.0012	BF	0.20	M	CR	GF	0.39
431	W24×131	6.7	35.6	80.76	0.0012	BF	0.30	M	CR	GF	0.41
432	W24×131	6.7	35.6	80.76	0.0012	BF	0.35	M	CR	GLF	0.42
433	W24×131	6.7	35.6	80.76	0.0012	BF	0.40	C	CR	GLF	0.43
434	W24×162	5.31	30.6	58.96	0.0019	BF	0.20	M	CR	GF	0.44

435	W24×162	5.31	30.6	58.96	0.0019	BF	0.30	M	CR	GF	0.45
436	W24×162	5.31	30.6	58.96	0.0019	BF	0.40	M	CR	GLF	0.47
437	W24×162	5.31	30.6	58.96	0.0019	BF	0.45	M	CR	LF	0.48
438	W24×162	5.31	30.6	58.96	0.0019	BF	0.50	C	CR	LF	0.49
439	W24×162	5.31	30.6	70.75	0.0019	BF	0.20	M	CR	GF	0.41
440	W24×162	5.31	30.6	70.75	0.0019	BF	0.30	M	CR	GLF	0.43
441	W24×162	5.31	30.6	70.75	0.0019	BF	0.35	M	CR	GLF	0.44
442	W24×162	5.31	30.6	70.75	0.0019	BF	0.40	M	CR	GLF	0.45
443	W24×162	5.31	30.6	70.75	0.0019	BF	0.45	C	CR	GLF	0.34
444	W24×162	5.31	30.6	78.61	0.0019	BF	0.20	M	CR	GF	0.40
445	W24×162	5.31	30.6	78.61	0.0019	BF	0.30	M	CR	GF	0.42
446	W24×162	5.31	30.6	78.61	0.0019	BF	0.35	M	CR	GLF	0.42
447	W24×162	5.31	30.6	78.61	0.0019	BF	0.40	C	CR	GLF	0.32
448	W24×207	4.14	24.8	58.38	0.0030	BF	0.20	M	CR	GF	0.44
449	W24×207	4.14	24.8	58.38	0.0030	BF	0.30	M	CR	GF	0.46
450	W24×207	4.14	24.8	58.38	0.0030	BF	0.40	M	CR	GLF	0.47
451	W24×207	4.14	24.8	58.38	0.0030	BF	0.45	M	CR	GLF	0.48
452	W24×207	4.14	24.8	58.38	0.0030	BF	0.50	C	CR	GLF	0.37
453	W24×207	4.14	24.8	70.06	0.0030	BF	0.20	M	CR	GF	0.42
454	W24×207	4.14	24.8	70.06	0.0030	BF	0.30	M	CR	GF	0.43
455	W24×207	4.14	24.8	70.06	0.0030	BF	0.40	M	CR	GF	0.45
456	W24×207	4.14	24.8	70.06	0.0030	BF	0.45	C	CR	GF	0.34
457	W24×207	4.14	24.8	77.84	0.0030	BF	0.20	M	CR	GF	0.40
458	W24×207	4.14	24.8	77.84	0.0030	BF	0.30	M	CR	GF	0.42
459	W24×207	4.14	24.8	77.84	0.0030	BF	0.40	M	CR	GF	0.44
460	W24×207	4.14	24.8	77.84	0.0030	BF	0.45	C	CR	GF	0.33
461	W24×207	4.14	24.8	89.52	0.0030	BF	0.20	M	CR	GF	0.38
462	W24×207	4.14	24.8	89.52	0.0030	BF	0.30	M	CR	GF	0.40
463	W24×207	4.14	24.8	89.52	0.0030	BF	0.40	C	CR	GF	0.30
464	W24×335	2.73	15.6	55.73	0.0070	BF	0.20	M	CR	GLF	0.45

465	W24×335	2.73	15.6	55.73	0.0070	BF	0.25	M	CR	LF	0.45
466	W24×335	2.73	15.6	55.73	0.0070	BF	0.30	C	CR	LF	0.23
467	W24×335	2.73	15.6	59.45	0.0070	BF	0.20	M	CR	GF	0.44
468	W24×335	2.73	15.6	59.45	0.0070	BF	0.30	M	CR	GF	0.45
469	W24×335	2.73	15.6	59.45	0.0070	BF	0.40	M	CR	GF	0.47
470	W24×335	2.73	15.6	59.45	0.0070	BF	0.50	M	CR	GF	0.49
471	W24×335	2.73	15.6	59.45	0.0070	BF	0.55	C	CR	GF	0.50
472	W24×335	2.73	15.6	70.59	0.0070	BF	0.20	M	CR	GF	0.41
473	W24×335	2.73	15.6	70.59	0.0070	BF	0.30	M	CR	GF	0.43
474	W24×335	2.73	15.6	70.59	0.0070	BF	0.40	M	CR	GF	0.45
475	W24×335	2.73	15.6	70.59	0.0070	BF	0.45	M	CR	GF	0.46
476	W24×335	2.73	15.6	70.59	0.0070	BF	0.50	C	CR	GF	0.35
477	W24×335	2.73	15.6	78.02	0.0070	BF	0.20	M	CR	GF	0.40
478	W24×335	2.73	15.6	78.02	0.0070	BF	0.30	M	CR	GF	0.42
479	W24×335	2.73	15.6	78.02	0.0070	BF	0.40	M	CR	GF	0.44
480	W24×335	2.73	15.6	78.02	0.0070	BF	0.45	M	CR	GF	0.45
481	W27×102	6.03	47.1	78.10	0.0008	BF	0.20	M	CR	LF	0.46
482	W27×102	6.03	47.1	78.10	0.0008	BF	0.25	M	CR	LF	0.46
483	W27×102	6.03	47.1	78.10	0.0008	BF	0.30	C	CR	LF	0.47
484	W27×102	6.03	47.1	78.10	0.0008	BF	0.35	C	CR	LF	0.25
485	W27×102	6.03	47.1	78.10	0.0008	BF	0.40	C	CR	LF	0.25
486	W27×102	6.03	47.1	89.25	0.0008	BF	0.20	M	CR	GLF	0.44
487	W27×102	6.03	47.1	89.25	0.0008	BF	0.25	M	CR	LF	0.45
488	W27×102	6.03	47.1	89.25	0.0008	BF	0.30	M	CR	LF	0.45
489	W27×102	6.03	47.1	89.25	0.0008	BF	0.35	C	CR	LF	0.23
490	W27×102	6.03	47.1	89.25	0.0008	BF	0.40	C	CR	LF	0.24
491	W27×102	6.03	47.1	100.40	0.0008	BF	0.20	M	CR	GLF	0.42
492	W27×102	6.03	47.1	100.40	0.0008	BF	0.25	M	CR	GLF	0.43
493	W27×102	6.03	47.1	100.40	0.0008	BF	0.30	C	CR	GLF	0.21
494	W27×102	6.03	47.1	111.50	0.0008	BF	0.15	M	CR	GF	0.41

495	W27×102	6.03	47.1	111.50	0.0008	BF	0.20	M	CR	GF	0.41
496	W27×102	6.03	47.1	111.50	0.0008	BF	0.25	C	CR	GF	0.42
497	W27×102	6.03	47.1	111.50	0.0008	BF	0.30	C	CR	GF	0.20
498	W27×114	5.41	42.5	77.10	0.0009	BF	0.20	M	CR	LF	0.46
499	W27×114	5.41	42.5	77.10	0.0009	BF	0.25	M	CR	LF	0.46
500	W27×114	5.41	42.5	77.10	0.0009	BF	0.30	M	CR	LF	0.47
501	W27×114	5.41	42.5	77.10	0.0009	BF	0.35	C	CR	LF	0.36
502	W27×114	5.41	42.5	77.10	0.0009	BF	0.40	C	CR	LF	0.25
503	W27×114	5.41	42.5	88.11	0.0009	BF	0.20	M	CR	GLF	0.44
504	W27×114	5.41	42.5	88.11	0.0009	BF	0.25	M	CR	GLF	0.45
505	W27×114	5.41	42.5	88.11	0.0009	BF	0.30	M	CR	LF	0.45
506	W27×114	5.41	42.5	88.11	0.0009	BF	0.35	C	CR	LF	0.35
507	W27×114	5.41	42.5	88.11	0.0009	BF	0.40	C	CR	LF	0.24
508	W27×114	5.41	42.5	99.12	0.0009	BF	0.20	M	CR	GLF	0.42
509	W27×114	5.41	42.5	99.12	0.0009	BF	0.25	M	CR	GLF	0.43
510	W27×114	5.41	42.5	99.12	0.0009	BF	0.30	C	CR	GLF	0.21
511	W27×114	5.41	42.5	99.12	0.0009	BF	0.40	C	CR	GF	0.23
512	W27×114	5.41	42.5	115.64	0.0009	BF	0.20	M	CR	GF	0.40
513	W27×114	5.41	42.5	115.64	0.0009	BF	0.25	M	CR	GF	0.41
514	W27×114	5.41	42.5	115.64	0.0009	BF	0.30	C	CR	GF	0.19
515	W27×114	5.41	42.5	115.64	0.0009	BF	0.40	C	CR	GF	0.21
516	W27×161	6.49	36.1	52.00	0.0012	BF	0.20	M	CR	LF	0.46
517	W27×161	6.49	36.1	52.00	0.0012	BF	0.30	M	CR	LF	0.47
518	W27×161	6.49	36.1	52.00	0.0012	BF	0.35	M	CR	LF	0.48
519	W27×161	6.49	36.1	52.00	0.0012	BF	0.40	M	CR	LF	0.49
520	W27×161	6.49	36.1	52.00	0.0012	BF	0.45	M	CR	LF	0.50
521	W27×161	6.49	36.1	52.00	0.0012	BF	0.50	C	CR	LF	0.39
522	W27×161	6.49	36.1	59.43	0.0012	BF	0.20	M	CR	LF	0.44
523	W27×161	6.49	36.1	59.43	0.0012	BF	0.30	M	CR	LF	0.46
524	W27×161	6.49	36.1	59.43	0.0012	BF	0.35	M	CR	LF	0.47

525	W27×161	6.49	36.1	59.43	0.0012	BF	0.40	M	CR	LF	0.47
526	W27×161	6.49	36.1	59.43	0.0012	BF	0.45	C	CR	LF	0.37
527	W27×161	6.49	36.1	70.57	0.0012	BF	0.20	M	CR	LF	0.42
528	W27×161	6.49	36.1	70.57	0.0012	BF	0.30	M	CR	LF	0.44
529	W27×161	6.49	36.1	70.57	0.0012	BF	0.35	M	CR	LF	0.45
530	W27×161	6.49	36.1	70.57	0.0012	BF	0.40	M	CR	LF	0.45
531	W27×161	6.49	36.1	70.57	0.0012	BF	0.45	C	CR	LF	0.23
532	W27×161	6.49	36.1	77.99	0.0012	BF	0.20	M	CR	GF	0.41
533	W27×161	6.49	36.1	77.99	0.0012	BF	0.30	M	CR	GLF	0.42
534	W27×161	6.49	36.1	77.99	0.0012	BF	0.35	M	CR	GLF	0.43
535	W27×161	6.49	36.1	77.99	0.0012	BF	0.40	M	CR	GLF	0.44
536	W27×161	6.49	36.1	77.99	0.0012	BF	0.45	C	CR	GLF	0.22
537	W27×217	4.71	28.7	50.60	0.0022	BF	0.20	M	CR	LF	0.46
538	W27×217	4.71	28.7	50.60	0.0022	BF	0.30	M	CR	LF	0.48
539	W27×217	4.71	28.7	50.60	0.0022	BF	0.40	M	CR	LF	0.49
540	W27×217	4.71	28.7	50.60	0.0022	BF	0.45	M	CR	LF	0.50
541	W27×217	4.71	28.7	50.60	0.0022	BF	0.50	M	CR	LF	0.50
542	W27×217	4.71	28.7	57.83	0.0022	BF	0.20	M	CR	LF	0.45
543	W27×217	4.71	28.7	57.83	0.0022	BF	0.30	M	CR	LF	0.46
544	W27×217	4.71	28.7	57.83	0.0022	BF	0.40	M	CR	LF	0.48
545	W27×217	4.71	28.7	57.83	0.0022	BF	0.45	M	CR	LF	0.48
546	W27×217	4.71	28.7	57.83	0.0022	BF	0.50	C	CR	LF	0.49
547	W27×217	4.71	28.7	68.67	0.0022	BF	0.20	M	CR	GF	0.42
548	W27×217	4.71	28.7	68.67	0.0022	BF	0.30	M	CR	GF	0.44
549	W27×217	4.71	28.7	68.67	0.0022	BF	0.35	M	CR	GLF	0.45
550	W27×217	4.71	28.7	68.67	0.0022	BF	0.40	M	CR	GLF	0.46
551	W27×217	4.71	28.7	68.67	0.0022	BF	0.45	M	CR	GLF	0.47
552	W27×217	4.71	28.7	68.67	0.0022	BF	0.50	C	CR	GLF	0.36
553	W27×217	4.71	28.7	79.51	0.0022	BF	0.20	M	CR	GF	0.40
554	W27×217	4.71	28.7	79.51	0.0022	BF	0.30	M	CR	GF	0.42

555	W27×217	4.71	28.7	79.51	0.0022	BF	0.35	M	CR	GF	0.43
556	W27×217	4.71	28.7	79.51	0.0022	BF	0.40	M	CR	GF	0.44
557	W27×217	4.71	28.7	79.51	0.0022	BF	0.45	C	CR	GF	0.33
558	W27×368	2.96	17.3	48.30	0.0057	BF	0.20	M	CR	GF	0.47
559	W27×368	2.96	17.3	48.30	0.0057	BF	0.30	M	CR	GF	0.48
560	W27×368	2.96	17.3	48.30	0.0057	BF	0.40	M	CR	GF	0.49
561	W27×368	2.96	17.3	48.30	0.0057	BF	0.45	M	CR	GLF	0.50
562	W27×368	2.96	17.3	48.30	0.0057	BF	0.50	M	CR	GLF	0.51
563	W27×368	2.96	17.3	48.30	0.0057	BF	0.55	M	CR	GLF	0.51
564	W27×368	2.96	17.3	58.65	0.0057	BF	0.20	M	CR	GF	0.44
565	W27×368	2.96	17.3	58.65	0.0057	BF	0.30	M	CR	GF	0.46
566	W27×368	2.96	17.3	58.65	0.0057	BF	0.40	M	CR	GF	0.47
567	W27×368	2.96	17.3	58.65	0.0057	BF	0.45	M	CR	GF	0.48
568	W27×368	2.96	17.3	58.65	0.0057	BF	0.50	M	CR	GF	0.49
569	W27×368	2.96	17.3	58.65	0.0057	BF	0.55	C	CR	GF	0.27
570	W27×368	2.96	17.3	69.00	0.0057	BF	0.20	M	CR	GF	0.42
571	W27×368	2.96	17.3	69.00	0.0057	BF	0.30	M	CR	GF	0.44
572	W27×368	2.96	17.3	69.00	0.0057	BF	0.40	M	CR	GF	0.46
573	W27×368	2.96	17.3	69.00	0.0057	BF	0.45	M	CR	GF	0.46
574	W27×368	2.96	17.3	69.00	0.0057	BF	0.50	C	CR	GF	0.47
575	W27×368	2.96	17.3	79.35	0.0057	BF	0.20	M	CR	GF	0.40
576	W27×368	2.96	17.3	79.35	0.0057	BF	0.30	M	CR	GF	0.42
577	W27×368	2.96	17.3	79.35	0.0057	BF	0.40	M	CR	GF	0.44
578	W27×368	2.96	17.3	79.35	0.0057	BF	0.45	M	CR	GF	0.45
579	W27×368	2.96	17.3	79.35	0.0057	BF	0.50	C	CR	GF	0.23
580	W30×108	6.89	49.6	83.70	0.0006	BF	0.20	M	CR	LF	0.46
581	W30×108	6.89	49.6	83.70	0.0006	BF	0.25	M	CR	LF	0.46
582	W30×108	6.89	49.6	83.70	0.0006	BF	0.30	C	CR	LF	0.24
583	W30×108	6.89	49.6	89.28	0.0006	BF	0.20	M	CR	LF	0.45
584	W30×108	6.89	49.6	89.28	0.0006	BF	0.25	M	CR	LF	0.46

585	W30×108	6.89	49.6	89.28	0.0006	BF	0.30	C	CR	LF	0.46
586	W30×108	6.89	49.6	100.44	0.0006	BF	0.20	M	CR	GLF	0.43
587	W30×108	6.89	49.6	100.44	0.0006	BF	0.25	M	CR	LF	0.44
588	W30×108	6.89	49.6	100.44	0.0006	BF	0.30	C	CR	LF	0.22
589	W30×108	6.89	49.6	117.18	0.0006	BF	0.15	M	CR	GLF	0.41
590	W30×108	6.89	49.6	117.18	0.0006	BF	0.20	M	CR	GLF	0.41
591	W30×108	6.89	49.6	117.18	0.0006	BF	0.25	C	CR	GF	0.07
592	W30×148	4.44	41.6	78.90	0.0011	BF	0.20	M	CR	GLF	0.46
593	W30×148	4.44	41.6	78.90	0.0011	BF	0.30	M	CR	GLF	0.47
594	W30×148	4.44	41.6	78.90	0.0011	BF	0.35	C	CR	GLF	0.25
595	W30×148	4.44	41.6	78.90	0.0011	BF	0.40	C	CR	GLF	0.26
596	W30×148	4.44	41.6	89.42	0.0011	BF	0.20	M	CR	GLF	0.45
597	W30×148	4.44	41.6	89.42	0.0011	BF	0.25	M	CR	GLF	0.45
598	W30×148	4.44	41.6	89.42	0.0011	BF	0.30	C	CR	GLF	0.35
599	W30×148	4.44	41.6	89.42	0.0011	BF	0.35	C	CR	GLF	0.24
600	W30×148	4.44	41.6	89.42	0.0011	BF	0.40	C	CR	GF	0.25
601	W30×148	4.44	41.6	99.94	0.0011	BF	0.20	M	CR	GLF	0.43
602	W30×148	4.44	41.6	99.94	0.0011	BF	0.25	M	CR	GLF	0.44
603	W30×148	4.44	41.6	99.94	0.0011	BF	0.30	C	CR	GLF	0.45
604	W30×148	4.44	41.6	99.94	0.0011	BF	0.40	C	CR	GF	0.23
605	W30×148	4.44	41.6	115.14	0.0011	BF	0.20	M	CR	GF	0.41
606	W30×148	4.44	41.6	115.14	0.0011	BF	0.25	C	CR	GF	0.42
607	W30×148	4.44	41.6	115.14	0.0011	BF	0.30	C	CR	GF	0.20
608	W30×148	4.44	41.6	115.14	0.0011	BF	0.40	C	CR	GF	0.22
609	W30×235	5.02	32.2	51.30	0.0018	BF	0.20	M	CR	LF	0.46
610	W30×235	5.02	32.2	51.30	0.0018	BF	0.30	M	CR	LF	0.48
611	W30×235	5.02	32.2	51.30	0.0018	BF	0.40	M	CR	LF	0.49
612	W30×235	5.02	32.2	51.30	0.0018	BF	0.45	M	CR	LF	0.50
613	W30×235	5.02	32.2	51.30	0.0018	BF	0.50	C	CR	LF	0.39
614	W30×235	5.02	32.2	58.14	0.0018	BF	0.20	M	CR	LF	0.45

615	W30×235	5.02	32.2	58.14	0.0018	BF	0.30	M	CR	LF	0.46
616	W30×235	5.02	32.2	58.14	0.0018	BF	0.40	M	CR	LF	0.48
617	W30×235	5.02	32.2	58.14	0.0018	BF	0.45	C	CR	LF	0.49
618	W30×235	5.02	32.2	58.14	0.0018	BF	0.50	C	CR	LF	0.38
619	W30×235	5.02	32.2	68.40	0.0018	BF	0.20	M	CR	GF	0.43
620	W30×235	5.02	32.2	68.40	0.0018	BF	0.30	M	CR	GLF	0.45
621	W30×235	5.02	32.2	68.40	0.0018	BF	0.40	M	CR	LF	0.46
622	W30×235	5.02	32.2	68.40	0.0018	BF	0.45	M	CR	LF	0.47
623	W30×235	5.02	32.2	78.66	0.0018	BF	0.20	M	CR	GF	0.41
624	W30×235	5.02	32.2	78.66	0.0018	BF	0.30	M	CR	GF	0.43
625	W30×235	5.02	32.2	78.66	0.0018	BF	0.40	M	CR	GLF	0.45
626	W30×235	5.02	32.2	78.66	0.0018	BF	0.45	C	CR	GLF	0.46
627	W30×357	3.45	21.6	49.60	0.0038	BF	0.40	M	CR	GLF	0.49
628	W30×357	3.45	21.6	49.60	0.0038	BF	0.45	M	CR	GLF	0.50
629	W30×357	3.45	21.6	49.60	0.0038	BF	0.50	M	CR	LF	0.51
630	W30×357	3.45	21.6	49.60	0.0038	BF	0.55	C	CR	LF	0.40
631	W30×357	3.45	21.6	59.52	0.0038	BF	0.30	M	CR	GF	0.46
632	W30×357	3.45	21.6	59.52	0.0038	BF	0.40	M	CR	GF	0.48
633	W30×357	3.45	21.6	59.52	0.0038	BF	0.50	C	CR	GF	0.26
634	W30×357	3.45	21.6	59.52	0.0038	BF	0.55	C	CR	GF	0.27
635	W30×357	3.45	21.6	66.13	0.0038	BF	0.20	M	CR	GF	0.43
636	W30×357	3.45	21.6	66.13	0.0038	BF	0.30	M	CR	GF	0.45
637	W30×357	3.45	21.6	66.13	0.0038	BF	0.40	M	CR	GF	0.46
638	W30×357	3.45	21.6	66.13	0.0038	BF	0.45	M	CR	GF	0.47
639	W30×357	3.45	21.6	66.13	0.0038	BF	0.50	M	CR	GF	0.48
640	W30×357	3.45	21.6	79.36	0.0038	BF	0.20	M	CR	GF	0.41
641	W30×357	3.45	21.6	79.36	0.0038	BF	0.30	M	CR	GF	0.42
642	W30×357	3.45	21.6	79.36	0.0038	BF	0.40	M	CR	GF	0.44
643	W30×357	3.45	21.6	79.36	0.0038	BF	0.45	C	CR	GF	0.22
644	W30×357	3.45	21.6	79.36	0.0038	BF	0.50	C	CR	GF	0.23

Cravero et al. (2020)										
645	W14 × 61	7.8	30.4	29.30	0.0018	PF	0.30	SC	SC	LF	1.09
646	W16 × 89	5.9	25.9	28.90	0.0022	PF	0.50	C	SC	LF	0.91
647	W14 × 82	5.9	22.4	29.00	0.0031	PF	0.75	C	SC	LF	0.99
Elkady and Lignos (2017a)										
648	W24×146	5.9	33.2	51.00	0.0010	FF	0.20	C	SC	LF	0.96
649	W24×146	5.9	33.2	51.00	0.0010	FF	0.50	C	SC	LF	0.59
650	W24×146	5.9	33.2	51.00	0.0010	BF	0.20	C	SC	LF	1.34
651	W24×146	5.9	33.2	51.00	0.0010	BF	0.20	C	CR	LF	0.56
652	W24×146	5.9	33.2	51.00	0.0010	BF	0.50	C	CR	LF	1.24
653	W24×84	5.9	45.9	79.00	0.0008	BF	0.20	C	SC	LF	0.94
654	W24×84	5.9	45.9	79.00	0.0008	BF	0.20	C	CR	LF	1.22
Fogarty and El-Tawil (2015)										
655	W18×86	7.2	33.4	68.40	0.0014	FP	0.15	SC	SC	GLF	0.76
656	W30×326	3.75	23.4	66.70	0.0033	FP	0.15	SC	SC	GLF	0.86
657	W14×132	7.15	17.7	47.90	0.0043	FP	0.15	SC	SC	GLF	0.76
658	W14×500	2.43	5.21	40.70	0.0383	FP	0.15	SC	SC	GF	0.87
659	W18×86	7.2	33.3	68.40	0.0014	FP	0.15	SC	SC	GLF	0.79
660	W24×117	7.53	39.2	61.26	0.0010	FP	0.15	SC	SC	GLF	0.66
661	W21×148	9.47	53.6	108.70	0.0004	FP	0.15	SC	SC	GLF	0.93
662	W16×26	7.97	56.8	161.10	0.0004	FP	0.15	SC	SC	GLF	0.63
663	W27×146	7.16	39.4	56.10	0.0010	FP	0.15	SC	SC	LF	1.14
664	W18×119	5.31	24.5	89.40	0.0026	FP	0.15	SC	SC	GLF	0.89
665	W30×326	3.75	23.4	33.40	0.0033	FP	0.15	SC	SC	GLF	1.04
666	W24×176	4.81	28.7	59.14	0.0068	FP	0.15	SC	SC	LF	1.07
667	W36×194	4.81	42.4	70.18	0.0009	FP	0.15	SC	SC	GLF	0.76
668	W40×278	3.31	33.3	71.41	0.0017	FP	0.15	SC	SC	GLF	1.06
669	W24×176	4.81	28.7	78.85	0.0068	FP	0.15	SC	SC	GLF	1.06
670	W24×176	4.81	28.7	39.42	0.0068	FP	0.15	SC	SC	LF	1.63
671	W36×487	3.19	21.4	45.29	0.0023	FP	0.15	SC	SC	GLF	0.91

Ozkula et al. (2017a)										
672	W24×176	4.81	28.7	71.05	0.0068	FF	0.18	C	SC	GLF	0.51
673	W24×176	4.81	28.7	71.05	0.0068	FF	0.36	C	SC	GLF	1.57
674	W24×176	4.81	28.7	71.05	0.0068	FF	0.54	C	SC	GLF	0.81
675	W24×131	6.7	35.6	72.73	0.0012	FF	0.00	C	SC	LF	0.81
676	W24×131	6.7	35.6	72.73	0.0012	FF	0.18	C	SC	LF	0.60
677	W24×131	6.7	35.6	72.73	0.0012	FF	0.18	SC	SC	LF	0.13
678	W24×131	6.7	35.6	72.73	0.0012	FF	0.36	C	SC	LF	0.36
679	W24×131	6.7	35.6	72.73	0.0012	FF	0.36	C	CR	LF	0.80
680	W24×131	6.7	35.6	72.73	0.0012	FF	0.54	C	SC	LF	0.25
681	W24×104	8.5	43.1	74.23	0.0008	FF	0.18	C	SC	LF	0.26
682	W24×104	8.5	43.1	74.23	0.0008	FF	0.36	C	SC	LF	0.00
683	W24×104	8.5	43.1	74.23	0.0008	FF	0.54	C	SC	LF	0.00
684	W24×84	5.9	45.9	110.77	0.0008	FF	0.18	C	SC	GLF	0.29
685	W24×84	5.9	45.9	110.77	0.0008	FF	0.36	C	SC	GLF	0.12
686	W24×55	6.94	54.6	161.19	0.0004	FF	0.18	C	SC	GLF	0.05
687	W24×55	6.94	54.6	161.19	0.0004	FF	0.27	C	SC	GLF	0.73
688	W24×55	6.94	54.6	161.19	0.0004	FF	0.27	C	SC	GLF	0.66
689	W24×176	4.81	28.7	71.05	0.0068	FF	0.54	SC	SC	GLF	0.11
690	W24×176	4.81	28.7	71.05	0.0068	BF	0.54	C	SC	GLF	0.33
691	W30×261	4.59	28.7	61.19	0.0022	FF	0.27	C	SC	GLF	0.37
692	W30×261	4.59	28.7	61.19	0.0022	FF	0.27	C	M	LF	1.05
693	W30×173	7.04	40.8	63.16	0.0010	FF	0.36	C	SC	LF	0.50
694	W30×173	7.04	40.8	63.16	0.0010	BF	0.36	C	SC	LF	1.12
695	W30×90	8.52	57.5	103.35	0.0004	FF	0.18	C	SC	LF	1.96
696	W18×192	3.27	16.7	77.42	0.0063	FF	0.18	C	SC	GLF	1.57
697	W18×130	4.65	23.9	80.00	0.0031	FF	0.36	C	SC	GLF	1.43
698	W18×130	4.65	23.9	80.00	0.0031	BF	0.36	C	SC	GLF	1.55
699	W18×76	8.11	37.8	82.76	0.0011	FF	0.36	C	SC	LF	1.71
Ozkula (2017)										

700	W14×455	2.62	5.66	41.10	0.0331	FF	0.18	C	SC	LF	1.42
701	W14×455	2.62	5.66	41.10	0.0331	FF	0.36	C	SC	LF	1.10
702	W14×455	2.62	5.66	41.10	0.0331	FF	0.54	C	SC	LF	0.87
703	W14×370	3.1	6.89	42.15	0.0241	FF	0.18	C	SC	LF	0.34
704	W14×370	3.1	6.89	42.15	0.0241	FF	0.36	C	SC	LF	0.38
705	W14×370	3.1	6.89	42.15	0.0241	FF	0.54	C	SC	LF	1.17
706	W14×233	4.62	10.7	43.90	0.0111	FF	0.18	C	SC	LF	0.60
707	W14×233	4.62	10.7	43.90	0.0111	FF	0.36	C	SC	LF	0.36
708	W14×233	4.62	10.7	43.90	0.0111	FF	0.54	C	SC	LF	0.52
709	W14×193	5.45	12.8	44.44	0.0080	FF	0.18	C	SC	LF	0.25
710	W14×193	5.45	12.8	44.44	0.0080	FF	0.36	C	SC	LF	0.26
711	W14×193	5.45	12.8	44.44	0.0080	FF	0.54	C	SC	LF	1.02
712	W14×176	5.97	13.7	44.78	0.0068	FF	0.18	C	SC	LF	0.92
713	W14×176	5.97	13.7	44.78	0.0068	FF	0.36	C	SC	LF	2.15
714	W14×176	5.97	13.7	44.78	0.0068	FF	0.54	C	SC	LF	0.91
715	W14×132	7.15	17.7	47.87	0.0043	FF	0.18	C	SC	LF	0.51
716	W14×132	7.15	17.7	47.87	0.0043	FF	0.36	C	SC	LF	0.79
717	W14×132	7.15	17.7	47.87	0.0043	FF	0.54	C	SC	LF	0.38
718	W12×252	2.89	6.96	53.89	0.0232	FF	0.18	C	SC	LF	1.50
719	W12×252	2.89	6.96	53.89	0.0232	FF	0.36	C	SC	LF	0.84
720	W12×252	2.89	6.96	53.89	0.0232	FF	0.54	C	SC	LF	-----
721	W12×170	4.03	10.1	55.90	0.0122	FF	0.18	C	SC	LF	-----
722	W12×170	4.03	10.1	55.90	0.0122	FF	0.36	C	SC	LF	-----
723	W12×170	4.03	10.1	55.90	0.0122	FF	0.54	C	SC	LF	-----
724	W12×152	4.46	11.2	56.43	0.0100	FF	0.18	C	SC	LF	-----
725	W12×152	4.46	11.2	56.43	0.0100	FF	0.36	C	SC	LF	-----
726	W12×152	4.46	11.2	56.43	0.0100	FF	0.54	C	SC	LF	-----
727	W12×87	7.48	18.9	46.91	0.0037	FF	0.18	C	SC	LF	-----
728	W12×87	7.48	18.9	46.91	0.0037	FF	0.36	C	SC	LF	-----
729	W12×87	7.48	18.9	46.91	0.0037	FF	0.54	C	SC	LF	-----

730	W12×65	9.92	24.9	47.68	0.0022	FF	0.18	C	SC	LF	-----
731	W12×65	9.92	24.9	47.68	0.0022	FF	0.36	C	SC	LF	-----
732	W12×65	9.92	24.9	47.68	0.0022	FF	0.54	C	SC	LF	-----
733	W12×58	7.82	27	47.81	0.0023	FF	0.18	C	SC	LF	-----
734	W12×58	7.82	27	47.81	0.0023	FF	0.36	C	SC	LF	-----
735	W12×58	7.82	27	47.81	0.0023	FF	0.54	C	SC	LF	-----
736	W10×112	4.17	10.4	44.78	0.0117	FF	0.18	C	SC	LF	-----
737	W10×112	4.17	10.4	44.78	0.0117	FF	0.36	C	SC	LF	-----
738	W10×112	4.17	10.4	44.78	0.0117	FF	0.54	C	SC	LF	-----
739	W10×88	5.18	13	45.63	0.0078	FF	0.18	C	SC	LF	-----
740	W10×88	5.18	13	45.63	0.0078	FF	0.36	C	SC	LF	-----
741	W10×88	5.18	13	45.63	0.0078	FF	0.54	C	SC	LF	-----
742	W10×68	6.58	16.7	46.33	0.0049	FF	0.18	C	SC	LF	-----
743	W10×68	6.58	16.7	46.33	0.0049	FF	0.36	C	SC	LF	-----
744	W10×68	6.58	16.7	46.33	0.0049	FF	0.54	C	SC	LF	-----
745	W10×49	8.93	23.1	47.24	0.0027	FF	0.18	C	SC	LF	-----
746	W10×49	8.93	23.1	47.24	0.0027	FF	0.36	C	SC	LF	-----
747	W10×49	8.93	23.1	47.24	0.0027	FF	0.54	C	SC	LF	-----
748	W10×33	9.15	27.1	61.86	0.0018	FF	0.18	C	SC	LF	-----
749	W10×33	9.15	27.1	61.86	0.0018	FF	0.36	C	SC	LF	-----
750	W10×33	9.15	27.1	61.86	0.0018	FF	0.54	C	SC	LF	-----
751	W33×141	6.01	49.6	74.07	0.0007	FF	0.18	C	SC	LF	-----
752	W33×141	6.01	49.6	74.07	0.0007	FF	0.36	C	SC	LF	-----
753	W33×141	6.01	49.6	74.07	0.0007	FF	0.54	C	SC	LF	-----
754	W33×130	6.73	51.7	75.31	0.0006	FF	0.18	C	SC	LF	-----
755	W33×130	6.73	51.7	75.31	0.0006	FF	0.36	C	SC	LF	-----
756	W33×130	6.73	51.7	75.31	0.0006	FF	0.54	C	SC	LF	-----
757	W30×211	5.74	34.5	75.60	0.0014	FF	0.18	C	SC	LF	-----
758	W30×211	5.74	34.5	75.60	0.0014	FF	0.36	C	SC	LF	-----
759	W30×211	5.74	34.5	75.60	0.0014	FF	0.54	C	SC	LF	-----

760	W30×173	7.04	40.8	61.40	0.0010	FF	0.18	C	SC	LF	-----
761	W30×173	7.04	40.8	61.40	0.0010	FF	0.36	C	SC	LF	-----
762	W30×173	7.04	40.8	61.40	0.0010	FF	0.54	C	SC	LF	-----
763	W30×124	5.65	46.2	75.30	0.0008	FF	0.18	C	SC	LF	-----
764	W30×124	5.65	46.2	75.30	0.0008	FF	0.36	C	SC	LF	-----
765	W30×124	5.65	46.2	75.30	0.0008	FF	0.54	C	SC	LF	-----
766	W30×108	6.89	49.6	78.10	0.0006	FF	0.18	C	SC	LF	-----
767	W30×108	6.89	49.6	78.10	0.0006	FF	0.36	C	SC	LF	-----
768	W30×108	6.89	49.6	78.10	0.0006	FF	0.54	C	SC	LF	-----
769	W30×90	8.52	57.5	101.40	0.0004	FF	0.18	C	SC	LF	-----
770	W30×90	8.52	57.5	101.40	0.0004	FF	0.36	C	SC	LF	-----
771	W30×90	8.52	57.5	101.40	0.0004	FF	0.54	C	SC	LF	-----
772	W27×161	6.49	36.1	66.90	0.0012	FF	0.18	C	SC	LF	-----
773	W27×161	6.49	36.1	66.90	0.0012	FF	0.36	C	SC	LF	-----
774	W27×161	6.49	36.1	66.90	0.0012	FF	0.54	C	SC	LF	-----
775	W27×102	6.03	47.1	78.10	0.0008	FF	0.18	C	SC	LF	-----
776	W27×102	6.03	47.1	78.10	0.0008	FF	0.36	C	SC	LF	-----
777	W27×102	6.03	47.1	78.10	0.0008	FF	0.54	C	SC	LF	-----
778	W24×131	6.7	35.6	72.70	0.0012	FF	0.18	C	SC	LF	-----
779	W24×131	6.7	35.6	72.70	0.0012	FF	0.36	C	SC	LF	-----
780	W24×131	6.7	35.6	72.70	0.0012	FF	0.54	C	SC	LF	-----
781	W24×104	8.5	43.1	74.23	0.0008	FF	0.18	C	SC	LF	-----
782	W24×104	8.5	43.1	74.23	0.0008	FF	0.36	C	SC	LF	-----
783	W24×104	8.5	43.1	74.23	0.0008	FF	0.54	C	SC	LF	-----
784	W24×76	6.61	49	75.00	0.0007	FF	0.18	C	SC	LF	-----
785	W24×76	6.61	49	75.00	0.0007	FF	0.36	C	SC	LF	-----
786	W24×76	6.61	49	75.00	0.0007	FF	0.54	C	SC	LF	-----
787	W24×55	6.94	54.6	89.55	0.0004	FF	0.18	C	SC	LF	-----
788	W24×55	6.94	54.6	89.55	0.0004	FF	0.36	C	SC	LF	-----
789	W24×55	6.94	54.6	89.55	0.0004	FF	0.54	C	SC	LF	-----

790	W21×147	5.44	26.1	73.20	0.0022	FF	0.18	C	SC	LF	-----
791	W21×147	5.44	26.1	73.20	0.0022	FF	0.36	C	SC	LF	-----
792	W21×147	5.44	26.1	73.20	0.0022	FF	0.54	C	SC	LF	-----
793	W21×132	6.01	28.9	73.72	0.0018	FF	0.18	C	SC	LF	-----
794	W21×132	6.01	28.9	73.72	0.0018	FF	0.36	C	SC	LF	-----
795	W21×132	6.01	28.9	73.72	0.0018	FF	0.54	C	SC	LF	-----
796	W21×111	7.05	34.1	74.48	0.0013	FF	0.18	C	SC	LF	-----
797	W21×111	7.05	34.1	74.48	0.0013	FF	0.36	C	SC	LF	-----
798	W21×111	7.05	34.1	74.48	0.0013	FF	0.54	C	SC	LF	-----
799	W21×93	4.53	32.3	65.20	0.0015	FF	0.18	C	SC	LF	-----
800	W21×93	4.53	32.3	65.20	0.0015	FF	0.36	C	SC	LF	-----
801	W21×93	4.53	32.3	65.20	0.0015	FF	0.54	C	SC	LF	-----
802	W21×73	5.6	41.2	79.56	0.0010	FF	0.18	C	SC	LF	-----
803	W21×73	5.6	41.2	79.56	0.0010	FF	0.36	C	SC	LF	-----
804	W21×73	5.6	41.2	79.56	0.0010	FF	0.54	C	SC	LF	-----
805	W21×62	6.7	46.9	81.36	0.0007	FF	0.18	C	SC	LF	-----
806	W21×62	6.7	46.9	81.36	0.0007	FF	0.36	C	SC	LF	-----
807	W21×62	6.7	46.9	81.36	0.0007	FF	0.54	C	SC	LF	-----
808	W18×106	5.96	27.2	72.20	0.0021	FF	0.18	C	SC	LF	-----
809	W18×106	5.96	27.2	72.20	0.0021	FF	0.36	C	SC	LF	-----
810	W18×106	5.96	27.2	72.20	0.0021	FF	0.54	C	SC	LF	-----
811	W18×86	7.2	33.4	73.00	0.0014	FF	0.18	C	SC	LF	-----
812	W18×86	7.2	33.4	73.00	0.0014	FF	0.36	C	SC	LF	-----
813	W18×86	7.2	33.4	73.00	0.0014	FF	0.54	C	SC	LF	-----
814	W18×76	8.11	37.8	81.20	0.0011	FF	0.18	C	SC	LF	-----
815	W18×76	8.11	37.8	81.20	0.0011	FF	0.36	C	SC	LF	-----
816	W18×76	8.11	37.8	81.20	0.0011	FF	0.54	C	SC	LF	-----
817	W18×71	4.71	32.4	70.60	0.0016	FF	0.18	C	SC	LF	-----
818	W18×71	4.71	32.4	70.60	0.0016	FF	0.36	C	SC	LF	-----
819	W18×71	4.71	32.4	70.60	0.0016	FF	0.54	C	SC	LF	-----

820	W18×65	5.06	35.7	71.00	0.0013	FF	0.18	C	SC	LF	-----
821	W18×65	5.06	35.7	71.00	0.0013	FF	0.36	C	SC	LF	-----
822	W18×65	5.06	35.7	71.00	0.0013	FF	0.54	C	SC	LF	-----
823	W14×82	5.92	22.4	48.39	0.0031	FF	0.18	C	SC	LF	-----
824	W14×82	5.92	22.4	48.39	0.0031	FF	0.36	C	SC	LF	-----
825	W14×82	5.92	22.4	48.39	0.0031	FF	0.54	C	SC	LF	-----
826	W14×74	6.41	25.4	48.39	0.0026	FF	0.18	C	SC	LF	-----
827	W14×74	6.41	25.4	48.39	0.0026	FF	0.36	C	SC	LF	-----
828	W14×74	6.41	25.4	48.39	0.0026	FF	0.54	C	SC	LF	-----
829	W14×68	6.97	27.5	48.78	0.0022	FF	0.18	C	SC	LF	-----
830	W14×68	6.97	27.5	48.78	0.0022	FF	0.36	C	SC	LF	-----
831	W14×68	6.97	27.5	48.78	0.0022	FF	0.54	C	SC	LF	-----
832	W14×53	6.11	30.9	75.00	0.0019	FF	0.18	C	SC	LF	-----
833	W14×53	6.11	30.9	75.00	0.0019	FF	0.36	C	SC	LF	-----
834	W14×53	6.11	30.9	75.00	0.0019	FF	0.54	C	SC	LF	-----
835	W14×48	6.75	33.6	75.39	0.0016	FF	0.18	C	SC	LF	-----
836	W14×48	6.75	33.6	75.39	0.0016	FF	0.36	C	SC	LF	-----
837	W14×48	6.75	33.6	75.39	0.0016	FF	0.54	C	SC	LF	-----
838	W14×38	6.57	39.6	77.42	0.0011	FF	0.18	C	SC	LF	-----
839	W14×38	6.57	39.6	77.42	0.0011	FF	0.36	C	SC	LF	-----
840	W14×38	6.57	39.6	77.42	0.0011	FF	0.54	C	SC	LF	-----
841	W12×50	6.31	26.8	61.22	0.0023	FF	0.18	C	SC	LF	-----
842	W12×50	6.31	26.8	61.22	0.0023	FF	0.36	C	SC	LF	-----
843	W12×50	6.31	26.8	61.22	0.0023	FF	0.54	C	SC	LF	-----
844	W12×35	6.31	36.2	72.73	0.0014	FF	0.18	C	SC	LF	-----
845	W12×35	6.31	36.2	72.73	0.0014	FF	0.36	C	SC	LF	-----
846	W12×35	6.31	36.2	72.73	0.0014	FF	0.54	C	SC	LF	-----
847	W40×362	3.99	30.5	73.33	0.0020	FF	0.18	C	SC	GLF	-----
848	W40×362	3.99	30.5	73.33	0.0020	FF	0.36	C	SC	GLF	-----
849	W40×362	3.99	30.5	73.33	0.0020	FF	0.54	C	SC	GLF	-----

850	W40×324	4.4	34.2	73.74	0.0016	FF	0.18	C	SC	GLF	-----
851	W40×324	4.4	34.2	73.74	0.0016	FF	0.36	C	SC	GLF	-----
852	W40×324	4.4	34.2	73.74	0.0016	FF	0.54	C	SC	GLF	-----
853	W40×297	4.8	36.8	74.58	0.0014	FF	0.18	C	SC	GLF	-----
854	W40×297	4.8	36.8	74.58	0.0014	FF	0.36	C	SC	GLF	-----
855	W40×297	4.8	36.8	74.58	0.0014	FF	0.54	C	SC	GLF	-----
856	W36×487	3.19	21.4	72.73	0.0039	FF	0.18	C	SC	GLF	-----
857	W36×487	3.19	21.4	72.73	0.0039	FF	0.36	C	SC	GLF	-----
858	W36×487	3.19	21.4	72.73	0.0039	FF	0.54	C	SC	GLF	-----
859	W36×330	4.49	31.4	75.20	0.0019	FF	0.18	C	SC	GLF	-----
860	W36×330	4.49	31.4	75.20	0.0019	FF	0.36	C	SC	GLF	-----
861	W36×330	4.49	31.4	75.20	0.0019	FF	0.54	C	SC	GLF	-----
862	W36×256	3.53	33.8	72.45	0.0017	FF	0.18	C	SC	GLF	-----
863	W36×256	3.53	33.8	72.45	0.0017	FF	0.36	C	SC	GLF	-----
864	W36×256	3.53	33.8	72.45	0.0017	FF	0.54	C	SC	GLF	-----
865	W36×210	4.48	39.1	69.77	0.0011	FF	0.18	C	SC	GLF	-----
866	W36×210	4.48	39.1	69.77	0.0011	FF	0.36	C	SC	GLF	-----
867	W36×210	4.48	39.1	69.77	0.0011	FF	0.54	C	SC	GLF	-----
868	W36×170	5.47	47.7	71.15	0.0007	FF	0.18	C	SC	GLF	-----
869	W36×170	5.47	47.7	71.15	0.0007	FF	0.36	C	SC	GLF	-----
870	W36×170	5.47	47.7	71.15	0.0007	FF	0.54	C	SC	GLF	-----
871	W33×354	3.85	25.7	70.60	0.0028	FF	0.18	C	SC	GLF	-----
872	W33×354	3.85	25.7	70.60	0.0028	FF	0.36	C	SC	GLF	-----
873	W33×354	3.85	25.7	70.60	0.0028	FF	0.54	C	SC	GLF	-----
874	W33×291	4.6	31	71.70	0.0019	FF	0.18	C	SC	GLF	-----
875	W33×291	4.6	31	71.70	0.0019	FF	0.36	C	SC	GLF	-----
876	W33×291	4.6	31	71.70	0.0019	FF	0.54	C	SC	GLF	-----
877	W33×169	4.71	44.7	72.00	0.0010	FF	0.18	C	SC	GLF	-----
878	W33×169	4.71	44.7	72.00	0.0010	FF	0.36	C	SC	GLF	-----
879	W33×169	4.71	44.7	72.00	0.0010	FF	0.54	C	SC	GLF	-----
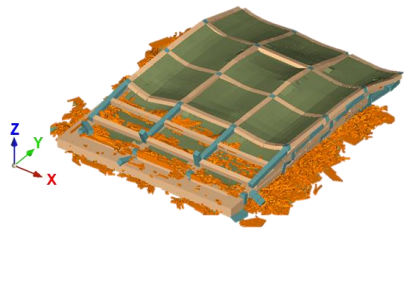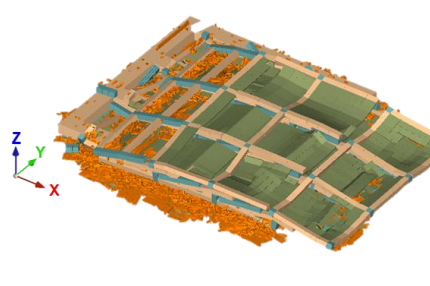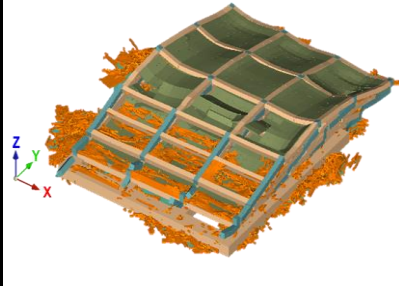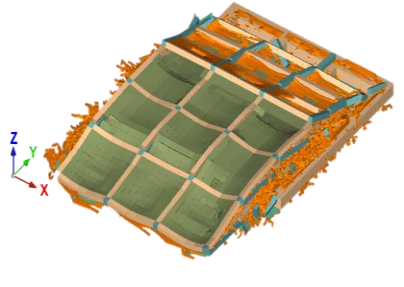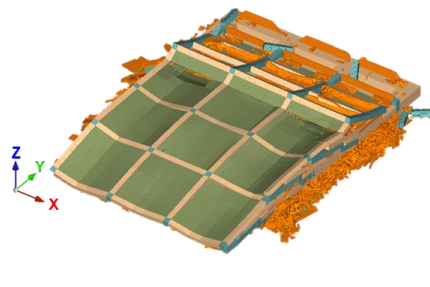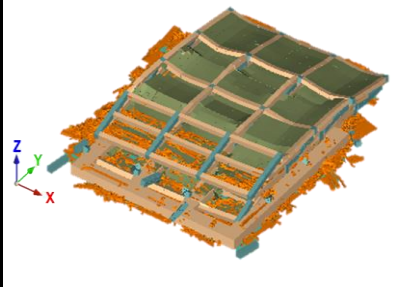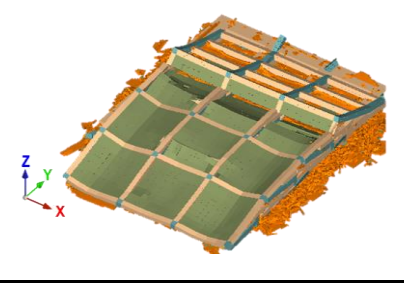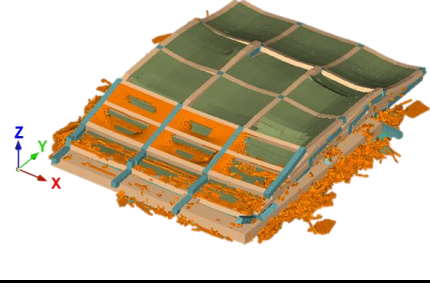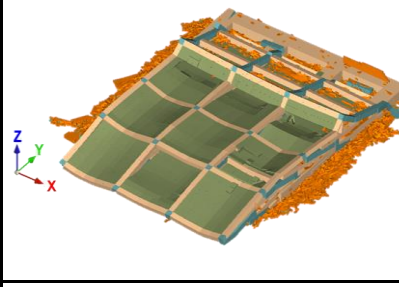
880	W30×326	3.75	23.4	73.30	0.0033	FF	0.18	C	SC	GLF	-----
881	W30×326	3.75	23.4	73.30	0.0033	FF	0.36	C	SC	GLF	-----
882	W30×326	3.75	23.4	73.30	0.0033	FF	0.54	C	SC	GLF	-----
883	W30×261	4.59	28.7	74.80	0.0022	FF	0.18	C	SC	GLF	-----
884	W30×261	4.59	28.7	74.80	0.0022	FF	0.36	C	SC	GLF	-----
885	W30×261	4.59	28.7	74.80	0.0022	FF	0.54	C	SC	GLF	-----
886	W30×261	4.59	28.7	59.50	0.0022	FF	0.18	C	SC	GLF	-----
887	W30×261	4.59	28.7	59.50	0.0022	FF	0.36	C	SC	GLF	-----
888	W30×261	4.59	28.7	59.50	0.0022	FF	0.54	C	SC	GLF	-----
889	W30×148	4.44	41.6	75.40	0.0011	FF	0.18	C	SC	GLF	-----
890	W30×148	4.44	41.6	75.40	0.0011	FF	0.36	C	SC	GLF	-----
891	W30×148	4.44	41.6	75.40	0.0011	FF	0.54	C	SC	GLF	-----
892	W27×307	3.46	20.6	70.40	0.0041	FF	0.18	C	SC	GLF	-----
893	W27×307	3.46	20.6	70.40	0.0041	FF	0.36	C	SC	GLF	-----
894	W27×307	3.46	20.6	70.40	0.0041	FF	0.54	C	SC	GLF	-----
895	W27×217	4.71	28.7	72.30	0.0022	FF	0.18	C	SC	GLF	-----
896	W27×217	4.71	28.7	72.30	0.0022	FF	0.36	C	SC	GLF	-----
897	W27×217	4.71	28.7	72.30	0.0022	FF	0.54	C	SC	GLF	-----
898	W27×129	4.55	39.7	76.00	0.0012	FF	0.18	C	SC	GLF	-----
899	W27×129	4.55	39.7	76.00	0.0012	FF	0.36	C	SC	GLF	-----
900	W27×129	4.55	39.7	76.00	0.0012	FF	0.54	C	SC	GLF	-----
901	W24×335	2.73	15.6	66.90	0.0070	FF	0.18	C	SC	GLF	-----
902	W24×335	2.73	15.6	66.90	0.0070	FF	0.36	C	SC	GLF	-----
903	W24×335	2.73	15.6	66.90	0.0070	FF	0.54	C	SC	GLF	-----
904	W24×250	3.49	20.7	68.80	0.0042	FF	0.18	C	SC	GLF	-----
905	W24×250	3.49	20.7	68.80	0.0042	FF	0.36	C	SC	GLF	-----
906	W24×250	3.49	20.7	68.80	0.0042	FF	0.54	C	SC	GLF	-----
907	W24×176	4.81	28.7	71.10	0.0022	FF	0.18	C	SC	GLF	-----
908	W24×176	4.81	28.7	71.10	0.0022	FF	0.36	C	SC	GLF	-----
909	W24×176	4.81	28.7	71.10	0.0022	FF	0.54	C	SC	GLF	-----

910	W24×103	4.59	39.2	78.40	0.0012	FF	0.18	C	SC	GLF	-----
911	W24×103	4.59	39.2	78.40	0.0012	FF	0.36	C	SC	GLF	-----
912	W24×103	4.59	39.2	78.40	0.0012	FF	0.54	C	SC	GLF	-----
913	W24×94	5.18	41.9	72.70	0.0010	FF	0.18	C	SC	GLF	-----
914	W24×94	5.18	41.9	72.70	0.0010	FF	0.36	C	SC	GLF	-----
915	W24×94	5.18	41.9	72.70	0.0010	FF	0.54	C	SC	GLF	-----
916	W24×84	5.86	45.9	110.80	0.0008	FF	0.18	C	SC	GLF	-----
917	W24×84	5.86	45.9	110.80	0.0008	FF	0.36	C	SC	GLF	-----
918	W24×84	5.86	45.9	110.80	0.0008	FF	0.54	C	SC	GLF	-----
919	W21×201	3.86	20.6	71.50	0.0041	FF	0.18	C	SC	GLF	-----
920	W21×201	3.86	20.6	71.50	0.0041	FF	0.36	C	SC	GLF	-----
921	W21×201	3.86	20.6	71.50	0.0041	FF	0.54	C	SC	GLF	-----
922	W21×166	4.57	25	72.20	0.0029	FF	0.18	C	SC	GLF	-----
923	W21×166	4.57	25	72.20	0.0029	FF	0.36	C	SC	GLF	-----
924	W21×166	4.57	25	72.20	0.0029	FF	0.54	C	SC	GLF	-----
925	W18×211	3.02	15.1	76.60	0.0074	FF	0.18	C	SC	GLF	-----
926	W18×211	3.02	15.1	76.60	0.0074	FF	0.36	C	SC	GLF	-----
927	W18×211	3.02	15.1	76.60	0.0074	FF	0.54	C	SC	GLF	-----
928	W18×192	3.27	16.7	76.00	0.0063	FF	0.18	C	SC	GLF	-----
929	W18×192	3.27	16.7	76.00	0.0063	FF	0.36	C	SC	GLF	-----
930	W18×192	3.27	16.7	76.00	0.0063	FF	0.54	C	SC	GLF	-----
931	W18×130	4.65	23.9	7.10	0.0031	FF	0.18	C	SC	GLF	-----
932	W18×130	4.65	23.9	71.10	0.0031	FF	0.36	C	SC	GLF	-----
933	W18×130	4.65	23.9	71.10	0.0031	FF	0.54	C	SC	GLF	-----
934	W18×130	4.65	23.9	78.50	0.0031	FF	0.18	C	SC	GLF	-----
935	W18×130	4.65	23.9	78.50	0.0031	FF	0.36	C	SC	GLF	-----
936	W18×130	4.65	23.9	78.50	0.0031	FF	0.54	C	SC	GLF	-----
937	W12×22	4.74	41.8	70.80	0.0010	FF	0.18	C	SC	GLF	-----
938	W12×22	4.74	41.8	70.80	0.0010	FF	0.36	C	SC	GLF	-----
939	W12×22	4.74	41.8	70.80	0.0010	FF	0.54	C	SC	GLF	-----

Appendix B

Seismic Debris Field for Collapsed RC Prototype Buildings

Table B-1 Seismic debris field for collapse scenarios of 4-Story Prototype Building

GM_1_0	**GM_1_45**	**GM_2_0**
GM_2_45	**GM_3_0**	**GM_3_45**
GM_4_0	**GM_4_45**	**GM_5_0**

GM_5_45

GM_6_0

GM_6_45

GM_7_0

GM_7_45

GM_8_0

GM_8_45

GM_9_0

GM_9_45

GM_10_0

GM_10_45

GM_11_0

GM_11_45

GM_12_0

GM_12_45

| GM_13_0 | GM_13_45 | GM_14_0 |

| GM_14_45 | GM_15_0 | GM_15_45 |

| GM_16_0 | GM_16_45 | GM_17_0 |

| GM_17_45 | GM_18_0 | GM_18_45 |

| GM_19_0 | GM_19_45 | GM_20_0 |
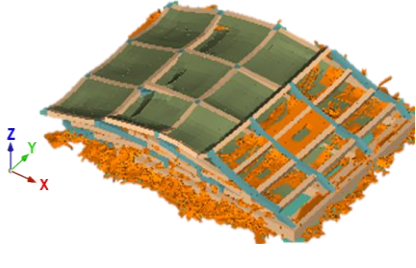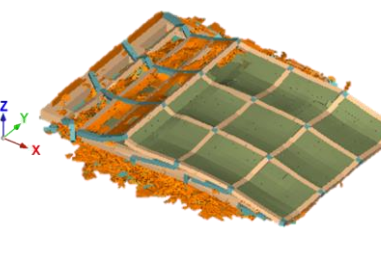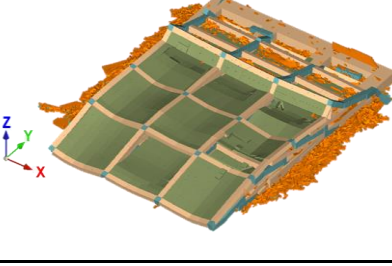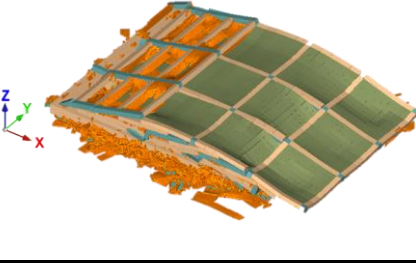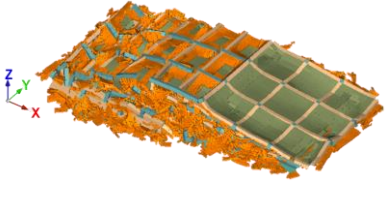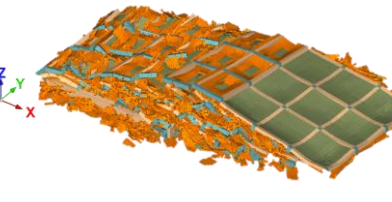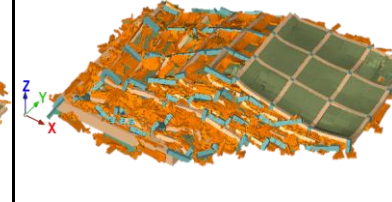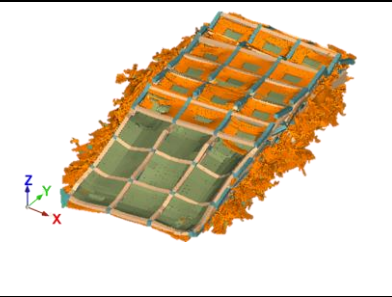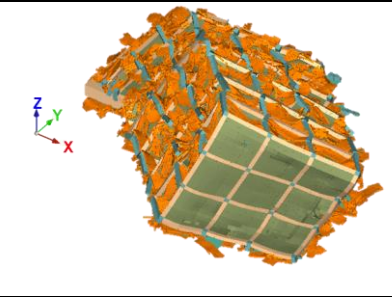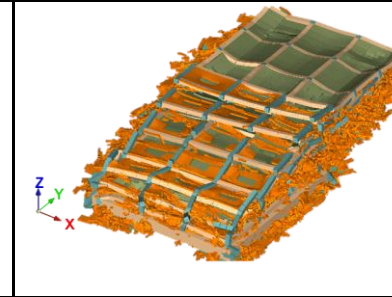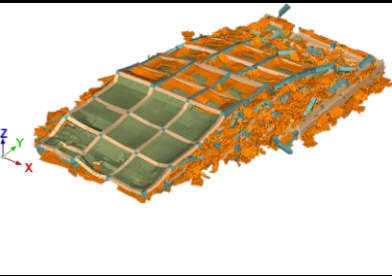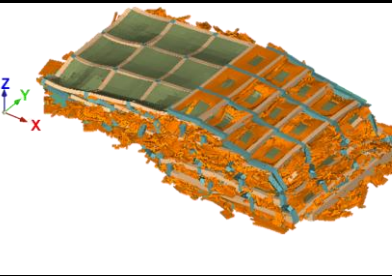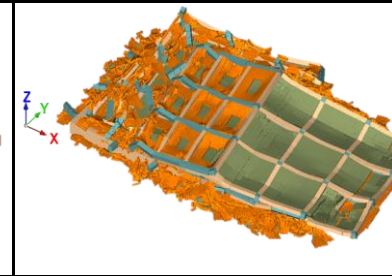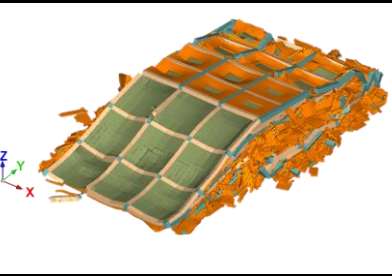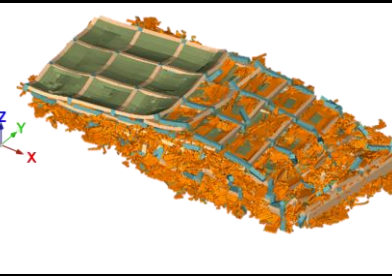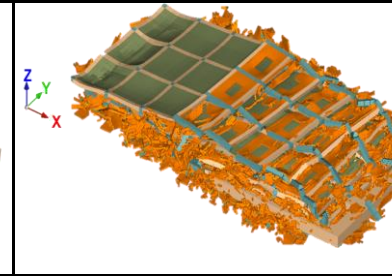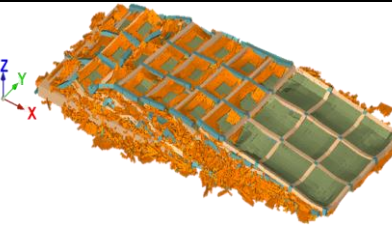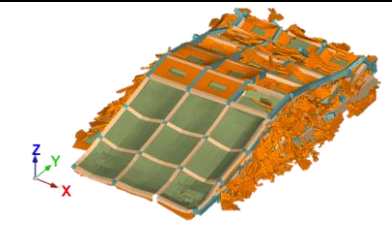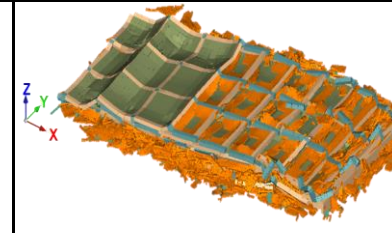
GM_20_45	GM_21_0	GM_21_45
GM_22_0	GM_22_45	

Table B-2 Seismic debris field for collapse scenarios of 8-Story Prototype Building

GM_1_0	**GM_1_45**	**GM_2_0**
GM_2_45	**GM_3_0**	**GM_3_45**
GM_4_0	**GM_4_45**	**GM_5_0**
GM_5_45	**GM_6_0**	**GM_6_45**
GM_7_0	**GM_7_45**	**GM_8_0**

GM_8_45	**GM_9_0**	**GM_9_45**
GM_10_0	**GM_10_45**	**GM_11_0**
GM_11_45	**GM_12_0**	**GM_12_45**
GM_13_0	**GM_13_45**	**GM_14_0**
GM_14_45	**GM_15_0**	**GM_15_45**
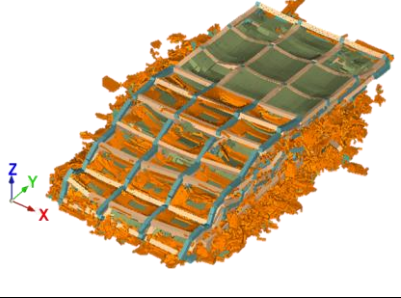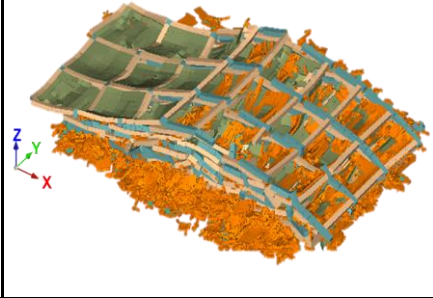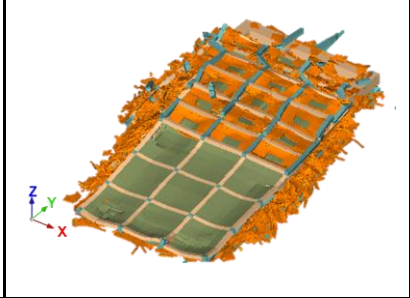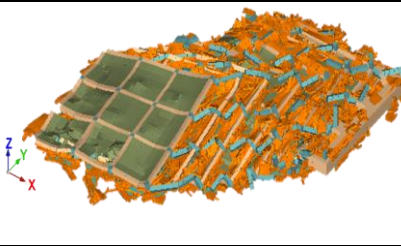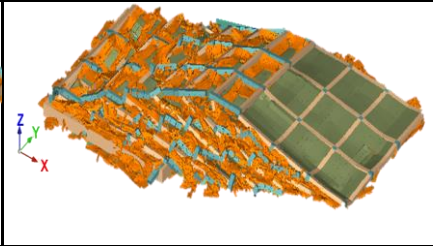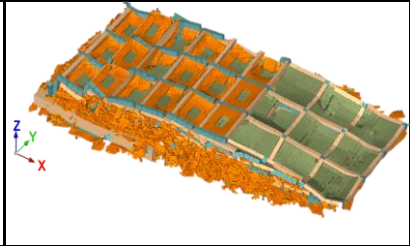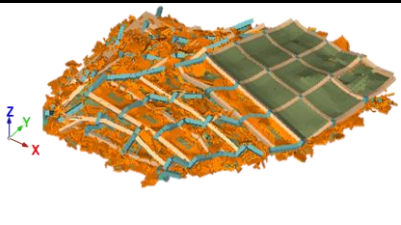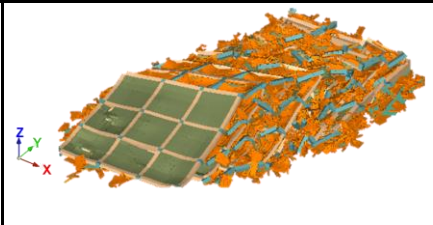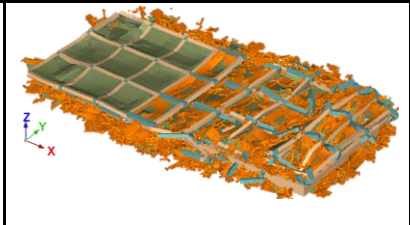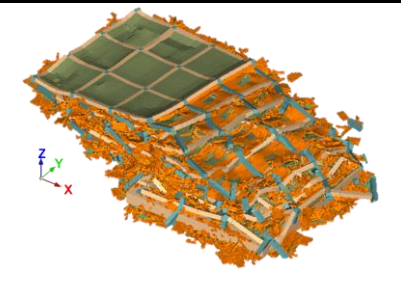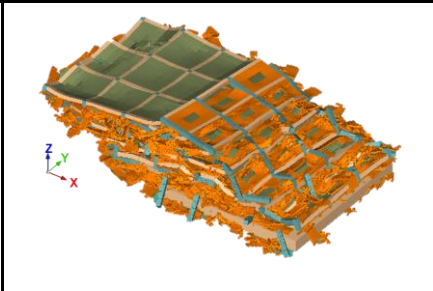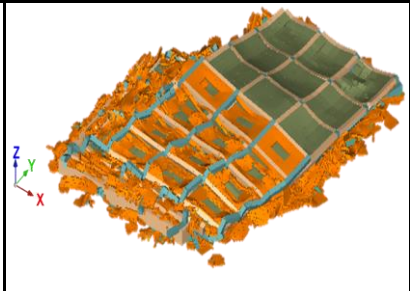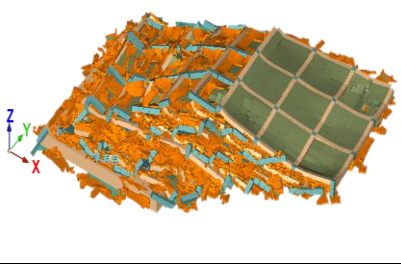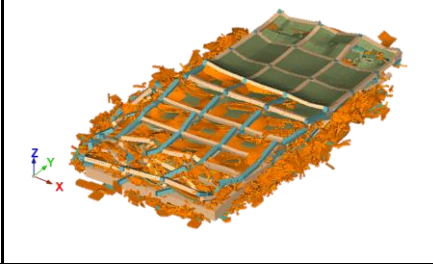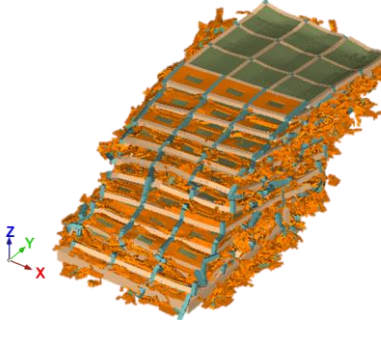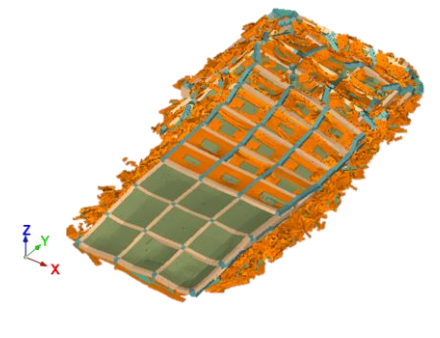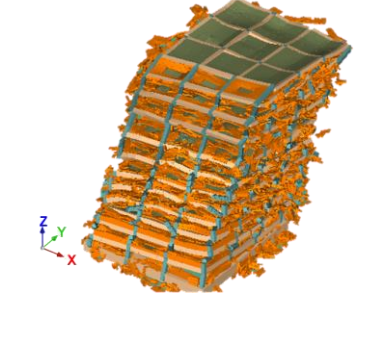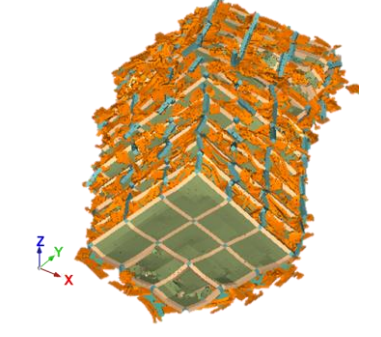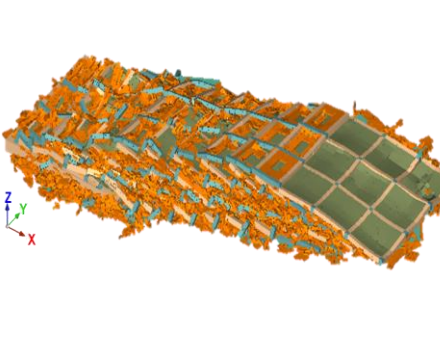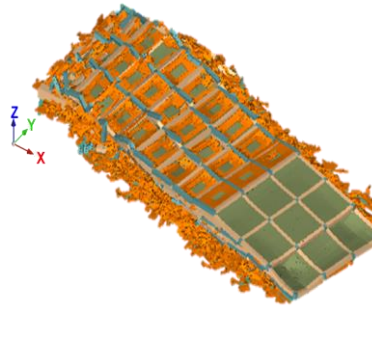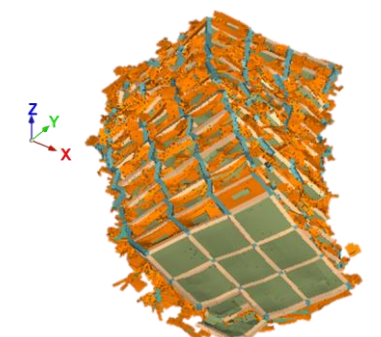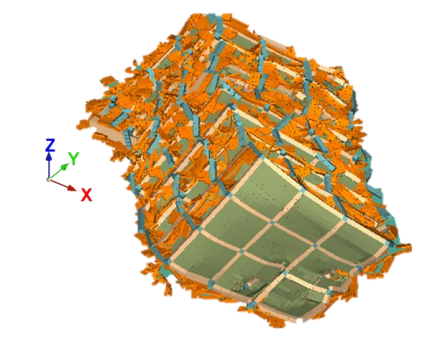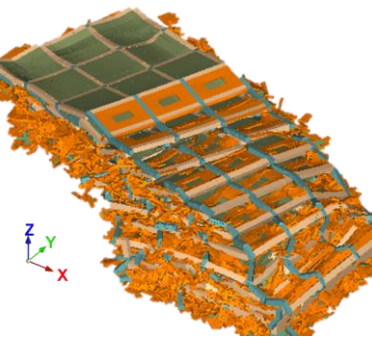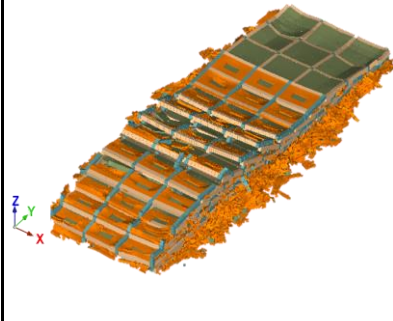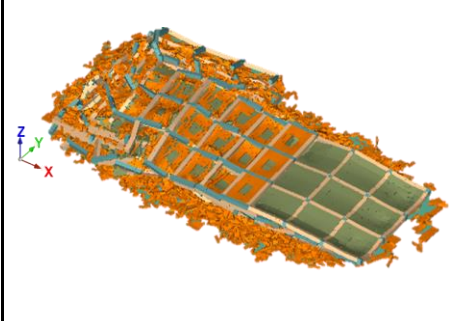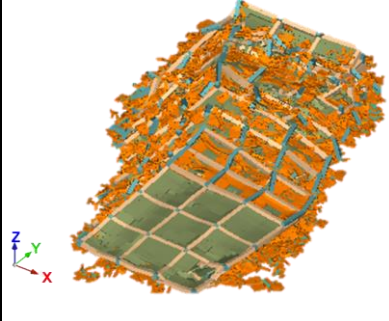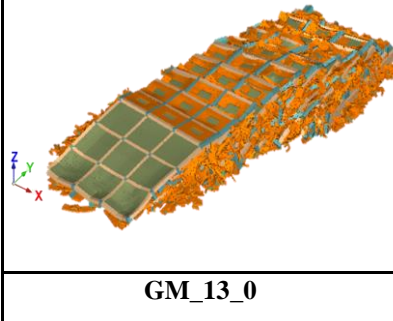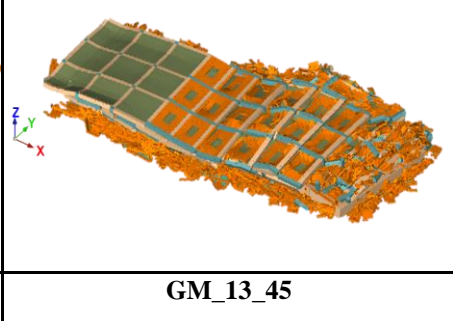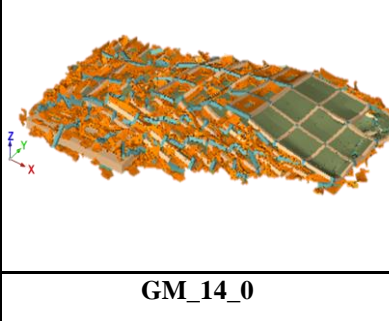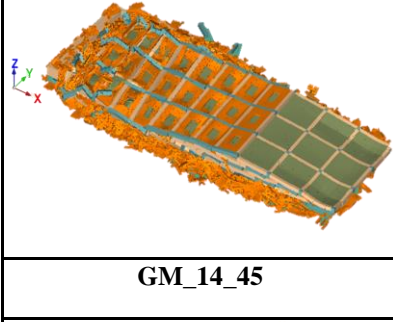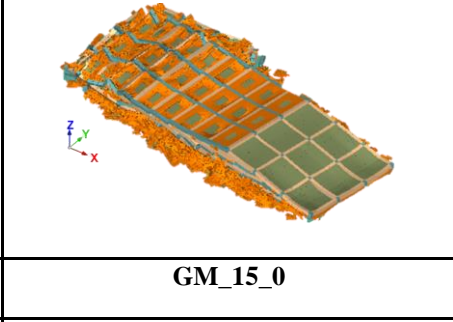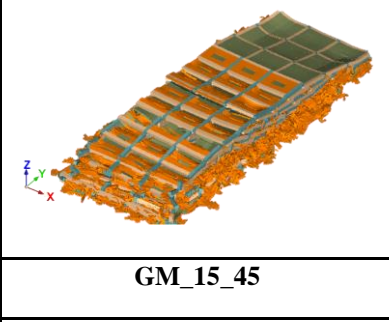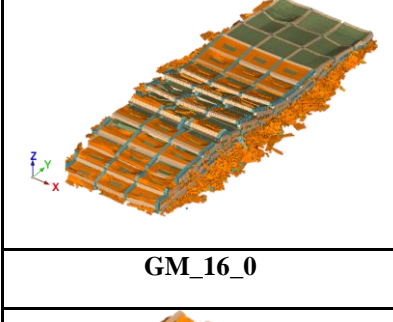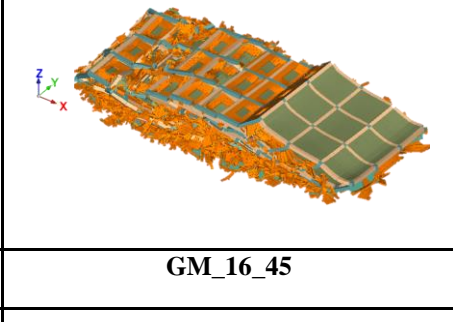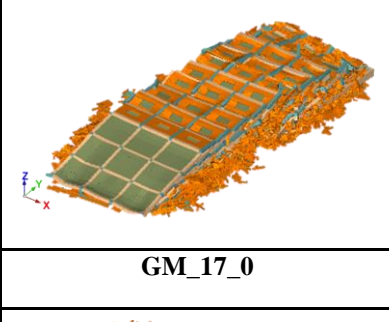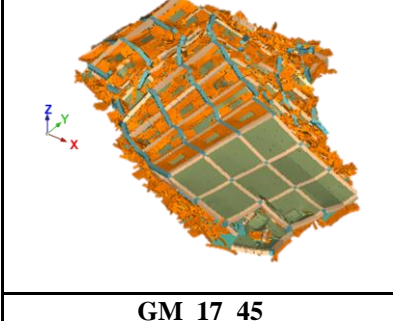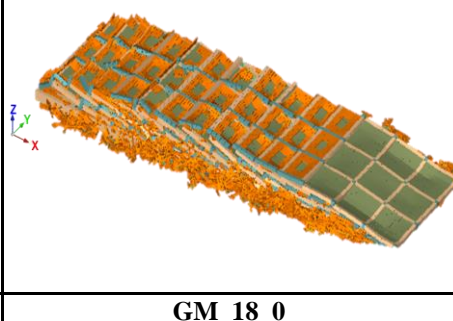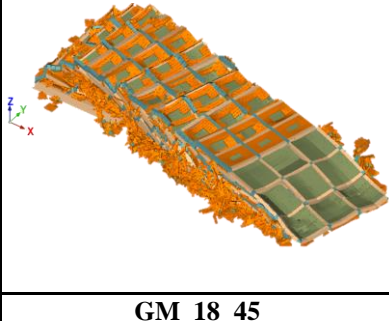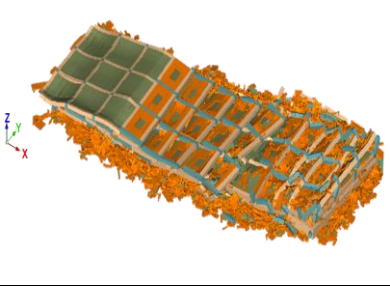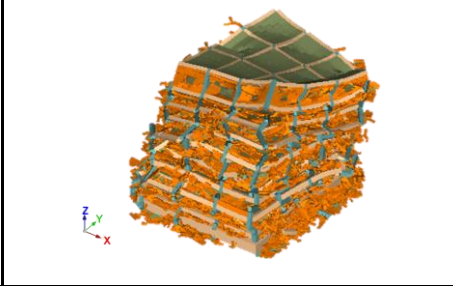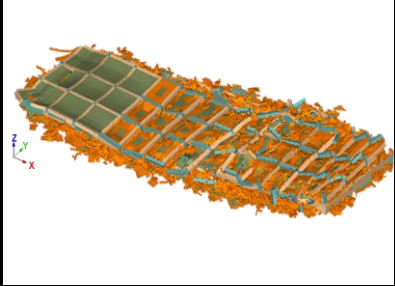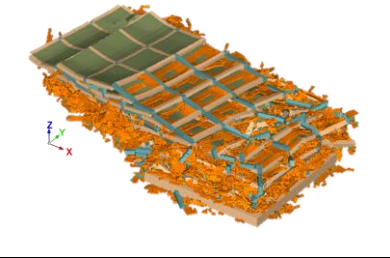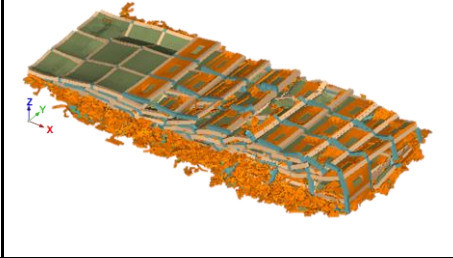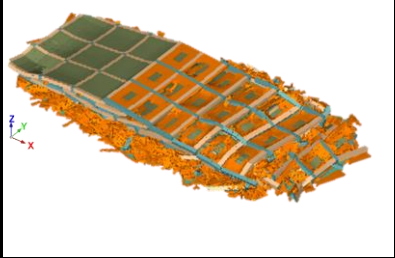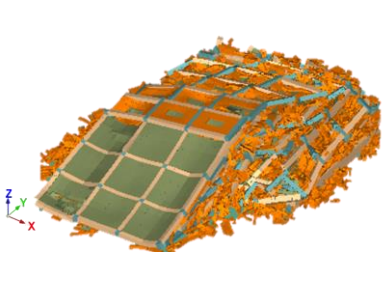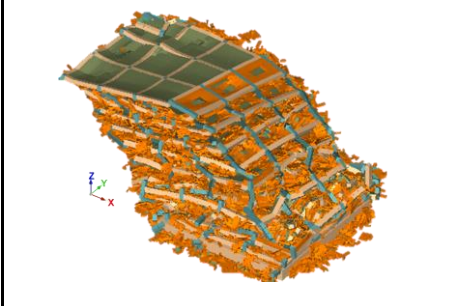
GM_16_0	**GM_16_45**	**GM_17_0**
GM_17_45	**GM_18_0**	**GM_18_45**
GM_19_0	**GM_19_45**	**GM_20_0**
GM_20_45	**GM_21_0**	**GM_21_45**
GM_22_0	**GM_22_45**	

Table B-3 Seismic debris field for collapse scenarios of 12-Story Prototype Building

GM_1_0	GM_1_45	GM_2_0
GM_2_45	GM_3_0	GM_3_45
GM_4_0	GM_4_45	GM_5_0

GM_5_45	**GM_6_0**	**GM_6_45**
GM_7_0	**GM_7_45**	**GM_8_0**
GM_8_45	**GM_9_0**	**GM_9_45**
GM_10_0	**GM_10_45**	**GM_11_0**

GM_11_45	GM_12_0	GM_12_45
GM_13_0	GM_13_45	GM_14_0
GM_14_45	GM_15_0	GM_15_45
GM_16_0	GM_16_45	GM_17_0
GM_17_45	GM_18_0	GM_18_45

GM_19_0	**GM_19_45**	**GM_20_0**
GM_20_45	**GM_21_0**	**GM_21_45**
GM_22_0	**GM_22_45**	

Appendix C

Definition of City Variables in City Simulator

Table C-1 Variables related to the city

Variable Name	Data Type	Size	Description
numBldg	double	1×1	Total number of buildings in the studied community
BldgCoords	double	numBldg×3	[x y z]: Coordinates of each building in the community in ft with respect to UTM coordinates
BldgHaz	double	numBldg×1	Hazus model No. (from Table 3.1 in Hazus (FEMA 2003)) to of each building in the community
BldgModels	Cell of char	numBldg×1	Building model (name of building database) of each building in the community
BldgOccup	double	numBldg×1	Occupancy of each building in the community according to FEMA P-58 (FEMA 2012a)
BldgPeriod	double	numBldg×1	Building fundamental period for each building in the community
Build_Mat	double	numBldg×1	Building material (1 = steel, 2 = RC, 3 = Wood, 4 = RM, 5 = URM) of each building in the community
Const_age	double	numBldg×1	Construction age of each building in the community
Employment	double	numBldg×1	Household employment status of each residential building in the community (1 = Employed, 0 = Unemployed)
Full_res	double	numBldg×1	Full time residence status of each residential building in the community (1 = Full time, 0 = Part time)
Income	double	numBldg×1	Household income of each residential building in the community.

Insurance	double	numBldg×1	Insurance status of each residential building in the community (1 = Insured, 0 = Uninsured)
Length_res	double	numBldg×1	Household length of residence in each residential building in the community (1 = Employed, 0 = Unemployed)
Minority	double	numBldg×1	Household minority status of each residential building in the community (1 = Minority, 0 = Majority)
Social_int	double	numBldg×1	% Social interaction of Household of each residential building in the community
Support	double	numBldg×1	Support received from governmental organization by the households in each residential building in the community (1 = Receive support, 0 = No support)
nlayer	double	1×1	Number of soil layers in the site of the studied community
xi	double	1×1	Damping of soil layers in the site of the studied community
h	double	nlayer×1	Depth of each soil layer in the site of the studied community.
G	double	nlayer×1	Shear modulus of each soil layer in the side of the studied community (in lb/ft^2)
Epiceneter	double	1×2	[x y]: Coordinates of the earthquake epicenter in ft with respect to UTM coordinates
gamma	double	nlayer×1	Unit weight of each soil layer in the side of the studied community (in lb/ft^3)

Table C-2 Variables related to the buildings

Variable Name	Data Type	Description
Basic_info	double	A vector of all the basic information related to the building
Basic_info[1]	double	Number of stories
Basic_info[2]	double	Total Length of Building (in ft)
Basic_info[3]	double	Total Width of Building (in ft)
Basic_info[4]	double	Total height of Building (in ft)
Basic_info[5]	double	Building orientation (in degrees)
Basic_info[6]	double	Replacement cost (in $)
Basic_info[7]	double	Replacement Time (in days)
Basic_info[8]	double	Structural system (1 = Moment frame, 2 = Braced Frame, 3 = Shear Wall)
Basic_info[9]	double	Design Code (1 = New (>1990), 2 = Moderate (1973-1990), 3 = Old (<1973))
Basic_info[10]	double	Degree of priority in the studied community
Basic_info[11]	double	Financing type (1 = Insurance, 2 = Private loans, 3 = Pre-arranged credit line)
Basic_info[12]	double	Order of repair with respect to other buildings in the community
Basic_info[13]	double	Number of beds before earthquake (if hospital building)
Basic_info[14]	double	Engineering contract type (0 = Engineering not in contract, 1 = Engineering on contract)
Basic_info[15]	double	Contactor contract type (0 = GC not in contract, 1 = GC on contract)
Cons_Fun	double	[Number of components × 32 × Number of floors] Consequence functions from FEMA P-58 (FEMA 2012a) for each component in the building
Cons_Fun[i][1]	double	Lower quantity for DS 1 of component i
Cons_Fun[i][2]	double	Upper quantity for DS 1 of component i
Cons_Fun[i][3]	double	Average repair cost for lower quantity of repairs for DS 1 of component i
Cons_Fun[i][4]	double	Average repair cost for upper quantity of repairs for DS 1 of component i
Cons_Fun[i][5]	double	COV of repair cost for DS 1 of component i
Cons_Fun[i][6]	double	Average repair cost for lower quantity of repairs for DS 2 of component i
Cons_Fun[i][7]	double	Average repair cost for upper quantity of repairs for DS 2 of component i
Cons_Fun[i][8]	double	COV of repair cost for DS 2 of component i
Cons_Fun[i][9]	double	Average repair cost for lower quantity of repairs for DS 3 of component i
Cons_Fun[i][10]	double	Average repair cost for upper quantity of repairs for DS 3 of component i
Cons_Fun[i][11]	double	COV of repair cost for DS 3 of component i

Cons_Fun[i][12]	double	Average repair cost for lower quantity of repairs for DS 4 of component i
Cons_Fun[i][13]	double	Average repair cost for upper quantity of repairs for DS 4 of component i
Cons_Fun[i][14]	double	COV of repair cost for DS 4 of component i
Cons_Fun[i][15]	double	Average repair cost for lower quantity of repairs for DS 5 of component i
Cons_Fun[i][16]	double	Average repair cost for upper quantity of repairs for DS 5 of component i
Cons_Fun[i][17]	double	COV of repair cost for DS 5 of component i
Cons_Fun[i][18]	double	Average repair cost for lower quantity of repairs for DS 1 of component i
Cons_Fun[i][19]	double	Average repair time for upper quantity of repairs for DS 1 of component i
Cons_Fun[i][20]	double	COV of repair time for DS 1 of component i
Cons_Fun[i][21]	double	Average repair time for lower quantity of repairs for DS 2 of component i
Cons_Fun[i][22]	double	Average repair time for upper quantity of repairs for DS 2 of component i
Cons_Fun[i][23]	double	COV of repair time for DS 2 of component i
Cons_Fun[i][24]	double	Average repair time for lower quantity of repairs for DS 3 of component i
Cons_Fun[i][25]	double	Average repair time for upper quantity of repairs for DS 3 of component i
Cons_Fun[i][26]	double	COV of repair time for DS 3 of component i
Cons_Fun[i][27]	double	Average repair time for lower quantity of repairs for DS 4 of component i
Cons_Fun[i][28]	double	Average repair time for upper quantity of repairs for DS 4 of component i
Cons_Fun[i][29]	double	COV of repair time for DS 4 of component i
Cons_Fun[i][30]	double	Average repair time for lower quantity of repairs for DS 5 of component i
Cons_Fun[i][31]	double	Average repair time for upper quantity of repairs for DS 5 of component i
Cons_Fun[i][32]	double	COV of repair time for DS 5 of component i
Frag_Curve	double	[Number of components × 18 × Number of floors] Fragility functions from FEMA P-58 (FEMA 2012a) for the DS of each component in the building
Frag_Curve[i][1]	double	DS 1, Median Demand of component i
Frag_Curve[i][2]	double	DS 2, Median Demand of component i
Frag_Curve[i][3]	double	DS 3, Median Demand of component i
Frag_Curve[i][4]	double	DS 4, Median Demand of component i
Frag_Curve[i][5]	double	DS 5, Median Demand of component i
Frag_Curve[i][6]	double	DS 1, Data Dispersion of component i
Frag_Curve[i][7]	double	DS 2, Data Dispersion of component i
Frag_Curve[i][8]	double	DS 3, Data Dispersion of component i
Frag_Curve[i][9]	double	DS 4, Data Dispersion of component i

Frag_Curve[*i*][10]	double	DS 5, Data Dispersion of component *i*
Frag_Curve[*i*][11]	double	Demand Parameter for damage of component *i* (1 = Story Drift Ratio, 2 = Peak Floor Acceleration, 3 = Peak Floor Velocity)
Frag_Curve[*i*][12]	double	DS type of component *i* (1=Sequential, 2=Mutually exclusive, 3=Simultaneous)
Frag_Curve[*i*][13]	double	Number of damage states of component *i*
Frag_Curve[*i*][14]	double	DS 1, Probability of component *i*
Frag_Curve[*i*][15]	double	DS 2, Probability of component *i*
Frag_Curve[*i*][16]	double	DS 3, Probability of component *i*
Frag_Curve[*i*][17]	double	DS 4, Probability of component *i*
Frag_Curve[*i*][18]	double	DS 5, Probability of component *i*
Frag_Curve2	double	[Number of components × 25 × Number of floors] Fragility functions from FEMA P-58 (FEMA 2012a) for the injuries and fatalities resulted from damage of each component in the building
Frag_Curve2[*i*][1]	double	DS 1 - Casualty Affected Area for component *i*
Frag_Curve2[*i*][2]	double	DS 2 - Casualty Affected Area for component *i*
Frag_Curve2[*i*][3]	double	DS 3 - Casualty Affected Area for component *i*
Frag_Curve2[*i*][4]	double	DS 4 - Casualty Affected Area for component *i*
Frag_Curve2[*i*][5]	double	DS 5 - Casualty Affected Area for component *i*
Frag_Curve2[*i*][6]	double	DS 1 Serious Injury Rate – Median for component *i*
Frag_Curve2[*i*][7]	double	DS 1 Serious Injury Rate – Dispersion for component *i*
Frag_Curve2[*i*][8]	double	DS 2 Serious Injury Rate – Median for component *i*
Frag_Curve2[*i*][9]	double	DS 2 Serious Injury Rate - Dispersion for component *i*
Frag_Curve2[*i*][10]	double	DS 3 Serious Injury Rate – Median for component *i*
Frag_Curve2[*i*][11]	double	DS 3 Serious Injury Rate - Dispersion for component *i*
Frag_Curve2[*i*][12]	double	DS 4 Serious Injury Rate – Median for component *i*
Frag_Curve2[*i*][13]	double	DS 4 Serious Injury Rate - Dispersion for component *i*
Frag_Curve2[*i*][14]	double	DS 5 Serious Injury Rate – Median for component *i*
Frag_Curve2[*i*][15]	double	DS 5 Serious Injury Rate - Dispersion for component *i*
Frag_Curve2[*i*][16]	double	DS 1 Loss of Life Rate - Median for component *i*
Frag_Curve2[*i*][17]	double	DS 1 Loss of Life Rate - Dispersion for component *i*
Frag_Curve2[*i*][18]	double	DS 2 Loss of Life Rate - Median for component *i*
Frag_Curve2[*i*][19]	double	DS 2 Loss of Life Rate - Dispersion for component *i*

Frag_Curve2[*i*][20]	double	DS 3 Loss of Life Rate - Median for component *i*
Frag_Curve2[*i*][21]	double	DS 3 Loss of Life Rate - Dispersion for component *i*
Frag_Curve2[*i*][22]	double	DS 4 Loss of Life Rate - Median for component *i*
Frag_Curve2[*i*][23]	double	DS 4 Loss of Life Rate - Dispersion for component *i*
Frag_Curve2[*i*][24]	double	DS 5 Loss of Life Rate - Median for component *i*
Frag_Curve2[*i*][25]	double	DS 5 Loss of Life Rate - Dispersion for component *i*
Frag_Curve3	double	[Number of components × 10 × Number of floors] Fragility functions from FEMA P-58 (FEMA 2012a) for the unsafe placard status evaluation
Frag_Curve3[*i*][1]	double	DS 1, Unsafe Placard Damage Median for component i
Frag_Curve3[*i*][2]	double	DS 2, Unsafe Placard Damage Median for component i
Frag_Curve3[*i*][3]	double	DS 3, Unsafe Placard Damage Median for component i
Frag_Curve3[*i*][4]	double	DS 4, Unsafe Placard Damage Median for component *i*
Frag_Curve3[*i*][5]	double	DS 5, Unsafe Placard Damage Median for component *i*
Frag_Curve3[*i*][6]	double	DS 1, Unsafe Placard Damage Dispersion for component *i*
Frag_Curve3[*i*][7]	double	DS 2, Unsafe Placard Damage Dispersion for component *i*
Frag_Curve3[*i*][8]	double	DS 3, Unsafe Placard Damage Dispersion for component *i*
Frag_Curve3[*i*][9]	double	DS 4, Unsafe Placard Damage Dispersion for component *i*
Frag_Curve3[*i*][10]	double	DS 5, Unsafe Placard Damage Dispersion for component *i*
Frag_Map	double	[Number of components × 1× Number of floors] mapping between FEMA P-58 (FEMA 2012a) and HAZUS (FEMA 2003) damage evaluation for components (1 = Structural component, 2 = Nonstructural drift sensitive component, 3 = Nonstructural acceleration sensitive component)
Frag_Quan	double	[Number of components × 1 × Number of floors] Quantities of each structural and nonstructural component in the building evaluated using Normative Quantities tool by FEMA P-58 (FEMA 2012a)
Frag_txt	Cell of Char	[Number of components × 1 ×Number of floors] Index of each structural and nonstructural component in the building based on FEMA P-58 (FEMA 2012a)
Rep_Seq	double	[Number of components × 1 × Number of floors] Repair sequence of each structural and nonstructural component in the building based on REDi (Almufti and Wilford 2013) methodology (1 = Sequence A, 2 = Sequence B, 3 = Sequence C, 4 = Sequence D, 5 = Sequence E, 6 = Sequence F, 7 = Structural)

REFERENCES

ACI (2005). *Building code requirements for structural concrete (ACI 318-05) and commentary (ACI 318R-05).*American Concrete Institute, Farmington Hills, MI, 2005; 443.

Adachi, T., and B. R. Ellingwood. 2009. "Serviceability assessment of a municipal water system under spatially correlated seismic intensities*." Comput. Aided Civ. Infrastruct. Eng.* 24 (4): 237–248

AHD (2018). "Individual Hospital Statistics for Tennessee". *American Hospital Directory*, < https://www.ahd.com/states/hospital_TN.html > (accessed Aug. 2018).

AISC. (2005). *Seismic Provisions for Structural Steel Buildings, ANSI/AISC 341-05*, American Institute for Steel Construction, Chicago, IL

AISC. (2016a). *Code of Standard Practice of Steel Buildings and Bridges*, ANSI/AISC 303-16, American Institute for Steel Construction, Chicago, IL

AISC. (2016b). *Seismic Provisions for Structural Steel Buildings*, ANSI/AISC 341-16, American Institute for Steel Construction, Chicago, IL

AISC. (2017). *Steel Construction Manual.* (15th ed.). American Institute for Steel Construction, Chicago, IL.

Almufti I, Willford M. (2013) "REDi TM rating system: resilience-based earthquake design initiative for the next generation of buildings." *ARUP Co.*

Almutairi, T., Naudi, K., Nairn, N., Ju, X., Whitters, J., and Ayoub, A. (2018). "Replacement of the distorted dentition of the cone-beam computed tomography scans for orthognathic surgery planning." *Journal of Oral and Maxillofacial Surgery*, 76(7), 1561-e1.

Alvanchi, A., Lee, S. H., and AbouRizk, S. (2011). "Modeling Framework and Architecture of Hybrid System Dynamics and Discrete Event Simulation for Construction." *Computer-Aided Civil and Infrastructure Engineering*, 26(2), 77–91.

Arasaratnam, P., Sivakumaran, K. S., and Tait, M. J. (2011). "True stress-true strain models for structural steel elements." *ISRN Civil Eng.*, 2011, 1–11

Aref A, and Dolatshahi AM (2013). "A three-dimensional cyclic meso-scale numerical procedure for simulation of unreinforced masonry structures." *Computers and Structures*, 120 (2013) 9–23.

Argyroudis, S., Selva, J., Gehl, P., and Pitilakis, K., 2015. "Systemic seismic risk assessment of road networks considering interactions with the built environment." *Computer-Aided Civil and Infrastructure Engineering* 30, 524–540.

Arias, A (1970). "A measure of earthquake intensity. In: Hansen RJ (ed) Seismic design for nuclear power plants." *MIT Press*, Cambridge MA, pp 438–483

ASCE. (2006). *Seismic Rehabilitation of Existing Buildings. ASCE/SEI 41-06*, American Society of Civil Engineers, Reston, VA

ASCE. (2016). *Minimum Design Loads and Associated Criteria for Buildings and Other Structures. ASCE/SEI 7-16*, American Society of Civil Engineers, Reston, VA

ASI (2018). Applied Science International, LLC, *Extreme loading for structures theoretical manual*; (2018).

Askarizadeh, L., Karbassi, A. R., Ghalibaf, M. B., and Nouri, J. (2016). "Management of post-earthquake construction debris in Tehran Metropolitan." *International Journal of Environmental Science and Technology*, 13(2), 639–648.

ASTM. (2019). *Standard Specification for General Requirements for Rolled Structural Steel Bars, Plates, Shapes, and Sheet Piling*, *ASTM A6 / A6M-19, ASTM* International, West Conshohocken, PA

AutoDesk. (2018). *User's guide-AutoCAD 2018*, San Rafael, CA.

Bendat, J. S., and Piersol, A. G. (1971). "Random data: analysis and measurement procedure". New York: Wiley

Bertero, V. V., Uang, C. M., Llopiz, C. R., and Igarashi, K. (1989). "Earthquake simulator testing of concentric braced dual system." *J. Struct. Eng.*, 115(8), 1877.

Beyer, K., J. Goldstein, R. Ramakrishnan, and U. Shaft. (1999). "When is 'nearest neighbor' meaningful?" *In Proc., Int. Conf. on Database Theory*. Berlin: Springer.

Biggs, N. L., Lloyd , E. K. and Wilson ,R. J. (1986) *Graph Theory* 1736-1936, 2nd edn, Oxford

Bishop, Christopher M. (2006). *Pattern Recognition and Machine Learning. Springer.* 315, 520.

BLS (2018). "About the Construction Sector." *U.S. Bureau of Labor Statistics*, <http://www.bls.gov/iag/tgs/iag23.htm > (accessed Aug. 2018).

BLS (2019). "About the Construction Sector." *U.S. Bureau of Labor Statistics*, <http://www.bls.gov/iag/tgs/iag23.htm > (accessed Jan. 2019).

Braun, O., McCallion, R., & Fazackerley, J. (1990). "Characteristics of midsized urban EMS systems." *Annals of Emergency Medicine*, 19(5), 536–546.

Breiman, L., J. Friedman, C. J. Stone, and R. A. Olshen. 1984. *Classification and regression trees. Boca Raton*, FL: CRC Press.

Brokopp, S., Charlene, B., & John, K. B. (2015). "Rebuild or Relocate ? Resilience and Postdisaster Decision-Making After Hurricane Sandy." *American Journal of Community Psychology*, 180–196. https://doi.org/10.1007/s10464-015-9727-x

Bruneau, M. and Reinhorn, A.M., (2004). "Seismic resilience of communities – conceptualization and operationalization." In: P. Fajfar and H. Krawinkler, eds. Performance-based seismic design-concepts and implementations, Proceedings of international workshop on performance based seismic design, 28 June–1 July, Bled, Slovenia, PEER report 2004/05, University of California at Berkeley, 161–172.

Bruneau, M. and Reinhorn, A.M., (2007). "Exploring the concept of seismic resilience for acute care facilities." *Earthquake Spectra*, 28 (1), 41–62.

Bruycker, M., Greco, D., Annino, I., Stazi, M. A., de Ruggiero, N., Triassi, M., de Kettenis, Y. P., and Lechat, M. F. (1983). "The 1980 earthquake in southern Italy: Rescue of trapped victims and mortality." *Bulletin of the World Health Organization*, 61(6), 1021–1025.

Burton, H. V, Miles, S. B., and Eeri, M. (2018). "Integrating Performance-Based Engineering and Urban Simulation to Model Post-Earthquake Housing Recovery." *Earthquake Spectra*, 34(4), 1763–1785. https://doi.org/10.1193/041017EQS067M

Burton, H. V., Deierlein, G., Lallemant, D., and Lin, T. (2016). "Framework for Incorporating Probabilistic Building Performance in the Assessment of Community Seismic Resilience," *J. Struct. Eng.*, 142(8), 1–11.

Burton, H. V., Deierlein, G., Lallemant, D., and Singh, Y. (2017). "Measuring the Impact of Enhanced Building Performance on the Seismic Resilience of a Residential Community," *Earthquake Spectra,* 33(4), 1347–1367.

Burton, H., Kang, H., Miles, S., Nejat, A., & Yi, Z. (2019). "A framework and case study for integrating household decision-making into post-earthquake recovery models." *International Journal of Disaster Risk Reduction*, *37*(May), 101167.

Campbell, K. W. and Y. Bozorgnia (2008) "NGA ground motion model for the geometric mean horizontal component of PGA, PGV, PGD and 5% damped linear elastic response spectra for periods ranging from 0.01 to 10s." *Earthquake Spectra*, 24(1), 139-171.

Castro, S., Poulos, A., and Herrera, C. (2019). "Modeling the Impact of Earthquake- Induced Debris on Tsunami Evacuation Times of Coastal Cities." *Earthquake Spectra*. 35(1), 137–158.

Ceferino, L., Mitrani-Reiser, J., Kiremidjian, A., Deierlein, G., and Bambarén, C. (2020). "Effective plans for hospital system response to earthquake emergencies." *Nature Communications*, 11(1)

Chandrasekhar, D. and Finn, D. (2015). "Influence of Household Recovery Capacity and Urgency on Post-Disaster Relocation: A Case Study of the Rockaways New York After Hurricane Sandy." Report submitted to the Quick Response Grant Program of the Natural Hazards Center, Boulder CO (September 2013).

Chao, S-H, Khandelwal, K., and El-Tawil, S. (2006), "Ductile Fracture Initiation in Shear Link Webs," *Journal of Structural Engineering, ASCE*, 132(8), pp. 1192 – 1200.

Chatterjee, B., and Poullis, C. (2019). "On Building Classification from Remote Sensor Imagery Using Deep Neural Networks and the Relation Between Classification and Reconstruction Accuracy Using Border Localization as Proxy." *16th Conference on Computer and Robot Vision* (CRV), 41–48.

Chatterjee, S., Hadi, A., and Price, B. (2000). *Regression analysis by example*, 3rd Ed., Wiley, New York.

Chen, Q.F., Y. Chen, and L. Chen. (1997). "Earthquake loss estimation with GDP and population data." *Acta Seimologica Sinica* 10(4):791–800.

Chi, B., and Uang, C. (2002). "Cyclic response and design recommendations of reduced beam section moment connections with deep columns." *J. Struct. Eng.*, (464), 464–473.

Cigolini, R., Pero, M., Rossi, T., and Sianesi, A. (2014). "Linking supply chain configuration to supply chain perfrmance: A discrete event simulation model." *Simulation Modelling Practice and Theory*, 40, 1–11.

Cimellaro, G. P., Arcidiacono, V., Reinhorn, A. M., and Bruneau, M. (2013). "Disaster resilience of hospitals considering emergency ambulance services." *Proceedings of the 2013 Structures Congress*, 2824–2836.

Cimellaro, G. P., Reinhorn, A. M., and Bruneau, M. (2010). "Framework for analytical quantification of disaster resilience." *Engineering Structures*, 32(11), 3639–3649.

Cimellaro, G. P., Renschler, C., Reinhorn, F., and Arendt, L. (2016). "PEOPLES: A Framework for Evaluating Resilience," *J. Struct. Eng*. 142(Rose 2004), 1–13.

Cireşan, D., Meier, U., Masci, J., and Schmidhuber, J. (2012). "Multi-column deep neural network for traffic sign classification." *Neural Networks*. 32 (2012) 333–338.

CNS. (2012). *Dimensions, mass and permissible variations of hot rolled steel sections*, *CNS 1490 G1011*, Bureau of Standards. Metrology & Inspection, MOEA, ROC

Cong, Z., Nejat, A., Liang, D., Pei, Y., & Javid, R. J. (2018). "Individual relocation decisions after tornadoes : a multi-level analysis," *Disasters*, 42(2), 233–250.

Coupland, R.M. (1994). "Epidemiological Approach to Surgical Management of the Casualties of War." *British Medical Journal* 308: 1693–6.

Cover, T., and P. Hart. (1967). "Nearest neighbor pattern classification." *IEEE Trans. Inf. Theory* 13 (1): 21–27

Cravero, J., Elkady, A., and Lignos, D. G. (2020). "Experimental Evaluation and Numerical Modeling of Wide-Flange Steel Columns Subjected to Constant and Variable Axial Load Coupled with Lateral Drift Demands," *J. Struct. Eng.*, 360(3), 1–19. 10.1061/(ASCE)ST.1943-541X.0002499

Cruise, R., and Gardner, L. (2006). "Measurement and prediction of geometric imperfections in structural stainless steel members." *Structural Engineering & Mecha*nics, 10.12989/sem.2006.24.1.063

DesRoches R, Comerio M, Eberhard M, Mooney W, Rix GJ. (2011). "Overview of the 2010 Haiti Earthquake." *Earthquake Spectra*;27(1_suppl1):1-21. doi:10.1193/1.3630129

Diederik Kingma and Jimmy Ba. Adam (2015). "A method for stochastic optimization." *In ICLR*, 2015.

Dinu, F., Marginean, I., Dubina, D., and Petran, I. (2016). "Experimental testing and numerical analysis of 3D steel frame system under column loss." *Engineering Structures*, 113, 59–70.

Domaneschi, M., Paolo, G., and Scutiero, G. (2019). "A simplified method to assess generation of seismic debris for masonry structures." *Engineering Structures*, 186 (December 2018), 306–320.

Drucker, Harris; Burges, Christ. C.; Kaufman, Linda; Smola, Alexander J.; and Vapnik, Vladimir N. (1997); "Support Vector Regression Machines", *Advances in Neural Information Processing Systems* 9, NIPS 1996, 155–161, MIT Press.

Dwyer, T. J., and Galambos, T. (1965). "Plastic behavior of tubular beam columns." ASCE Proceedings, *J. of the Structural Division*, 91(4), 153.

Edwards, W. (1971). "Social utilities." *The Engineering Economist* Summer Symposium Series 6,119-129.

Elkady, A., and Lignos, D. G. (2015). "Analytical investigation of the cyclic behavior and plastic hinge formation in deep wide-flange steel beam-columns" *Bull. Earthquake Eng.*, 1097–1118. 10.1007/s10518-014-9640-y

Elkady, A., and Lignos, D. G. (2017a). "Full-Scale Cyclic Testing of Deep Slender Wide-Flange Steel Beam-Columns under Unidirectional and Bidirectional Lateral Drift Demands." *16th World Conference on Earthquake*

Elkady, A., and Lignos, D. G. (2017b). "Stability requirements of deep steel wide-flange columns under cyclic loading." *Proceedings of the Annual Stability Conference Structural Stability Research Council* 2017, (2010), 1–13.

Elkady, A., and Lignos, D. G. (2018). "Improved Seismic Design and Nonlinear Modeling Recommendations for Wide-Flange Steel Columns, " *J. Struct. Eng*., 144(9), 1–13. 10.1061/(ASCE)ST.1943-541X.0002166.

Ellingwood, B. R., Cutler, H., Gardoni, P., Peacock, W. G., van de Lindt, J. W., and Wang, N. (2016). "The Centerville virtual community: A fully integrated decision model of interacting physical and social infrastructure systems." *Sustainable and Resilient Infrastructure,* 1(3–4), 95–107.

El-Tawil, S., Li, H. and Kunnath, S. (2014), "Computational Simulation of Gravity-Induced Progressive Collapse of Steel Frame Buildings: Current Trends and Future Research Needs," *J. Struct. Eng*., 140, SPECIAL ISSUE: Computational Simulation in Structural Engineering, A2513001, http://dx.doi.org/10.1061/(ASCE)ST.1943-541X.0000897

El-Tawil, S., Mikesell, T. D., and Kunnath, S. K. (2000) "Effect of Local Details and Material Properties on Inelastic Behavior of FR Steel Connections," *Journal of Structural Engineering, ASCE*, 126(1), pp. 79 - 87.

EMDAT, OFDA/CRED *International Disaster Database*. Université catholique de Louvain – Brussels – Belgium, 2020.

Emrtath, P. (2013). "Latest Calculations Show Average Buyer Expected to Stay in a Home 13 Years Special". Special Studies, *National Association of Home Builders*, January 3, 2013.

Engelmann, B. E., Whirley, R. G., and Goudreau, G. L. (1989). "A simple shell element formulation for large-scale elastoplastic analysis." *Analytical and computational models of shells*, New York, NY.

Evans, S. P. (1976). "Derivation and analysis of some models for combining trip distribution and assignment." *Transportation Research*, 10, 37-57

Fadden, M. and McCormick, J. (2012). "Cyclic Quasi-Static Testing of Hollow Structural Section Beam Members." *J. Struct. Eng*., 10.1061/(ASCE)ST.1943-541X.0000506, 2012.138:561-570.

FARO. (2016) *FARO Edge and FARO Laser ScanArm Edge Manual*, April 2016. (2016).

Fathalla, E. and Salem, H. (2018). " Parametric Study on Seismic Rehabilitation of Masonry Buildings Using FRP Based upon 3D Non-Linear Dynamic Analysis" *Buildings*, 2018,8 124.

Fawcett, W., and Oliveira, C. S. (2000). "Casualty treatment after earthquake disasters: Development of a regional simulation model." *Disasters*, 24(3), 271–287.

Fell, B.V., Kanvinde, A.M., Deierlein, G.G., Myers, A.T. and Fu, X. (2006). "Buckling and Fracture of Concentric Braces Under Inelastic Cyclic Loading." *Steel Tips Series*, *Structural Steel Education Council*, Moraga, CA.

FEMA (2003). "Earthquake loss estimation methodology: Technical manual." *National Institute of Building for the Federal Emergency Management Agency*, Washington, DC.

FEMA (2007). "Public Assistance: Debris Management Guide", *National Institute of Building for the Federal Emergency Management Agency*, Washington, DC.

FEMA (2009), "Quantification of Building Seismic Performance Factors (ATC-63 Project)," FEMA P695, Federal Emergency Management Agency, Washington D.C., 2009.

FEMA (2010). "Debris Estimating Field Guide." FEMA 329, *Federal Emergency Management Agency*, Washington, DC.

FEMA. (2012a). "Seismic performance assessment of buildings. FEMA P58-1" *Applied Technology Council*, Redwood City, CA.

FEMA. (2012b). "Performance Assessment Calculation Tool (PACT). FEMA P58-3." *Applied Technology Council,* Redwood City, CA.

Feng, K., Li, Q., and Ellingwood, B. R. (2020). "Post-earthquake modelling of transportation networks using an agent-based model." *Structure and Infrastructure Engineering*, 16(11), 1578–1592.

Fisher, R. A (1936) ."The Use of Multiple Measurements in Taxonomic Problems". *Annals of Eugenics*, Vol. 7, pp. 179–188.

Fogarty, J., and El-Tawil, S. (2015). "Collapse resistance of steel columns under combined axial and lateral loading." *J. Struct. Eng.,* 10.1061/(ASCE)ST.1943-541X.0001350, 04015091.

Fogarty, J., Wu, T.-Y., and El-Tawil, S. (2017). "Collapse Response and Design of Deep Steel Columns Subjected to Lateral Displacement." *J. Struct. Eng.,* 10.1061/(ASCE)ST.1943-541X.0001848, 04017130.

Folz, B., and Filiatrault, A. (2001). "Cyclic Analysis of Wood Shear Walls."*Journal of Structural Engineering*., 127(4), 433-441.

Foutch, D. A., Goel, S., and Roeder, C. (1987). "Seismic testing of full-scale steel building: Part I." *J. Struct. Eng.*, 113(11), 2111.

Friedman, J., T. Hastie, and R. Tibshirani. (2001). *The elements of statistical learning*: Springer series in statistics. Berlin: Springer.

Fukuta, T., Nishiyama, I., Yamanouchi, H., & Kato, B. (1989). "Seismic performance of steel frames with inverted V braces." *J. Struct. Eng.*, 115, 2016.

Grunwald, C., Khalil, A. A., Schaufelberger, B., Maria, E., Pellecchia, C., Iuliis, E. De, and Riedel, W. (2018). "Reliability of collapse simulation – Comparing finite and applied element method at different levels." *Engineering Structures*, 176(August), 265–278.

Gu, X., Wang, X., Yin, X., Lin, F., and Hou, J. (2014). "Collapse simulation of reinforced concrete moment frames considering impact actions among blocks." *Engineering Structures*, 65, 30–41.

Hamrock, E., Paige, K., Parks, J., Scheulen, J., and Levin, S. (2013). "Discrete event simulation for healthcare organizations: A tool for decision making." *Journal of Healthcare Management*, 58(2), 110–124.

Han, S.-W, Kim, W.-T and Foutch, Douglas A. (2007). "Seismic Behavior of HSS Bracing Member according to Width–Thickness Ratio under Symmetric Cyclic Loading." *J. Struct. Eng.*, 10.1061/(ASCE)0733-9445(2007)133:2(264)

Hasan, I., Bahalkeh, E., and Yih, Y. (2020). "Evaluating intensive care unit admission and discharge policies using a discrete event simulation model." *Simulation*, 96(6), 501–518.

Haselton, C (2006). "Assessing Seismic Collapse Safety of Modern Reinforced Concrete Moment-Frame Buildings." *The Blume Earthquake Engineering Center*, Stanford University.

Haselton, C. B. and Deierlein, G. G., (2007) "Assessing Seismic Collapse Safety of Modern Reinforced Concrete Moment Frame Buildings," Report No. 156, The John, A. Blume Earthquake Engineering Center, Department of Civil and Environmental Engineering, Stanford University, February 2007.

Hassan, E. M., and Mahmoud, H. (2020) "An integrated socio-technical approach for post-earthquake recovery of interdependent healthcare system." *Reliab. Eng. Syst. Saf.* doi:10.1016/j.ress.2020.106953.

Hikichi, H., Sawada, Y., Tsuboya, T., Aida, J., Kondo, K., Koyama, S., & Kawachi, I. (2017). "Residential relocation and change in social capital : A natural experiment from the 2011 Great East Japan Earthquake and Tsunami," *Science Advances*, (July), 1–10.

Hirokawa, N., and Osaragi, T. (2015). "Earthquake Disaster Simulation System : Integration of Models for Building Collapse , Road Blockage , and Fire Spread" *Journal of Disaster Research* Vol.11 No.2, 2016.

Hsu, C.-W. and Lin, C.-J. (2002). "A comparison of methods for multi-class support vector machines", *IEEE Transactions on Neural Networks*, 13, 415-425.

Huang, H., and Burton, H. V. (2019). "Classification of in-plane failure modes for reinforced concrete frames with infills using machine learning." *J. Build. Eng.*, 25(November 2018), 100767

Huang, Y., and Mahin, S. A. (2010). "Simulating the inelastic seismic behavior of steel braced frames including the effects of low-cycle fatigue." *Rep. No. PEER 2010/104*, Pacific Earthquake Engineering Research Center, Univ. of California at Berkeley, CA

I.I.I. (2018). "Background on: Earthquake insurance and risk." *Insurance Information Institute*. (October 2018).

Ibarra, L. F., and Krawinkler, H. (2005). "Global collapse of frame structures under seismic excitations," *Technical Report 152*, The John A. Blume Earthquake Engineering Research Center, Department of Civil Engineering, Stanford University, Stanford, CA.

IBC (2003). *International Building Code*. Falls Church, VA.

ICBO (1967). *Uniform Building Code*. Pasadena, CA.

ICOR (2019). "Interdependencies in Community Resilience (ICOR) project." https://icor.engin.umich.edu/ (Accessed Feb 2019)

Idriss, I.M. and Seed, H.B. (1968) "Seismic Response of Horizontal Soil Layers." *Journal of the soil and Foundations Division, ASCE,* Vol. 94 No. SM4, July, pp. 1001:1031.

Isard, W. (Ed.). (1956). *Location and space-economy*. The MIT Press: London, England.

James, G., D.Witten, T. Hastie, and R. Tibshirani. (2013). *An introduction to statistical learning*. New York: Springer.

Jun, J. B., Jacobson, S. H., and Swisher, J. R. (1999). "Application of discrete-event simulation in health care clinics: A survey." *Journal of the Operational Research Society*, 50(2), 109–123.

Kammouh, O., Dervishaj, G., and Cimellaro, G. P. (2018). "Quantitative Framework to Assess Resilience and Risk at the Country Level," *ASCE-ASME J. Risk Uncertainty Eng. Syst* 4(1), 2–15. https://doi.org/10.1061/AJRUA6.0000940.

Khalil, A. A. (2012). "Enhanced Modeling of Steel Structures for Progressive Collapse Analysis Using the Applied Element Method," *J. Perform. Constr. Facil*., 26(December), 766–779.

Kim, J., Deshmukh, A., and Hastak, M. (2018). "A framework for assessing the resilience of a disaster debris management system." *International Journal of Disaster Risk Reduction*, 28(January), 674–687.

Kirsch TD, Mitrani-Reiser J, Bissell R, Sauer LM, Mahoney M, Holmes WT, Santa Cruz N, and de la Maza F. (2010), "Impact on hospital functions following the 2010 Chilean earthquake." *Disaster Med Public Health Prep*. 2010 Jun;4(2):122-8.

Knerr, S., Personnaz, L., and Dreyfus, G., (1990). "Single-layer learning revisited: A stepwise procedure for building and training neural network." *Neurocomputing: Algorithms, Architectures and Applications, NATO ASI*, Berlin: Springer-Verlag.

Kong, A. M., (2015)"Finite Element Analysis of a Conventional Wood Shear Wall Using Detailed Nail Parameters and Thermal Performance of Various Green Framing Arrangements" A Thesis Presented to the Faculty of the Department of Civil Engineering California State University, Los Angeles. (December 2015)

Kunnath, S. K., Bao, Y. and El-Tawil, S. (2018), "Advances in Computational Simulation of Gravity-Induced Progressive Collapse of RC Frame Buildings" *Journal of Structural*

Engineering, ASCE, 144(2): 03117003, https://doi.org/10.1061/(ASCE)ST.1943-541X.0001938.

Kurata, M., Nakashima, M., and Suita, K. (2005). "Effect of column base behavior on the seismic response of steel moment frames. "*J. Earthquake Engineering*, 9(2), 415-438.

Lachenbruch, P. A., and M. Goldstein. (1979). "Discriminant analysis." *Biometrics* 35 (1): 69–85

Lee, S., and Goel, S. (1987). "Seismic behavior of hollow and concrete-filled square tubular bracing members" *Rep. No. UMCE 87-11*, Department of Civil Engineering, University of Michigan, Ann Arbor, MI.

Lee, Y. S., Kirka, M. M., Ferguson, J., and Paquit, V. C. (2020). "Correlations of cracking with scan strategy and build geometry in electron beam powder bed additive manufacturing." Additive Manufacturing, 32, 101031.

Lemaitre,J. (1992). *A course on Damage Mechanics*. Springer-Verlag.

Liel, A. B. (2008). "Assessing the Collapse Risk of California's Existing Reinforced Concrete Frame Structures: Metrics for Seismic Safety Decisions." *Civil and Environmental Engineering, Stanford University.*

Lignos, D. G., and Krawinkler, H. (2012). "Sidesway Collapse of Deteriorating Structural Systems under Seismic Excitations," Technical *Report 177*, The John A. Blume Earthquake Engineering Research Center, Department of Civil Engineering, Stanford University, Stanford, CA.

Lignos, D.G., Hikino, T., Matsuoka, Y. and Nakashima, M. (2013). "Collapse Assessment of Steel Moment Frames Based on E-Defense Full-Scale Shake Table Collapse Tests." *J. Struct. Eng.*, 10.1061/(ASCE)ST.1943-541X.0000608, 139(1): 120-132.

Lin YK. (1996) "*Probabilistic Theory of Structural Dynamics*." Robert E. Krieger Publishing, Melbourne, FL, 1996.

Lin, P., and Wang, N. (2017). "Stochastic post-disaster functionality recovery of community building portfolios I: Modeling." *Structural Safety*, 69, 96–105.

Lin, P., and Wang, N. (2019). "A Probabilistic Framework for Post-Disaster Functionality Recovery of Community Building Portfolios" *13th International Conference on Applications of Statistics and Probability in Civil Engineering*, *ICASP13* Seoul, South Korea, May 26-30, 2019 1–8.

Lin, S-Y, Chuang, W-C, Xu, L., El-Tawil, S., Spence, S.M.J., Kamat, V.R., Menassa, C. C., and McCormick, J.P. (2019). "Simple Real-Time Infrastructure (SRTI): A Distributed Computing Software Solution for Hazards Simulation," Submitted for Publication in *Natural Hazards Review*, ASCE.

Maekawa K, and Okamura H. (1983) "The deformational behavior and constitutive equation of concrete using the elasto-plastic and fracture model." *J Facul Eng*, The University of Tokyo 1983;37(2).

Mangalathu, S., and J.-S. Jeon. (2018). "Classification of failure mode and prediction of shear strength for reinforced concrete beam-column joints using machine learning techniques." *Eng. Struct*. 160 (Apr): 85–94.

Mangalathu, S., and Jeon, J. S. (2019). "Machine Learning-Based Failure Mode Recognition of Circular Reinforced Concrete Bridge Columns: Comparative Study." *J. Struct. Eng*., 145(10), 1–12.

Mangalathu, S., G. Heo, and J.-S. Jeon. (2018). "Artificial neural network based multi-dimensional fragility development of skewed concrete bridge classes." *Eng. Struct*. 162 (May): 166–176.

Mangalathu, S., Sun, H., Nweke, C. C., Yi, Z., and Burton, H. V. (2020). "Classifying earthquake damage to buildings using machine learning." *Earthquake Spectra*, 36(1), 183–208.

Markhvida, M., and Baker, J. W. (2018). "Unification of Seismic Performance Estimation and Real Estate Investment Analysis to Model Post-Earthquake Building Repair Decisions." *Earthquake Spectra*, 34(4), 1787–1808. https://doi.org/10.1193/030118EQS048M

Masoomi, H., S. M., Van de Lindt, J. W., and F., Peek, L., (2018). "Quantifying Socioeconomic Impact of a Tornado by Estimating Population Outmigration as a Resilience Metric at the Community Level." *Journal of Structural Engineering*, 144(5), 1–17.

McKenna F, Fenves GL, and Scott MH. (2000) "Open system for earthquake engineering simulation." *Berkeley (CA): University of California*.

McLachlan, G. (2004). *Discriminant analysis and statistical pattern recognition*. Hoboken, NJ: Wiley.

Meguro K, and Tagel-Din H (2000). "Applied element method for structural analysis: theory and application for linear materials." *Struct Eng/Earthquake Eng JSCE*; 17(1):21s–35s.

Meguro, K. (2001). "Applied element method: a new efficient tool for design of structure considering its failure behaviour," *Institution of Industrial Science (IIS)*. Japan, September: The university of Tokyo; 2001. p. 1–20.

Memphis Metropolitan Planning Organization (MPO). (2016). "Travel Demand Model Documentation. Livability 2040: Regional Transportation Plan" Appendix B.

Miles, S. B., and Chang, S. E. (2003). "Urban disaster recovery: A framework and simulation model." *MCEER-03-0005*, Multidisciplinary Center for Earthquake Engineering Research, Buffalo, NY.

Miles, S. B., and Chang, S. E. (2006). "Modeling community recovery from earthquakes." *Earthquake Spectra*, 22(2), 439–458.

Miles, S. B., and Chang, S. E. (2011). "ResilUS: A community-based disaster resilience model." *Cartogr. Geogr. Inf. Sci.*, 38(1), 36–51.

Mitrani-Reiser, J., Mahoney, M., Holmes, W. T., De La Llera, J. C., Bissell, R., and Kirsch, T. (2012). "A functional loss assessment of a hospital system in the Bío-Bío province." *Earthquake Spectra*, 28(S1), S473-S502.

Mulvey, J. M., Awan, S. U., Qadri, A. A., and Maqsood, M. A. (2008). "Profile of injuries arising from the 2005 Kashmir Earthquake: The first 72 h." *Injury*, 39(5), 554–560.

Naderpour, H., and Mirrashid, M. (2019). "Classification of failure modes in ductile and non-ductile concrete joints." *Eng. Failure Analysis*, 103 (December 2018), 361–375.

Nakashima, M., and Liu, D. (2005). "Instability and complete failure of steel columns subjected to cyclic loading." *J. Engineering Mechanics*, 131(6), 559.

NBI (2019). 〈 https://www.fhwa.dot.gov/bridge/nbi/ascii2019.cfm 〉 *National Bridge Inventory* (Apr. 15, 2020).

NCES (2019). "Back to school statistics" *National Center for Education Statistics*. <https://nces.ed.gov/fastfacts/display.asp?id=372>, (Accessed March 2019).

NCSA (2018). "ERGO-EQ Platform for Multi-Hazard Assessment, Response, and Planning." *National Center for Supercomputing Applications and Mid America Earthquake Center*, < http://ergo.ncsa.illinois.edu/?page_id=44>, (accessed August 2018).

Nejat, A., Cong, Z., & Liang, D. (2016). "Family Structures, Relationships, and Housing Recovery Decisions after Hurricane Sandy," *Buildings*, 1–16.

Newell, J., and Uang, C. (2006). "Cyclic behavior of steel columns with combined high axial load and drift demand." *Rep. No. SSRP-06/22*, Dept. of Structural Engineering, Univ. of California, San Diego, La Jolla, CA.

Nishino, T., Tanaka, T., and Hokugo, A., (2012). "An evaluation method for the urban post-earthquake fire risk considering multiple scenarios of fire spread and evacuation," *Fire Safety Journal*. 54, 167–180.

NIST. (2010) "Evaluation of the FEMA P695 methodology for quantification of building seismic performance factors" *NIST GCR* 10-917-8. Gaithersburg, MD: National Institute of Standards and Technology.

Nobuhara, R., Sumiyoshi, Y., and Miyano, M. (2000). "Study of Casualties Due to Earthquake Disasters and Other Accidents in Japan." *Proc. 12th World Conference on Earthquake Engineering,* Auckland, New Zealand, Paper No., 1–6.

Nojima, N. (2012). "Restoration Processes of Utility Lifelines in the Great East Japan Earthquake Disaster, 2011." *15th World Conference on Earthquake Engineering* (*15WCEE*), Lisbon, Portugal, September 24-28, 2012.

Norman, R. D., and Smith, H. (1998). *Applied Regression Analysis*. Hoboken, NJ: Wiley-Interscience, pp. 307–312.

Ozkula, G. (2017). "Seismic Behavior, Modeling and Design of Deep Wide-Flange Steel Columns for Special Moment Frames." *UC San Diego*.

Ozkula, G., Harris, J., and Uang, C.M. (2017a). "Classifying Cyclic Buckling Modes of Steel Wide-Flange Columns under Cyclic Loading" *Proceedings of the Structures Congress 2017*, 6–7 April 2017, Denver, CO

Ozkula, G., Harris, J., and Uang, C.M. (2017b). "Observations from Cyclic Tests on Deep, Wide-Flange Beam-Columns." *Engineering Journal*, 56(1), 3–5.

Packer, J., Sherman, D., and Lecce, M. (2010). "Steel design guide 24: Hollow structural section connections." *American Institute of Steel Construction*, Chicago, IL.

Padgett, J.E. and DesRoches, R. (2007). "Bridge functionality relationships for improved seismic risk assessment of transportation networks." *Earthquake Spectra*, 23, 115– 30.

Padilla-llano, D. A., Zhao, X., Moen, C. D., and Schafer, B. (2014). "Initial geometric imperfection measurement and characterization of cold- formed steel C-section structural members with 3D non-contact measurement techniques." *Proceedings of the Annual Stability Conference Structural Stability Research Council Toronto*, Canada, March 25-28, 2014.

Patil, T.R., and Sherekar, S.S. (2013). "Performance Analysis of Naive Bayes and J 48 Classification Algorithm for Data Classification." *International Journal of Computer Science and Applications* Vol. 6, No.2, (Apr 2013)

PEER (2018). "PEER Ground Motion Database." *Pacific Earthquake Engineering Research Center* <https://ngawest2.berkeley.edu/> (Accessed Aug. 2018).

PEER (2019). "PEER Ground Motion Database." *Pacific Earthquake Engineering Research Center* <https://ngawest2.berkeley.edu/> (Accessed Jan. 2019).

Phalkey, R., Reinhardt, J. D., and Marx, M. (2011). "Injury epidemiology after the 2001 Gujarat earthquake in India: a retrospective analysis of injuries treated at a rural hospital in the Kutch district immediately after the disaster." *Global Health Action*, 4, 7196.

Polese, M., Ludovico, M. Di, and Prota, A. (2018). "Post-earthquake reconstruction: A study on the factors in fl uencing demolition decisions after 2009 L' Aquila earthquake." *Soil Dynamics and Earthquake Engineering*, 105 (April 2017), 139–149. https://doi.org/10.1016/j.soildyn.2017.12.007

Potter, S. H., Becker, J. S., Johnston, D. M., and Rossiter, K. P. (2015). "An overview of the impacts of the 2010-2011 Canterbury earthquakes." *International Journal of Disaster Risk Reduction*, 14, 6–14. https://doi.org/10.1016/j.ijdrr.2015.01.014

Pressman, S. (2015). "Defining and Measuring the Middle Class," *American Institute of Economic Research* (August 2015).

Quagliarini, E., Bernardini, G., Wazinski, C., Spalazzi, L., and D'Orazio, M., (2016). "Urban scenarios modifications due to the earthquake: Ruins formation criteria and interactions with pedestrians' evacuation." *Bulletin of Earthquake Engineering* 14, 1071–1101.

Rasmussen, C. E. and Williams, C. K. I.(2006). *Gaussian Processes for Machine Learning*. MIT Press. Cambridge, Massachusetts.

Ravari, Z. N. A., Ghazi, I., and Kahani, M. M., (2016). "Study the vulnerability and blocking of streets after earthquake (Case study: Kerman Shariati and Shahid Beheshti Streets and Jomhuri Boulevard)." *International Journal of Health System and Disaster Management* 4, 25–30.

Ristic, D., Yamada, Y., and Iemura, H. (1986). "Stress–strain based modeling of hysteretic structures under earthquake induced bending and varying axial loads," *Research report No. 86-ST-01*, School of Civil Engineering, Kyoto University, Kyoto, Japan.

Robinson, S. (2004). "*Simulation – The practice of model development and use*." Wiley.

Rodkin, M. V, & Korzhenkov, A. M. (2019). "Estimation of maximum mass velocity from macroseismic data : A new method and application to archeoseismological data." *Geodesy and Geodynamics* ,10(4), 321–330.

Ryu, H., Luco, N., Uma, S. R., and Liel, A. B. (2011), "Developing fragilities for mainshock-damaged structures through incremental dynamic analysis," *Proceedings of the Ninth Pacific Conference on Earthquake Engineering Building an Earthquake-Resilient Society*, April 2011, Auckland, New Zealand.

Schafer, B. W., and Peko, T. (1998). "Computational modeling of cold-formed steel : characterizing geometric imperfections and residual stresses." *Journal of Constructional Steel Research* 47, 193–210.

Sediek, O. A, El-Tawil, S. and McCormick, J. (2021a), "Seismic Debris Field for Collapsed RC Moment Resisting Frame Buildings," Accepted for publication in *J. Struct. Eng.*

Sediek, O. A, El-Tawil, S. and McCormick, J. (2021b), "A Case Study for Modeling Interdependencies Between the Building Portfolio, Transportation Network, and Healthcare System in the Community," DesignSafe-CI. DOI: 10.17603/ds2-m3b2-re28

Sediek, O. A., Wu, T.-Y, El-Tawil, S., and McCormick, J. (2020a). "Discussion of "Experimental Evaluation and Numerical Modeling of Wide-Flange Steel Columns Subjected to Constant and Variable Axial Load Coupled with Lateral Drift Demands" by Julien Cravero, Ahmed Elkady, and Dimitrios G. Lignos." *J. Struct. Eng.* 147(3), 07020019, https://doi.org/ 10.1061 /(ASCE)ST.1943-541X.0002946

Sediek, O. A., Wu, T.-Y, McCormick, J., and El-Tawil, S. (2020b). "Collapse Behavior of Hollow Structural Section Columns under Combined Axial and Lateral Loading." *J. Struct. Eng.*, 10.1061/(ASCE)ST.1943-541X.0002637.

Sediek, O. A., Wu, T.-Y, McCormick, J., and El-Tawil, S. (2020c) "SCNet: A Multi-attribute Data Set for Seismic Collapse Behavior of Deep Steel Wide-Flange Columns." in Prediction of Seismic Collapse Behavior of Deep Steel Wide-Flange Columns Using Machine Learning Methods. *DesignSafe-CI*; DOI: 10.17603/ds2-wz53-4660

Sediek, O.A.; Lin, S.Y.; Hlynka, A.; El-Tawil, S. McCormick, J. (2020d) "Interdisciplinary Multi-Language Community Resilience Simulation using Simple Run-Time Infrastructure (SRTI)." DesignSafe-CI. https://doi.org/10.17603/ds2-ycra-9v54

Selvaraj, S., and Madhavan, M. (2018). "Geometric Imperfection Measurements and Validations on Cold-Formed Steel Channels Using 3D Noncontact Laser Scanner." *J. Struct. Eng*., 144(3), 1–14. 10.1061/(ASCE)ST.1943-541X.0001993

Shiraki, N., Shinozuka, M., Moore, J. E., Chang, S. E., Kameda, H., and Tanaka, S. (2007). "System risk curves: Probabilistic performance scenarios for highway networks subject to earthquake damage." *J. Infrastruct. Syst*.

Siam, A., Ezzeldin, M., and El-Dakhakhni, W. (2019). "Machine learning algorithms for structural performance classifications and predictions: Application to reinforced masonry shear walls." *Structures*, 22(December 2018), 252–265.

Simard, P. Y., D. Steinkraus, and J. Platt (2003). "Best practice for convolutional neural networks applied to visual document analysis." In Proceedings International Conference on Document Analysis and Recognition (ICDAR), pp. 958– 962. *IEEE Computer Society*.

Sladojevic, S., Arsenovic, M., Anderla, A., Culibrk, D., and Stefanovic, D. (2016). "Deep Neural Networks Based Recognition of Plant Diseases by Leaf Image Classification," *Computational Intelligence and Neuroscience*, Volume 2016, Article ID 3289801, 11 pages.

Soong, TT ,and Grigoriu, M. (1993) "*Random Vibration of Mechanical and Structural Systems*." Prentice Hall, Englewood Cliffs.

SRTI (2019). "Simple Real Time Interface (SRTI)" https://github.com/hlynka-a/SRTI (Accessed Feb 2019)

Statistical Atlas (2018). "Population of Shelby County, Tennessee." *Educational Attainment in the United States - Statistical Atlas,* <https://statisticalatlas.com/county/Tennessee/Shelby-County/Population >, (accessed Aug. 2018).

Su, Y., Yang, L., and Jin, Z., (2008). "Simulation and system dynamics models for transportation of patients following a disaster." *Proceedings of* 2008 *International Workshop on Modelling, Simulation and Optimization*, WMSO 2008, 93–96.

Sutley, E. J., Lindt, J. W. Van De, and Peek, L. (2017). "Community-Level Framework for Seismic Resilience. I: Coupling Socioeconomic Characteristics and Engineering Building Systems," *Nat. Hazards Rev*., 18(3).

Suzuki, Y. and Lignos, D.G. (2014). "Development of loading protocols for experimental testing of steel columns subjected to combined high axial load and lateral drift demands near collapse." *10th National Conference on Earthquake Engineering*, Anchorage, Alaska: EERI.

Suzuki, Y. and Lignos, D.G. (2017). "collapse behavior of steel columns as part of steel frame buildings: experiments and numerical models." *16th. World Conference on Earthquake Engineering*, Santiago, Chile.

Tabata, T., Onishi, A., Saeki, T., and Tsai, P. (2019). "Earthquake disaster waste management reviews: Prediction, treatment, recycling, and prevention." *International Journal of Disaster Risk Reduction,* 36(December 2018), 101-119.

Tremblay, R. (2002). "Inelastic seismic response of steel bracing members." *J. Constructional Steel Research*, 58(5-8), 665.

Uang, C.M., Ozkula, G., and Harris, J. (2015). "Observations from cyclic tests on deep, slender wide-flange structural steel beam-column members." *Proc. of Annual Stability Conference, SSRC, Chicago, IL.*

UNDP (2010). "Empowering Haiti to build a better future: Debris management-programme outline." *United Nations Development Programme*. Retrieved from www.undp.org/haiti.

US Census Bureau. (2017 a). "Percentage distribution of household income in the United States in 2017." *In Statista - The Statistics Portal*. Retrieved March 6, 2019, from https://www.statista.com/statistics/203183/percentage-distribution-of-household-income-in-the-us/.

US Census Bureau. (2017b). "Comparative Demographic Estimates 2017 American Community Survey 1-Year Estimates." Retrieved March 7, 2019 https://factfinder.census.gov/faces/tableservices/jsf/pages/productview.xhtml?pid=ACS_16_1YR_CP05&prodType=table

USGS (2018). "Memphis, Shelby County Seismic Hazard Maps and Data Download". *The United States Geological Survey* https://earthquake.usgs.gov/hazards/urban/memphis/grid_download.php>, (Accessed Aug. 2018).

Vamvatsikos D, and Cornell CA. (2002) "Incremental dynamic analysis". *Earthquake Engineering & Structural Dynamics*;31(3):491–514. DOI: 10.1002/eqe.141.

Vapnik, V. N. (1995). *The Nature of Statistical Learning Theory*. New York: SpringerVerlag.

Vishnu, N., Kameshwar, S., and Padgett, J. E. (2018). "A framework for resilience assessment of highway transportation networks." *Routledge Handbook of Sustainable and Resilient Infrastructure*, 1, 216–238.

Vona, M., Mastroberti, M., Mitidieri, L., & Tataranna, S. (2018). "New resilience model of communities based on numerical evaluation and observed post seismic reconstruction

process." *International Journal of Disaster Risk Reduction*, 602–609. https://doi.org/10.1016/j.ijdrr.2018.01.010

Wang, T., McCormick, J. P., Yoshitake, N., Pan, P., Murata, Y., and Nakashima, M. (2008). "Collapse simulation of a four-story steel moment frame by a distributed online hybrid test." *Earthquake Engineering Structural Dynamics*, 37(6), 955.

Wardrop, J. (1952). "Some Theoretical Aspects of Road Traffic Research." *Proceedings of the Institute of Civil Engineers, Part II,* 1, 325-378.

Weiner,E. (1997). U*rban Transportation Planning in the United States: An Historical Overview* (fifth edition), Report DOT-T-97-24, US Department of Transportation, Washington, DC

Wilson, G. A. (2013). "Community resilience, social memory and the post-2010 Christchurch (New Zealand) earthquakes." *Area* 45(2), 207–215. https://doi.org/10.1111/area.12012

Wu, T.-Y, El-Tawil, S., and McCormick, J. (2018a). "Highly Ductile Limits for Deep Steel Columns." *J. Struct. Eng*., 10.1061/(ASCE)ST.1943-541X.0002002, 04018016.

Wu, T.-Y., El-Tawil, S., and McCormick, J. (2018b). "Seismic collapse response of steel moment frames with deep columns." J. Struct. Eng., 10.1061/(ASCE)ST.1943-541X.0002150, 04018145.

Wu, T.-Y., El-Tawil, S., and McCormick, J. (2019). "Effect of cyclic flange local buckling on the capacity of steel members." *Eng. Struct*., 200. 10.1016/j.engstruct.2019.109705.

Xiao, Y., and Zandt, S. Van. (2012). "Building Community Resiliency: Spatial Links between Household and Business Post-disaster Return", *Urban studies*, 49(11), 2523–2542. https://doi.org/10.1177/0042098011428178

Xie, Y., Ebad Sichani, M., Padgett, J. E., & DesRoches, R. (2020). "The promise of implementing machine learning in earthquake engineering: A state-of-the-art review." *Earthquake Spectra*. https://doi.org/10.1177/8755293020919419

Xu, W., Yang, W., Zhang, C., and Yu, D. (2017). "Shake Table Test for the Collapse Investigation of a Typical Multi-Story Reinforced Concrete Frame Structure in the Meizoseismal Area." *Appl. Sci*. 2017, 7, 593.

Zeinoddini, V. M., and Schafer, B. W. (2012). "Simulation of geometric imperfections in cold-formed steel members using spectral representation approach." *Thin Walled Structures*, 60, 105–117. 10.1016/j.tws.2012.07.001

Zerin, A. I., Hosoda, A., Salem, H., and Amanat, K. M. (2017). "Seismic Performance Evaluation of Masonry Infilled Reinforced Concrete Buildings Utilizing Verified Masonry Properties in Applied Element Method." *Journal of Advanced Concrete Technology* , 15, 227–243.

Zhang, X., Mahadevan, S., and Goebel, K. (2019). "Network Reconfiguration for Increasing Transportation System Resilience Under Extreme Events." *Risk Analysis*, 39(9), 2054–2075.

Zhang, Y., Burton, H. V., Sun, H., and Shokrabadi, M. (2018). "A machine learning framework for assessing post-earthquake structural safety." *Structural Safety*, 72, 1–16.

Zhao, X., Tootkaboni, M., and Schafer, B. W. (2015). "Development of a Laser-Based Geometric Imperfection Measurement Platform with Application to Cold-Formed Steel Construction" *Experimental Mechanics*, 1779–1790, 10.1007/s11340-015-0072